Synthesis of colloidal semiconductor heterostructures for photocatalysis

Michael Job Enright

A dissertation

submitted in partial fulfillment of the

requirements for the degree of

Doctor of Philosophy

University of Washington

2019

Reading Committee:

Brandi M. Cossairt, Chair

Daniel R. Gamelin

D. Michael Heinekey

Program Authorized to Offer Degree:

Chemistry

University of Washington

Abstract

Synthesis of colloidal semiconductor heterostructures for photocatalysis

Michael Job Enright

Chair of the Supervisory Committee:

Assistant Professor Brandi M. Cossairt

Department of Chemistry

The development of colloidal nanoscale semiconductors for next-generation technologies is attractive due to their size-dependent optoelectronic properties and compatibility with solution-based manufacturing methods. This versatile class of nanomaterials holds great promise for light absorption, emission, and energy conversion. However, while the synthesis of single component, isotropic nanocrystals is well developed, the true promise of these materials is in their customization within heterostructure motifs where significant synthetic challenges remain. In

particular, colloidal semiconductor nanomaterial heterostructures hold great potential as photocatalysts. Efficient electron-hole recombination is promoted by quantum confinement making traditional quantum dots non-ideal for photocatalytic applications. However, charge carriers can be thermodynamically separated across a nanoheterostructure interface. This prolongs the lifetime of photogenerated charge carriers, paving the way for efficient photoredox chemistry. This thesis uncovers the underlying, generalizable principles for accessing tailor-made heterostructures to provide a roadmap for accessing desirable colloidal semiconductor nanoheterostructures. The generalized rubrics describe strategies and identify potential pitfalls for the synthesis of desirable nanostructures, even if explicit examples of the target structure have not been previously reported. Beyond developing anisotropic heterostructures with rod and tetrapod morphologies, this work demonstrates a new application for nanomaterial photocatalysis by using quantum dots to cleave C-O bonds in biomass model substrates. In all, this thesis makes strides in developing our understanding of how to design and synthesize colloidal semiconductor nanoheterostructures, and of the use of nanomaterials in photolytic applications.

.

TABLE OF CONTENTS

LIST OF FIGURES

LIST OF TABLES

LIST OF SCHEMES

ACKNOWLEDGEMENTS

During Brandi's introduction of me for my defense presentation I was honored to have my work ethic and laboratory presence be compared to Lebron James. However, even Lebron receives assistance from family, friends, teammates/coworkers, and coaches/mentors to achieve success. I want to thank my advisor, Brandi Cossairt, for being a fantastic mentor, supporting my researching interests, and pointing me in the right direction to achieve my research and professional goals. Brandi exemplifies the mentorship qualities of the very best advisors and coaches. The virtue I appreciated the most is her loyalty to her students. I always knew Brandi had my back throughout my graduate school education (even when I broke a piece off of a 6-month-old Schlenk line) and her continual support over the last 5 years is a defining pillar of my success in the lab.

I want to thank all of my coworkers in the Cossairt lab for creating an environment of both intellectual and social growth. Thank you, Florence Dou, Forrest Eagle, Betsy Flowers, Max Friedfeld, Dylan Gary, Benjamin Glassy, Danielle Henckel, Kira Hughes, Cecilia Johnson, Daniel Kroupa, Madison Monahan, Beth Mundy, Ian Murphy, Mike Norris, Nayon Park, Andrew Ritchhart, Tyler Robison, Coleman Schwartz, Jenny Stein, and definitely David Ung. Brandi and the Cossairt lab have created a special workplace for fostering and sharing new ideas. To me, CHB 317 is not just a location where I do my work, it is a place I want to be every day. To my undergraduates, Harrison Sarsito, Noushyar Panahpour Eslami, Nathan Lai, Zephyr Pitre, Kito Gilbert-Bass, Eric Riesel, and Shenwei Wu, I learned so much from you from the many hours we spent together and I am especially grateful for all of the outstanding work you have done to assist the lab's and my research projects. You taught me the two-headed dragon lifestyle and it is a great lifestyle for doing excellent research.

To my friends, thank you for being both excellent company and also a fun outlet to recharge when not in the lab. From floating down the Snoqualmie river and innertube basketball to hiking in the PNW's great outdoors and ICERs, I am appreciative of everything I had the opportunity to experience during the last 5 years. Thank you Maike Blakely, Jarred Olson, and Braden Zahora for getting me out of the lab for fun, hog wild activities. I am also grateful for all of my friends from the Midwest who made the trip out to Seattle to visit Elizabeth and me and stayed at Le Château d'Enright.

I also want to thank my family, which significantly increased in size in the summer of 2017, for being a pillar of support throughout graduate school. I can always rely on Robert and my parents for support and motivation when experiments do not always succeed in the lab. Most importantly, I want to thank my wife, Elizabeth, who joined me in Seattle for graduate studies. Thank you, Elizabeth, for always being my best and most supportive friend.

DEDICATION

To everyone who helped me accomplish my work, especially Elizabeth.

Chapter 1. INTRODUCTION

1.1 OVERVIEW

The synthesis of nanometer scale crystals has evolved since their first use as metallic glitters on ancient Mesopotamian pottery[1] and as ruby-red colorants in stained glass windows.[2] The last few decades have seen the degree of synthetic sophistication progress to enable the use of designer nanomaterials with tailored morphologies and surface chemistries in applications including biomedicine, color-conversion, and catalysis.[3-4] Today, synthetic efforts are increasingly focused on the atomically-precise synthesis of complex nanostructures with well-defined compositions. The purpose of this introduction is to summarize progress in the field towards the development of robust, reproducible synthetic techniques for accessing customizable colloidal semiconductor heterostructures. A focus on our current understanding of the mechanisms of crystal growth and composition evolution will be highlighted to extract generalizable design principles for semiconductor nanomaterials which are then used to develop clearly defined rules for heterostructure assembly.

Colloidal synthesis offers a versatile, inexpensive, scalable, solution-phase approach to creating semiconductor nanocrystals with tunable optical and electronic properties.[5-9] Semiconductor quantum dots hold potential to replace and improve many existing technologies, including display devices,[10-14] biological imaging, and medical delivery agents,[15-23] and light-driven catalysis for fuels and commodity

chemicals.[24-29] Heterostructured nanomaterials can offer additional functionality with respect to optoelectronic properties through spatial confinement or delocalization of charge carriers. For example, type I heterostructures possess a nested band alignment in which the conduction and valence band energy levels of one component semiconductor straddle the bands of the other semiconductor component.[30] This nested structure confines holes and electrons to the smaller band gap material and can give rise to higher photoluminescence quantum yields for improved application in photoemission devices by insulating and passivating defects at the core. Type II heterostructures, on the other hand, arise from materials with offset conduction and valence bands in which both the conduction and valence band edges of one material are at higher energies relative to the second material. This offset band alignment facilitates charge carrier separation across the heterojunction interface because regardless of which material serves as the light absorber, electrons will localize to the lowest energy conduction band while holes will be confined to the highest energy valence band. Type II heterostructures can be well suited for catalytic and photovoltaic applications due to slower charge carrier recombination that occurs on the nanosecond time scale as opposed to picosecond and faster times for exciton recombination in analogous single material systems.[31] In addition, because the photogenerated electron and hole are physically separated, Auger processes are also greatly suppressed.[32-34]

To date, a breadth of synthetic methods that have been developed for accessing, in particular, II-VI nanocrystal heterostructures. This introduction provides a review of the concepts governing core-shell heterostructure synthesis , as well as more complex anisotropic heterostructures that require more specialized synthetic methods, but that offer additional functionality. Three principle approaches for obtaining colloidal anisotropic heterostructures will be featured both in this review and through original work in subsequent chapters: top-down synthesis *via* cation exchange (Chapter 2), one-pot approaches from molecular precursors (Chapter 3), and seeded assembly (Chapter 3 and 4). Ultimately, it is found

that seeded assembly offers the greatest control and enables the most predictable product structures, but one-pot methods and top-down/post synthetic approaches (*i.e.* cation exchange) provide serviceable approaches as well as offering a more comprehensive understanding of how to obtain tailor-made colloidal semiconductor heterostructures.

An underlying goal throughout the process of heterostructure development is to ultimately use these materials as catalysts for light-driven transformations. While the hydrogen and oxygen evolution reactions dominate the field of photoredox catalysis with nanomaterials, they are increasingly viewed as competent materials for a wide range of organic transformations.[24-29] In an effort to expand the scope of nanoparticle driven photocatalysis, the light-induced cleavage of carbon oxygen bonds with quantum dots is developed as a model for both bond cleavage reactions with nanostructures as well as depolymerization of biomass (Chapter 5).

1.2 Core/Shell Quantum Dots

The most widely explored and developed colloidal heterostructures are core/shell quantum dots, including type I, type II, and advanced gradient or multi-shell structures (Figure 1.1). A common trademark of type I core/shell quantum dots is that a wide bandgap, protective shell assists in confining excitons to the core material while passivating defects that could create trap states and alternative modes of non-radiative exciton relaxation. This gives rise to quantum dots with high quantum yields, and tunable emission features that are better isolated from environmental influences, making these materials the leading choice for lighting, display, and imaging applications.[11, 35-36] The offset band structure of type II core/shell quantum dots leads to a red-shift in the heterostructure band gap and introduces a physical mechanism for charge separation, leading to suppression of Auger processes.[32-34, 37] Spherical type II core–shell heterostructures have therefore shown promise for photovoltaic and

photoelectrochemical applications.[38-39] In addition to traditional core/shell heterostructures where the shell thickness is typically a few monolayers, ultra-thick-shelled, or "giant" quantum dots, in particular CdSe/CdS core/shell QDs with shell thicknesses greater than 10 monolayers, have demonstrated impressive photophysical properties including blinking suppression and strongly reduced nonradiative Auger effects.[40-42] These giant QDs also exhibit enhanced chemical and photostability, making them ideal candidates for a range of single-particle photophysical experiments.

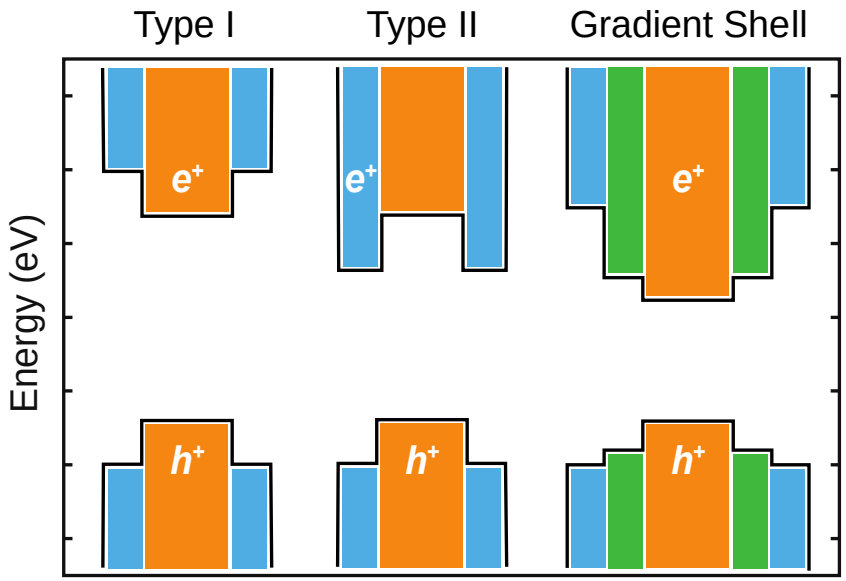

Figure 1.1. Energy level diagram of type I, type II, and representative gradient core-multishell semiconductor heterostructures.

Along with band alignment, the requirement of an epitaxial interface between the core and shell materials is critical in realizing the idealized function of core/shell QDs, requiring precision control over the synthesis. One pot synthetic methods have been developed, but require pre-designed control over the relative reactivities of the molecular precursors used to access both materials, with the core precursors requiring elevated reactivity to produce nuclei.[43-45] Because of this, core/shell QDs are predominantly synthesized in a multi-step procedure that involves core synthesis and purification,

followed by subsequent shell growth.[46-47] Independent nucleation of the shell material and uncontrolled core ripening is generally prevented by maintaining a lower temperature during shell growth than is used for core synthesis.[36] The shell growth step can be carried out using a variety of approaches: slow addition of low-reactivity precursors,[36, 48] selective ionic layer adhesion and reaction (SILAR),[40, 49-50] and colloidal atomic layer deposition.[51] The most advanced and well-developed shell-growth strategy that enables retention of crystalline quality and minimal introduction of defects across a range of shell thicknesses is the SILAR method.[50, 52] In this method the shell material is added one monolayer at a time by the sequential addition of cation and anion precursors to the QD cores.[50] When compared to earlier approaches that relied on co-injection of cation and anion precursors, SILAR offers the advantage of higher shell growth temperatures due to the self-limiting nature of the reaction chemistry and prevents nucleation of nanocrystals. SILAR is likely not required for growth of thin shells and is perhaps not required in the case of lattice-matched systems;[48] however, this approach was clearly shown to improve the size distribution of moderately thick-shell CdSe/ZnS core/shell NQDs (large lattice match: 12%) compared to their single-injection counterparts.[53] Moreover, SILAR can be combined or modified by thermal cycling to enable low-temperature, conformal coating of QDs followed by an elevated temperature annealing or crystallization step where finer morphological control is required.[54]

Core/multi-shell QD heterostructures have also been assembled to maximize the benefits of type I and type II systems. While core/shell systems can improve charge separation by localizing charge carriers to the core or shell, undesirable exciton leakage across the core and shell boundary is not entirely prevented despite the offset energy levels. Thus, thicker shells are required to protect confined excitons in type I systems or better separate charge carriers in type II arrangements. Lattice mismatches between materials, however, may limit the sizes of the core or shell that may be used as well as create strain induced defects that introduce new modes of non-radiative recombination that the protective shell is

designed to diminish. A commonly highlighted example of lattice mismatch challenges in type I structures is using ZnS as a shell for CdSe;[55] the 12% lattice mismatch between the two materials limits shell growth to only a few (2–3) monolayers. The lattice mismatch between ZnSe and CdSe is only 6.3% and the mismatch is even smaller, 3.9%, for CdS and CdSe. While the lattice mismatch improves, the energy offsets decrease. The core/multi-shell approach provides a gradient of progressively increasing bandgaps between a CdSe core and ZnS shell such as: CdSe/CdS/(Cd,Zn)S/ZnS[36, 53] and CdSe/ZnSe/ZnS.[56-57] The layered shells facilitate a smooth change in lattice parameter to the greater band gap offset. The gradient alloy layer serves these systems by facilitating a smooth, tunable transition between two layers that would otherwise have a large lattice mismatch. In addition, systematic, thermally driven interfacial alloying of shell layers can provide a mechanism to control the electronic structure in QD heterostructures and enable switching between type I and type II configurations.[58] Precise tailoring of the individual shell thicknesses to compensate for the various exciton decay pathways can even allow for balancing the competing effects of induced latticed strain and confinement potential to enable the realization of smaller sized QDs with reduced blinking.[59]

1.3 Anisotropic Nanocrystals

For all their utility in emissive applications and in enabling detailed investigation of the fundamental photophysics of colloidal nanocrystal heterostructures, core–shell quantum dots can be limited in terms of their practical application in schemes where charge separation is desired. Considering photocatalysis as an illustrative example, in type II core–shell structures, one of the charge carriers will be confined to the core while the other carrier may be extracted from the shell at the surface to facilitate redox reactions. To envision using these core–shell structures as long-term photosensitizers, and to avoid energy loss due to charge recombination, the hole or electron localized to the core must be

efficiently quenched through application of an applied bias or by a sacrificial chemical redox equivalent. In solution and in the presence of sacrificial donors, hole refilling from the donor is often competitive with back electron transfer between a substrate and the nanocrystal.[60-62] For quantum dots adsorbed to electrodes, hole refilling must proceed *via* electron transfer from the electrode surface through the tethering ligands and into the quantum dot. In a representative system, the rate of hole refilling *via* an electrode was slower than back electron transfer from a methyl viologen substrate.[63] Even using conjugated linkers to improve electronic communication between the electrode and nanoparticle does not facilitate hole replenishment at a competitive rate to back electron transfer. Type II heterostructures are designed to trap holes away from the electron to prolong exciton lifetimes and reduce the rates of parasitic back electron transfer reactions. However, in core/shell type II systems, only one of the materials presents a directly accessible surface. Thus, these structures rely on electron tunneling to resupply charge carriers (*i.e.* holes confined to the core). To obtain type II heterostructures without systemic inefficiencies that lead to energy loss from charge recombination, both materials in the heterostructure must be physically accessible for charge carriers to be replaced *via* a wire or sacrificial donor.

To get around the physical challenges regarding charge replenishment, alternative structural motifs must be utilized to better facilitate the cyclical process of excitation, charge transfer, and regeneration. Anisotropic heterostructures retain all of the excitation and charge separation benefits afforded by the core–shell structure but also offer greater customizability, physical access to both materials across the heterojunction for unimpeded charge replenishment, and unique facets and materials for selective functionalization.[64] A key challenge for adopting efficient and inexpensive nanomaterials into photocatalytic and photovoltaic applications is the lack of robust synthetic methods for obtaining anisotropic heterostructures. For translation to market, processes for preparing anisotropic

nanocrystal heterostructures must be scalable and inexpensive, making solution processing one of a few suitable methods.

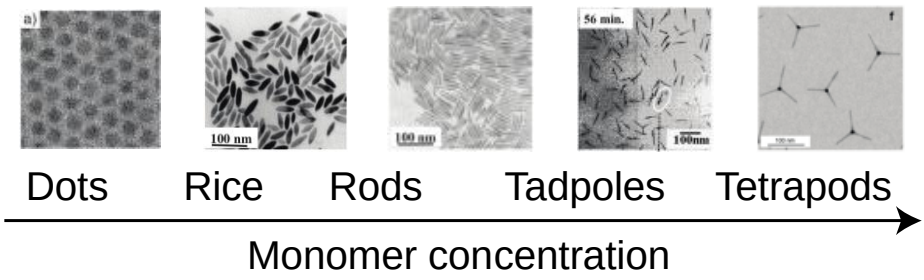

Figure 1.2. Example structures that can be obtained from one-pot, bottom-up colloidal synthetic methods. While synthetic conditions will ultimately dictate the product nanomaterial shape and structure, a corollary trend between shape and monomer concentration is observed here. Dots: Reprinted with permission from D. V. Talapin, A. L. Rogach, A. Kornowski, M. Haase, and H. Weller, *Nano Lett.*, 2001, **1**, 207–211. Copyright 2001 American Chemical Society.[46] Rice, rods, tadpoles: Reprinted with permission from Z. A. Peng and X. Peng, *J. Am. Chem. So*c., 2002, **124**, 3343–3353. Copyright 2002 American Chemical Society.[65] Tetrapods: Reprinted by permission from Nature Research: L. Manna, D. J. Milliron, A. Meisel, E. C. Scher and A. P. Alivisatos, Controlled growth of tetrapod-branched inorganic nanocrystals, *Nat. Mater.*, 2003.[66]

Colloidal methods for semiconductor nanocrystal synthesis have demonstrated reproducible procedures for synthesizing a myriad of shapes (Figure 1.2): dots,[6, 46, 67-69] rods,[65, 68, 70] arrows,[70] rice,[65] teardrops,[70] tetrapod,[65, 70] and wire nanoarchitectures,[71] among others. In a typical one-pot approach, colloidal semiconductors are synthesized using a hot-injection method where precursors are rapidly added to a pre-heated solution of solvent and surfactants.[67] The elevated temperature leads to rapid monomer formation. Ultimately, per the La Mer nucleation model, the number of monomers reaches a

critical concentration, which leads to nucleation.[72] Remaining monomers assemble on the surface of the growing nanocrystal. In the case of isotropic nanocrystals growth can be allowed to proceed to completion in many cases without detrimental ripening effects, however in the case of anisotropic nanocrystals where maintaining kinetic growth conditions is crucial, the reaction is typically quenched at a prescribed point by rapidly reducing the temperature or seizing the reaction with an additive.

Structural diversity is obtained by exploiting distinct reaction conditions to obtain specific products. Precursor injection temperature and ligand concentration are important variables because these conditions can set the phase of the nanostructure. Cadmium selenide provides an illustrative example. CdSe typically forms in the kinetic zinc blende phase at low temperature. Nucleation at temperatures above 300 °C or thermal annealing of zinc blende nanocrystals gives rise to crystalline wurtzite CdSe. Interestingly, given the relatively small difference in energy between the zinc blende and wurtzite structures (1.4 meV per CdSe unit), it has been observed that the ligand-surface interaction can play a large role in phase determination at a given temperature, with carboxylate ligands stabilizing the zinc blende structure and phosphonate ligands stabilizing the wurtzite structure.[73] Furthermore, by adjusting the concentration of monomers in the reaction solution, distinct shapes can be targeted. Spherical nanocrystals form at the lowest monomer concentrations, followed by rice grains, rods, and then branched structures with increased concentration.[65] Spherical nanocrystals are the most thermodynamically stable shape[65, 74] across this spectrum of products and are also the product of Ostwald ripening.[75-77] This concentration dependence is a fluid spectrum; elongated structures can readily be obtained by bolstering the monomer concentration in a sample of growing spheres. Conversely, spheres can be evolved from their higher aspect ratio counterparts if left in solution with a low monomer concentration.

There are three distinct mechanistic stages in the temporal evolution of anisotropic structures (Figure 1.3).[74] To promote elongation of the nanocrystal, wurtzite structures are preferred due to the higher chemical potential along the structure's (0001) axis (also known as the *c*-axis). Each growing nanocrystal is surrounded by a diffusion sphere defined by a concentration gradient between the bulk solution and the stagnant solution about the nanocrystal. Monomers near the crystal (within the diffusion sphere) readily add to the surface of the nanocrystal leading to continued diffusion of monomer in solution into the sphere. The first mechanistic stage is growth along the long *c*-axis. At high monomer concentrations, growth occurs nearly exclusively along the *c*-axis, the face of the nanocrystal with the highest chemical potential.[78] As available monomer is consumed by the growing nanocrystal, the relative concentration of monomer in solution decreases and moves into the diffusion sphere at a slower rate. At this intermediate growth concentration, known as the 3D-growth regime, monomers grow on all facets simultaneously.[74] The third stage occurs after the concentration of monomers diminishes sufficiently to no longer drive new monomer to enter the diffusion sphere. At this point, interparticle diffusion occurs where monomers from the rod ends migrate towards the middle of the nanorod to give isometric products.[74] For CdSe, these stages were identified quantitatively by tracking cadmium concentration in solution by mass. From 1.4–2% the rods are in the 1D-growth regime and enter the 3D-growth regime at 0.5–1.4% cadmium by mass. At 0.5%, the cadmium mass percentage concentration remains constant as the nanocrystals exist in the interparticle diffusion regime.[74]

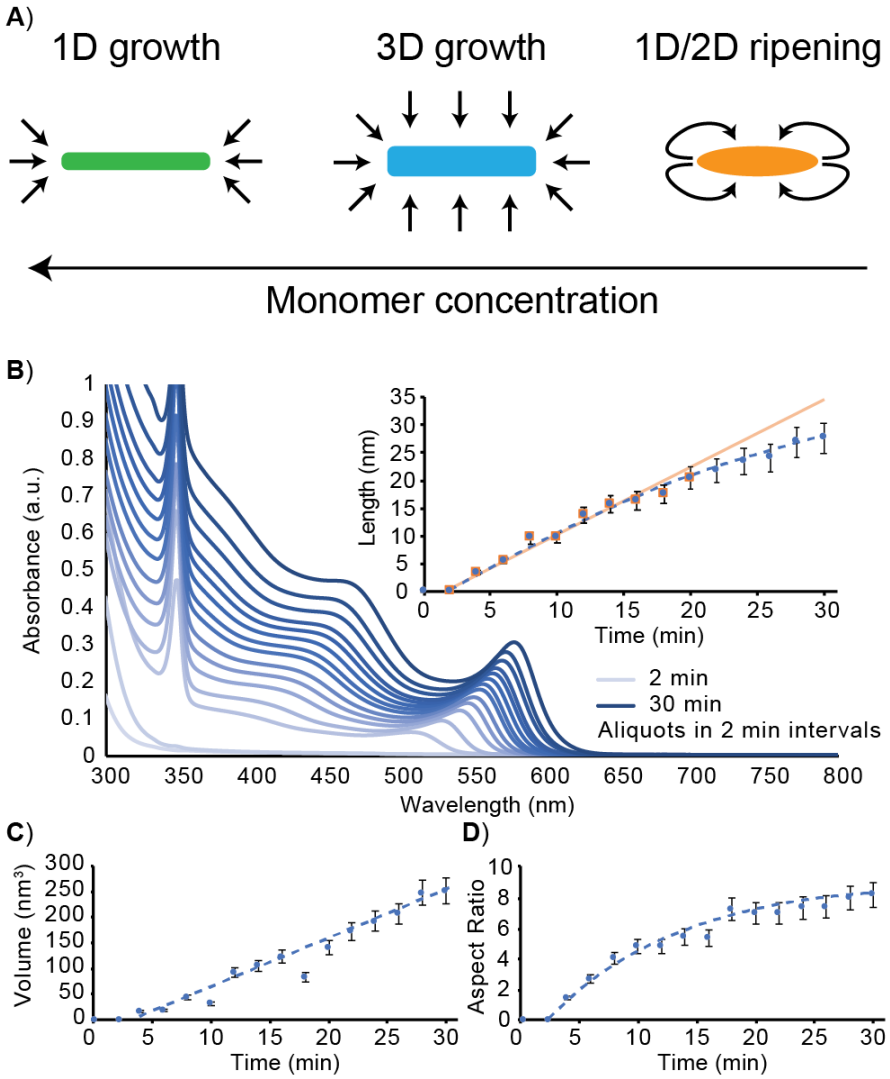

Figure 1.3. Mechanism and evaluation of nanorod growth. (A) Three stages of anisotropic nanostructure growth as a function of monomer concentration. Arrows indicate the direction of diffusing monomers. (B–D) Evaluation of unseeded CdSe nanorod growth. (B) UV-Vis spectra at 2 min intervals over the first 30 min of nanorod growth. Nanorod dimensions measured using TEM analysis as a function of time are plotted for length (B, inset), volume (C), and aspect ratio (D). The equation for the line of best fit for the volume *vs.* time relationship is $y = 9.7919x - 44.591$. (B–D) Adapted from ref. 79 with permission from The Royal Society of Chemistry.[79]

Transitions between kinetic and thermodynamic growth regimes are observable by tracking nanomaterial growth using transmission electron microscopy. In a representative case, we have conducted profile mapping of length and aspect ratio of growing CdSe nanorods showed the transition point between 1-D and 3-D growth to occur within 20 min of precursor injection with trioctylphosphine selenide in a cadmium tetradecylphosphonate bath. The transition from 1-D to 3-D growth is indicated by a characteristic tapering off of length growth and a plateau of aspect ratio (Figure 1.3).[79] Furthermore, tracking nanocrystal width and volume change over time revealed a growth rate of 2.9 to 3.5 monomer rod^{-1} s^{-1} for unseeded and seeded CdSe nanorods respectively growing at 250 °C. This type of quantitative evaluation of growing anisotropic structures offers a template for determining when kinetic growth conditions have been established for nanostructures. Similar analysis has also shown CdS nanorods to assemble at 36 monomers rod^{-1} s^{-1} upon wurtzite seeds while length growth predominates for 13.5 minutes of crystal growth.[79] The monomer concentration ranges used to access rod elongation are only a small component of the spectrum of monomer concentrations that give nanocrystals. As monomer concentrations are decreased, spherical quantum dots are formed. Considering the relationship between 1-D and 3-D growth it is unsurprising that lower aspect ratio nanocrystals would form under reduced monomer conditions. Alternatively, increasing the monomer concentration above rod growth conditions has led to tetrapod and branched structure formation.[65, 70, 78]

A challenge for reproducibility in colloidal systems is exclusively promoting nucleation at a single point early in the reaction before conditions for nanocrystal growth are established. To achieve monodisperse nanoparticles, the temporal progression of precursor conversion, nucleation, and growth must be balanced to generate conditions that enable all of the evolving crystals to have effectively the same growth history.[80] An additional challenge in systems designed to target more advanced nanostructures is that the solution conditions may not favor the same kinetic growth conditions

throughout the reaction, potentially leading to phase transitions in the growing nanocrystal.[66] Furthermore, due to the need to control both nucleation and growth conditions in a single reaction, tuning the nanocrystal shape, size, and structure becomes increasingly difficult.

Tetrapod synthesis is a clear demonstration of overcoming the challenges associated with balancing nucleation, growth, and differences in stability between the cubic and hexagonal crystal phases (Figure 1.4).[66, 70, 81] For example, nanotetrapods of CdSe[70] and CdTe[66, 81] were assembled in a one-pot synthesis by first obtaining zinc blende cores *in situ* with four (111) facets with growth of four wurtzite rod arms, each terminated with wurtzite $(000\bar{1})$ facets. A requirement for the *in situ* synthesis of nanotetrapods is that the energy difference between wurtzite and zinc blende structures must be low so that switching between the two phases is possible, but not so low that there is no energetic preference for one phase over the other. In highly ionic and covalent systems, the energy difference between the different crystal structures is too high (>10 meV per atom) to enable *in situ* polytypism.[82] Conversely, the energy difference between phases of several II–VI semiconductors, (CdS, CdSe, and ZnS) is barely a few meV per atom, which makes it challenging to create conditions that change the accessible phase over the course of a reaction. Interestingly, cadmium telluride falls into a sweet spot that allows selective nucleation of zinc blende cores, which are still favored at high temperatures that typically promote wurtzite assembly, before ultimately growing wurtzite arms upon the core's (111) planes. Wurtzite growth is the preferred crystallinity at high temperatures when alkyl phosphonate ligands are present.[82] Despite the low phase transition energy barrier between zinc blende and wurtzite crystal structures for CdSe, tetrapods were still obtained in mixtures of rods due to some nucleation of zinc blende cores in conditions that predominately promote wurtzite growth.[70] While these pioneering syntheses of tetrapods demonstrated the ability to elicit structural complexity within a single reaction environment, the narrow window of conditions (temperature and ligand concentration) in combination with characteristics of the

material (nucleation of zinc blende nanocrystals even under wurtzite promoted growth conditions) limits the generality of these methods.

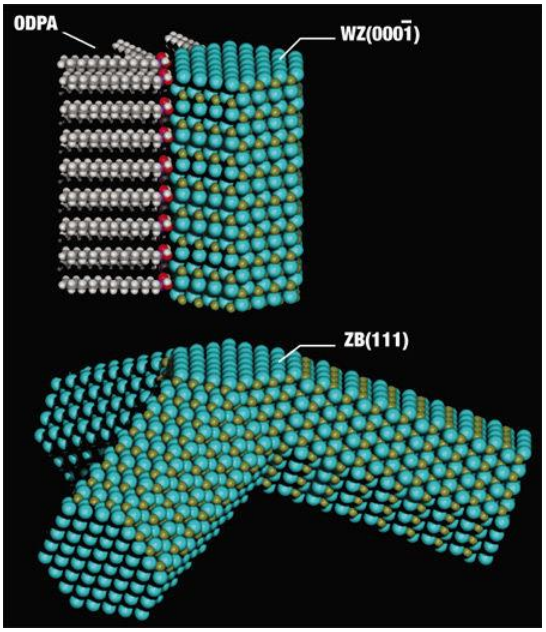

Figure 1.4. A dissected view of the core and arm facets of a II–VI tetrapod. Phosphonate ligands selectively bind to the circumferential facets of the wurtzite tetrapod arms. Reprinted by permission from Nature Research: L. Manna, D. J. Milliron, A. Meisel, E. C. Scher and A. P. Alivisatos, Controlled growth of tetrapod-branched inorganic nanocrystals, *Nat. Mater.*, 2003.[66]

1.4 ANISOTROPIC HETEROSTRUCTURES IN ONE-POT FROM MOLECULAR PRECURSORS

The next level of complexity in colloidal nanocrystal synthesis from anisotropic nanocrystals is anisotropic heterostructures. This chemistry has been enabled for II–VI semiconductors by the development of simple, scalable methods for generating the starting seeds. Prior to 2001, cadmium chalcogenide nanocrystals were customarily synthesized using dimethyl cadmium ($Cd(CH_3)_2$).

However, in addition to high cost and thermal instability, $Cd(CH_3)_2$ is both pyrophoric and toxic. In a pivotal study on cadmium chalcogenide nanocrystal synthesis, Peng and Peng reported that CdO could replace $Cd(CH_3)_2$, giving rise to high quality quantum dots and rods for CdS, CdSe, and CdTe.[83] This new scheme provided a more reproducible, straightforward, and scalable synthetic approach accessible to even undergraduate chemists.[84]

When using CdO as a precursor, the active cadmium source is generated *in situ* and is already present in solution for hot injection of the chalcogenide reagent. Korgel *et al.* took advantage of this approach to elongate CdE (E = S, Se, Te) nanorods with a series of chalcogenide precursor injections.[85] The initial chalcogenide injection seeded CdE growth and each subsequent addition selectively grew epitaxially on the (0001) hexagonal planes to elongate the nanorods. By changing the identity of the chalcogenide during subsequent additions, this procedure was used to generate heterostructures with a well-defined transition between the two components of the heterostructure without obvious stacking faults (Figure 1.5).[85] Depending on the relative bandgap alignment of the components of the heterostructure, modulation of the photoluminescence quantum yield by an order of magnitude was realized. Upon depletion of the cadmium–phosphonate complex and continued heating, the nanorod ends were observed to ripen into spheres with a significant number of stacking faults. Ripening was not observed for the core rod components and could be prevented at the ends with rapid quenching of the reaction upon completion of nanorod growth.

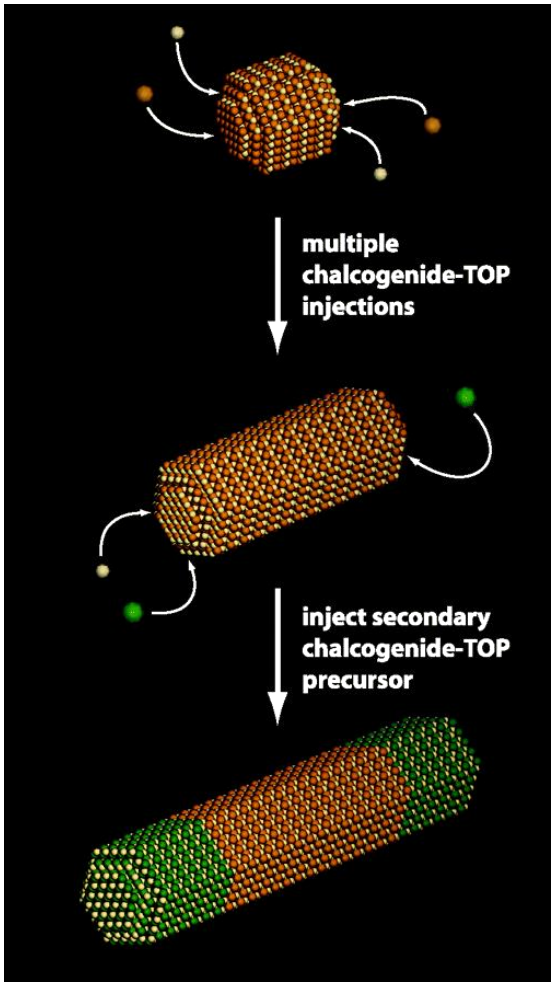

Figure 1.5. General outline of growth of cadmium chalcogenide nanorod and nanorod heterostructures. Multiple injections of chalcogenide precursor in a bath of cadmium precursor yields growth along the *c*-axis. Changing the chalcogenide precursor in subsequent additions gives growth of the new cadmium chalcogenide component to yield rod-rod heterostructures. Reprinted with permission from F. Shieh, A. E. Saunders, and B. A. Korgel, *J. Phys. Chem. B*, 2005, **109**, 8538–8542. Copyright 2005 American Chemical Society.[85]

Using a comparable growth procedure in which preformed cadmium phosphonate is present in excess upon addition of chalcogenide, Alivisatos and co-workers demonstrated control over nanocrystal composition and branching throughout a nanoheterostructure synthesis.[86] This work elaborated on

similar studies that showed zinc blende–wurtzite polytypism in CdTe tetrapods enabled arrangement of four wurtzite quantum rods of the same composition about a central zinc blend quantum dot core.[66] From rod elongation of cadmium chalcogenides (or from the wurtzite arms of a tetrapod) stacking faults form zinc blende segments that serve as scaffolds for growth of new branches. The zinc blende facets branch the growing nanocrystal by forming several identical facets that, upon nucleation of new branches, revert to anisotropic wurtzite growth. Zinc blende formation is facilitated when the system is supersaturated with precursor immediately following injection, followed by wurtzite growth as the precursor is consumed. Furthermore, the size of the core and secondary tetrapods and the distance between them could be regulated with careful timing of subsequent additions and amounts of precursors.[86]

Anisotropic heterostructure development has made significant strides in systems that conserve the cation or anion sublattice, however, the current scope of heterostructures containing materials that differ with respect to both the cation and anion components is limited. Breaking the need to retain a cation or anion sublattice throughout the entire heterostructure is valuable for designing structures with greater offset conduction and valence bands to better separate charge carriers and prolong exciton lifetimes. A major pitfall of anisotropic heterostructure assembly from molecular precursors is that a one-pot approach hinders development of new material combinations. Anisotropic nanocrystal growth often only occurs in a narrow range of synthetic conditions, such as high monomer concentration. Direct addition of precursors for a different material with the expectation that nanocrystal growth will be exclusively of the new component is synthetically challenging. The presence of remaining monomer from growth of the core promotes competitive alloying or cation exchange processes instead of heterostructures with clearly defined interfaces.

1.5 HETEROSTRUCTURES USING TOP-DOWN, POST-SYNTHETIC METHODS

As demonstrated by the bottom-up synthetic methods using molecular precursors, a spectrum of sizes and shapes of nanocrystals can be obtained from one-pot synthetic approaches. Core/shell dots, heterodumbells, and heteronanorods are some of the most sophisticated structures obtainable in colloidal systems. However, accessing these heterostructures for all material combinations *via* heteroepitaxial growth techniques can be challenging. Top-down cation exchange methods offer new opportunities for accessing heterostructures and tuning the optoelectronic properties of nanocrystals. In fact, large libraries of distinct heterostructured nanoparticles with precisely defined materials and interfaces can be amassed using cation exchange and post synthetic modification procedures, with Schaak *et al.*'s collection of 47 metal sulfide nanostructures as an illustrative case.[87] Cation exchange is a particularly useful approach to tune a quantum dot's band gap, Fermi level, and emissive properties through dopant incorporation.[88-97] Cation exchange that is allowed to proceed to a greater extent than just a few percent dopant ion incorporation leads to changes in the structural and optoelectrical properties of the nanostructure and can be an effective means of obtaining heterostructures.[96, 98-103] Furthermore, in some anion sublattices, cation exchange can be sufficiently well controlled to give a range of structures from homogeneous alloys, to gradient alloys, to core/shell quantum dots (Figure 1.6).[98, 101, 104]

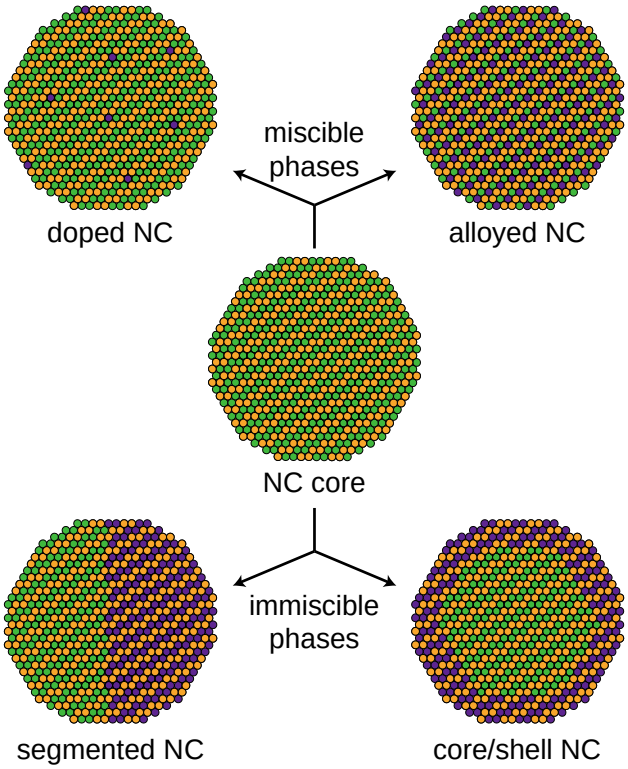

Figure 1.6. Cation exchange mediated synthesis of doped, alloyed, segmented, and core/shell heterostructures.

For example, cation exchange of Cd^{2+} and Zn^{2+} for Pb^{2+} in chalcogenide lattices has been accomplished to yield lead chalcogenide nanostructures that retain the original chalcogenide (sulfide, selenide, or telluride) lattice. This process was observed to be thermally activated and the extent of the reaction controlled by modulating temperature and reaction duration. In particular, anisotropic cation exchange on spherical cadmium chalcogenide nanocrystals could be accomplished with exchange starting at one edge of the nanocrystal and proceeding along the (111) direction to leave a sharp interface on the (111) crystallographic plane.[105] The final, incomplete cation exchange products in sulfide and selenide lattices are quasi-spherical, Janus-type CdS/PbS and CdSe/PbSe heterostructures, respectively. It was demonstrated that the degree of conversion to the lead chalcogenide component was directly dependent upon the initial temperature for the partial exchange reactions.[105] Replacement of Cd^{2+} with

lead can also be accomplished in two steps by first replacing the cadmium with copper and then substituting the copper with lead.[106] In the case of selenide lattices, cation exchange has been observed in both directions for Pb^{2+} and Cd^{2+}.[104, 107] Exchange of Cd^{2+} for Pb^{2+} is driven by a vacancy assisted migration mechanism.[107] Incomplete exchange led to the formation of core/shell PbSe/CdSe.

Moreover, de Mello Donega and co-workers demonstrated thermally tunable cation exchange in which Zn^{2+} and Cd^{2+} exchange in a selenium sublattice to give a distribution of (Zn,Cd)Se nanocrystals. The spectrum of structures accessed in this system (from core/shell nanocrystals, to alloys) enabled tailoring of the optoelectronic properties and charge carrier localization.[101] Starting from zinc blende ZnSe, treatment with $Cd(oleate)_2$ at 150 °C provided core/shell ZnSe/CdSe with clearly defined core and shell components. The same $Cd(oleate)_2$ treatment at temperatures between 200 and 220 °C gave gradient $(Zn_{1-x}Cd_x)Se$ alloy nanocrystals with increasingly smooth gradients from core to outer shell with increased temperature. Above 240 °C, homogeneous $(Zn_{1-x}Cd_x)Se$ alloys were obtained. This trend holds for nanocrystals over a range of quantum confined dimensions. Further post-synthetic thermal annealing of core/shell and gradient nanostructures yielded homogeneous $(Zn_{1-x}Cd_x)Se$ alloys, regardless of starting composition and structure. The mechanism proposed for this process is that cation exchange rapidly occurs at the nanocrystal surface followed by slower, thermally activated solid-state cation diffusion into the selenium sublattice. Mediated by Frenkel pairs, interstitial Zn^{2+} migrates outward while incoming Cd^{2+} diffuses towards the core *via* a vacancy hoping mechanism. Since new layers of material are not added to the nanocrystal, the size of the nanocrystal remains relatively unchanged. This cation exchange process is promoted by the greater stability of $Zn(oleate)_2$ in solution *vs.* $Cd(oleate)_2$ as well as the greater bond strength between Cd–Se over Zn–Se.[101]

The activation barrier for cation exchange of Cd^{2+} in ZnSe has been determined to be between 30 and 40 kJ mol^{-1}.[108] Our investigations have revealed that in the softer telluride sublattice, the

activation barrier to cation exchange between Cd^{2+} and Zn^{2+} in ZnTe nanorods was measured to be 24 kJ mol^{-1} following initial adsorption of cadmium to the nanorod surface.[98] The low activation barrier for cation exchange in ZnTe has enabled core/shell nanorods with thin CdTe shells at room temperature and alloyed $(Zn_{1-x}Cd_x)Te$ nanorods at 75 °C. Further evaluation of cation exchange in the $(Zn_{1-x}Cd_x)Te$ system revealed that cation exchange could be slowed by starving the system of Cd^{2+}, which results in incomplete surface passivation.[98]

The aforementioned cation exchange studies on isotropic starting materials highlight synthetic challenges associated with heterostructure development. Nanocrystal growth typically occurs at elevated temperatures, readily driving cation exchange preferentially to nanocrystal growth due to the low energetic barriers in chalcogenide lattices. Thus, attempts to grow cadmium chalcogenide components on zinc chalcogenide seeds have been unsuccessful. However, cation exchange procedures have been devised to directly give anisotropic heterostructures by selectively exchanging on a single edge or select facet to give rod-rod or hetero-octopod heterostructures.[109-110] For example, anisotropic CdS/Cu_2S heterostructures were created *via* cation exchange between copper and cadmium to give heterostructure nanorods.[109] Since the orthorhombic form of Cu_2S and the hexagonal (wurtzite) form of CdS both have hexagonal close-packed structures with nearly identical sulfur sublattices, cation exchange is readily facilitated without imposing significant strain to the nanorod lattice or interface between the copper and cadmium components.[111] In fact, even when all cadmium is exchanged for copper to give Cu_2S nanorods, the size and shape is conserved with only an 8% contraction in lattice volume.[109] The (001) axis of the orthorhombic Cu_2S component lies parallel to the hexagonal CdS(0001) plane. The difference between relative activation barriers for nucleation at the $(000\bar{1})$ and (0001) end facets of CdS gives rise to asymmetric cation exchange. The formation energy for Cu_2S at the $(000\bar{1})$ end is lower by ~0.18 eV per Cd–Cu–S unit compared to the (0001) end, due to the presence

of three dangling bonds per atom, thereby promoting surface passivation by seeding orthorhombic Cu_2S preferentially.[112] Nucleation at the end facet is the main kinetic barrier for cation exchange. Once nucleation has occurred, the kinetic barrier for further cation exchange is lowered and promotes continued exchange into the anionic sublattice.[113-114] It was also observed that increasing the diameter of the CdS nanorod offered flatter CdS nanorod ends and better promoted cation exchange exclusively at the $(000\bar{1})$ end.[109] Similarly, selective exchange was observed in CdSe/CdS octopods. Partial cation exchange between copper and cadmium at the arm tips gave ternary nano-octopods with cubic sphalerite CdSe cores, hexagonal wurtzite CdS arms, and hexagonal Cu_2S ends.[110] However, the only way to promote asymmetric cation exchange in these systems is to maintain a low concentration of Cu^+ ions. Elevated concentrations of Cu^+ led to indiscriminate cation exchange at both ends of the CdS nanorods or more rapid exchange of all cadmium for copper (Figure 1.7).

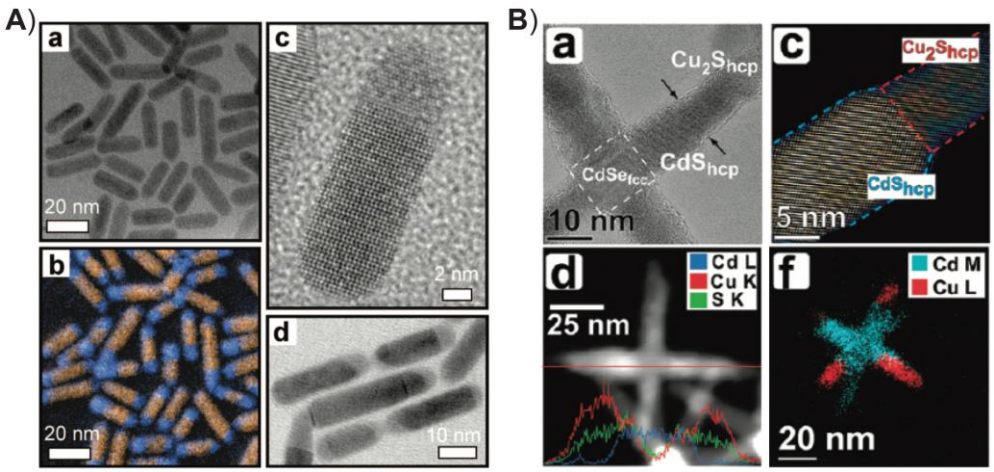

Figure 1.7. TEM images of selective cation exchange of Cu^+ for Cd^{2+} in sulfide sublattices. Images are of nanorods (A) and octopods (B). (A) Reprinted with permission from B. Sadtler, D. O. Demchenko, H. Zheng, S. M. Hughes, M. G. Merkle, U. Dahmen, L.-W. Wang and A. P. Alivisatos, *J. Am. Chem. Soc.*, 2009, **131**, 5285–5293. Copyright 2009 American Chemical Society.[109] (B) Reprinted with permission from K. Miszta, D. Dorfs, A. Genovese, M. R. Kim and L. Manna, *ACS Nano*, 2011, **5**, 7176–7183. Copyright 2011 American Chemical Society.[110]

Cation exchange is dependent on a number of variables: temperature, relative bond strengths of the pre- and post-cation exchange materials, stability of the exchanging and departing ions in solution, reactivity and concentration of other species in solution, and purification procedures used to clean the nanocrystals. In general, increasing the temperature increases the rate and extent of cation exchange.[98, 101] However, when the anion precursor is also present in solution, increasing the temperature facilitates monomer formation to better enable shell growth preferentially over the competing cation exchange pathway.[115] A principle driving force of cation exchange is the relative stability of the exchanging and departing cations in solution. Typically, harder Lewis acids will preferentially depart the nanocrystal lattice in the presence of hard Lewis base ligands, such as oleate. Reactive ligands, especially oleates

and thiols, will also assist in etching nanocrystals, which better facilitates adsorption of the new cation at the nanocrystal surface. Saturation of the nanocrystal surface is vital for promoting and prolonging cation exchange. Similarly, the bond strength of the cations to the anionic lattice will be a determining factor in cation exchange progressing forward. When formation enthalpies favor the new cation, a thermodynamic driving force exists to enable the cation exchange process.

Lastly, ligands can also be used to passivate the surface and mitigate cation exchange. Recently, it was shown that residual acetate ligands on nanocrystal surfaces slowed down cation exchange and etching processes.[115] While cation exchange is a powerful tool for obtaining precisely tunable nanomaterials,[91, 98-101, 103, 116] meeting all of the criteria for cation exchange for any given combination of cations is still limited, preventing access to some desirable systems.

Another top-down approach for obtaining heterostructures with a clearly defined interface is thermally induced atomic reconstruction. For example, thermal annealing of PbSe/CdSe core/shell quantum dots led to the formation of Janus type segregated bi-hemispheric heterostructures joined by a common (111) Se plane.[117] Using *in situ* TEM, the structural and morphological reconstruction was observed to be primarily driven by reconstruction of the CdSe shell. At temperature ranges between 150 °C and 200 °C, the CdSe shell migrates to one side of the heteronanocrystal to separate into a CdSe and a PbSe section. When the volumes of CdSe and PbSe are equivalent, the resulting product is perfect bi-hemispheric heteronanospheres. At unequal volumes, the two phases still segregate under thermal annealing but instead form two spheres bound together by a selenium (111) atomic plane. The joining (111) plane forms a near perfect heterointerface between the cubic zinc-blende CdSe and the octahedral PbSe structures. The presence of oleate capping ligands at the surface prevented coalescence and inter-particle ripening (Figure 1.8).

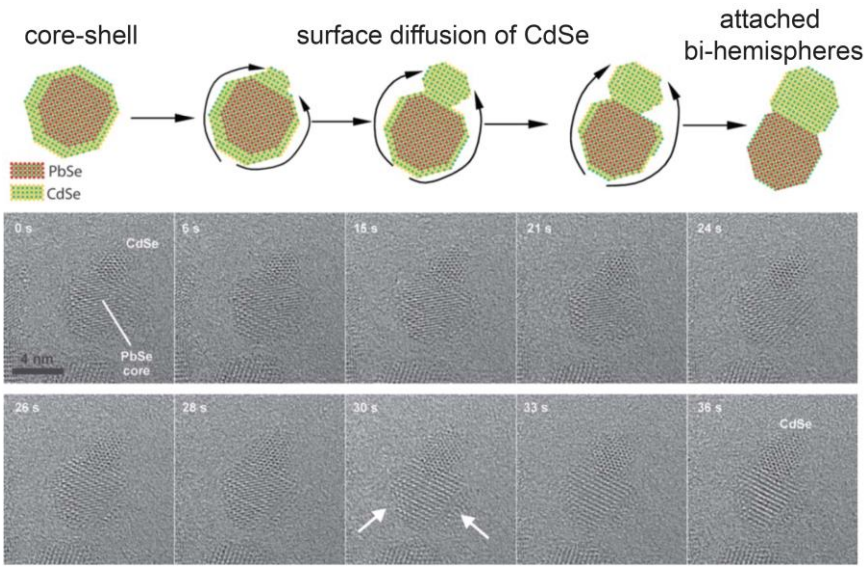

Figure 1.8. Evolution of PbSe/CdSe core/shell nanoparticles to Janus-type bi-hemisphere particles joined by the selenium (111) atomic plane. Reproduced from ref. [117] with permission from The Royal Society of Chemistry.[117]

1.6 ANISOTROPIC HETEROSTRUCTURES FROM ISOLATED SEEDS

We can learn several lessons from the growth of anisotropic nanostructures from molecular precursors and from top-down methods like cation exchange. However, it remains a challenge to obtain a target heterostructure with a particular shape and combination of materials with only a one-pot synthesis. We are also severely limited in accessing certain heterostructures with post-synthetic modification due to limitations in ion diffusivity in many lattice types. However, we can use much of the knowledge generated in the direct synthesis of anisotropic heterostructures from one-pot procedures using molecular precursors to develop seeded growth approaches that enable predictable access to tailor-made nanostructures.

As a representative case in point, anisotropic CdS/ZnSe is a highly sought after heterostructure due to the type II band structure. Attempts to obtain these structures typically involve treatment of

purified CdS nanorods with zinc and selenium precursors.[118] It has been observed that treatment of zinc chalcogenide nanomaterials with cadmium precursors will preferentially lead to cation exchange under typical nanocrystal growth conditions even when excess chalcogenide is available in the system.[98, 101] Conversely, treatment of cadmium chalcogenide nanomaterials with zinc precursors does not lead to cation exchange. Instead, spherical ZnSe tips assemble on the (0001) and $(000\bar{1})$ facets of the CdS rod while suppressing shelling to a fraction of a monolayer.[118] More recently, it was observed that cadmium chalcogenide nanorods etch anisotropically when treated with zinc oleate.[119] The same directional etching of the nanorod ends was also observed with sodium oleate but not with oleic acid. Nanorod etching with zinc and sodium oleate led to a build-up of cadmium oleate in solution, which could subsequently be deposited epitaxially as CdSe upon the CdS nanorods with the addition of trioctylphosphine selenide. Despite the abundance of zinc precursor in solution, CdSe preferentially formed at the surface of the CdS nanorods over ZnSe and independent nucleation of new CdSe nanoparticles away from the nanorod. ZnSe growth could be obtained if the system was subjected to higher temperatures or by increasing the amount of excess oleic acid present while adding zinc and selenium precursors simultaneously.[119]

As illustrated by the previous example, seeded growth of anisotropic heterostructures is intrinsically a multi-step process that begins with having a monodisperse sample of nanocrystal seeds with clearly defined surface facets. In fact today, many straightforward and inexpensive syntheses exist for obtaining monodisperse quantum dot samples in high yields; some of these syntheses can even be completed by high school and undergraduates with minimal laboratory experience within a single laboratory session.[84, 120-125] While multiple-step syntheses may initially seem to add complexity to a synthetic work flow, seeded growth of nanocrystals can in fact provide a convenient way to assemble heterostructures with more advanced shape, structure, compositional complexity, and functionality.[79,

[126] The increasing value of multicomponent heterostructures is reflected in the increasing research focus on integrating multiple inorganic components.[47, 127-131]

One emergent area of success in the seeded growth of anisotropic heterostructures has been the development of so-called dot-in-rod structures.[126, 132-136] These structures have received the most attention in type II and quasi-type II system applications because of the spatial separation of excitons into different components of the nanocrystal. Compared to core–shell structures, dot-in-rod structures show promise for photocatalysis.[137] In one such application, CdS nanorods seeded with CdSe cores and metal tips demonstrated efficient long-lasting charge carrier separation with reduced back charge transfer reactions from reaction partners compared to unseeded rods with identical metal tips. The seeded systems were found to significantly increase activity for hydrogen production under orange light illumination with better stability than the analogous seedless rods.[137]

Access to dot-in-rod and related heterostructures with a variety of morphologies has been demonstrated by starting with seeds with differing crystal phases without significant alteration of synthetic conditions (Figure 1.9). Alivisatos *et al.* showed that CdSe seeds could readily promote CdSe/CdS nanorods (from wurtzite seeds) or tetrapods (from zinc blende seeds) by starting with the same size spherical seeds but different crystal structures.[126] In these types of seeded rod assembly syntheses, conditions similar to those designed to facilitate typical one-pot CdS nanorod growth are established. However, during the induction time (typically 1–4 min for CdS nanorods) a concentrated solution of CdSe seeds are rapidly added to the reaction mixture. CdS monomers readily nucleate upon the surface of the CdSe seeds, and nanorod or nanotetrapod growth begins.[127, 138]

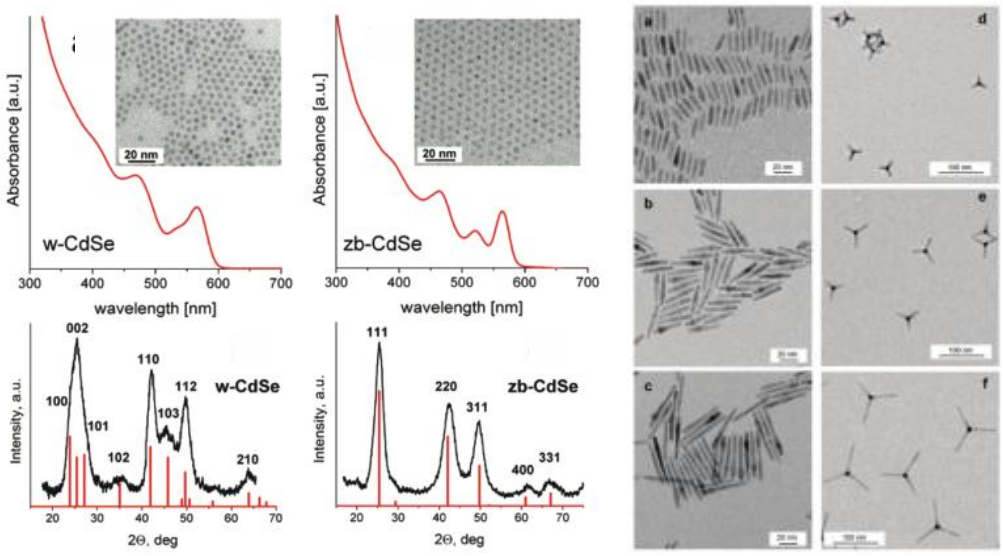

Figure 1.9. CdSe/CdS heterostructures obtained from spherical wurtzite and zinc blende CdSe seeds. Spherical wurtzite CdSe gives 1-D CdSe/CdS nanorods, while zinc blende seeds of equivalent size yield tetrapod nanoarchitectures with CdSe cores and CdS arms under similar reaction conditions. Wurtzite seeds promote 1-D rod growth while zinc blende scaffolds give tetrapod products. Reprinted with permission from D. V. Talapin, J. H. Nelson, E. V. Shevchenko, S. Aloni, B. Sadtler and A. P. Alivisatos, *Nano Lett.*, 2007, **7**, 2951–2959. Copyright 2007 American Chemical Society.[126]

Further tailoring of these seeded heterostructures is possible using ligand control. Alkyl phosphonate ligands are known to selectively stabilize the lateral, non-polar facets of hexagonal wurtzite nanocrystals.[74, 83] These ligands can be used to force growth in certain directions due to reduced reactivity on the ligand bound circumferential facets.[5, 70] Thus, when seeds are introduced to a system with abundant phosphonic acid that selectively binds to the $(10\bar{1}0)$ facets of w-CdS and w-CdSe, growth is slowed in those directions to promote growth exclusively along the growing *c*-axis of the wurtzite crystal.[139] Additionally, nucleation occurs primarily on the (0001) and $(000\bar{1})$ facets of the CdSe seed which leads to CdS growth in the (0001) and $(000\bar{1})$ directions.[138] The lattice mismatch between the

two materials is less than 4% which promotes favorable epitaxial growth.[36, 53] In these studies, it was observed that the CdSe seed was regularly positioned away from the center of the nanorod. This is due to the slightly greater reactivity of the $(000\bar{1})$ *vs.* the similar, but not identical, (0001) facet as discussed previously.[70] The exact location of the core in a nanorod depends on the relative growth rates of the ends and the exact core location can be controlled by using ligands to selectively passivate one end to slow growth in that direction.[140] The length of wurtzite nanorods could be controlled to give highly crystalline nanorods between 10–63 nm long with aspect ratios approaching 13.[126] A similar range of customizability could be obtained for the arms of tetrapods, which could be modified to lengths of 5–50 nm. Length of the rods and tetrapod arms was controlled by altering the concentration of CdSe seeds while all other reaction parameters remained the same.

Precise control over nanocrystal component dimensions affords tailored exciton distribution and dynamics in nanoheterostructures.[141-142] One of the more comprehensive studies of ligand mediated control over nanorod and heterostructure dimensionality was reported by Lee and co-workers using a dual diameter nanorod system.[140] In this work, two distinctly segmented components of a single nanorod have different diameters and were used to monitor the axial growth rates of the two components using transmission electron microscopy. Monitoring the growth rates of the dual diameter nanorod offered a quantitative correlation between ligand population and growth rate at the (0001) and $(000\bar{1})$ facets. Dot-in-rod heterostructures were also prepared, and as previously shown, the exact position of the dot within the rod could be varied by modulating the concentration of phosphonate ligands of different chain lengths.[140] The greater the ratio of long chain to short chain phosphonate ligand in the reaction, the more offset the core resides from the center of the nanorod. This illustrates that long chain phosphonate can selectively impede growth upon the (0001) end by reducing monomer diffusivity to the (0001) surface. The $(000\bar{1})$ surface grows at a constant rate regardless of the fraction of long chain phosphonate present,

which leads to CdSe growth of 19 nm min^{-1} at the $(000\bar{1})$ end irrespective of the ligand. Ultimately, the $(000\bar{1})$ end facets are replaced by $(01\bar{1}\bar{1})$ slant facets when the monomer concentration in solution is reduced. Since $(01\bar{1}\bar{1})$ and (0001), facets have comparable growth rates in the axial direction, continued nanorod extension is dramatically curtailed when reactive monomer is consumed.[140] Due to the complexity in predicting such phenomena, ligand mediated growth modulation is underutilized for developing heterostructures of customizable dimensions, despite how such morphological control over core position and rod component dimensions can dramatically affect exciton dynamics and polarized optical transitions in semiconductor nanostructures (Figure 1.10).

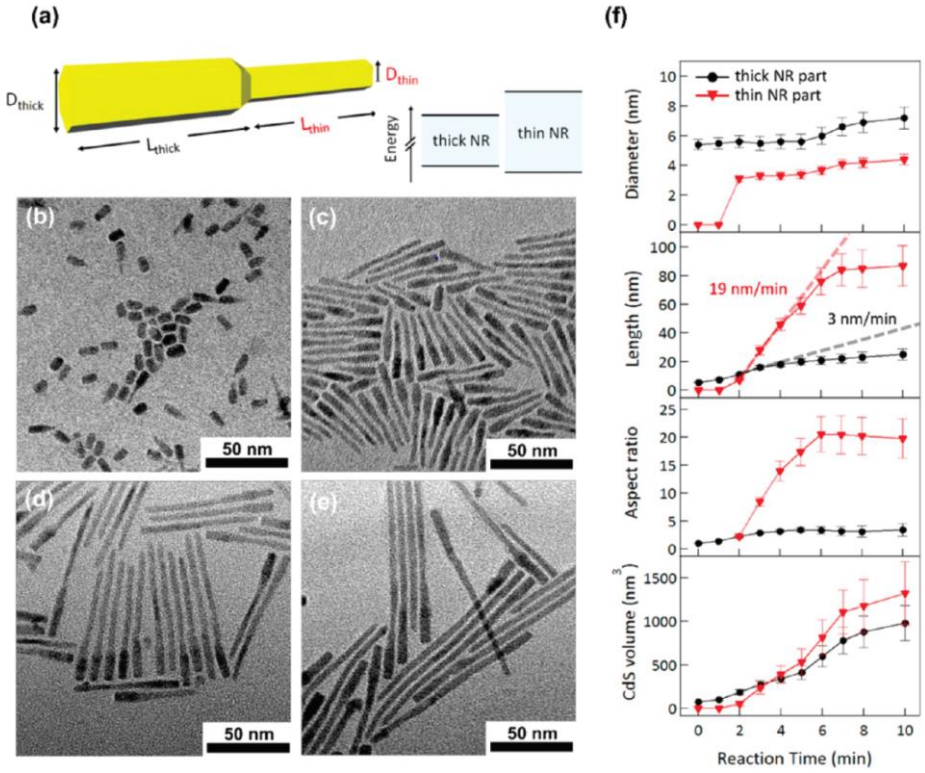

Figure 1.10. Assembly and evaluation of dual diameter heterostructures. (a) A schematic representation of a dual diameter heterostructure with a representative energy level diagram. TEM images of the CdSe/CdS nanorods at 2 min (b), 3 min (c), 5 min (d), and 10 min (e). (f) The diameter, length, aspect ratio, and volume of the thick and thin components over time. Reprinted with permission from D. Kim, Y. K. Lee, D. Lee, W. D. Kim, W. K. Bae and D. C. Lee, *ACS Nano*, 2017, **11**, 12461–12472. Copyright 2017 American Chemical Society.[140]

While it is widely known that ligands can be used to selectively passivate surfaces of growing crystals, ligands can also be used to control concentrations of available monomer in solution. Our recent work has shown that controlling monomer concentrations, especially when using seeds, is valuable for controlling the dimensions and morphology of the new nanomaterial component. Monomers, the reactive nanocrystal growth reagent, can reside in an equilibrium with ligand bound monomer precursor. As nanocrystals assemble, only a small percentage of ligand is associated with the growing nanocrystal

compared to the material incorporated in the colloid. The residual ligand left in solution pushes the equilibrium between monomer and precursor back towards the original precursor, thereby hindering monomer assembly and nanocrystal growth. In nanorod syntheses, the changing monomer concentration can dictate whether growth proceeds in a single direction to elongate the nanorod (1-D growth) or facilitate growth in all directions simultaneously (3-D growth). In rod growth systems, there exists a threshold of ligand *vs.* remaining monomer precursor that dictates the growth regime and therefore the nanocrystal product dimensions. Remaining below this threshold allows continued 1-D growth, while spiking a synthesis with additional ligand can force premature entrance into the 3-D growth regime.[79] This enables a new level of control over heterostructure component dimensions (Figure 1.11).

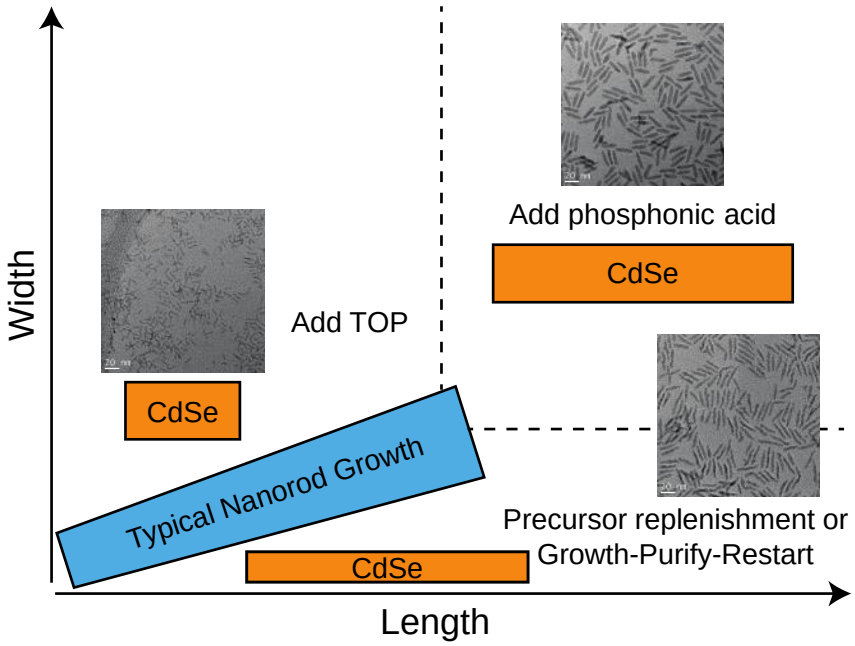

Figure 1.11. Illustration of the array of structures attainable from a synthesis of CdSe nanorods. Modification of the synthesis of CdSe nanorods with additional precursor or ligand yields monodisperse products of a range of dimensions.

Access to a diversity of valuable double and multi-heterojunction nanostructures is challenging using exclusively one-pot bottom-up or post-synthetic top-down synthetic techniques. Starting with anisotropic seeds has recently provided a wealth of new heterostructures, beyond dot-in-rod architectures.[143-146] These structures have demonstrated enhancements to desirable properties, such as improved photoluminescence or increased charge carrier lifetimes. One example is the double heterojunction nanobarbell (Figure 1.12). In these systems, a nanorod seed is used as a scaffold for growing spherical quantum dots and even shell or multi-shell ends. In these cases, the incorporation of subsequent heterostructure components upon a nanorod seed is facilitated using similar procedures to one-pot syntheses of nanostructures. The key difference is replacing the nucleation step with the addition of seeds. Instead, monomers of the new nanocrystal nucleate upon specific facets of the starting seed to give heterostructures. Selective and directed growth upon specific seed facets clearly offers a versatile strategy for developing tailor-made colloidal heterostructure semiconductors.

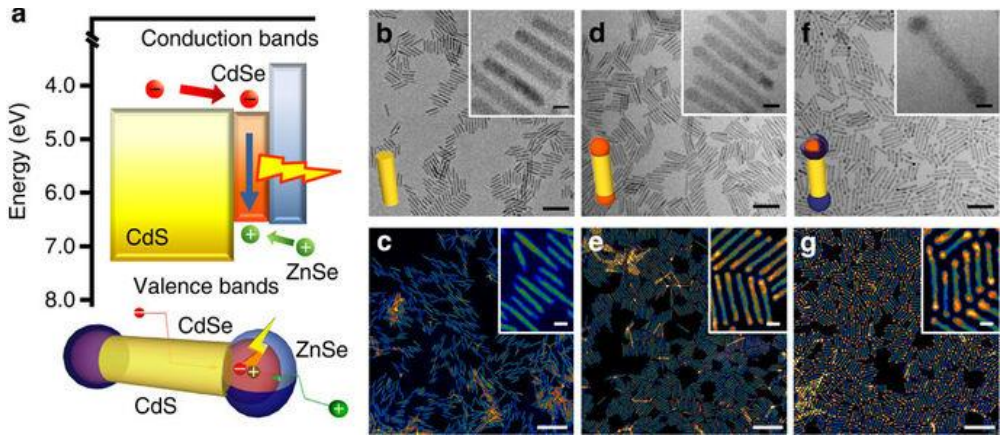

Figure 1.12. Double heterojunction nanorod structures with a barbell type construction. (a) An energy band diagram of the components of the nanobarbell system. (b and c) TEM images of the CdS nanorod scaffold, (d and e) CdS/CdSe nanobarbells and (f and g) CdS/CdSe/ZnSe nanorod-barbell multijunction heterostructures. The scale bar is 50 nm for (b), (d), and (f) with 5 nm scale bar for the insets. For (c), (e), and (g), the scale bar is 100 nm with a 10 nm scale bar for the insets. Reprinted by permission from Nature Research: Double-heterojunction nanorods, N. Oh, S. Nam, Y. Zhai, K. Deshpande, P. Trefonas and M. Shim, *Nat. Commun.*, 2014.[143]

1.7 OUTLOOK ON ANISOTROPIC STRUCTURE ASSEMBLY

Anisotropic heterostructures are less readily accessible than their spherical counterparts due to the narrow range of reaction conditions required to facilitate anisotropic crystal growth. One-pot synthetic methods are the simplest and most readily scaled, but often are not broadly generalizable to a variety of compositions given the requirement of carefully balancing the precursor conversion kinetics of more than two interacting components. Post synthetic alloying of nanomaterials, while useful for tuning the properties of a given system across a spectrum of compositions, relies on the diffusivity of ions of interest in the host lattice, limiting this approach to specific combinations of materials. Seeded material assembly of nanocrystal heterostructures is a versatile approach that is benefited by the well-

established chemistry that has been developed to generate the parent seeds. By using easily synthesized seeds with clearly defined morphologies and surface chemistries, a range of customizable structures with tunable properties can be subsequently obtained in a pseudo-one-pot synthetic approach. In general, seeded syntheses adopt the nanocrystal growth conditions from traditional one-pot approaches but bypass the nucleation event. Since nanocrystal nucleation is replaced with addition of pre-formed seeds, growth conditions can be directly established without devising procedures to separate nucleation and growth events.

The majority or existing synthetic methods have primarily focused on developing II–VI nanocrystal heterostructures. These materials have been the most well studied because of the abundance of available precursor combinations and their excellent photophysical properties. Chalcogenide based nanomaterials also benefit from residing in a sweet spot for facilitating nanocrystal assembly, cation exchange, polytypism, and facet directed growth that have driven the field forward. Access to colloidal nanocrystal heterostructures for other classes of semiconductors, including III–V and group IV materials, has been more limited. While challenges remain in preparing even the simplest core–shell heterostructures for these material classes, the seeded growth approach provides a reasonable direction for further synthetic development. In addition, limited examples of controlling anisotropy to access, for example, pure phase nanorods, provides additional motivation for synthetic methods advancement. After these synthetic tools are developed, it is likely that access to complex heterostructures will be best approached using a seeded assembly strategy based on the principles that have been established for II–VI systems. This motivation to advance synthetic methods for anisotropic heterostructure assembly from seeds lends itself well to customization of structure and band edge combinations to better design more efficient type I or type II heterostructures.

1.8 PHOTOCATALYSIS WITH NANOMATERIALS

Nanomaterial heterostructures have the potential to better facilitate photoredox processes as compared to their single material counterparts because of their ability to separate charge across the heterostructure interface when the band edges are in a staggered, Type II, configuration. Furthermore, anisotropic nanostructures show greater promise than their spherical counterparts.[137] However, for the value of anisotropic heterostructure photocatalysis to ever reach its full potential, nanomaterial driven photocatalysis must be better understood. Ever since the first report by Fujishima and Honda using TiO_2 photoanodes to promote UV light induced photo-assisted decomposition of water into hydrogen and oxygen,[147] the field of photocatalysis with semiconductor nanostructures has boomed with the sunlight to hydrogen conversion being a defining model system.[148-162] While hydrogen generation is an extremely important process and accounts for a major component of global energy consumption through steam reforming to generate hydrogen used in the production of ammonia via the Haber-Bosch process, hydrogen evolution is only one reaction of many valuable industrial scale chemical processes that could be facilitated by nanoscale catalytic materials.

The largest industrial energy users are the chemical and petrochemical sectors which account for about 10% of total global energy demand and produce around 7% of global industrial greenhouse gas emissions.[163] Since 90% of chemical processes use catalysts for efficient production, catalyst development is valuable for energy conservation and reducing greenhouse gas production. Projections for catalyst development suggest new catalyst technologies could yield energy savings of up to 13 exajoules by 2050.[163] Photocatalysts are an especially valuable class of catalysts because they absorb sunlight to drive energetically unfavorable or slow chemical processes. Despite semiconductor nanoparticles possessing properties such as high photostability, large extinction coefficients (10^5–10^6 L/mol·cm), tunable optoelectrical properties, customizable

surface chemistry, and high durability compared to their molecular counterparts,[137, 164-171] they have been underexplored as photoredox catalysts.[172-176]

One potential application is biomass depolymerization. Biomass is an inexpensive, renewable, and abundant resource with great potential as a chemical feedstock. A major component of biomass is lignin, an aromatic biopolymer responsible for providing structural support and shape to plants that constitutes roughly 30% of all non-fossil organic carbon on earth.[177] In fact lignocellulosic biomass is widely considered the most sustainable carbon alternative to petroleum.[178-179] Furthermore, lignin is composed of a diversity of electron-rich phenylpropanols, which are high-value aromatics with potential broad usage in pharmaceuticals, fertilizers, and many other industries.[180-181] Current industrial processing of biomass is predominantly performed using traditional Kraft, sulfite, or soda pulping methods, and while these processes give some marketable substances, these techniques require techniques that are often too energy-intensive and harsh to allow for production of useful commodity chemicals.[182-183] Thus, development of reliable methods for compound isolation from lignin remains underdeveloped.[184-185] Due to these challenges, lignin is principally used as a combustible fuel source.

In an effort to valorize lignin, a variety of approaches have focused on molecular catalysts to isolate high-value components through targeted cleavage of abundant β-O-4 linkages, which account for 45–60% of all linkages in the complex lignin polymer backbone.[186-187] Reductive, oxidative, and redox-neutral pathways have all been successfully used in cleavage of C_α–O bonds in substrates that model the greater lignin macrostructure.[188-197] However, these processes typically require temperatures in excess of 80 °C, an over pressure of hydrogen, and an expensive late-row transition-metal catalyst. Recently, a visible light absorbing iridium catalyst, $[Ir(ppy)_2(dtbbpy)]PF_6$, was used to selectively drive C-O bond cleavage at ambient pressure and

temperature under visible light.[188, 197-199] While this catalyst required prerequisite oxidation of lignin's native benzylic alcohols to benzylic ketones, resulting in a multistep route to depolymerization products, these discoveries open the door to further photo-redox catalyst development.[185, 188, 200]

In comparison to molecular light harvesters, such as the aforementioned iridium catalyst and other traditional transition-metal-based photocatalysts, quantum dots have demonstrated longer-lived excited states, greater photostability, increased photon absorbance per molecule, and broader absorption spectra.[20-21] Thus, quantum dots and related nanoscale materials should be considered as viable photoredox catalysts for processes beyond hydrogen evolution. With tunable electronic properties and redox potentials as well as modifiable size, shape, structure and surface chemistry, quantum dots have a great number of customizable parameters to optimize for a particular photocatalytic system.[201] The increased surface area of a nanomaterial compared to traditional molecular catalysts could lead to increased probability of catalyst–substrate encounters and enhanced turnover rate. So far, work with quantum dots and biomass has been limited to primitive approaches where lignocellulose is used as an electron reservoir for hydrogen evolution but fails to take advantage of the unique, aromatic-rich bio-framework of lignin.[202] Development of quantum dots for selective C-O bond cleavage in biomass depolymerization model systems holds great promise for furthering the fields of biomass valorization and more general development of nanomaterials as photoredox catalysts.[203]

1.9 REFERENCES

(1) Sattler, K. D., *Handbook of Nanophysics: Nanoparticles and Quantum Dots*. CRC Press: 2016.

(2) Faraday, M., The Bakerian Lecture. —Experimental relations of gold (and other metals) to light. *Phil. Trans. R. Soc.* **1857,** *147*, 145-181.

(3) Taton, T. A., Nanostructures as tailored biological probes. *Trends Biotechnol.* **2002,** *20*, 277-279.

(4) Talapin, D. V.; Lee, J.-S.; Kovalenko, M. V.; Shevchenko, E. V., Prospects of Colloidal Nanocrystals for Electronic and Optoelectronic Applications. *Chem. Rev.* **2010,** *110*, 389-458.

(5) Peng, X.; Manna, L.; Yang, W.; Wickham, J.; Scher, E.; Kadavanich, A.; Alivisatos, A. P., Shape control of CdSe nanocrystals. *Nature* **2000,** *404*, 59-61.

(6) Alivisatos, A. P., Semiconductor Clusters, Nanocrystals, and Quantum Dots. *Science* **1996,** *271*, 933-937.

(7) Mitzi, D. B., *Solution Processing of Inorganic Materials*. John Wiley & Sons, Inc.: 2008.

(8) Markovich, G.; Collier, C. P.; Henrichs, S. E.; Remacle, F.; Levine, R. D.; Heath, J. R., Architectonic Quantum Dot Solids. *Acc. Chem. Res.* **1999,** *32*, 415-423.

(9) Brus, L., Electronic wave functions in semiconductor clusters: experiment and theory. *J. Phys. Chem.* **1986,** *90*, 2555-2560.

(10) Tessler, N.; Medvedev, V.; Kazes, M.; Kan, S.; Banin, U., Efficient Near-Infrared Polymer Nanocrystal Light-Emitting Diodes. *Science* **2002,** *295*, 1506-1508.

(11) Shirasaki, Y.; Supran, G. J.; Bawendi, M. G.; Bulović, V., Emergence of colloidal quantum-dot light-emitting technologies. *Nat. Photonics* **2012,** *7*, 13.

(12) Liu, S.; Liu, W.; Ji, W.; Yu, J.; Zhang, W.; Zhang, L.; Xie, W., Top-emitting quantum dots light-emitting devices employing microcontact printing with electricfield-independent emission. *Sci. Rep.* **2016,** *6*, 22530.

(13) Colvin, V. L.; Schlamp, M. C.; Alivisatos, A. P., Light-emitting diodes made from cadmium selenide nanocrystals and a semiconducting polymer. *Nature* **1994,** *370*, 354.

(14) Dabbousi, B. O.; Bawendi, M. G.; Onitsuka, O.; Rubner, M. F., Electroluminescence from CdSe quantum-dot/polymer composites. *Appl. Phys. Lett.* **1995,** *66*, 1316-1318.

(15) Alivisatos, A. P.; Gu, W.; Larabell, C., Quantum Dots as Cellular Probes. *Annu. Rev. Biomed. Eng.* **2005,** *7*, 55-76.

(16) Chan, W. C. W.; Maxwell, D. J.; Gao, X.; Bailey, R. E.; Han, M.; Nie, S., Luminescent quantum dots for multiplexed biological detection and imaging. *Curr. Opin. Biotechnol.* **2002,** *13*, 40-46.

(17) Jaiswal, J. K.; Mattoussi, H.; Mauro, J. M.; Simon, S. M., Long-term multiple color imaging of live cells using quantum dot bioconjugates. *Nat. Biotechnol.* **2002,** *21*, 47.

(18) Medintz, I. L.; Uyeda, H. T.; Goldman, E. R.; Mattoussi, H., Quantum dot bioconjugates for imaging, labelling and sensing. *Nat. Mater.* **2005,** *4*, 435.

(19) Larson, D. R.; Zipfel, W. R.; Williams, R. M.; Clark, S. W.; Bruchez, M. P.; Wise, F. W.; Webb, W. W., Water-Soluble Quantum Dots for Multiphoton Fluorescence Imaging in Vivo. *Science* **2003,** *300*, 1434-1436.

(20) Chan, W. C. W.; Nie, S., Quantum Dot Bioconjugates for Ultrasensitive Nonisotopic Detection. *Science* **1998,** *281*, 2016-2018.

(21) Bruchez, M.; Moronne, M.; Gin, P.; Weiss, S.; Alivisatos, A. P., Semiconductor Nanocrystals as Fluorescent Biological Labels. *Science* **1998,** *281*, 2013-2016.

(22) Winnik, F. M.; Maysinger, D., Quantum Dot Cytotoxicity and Ways To Reduce It. *Acc. Chem. Res.* **2013,** *46*, 672-680.

(23) Mattoussi, H.; Palui, G.; Na, H. B., Luminescent quantum dots as platforms for probing in vitro and in vivo biological processes. *Adv. Drug Deliv. Rev.* **2012,** *64*, 138-166.

(24) Qiu, F.; Han, Z.; Peterson, J. J.; Odoi, M. Y.; Sowers, K. L.; Krauss, T. D., Photocatalytic Hydrogen Generation by CdSe/CdS Nanoparticles. *Nano Lett.* **2016,** *16*, 5347-5352.

(25) Zhou, Y.; Hu, W.; Ludwig, J.; Huang, J., Exceptionally Robust CuInS2/ZnS Nanoparticles as Single Component Photocatalysts for H2 Evolution. *J. Phys. Chem. C* **2017,** *121*, 19031-19035.

(26) Kandi, D.; Martha, S.; Parida, K. M., Quantum dots as enhancer in photocatalytic hydrogen evolution: A review. *Int. J. Hydrogen Energy* **2017,** *42*, 9467-9481.

(27) Lian, S.; Kodaimati, M. S.; Dolzhnikov, D. S.; Calzada, R.; Weiss, E. A., Powering a CO2 Reduction Catalyst with Visible Light through Multiple Sub-picosecond Electron Transfers from a Quantum Dot. *J. Am. Chem. Soc.* **2017,** *139*, 8931-8938.

(28) Jensen, S. C.; Bettis Homan, S.; Weiss, E. A., Photocatalytic Conversion of Nitrobenzene to Aniline through Sequential Proton-Coupled One-Electron Transfers from a Cadmium Sulfide Quantum Dot. *J. Am. Chem. Soc.* **2016,** *138*, 1591-1600.

(29) Caputo, J. A.; Frenette, L. C.; Zhao, N.; Sowers, K. L.; Krauss, T. D.; Weix, D. J., General and Efficient C–C Bond Forming Photoredox Catalysis with Semiconductor Quantum Dots. *J. Am. Chem. Soc.* **2017,** *139*, 4250-4253.

(30) Wright, M.; Uddin, A., Organic—inorganic hybrid solar cells: A comparative review. *Sol. Energy Mater. Sol. Cells* **2012,** *107*, 87-111.

(31) Pandey, A.; Guyot-Sionnest, P., Slow Electron Cooling in Colloidal Quantum Dots. *Science* **2008,** *322*, 929-932.

(32) Zegrya, G. G.; Andreev, A. D., Mechanism of suppression of Auger recombination processes in type-II heterostructures. *Appl. Phys. Lett.* **1995,** *67*, 2681-2683.

(33) Dennis, A. M.; Mangum, B. D.; Piryatinski, A.; Park, Y.-S.; Hannah, D. C.; Casson, J. L.; Williams, D. J.; Schaller, R. D.; Htoon, H.; Hollingsworth, J. A., Suppressed Blinking and Auger Recombination in Near-Infrared Type-II InP/CdS Nanocrystal Quantum Dots. *Nano Lett.* **2012,** *12*, 5545-5551.

(34) Hollingsworth, J. A., Heterostructuring Nanocrystal Quantum Dots Toward Intentional Suppression of Blinking and Auger Recombination. *Chem. Mater.* **2013,** *25*, 1318-1331.

(35) Pu, Y.; Cai, F.; Wang, D.; Wang, J.-X.; Chen, J.-F., Colloidal Synthesis of Semiconductor Quantum Dots toward Large-Scale Production: A Review. *Ind. Eng. Chem. Res.* **2018,** *57*, 1790-1802.

(36) Reiss, P.; Protière, M.; Li, L., Core/Shell Semiconductor Nanocrystals. *Small* **2009,** *5*, 154-168.

(37) Kim, S.; Fisher, B.; Eisler, H.-J.; Bawendi, M., Type-II Quantum Dots: CdTe/CdSe(Core/Shell) and CdSe/ZnTe(Core/Shell) Heterostructures. *Journal of the American Chemical Society* **2003,** *125*, 11466-11467.

(38) Itzhakov, S.; Shen, H.; Buhbut, S.; Lin, H.; Oron, D., Type-II Quantum-Dot-Sensitized Solar Cell Spanning the Visible and Near-Infrared Spectrum. *J. Phys. Chem. C* **2013,** *117*, 22203-22210.

(39) Xu, F.; Yang, X.-G.; Luo, S.; Lv, Z.-R.; Yang, T., Enhanced performance of quantum dot solar cells based on type II quantum dots. *J. Appl. Phys.* **2014,** *116*, 133102.

(40) Chen, Y.; Vela, J.; Htoon, H.; Casson, J. L.; Werder, D. J.; Bussian, D. A.; Klimov, V. I.; Hollingsworth, J. A., "Giant" Multishell CdSe Nanocrystal Quantum Dots with Suppressed Blinking. *Journal of the American Chemical Society* **2008,** *130*, 5026-5027.

(41) Mahler, B.; Spinicelli, P.; Buil, S.; Quelin, X.; Hermier, J.-P.; Dubertret, B., Towards non-blinking colloidal quantum dots. *Nat. Mater.* **2008,** *7*, 659.

(42) Htoon, H.; Malko, A. V.; Bussian, D.; Vela, J.; Chen, Y.; Hollingsworth, J. A.; Klimov, V. I., Highly Emissive Multiexcitons in Steady-State Photoluminescence of Individual "Giant" CdSe/CdS Core/Shell Nanocrystals. *Nano Lett.* **2010,** *10*, 2401-2407.

(43) Zhou, C.; Chen, Q.; Wang, G.; Guan, A.; Xu, J.; Liu, X.; Shi, Z.; Zhou, L., One-pot synthesis of CdSe@CdS core@shell quantum dots and their photovoltaics application in quantum-dot-sensitized ZnO nanorods. *J. Photochem. Photobiol.* **2017,** *332*, 251-257.

(44) Zhai, C.; Zhang, H.; Du, N.; Chen, B.; Huang, H.; Wu, Y.; Yang, D., One-Pot Synthesis of Biocompatible CdSe/CdS Quantum Dots and Their Applications as Fluorescent Biological Labels. *Nanoscale Res Lett* **2010,** *6*, 31.

(45) Mekis, I.; Talapin, D. V.; Kornowski, A.; Haase, M.; Weller, H., One-Pot Synthesis of Highly Luminescent CdSe/CdS Core−Shell Nanocrystals via Organometallic and "Greener" Chemical Approaches. *The Journal of Physical Chemistry B* **2003,** *107*, 7454-7462.

(46) Talapin, D. V.; Rogach, A. L.; Kornowski, A.; Haase, M.; Weller, H., Highly Luminescent Monodisperse CdSe and CdSe/ZnS Nanocrystals Synthesized in a Hexadecylamine−Trioctylphosphine Oxide−Trioctylphospine Mixture. *Nano Letters* **2001,** *1*, 207-211.

(47) Hines, M. A.; Guyot-Sionnest, P., Synthesis and Characterization of Strongly Luminescing ZnS-Capped CdSe Nanocrystals. *The Journal of Physical Chemistry* **1996,** *100*, 468-471.

(48) Chen, O.; Zhao, J.; Chauhan, V. P.; Cui, J.; Wong, C.; Harris, D. K.; Wei, H.; Han, H.-S.; Fukumura, D.; Jain, R. K.; Bawendi, M. G., Compact high-quality CdSe–CdS core–shell nanocrystals with narrow emission linewidths and suppressed blinking. *Nat. Mater.* **2013,** *12*, 445.

(49) Greytak, A. B.; Allen, P. M.; Liu, W.; Zhao, J.; Young, E. R.; Popovic, Z.; Walker, B. J.; Nocera, D. G.; Bawendi, M. G., Alternating layer addition approach to CdSe/CdS core/shell quantum dots with near-unity quantum yield and high on-time fractions. *Chem. Sci.* **2012,** *3*, 2028-2034.

(50) Tan, R.; Blom, D. A.; Ma, S.; Greytak, A. B., Probing Surface Saturation Conditions in Alternating Layer Growth of CdSe/CdS Core/Shell Quantum Dots. *Chem. Mater.* **2013,** *25*, 3724-3736.

(51) Ithurria, S.; Talapin, D. V., Colloidal Atomic Layer Deposition (c-ALD) using Self-Limiting Reactions at Nanocrystal Surface Coupled to Phase Transfer between Polar and Nonpolar Media. *J. Am. Chem. Soc.* **2012,** *134*, 18585-18590.

(52) Ghosh, Y.; Mangum, B. D.; Casson, J. L.; Williams, D. J.; Htoon, H.; Hollingsworth, J. A., New Insights into the Complexities of Shell Growth and the Strong Influence of Particle Volume in Nonblinking "Giant" Core/Shell Nanocrystal Quantum Dots. *J. Am. Chem. Soc.* **2012,** *134*, 9634-9643.

(53) Xie, R.; Kolb, U.; Li, J.; Basché, T.; Mews, A., Synthesis and Characterization of Highly Luminescent CdSe−Core CdS/Zn0.5Cd0.5S/ZnS Multishell Nanocrystals. *J. Am. Chem. Soc.* **2005,** *127*, 7480-7488.

(54) Blackman, B.; Battaglia, D. M.; Mishima, T. D.; Johnson, M. B.; Peng, X., Control of the Morphology of Complex Semiconductor Nanocrystals with a Type II Heterojunction, Dots vs Peanuts, by Thermal Cycling. *Chem. Mater.* **2007,** *19*, 3815-3821.

(55) Donega, C. d. M., Synthesis and properties of colloidal heteronanocrystals. *Chem. Soc. Rev.* **2011,** *40*, 1512-1546.

(56) Bleuse, J.; Carayon, S.; Reiss, P., Optical properties of core/multishell CdSe/Zn(S,Se) nanocrystals. *Phys. E.* **2004,** *21*, 331-335.

(57) Talapin, D. V.; Mekis, I.; Götzinger, S.; Kornowski, A.; Benson, O.; Weller, H., CdSe/CdS/ZnS and CdSe/ZnSe/ZnS Core−Shell−Shell Nanocrystals. *J. Phys. Chem. B* **2004,** *108*, 18826-18831.

(58) Boldt, K.; Kirkwood, N.; Beane, G. A.; Mulvaney, P., Synthesis of Highly Luminescent and Photo-Stable, Graded Shell CdSe/CdxZn1–xS Nanoparticles by In Situ Alloying. *Chem. Mater.* **2013,** *25*, 4731-4738.

(59) Omogo, B.; Gao, F.; Bajwa, P.; Kaneko, M.; Heyes, C. D., Reducing Blinking in Small Core–Multishell Quantum Dots by Carefully Balancing Confinement Potential and Induced Lattice Strain: The “Goldilocks” Effect. *ACS Nano* **2016,** *10*, 4072-4082.

(60) Abdellah, M.; Zhang, S.; Wang, M.; Hammarström, L., Competitive Hole Transfer from CdSe Quantum Dots to Thiol Ligands in CdSe-Cobaloxime Sensitized NiO Films Used as Photocathodes for H2 Evolution. *ACS Energy Lett.* **2017,** *2*, 2576-2580.

(61) Kodaimati, M. S.; McClelland, K. P.; He, C.; Lian, S.; Jiang, Y.; Zhang, Z.; Weiss, E. A., Viewpoint: Challenges in Colloidal Photocatalysis and Some Strategies for Addressing Them. *Inorg. Chem.* **2018,** *57*, 3659-3670.

(62) Jin, S.; Zhang, J.; Schaller, R. D.; Rajh, T.; Wiederrecht, G. P., Ultrafast Charge Separation from Highly Reductive ZnTe/CdSe Type II Quantum Dots. *J. Phys. Chem. Lett* **2012,** *3*, 2052-2058.

(63) Norris, M. R.; Cossairt, B. M., CdSe on a mesoporous transparent conducting oxide scaffold as a photocathode. *J. Mater. Chem. A.* **2015,** *3*, 14585-14591.

(64) Moonsub, S., Colloidal nanorod heterostructures for photovoltaics and optoelectronics. *J. Phys. D: Appl. Phys.* **2017,** *50*, 173002.

(65) Peng, Z. A.; Peng, X., Nearly Monodisperse and Shape-Controlled CdSe Nanocrystals via Alternative Routes: Nucleation and Growth. *Journal of the American Chemical Society* **2002,** *124*, 3343-3353.

(66) Manna, L.; Milliron, D. J.; Meisel, A.; Scher, E. C.; Alivisatos, A. P., Controlled growth of tetrapod-branched inorganic nanocrystals. *Nat. Mater.* **2003,** *2*, 382.

(67) Murray, C. B.; Norris, D. J.; Bawendi, M. G., Synthesis and characterization of nearly monodisperse CdE (E = sulfur, selenium, tellurium) semiconductor nanocrystallites. *Journal of the American Chemical Society* **1993,** *115*, 8706-8715.

(68) Hu, J.; Li, L.-s.; Yang, W.; Manna, L.; Wang, L.-w.; Alivisatos, A. P., Linearly Polarized Emission from Colloidal Semiconductor Quantum Rods. *Science* **2001,** *292*, 2060-2063.

(69) Peng, X.; Wickham, J.; Alivisatos, A. P., Kinetics of II-VI and III-V Colloidal Semiconductor Nanocrystal Growth: "Focusing" of Size Distributions. *Journal of the American Chemical Society* **1998,** *120*, 5343-5344.

(70) Manna, L.; Scher, E. C.; Alivisatos, A. P., Synthesis of Soluble and Processable Rod-, Arrow-, Teardrop-, and Tetrapod-Shaped CdSe Nanocrystals. *Journal of the American Chemical Society* **2000,** *122*, 12700-12706.

(71) Tsivion, D.; Schvartzman, M.; Popovitz-Biro, R.; von Huth, P.; Joselevich, E., Guided Growth of Millimeter-Long Horizontal Nanowires with Controlled Orientations. *Science* **2011,** *333*, 1003-1007.

(72) Pound, G. M.; La Mer, V. K., Kinetics of Crystalline Nucleus Formation in Supercooled Liquid Tin1,2. *J. Am. Chem. Soc.* **1952,** *74*, 2323-2332.

(73) Gao, Y.; Peng, X., Crystal Structure Control of CdSe Nanocrystals in Growth and Nucleation: Dominating Effects of Surface versus Interior Structure. *J. Am. Chem. Soc.* **2014,** *136*, 6724-6732.

(74) Peng, Z. A.; Peng, X., Mechanisms of the Shape Evolution of CdSe Nanocrystals. *J. Am. Chem. Soc.* **2001,** *123*, 1389-1395.

(75) Marqusee, J. A.; Ross, J., Kinetics of phase transitions: Theory of Ostwald ripening. *J. Chem. Phys.* **1983,** *79*, 373-378.

(76) Oriani, R. A., Ostwald ripening of precipitates in solid matrices. *Acta Metall.* **1964,** *12*, 1399-1409.

(77) Marqusee, J. A.; Ross, J., Theory of Ostwald ripening: Competitive growth and its dependence on volume fraction. *J. Chem. Phys.* **1984,** *80*, 536-543.

(78) Peng, X., Mechanisms for the Shape-Control and Shape-Evolution of Colloidal Semiconductor Nanocrystals. *Adv. Mater.* **2003,** *15*, 459-463.

(79) Enright, M. J.; Sarsito, H.; Cossairt, B. M., Kinetically controlled assembly of cadmium chalcogenide nanorods and nanorod heterostructures. *Mater. Chem. Front.* **2018**.

(80) Gary, D. C.; Glassy, B. A.; Cossairt, B. M., Investigation of Indium Phosphide Quantum Dot Nucleation and Growth Utilizing Triarylsilylphosphine Precursors. *Chem. Mater.* **2014,** *26*, 1734-1744.

(81) Carbone, L.; Kudera, S.; Carlino, E.; Parak, W. J.; Giannini, C.; Cingolani, R.; Manna, L., Multiple Wurtzite Twinning in CdTe Nanocrystals Induced by Methylphosphonic Acid. *J. Am. Chem. Soc.* **2006,** *128*, 748-755.

(82) Yeh, C.-Y.; Lu, Z. W.; Froyen, S.; Zunger, A., Zinc-blende\char21{}wurtzite polytypism in semiconductors. *Phys. Rev. B* **1992,** *46*, 10086-10097.

(83) Peng, Z. A.; Peng, X., Formation of High-Quality CdTe, CdSe, and CdS Nanocrystals Using CdO as Precursor. *J. Am. Chem. Soc.* **2001,** *123*, 183-184.

(84) Landry, M. L.; Morrell, T. E.; Karagounis, T. K.; Hsia, C.-H.; Wang, C.-Y., Simple Syntheses of CdSe Quantum Dots. *J. Chem. Educ.* **2014,** *91*, 274-279.

(85) Shieh, F.; Saunders, A. E.; Korgel, B. A., General Shape Control of Colloidal CdS, CdSe, CdTe Quantum Rods and Quantum Rod Heterostructures. *J. Phys. Chem. B* **2005,** *109*, 8538-8542.

(86) Milliron, D. J.; Hughes, S. M.; Cui, Y.; Manna, L.; Li, J.; Wang, L.-W.; Paul Alivisatos, A., Colloidal nanocrystal heterostructures with linear and branched topology. *Nature* **2004,** *430*, 190.

(87) Fenton, J. L.; Steimle, B. C.; Schaak, R. E., Tunable intraparticle frameworks for creating complex heterostructured nanoparticle libraries. *Science* **2018,** *360*, 513-517.

(88) Mocatta, D.; Cohen, G.; Schattner, J.; Millo, O.; Rabani, E.; Banin, U., Heavily Doped Semiconductor Nanocrystal Quantum Dots. *Science* **2011,** *332*, 77-81.

(89) Sahu, A.; Kang, M. S.; Kompch, A.; Notthoff, C.; Wills, A. W.; Deng, D.; Winterer, M.; Frisbie, C. D.; Norris, D. J., Electronic Impurity Doping in CdSe Nanocrystals. *Nano Lett.* **2012,** *12*, 2587-2594.

(90) Eilers, J.; Groeneveld, E.; de Mello Donegá, C.; Meijerink, A., Optical Properties of Mn-Doped ZnTe Magic Size Nanocrystals. *J. Phys. Chem. Lett* **2012,** *3*, 1663-1667.

(91) Creutz, S. E.; Fainblat, R.; Kim, Y.; De Siena, M. C.; Gamelin, D. R., A Selective Cation Exchange Strategy for the Synthesis of Colloidal Yb3+-Doped Chalcogenide Nanocrystals with Strong Broadband Visible Absorption and Long-Lived Near-Infrared Emission. *J. Am. Chem. Soc.* **2017,** *139*, 11814-11824.

(92) Werts, M. H. V.; Verhoeven, J. W.; Hofstraat, J. W., Efficient visible light sensitisation of water-soluble near-infrared luminescent lanthanide complexes. *J. Chem. Soc., Perkin Trans. 2* **2000**, 433-439.

(93) Dong, J.; Bass, M.; Mao, Y.; Deng, P.; Gan, F., Dependence of the Yb3+ emission cross section and lifetime on temperature and concentration in yttrium aluminum garnet. *J. Opt. Soc. Am. B* **2003,** *20*, 1975-1979.

(94) Hu, J.-Y.; Ning, Y.; Meng, Y.-S.; Zhang, J.; Wu, Z.-Y.; Gao, S.; Zhang, J.-L., Highly near-IR emissive ytterbium(iii) complexes with unprecedented quantum yields. *Chem. Sci.* **2017,** *8*, 2702-2709.

(95) Sytnyk, M.; Kirchschlager, R.; Bodnarchuk, M. I.; Primetzhofer, D.; Kriegner, D.; Enser, H.; Stangl, J.; Bauer, P.; Voith, M.; Hassel, A. W.; Krumeich, F.; Ludwig, F.; Meingast, A.; Kothleitner, G.; Kovalenko, M. V.; Heiss, W., Tuning the Magnetic Properties of Metal Oxide Nanocrystal Heterostructures by Cation Exchange. *Nano Lett.* **2013,** *13*, 586-593.

(96) Yang, J.; Muckel, F.; Baek, W.; Fainblat, R.; Chang, H.; Bacher, G.; Hyeon, T., Chemical Synthesis, Doping, and Transformation of Magic-Sized Semiconductor Alloy Nanoclusters. *J. Am. Chem. Soc.* **2017,** *139*, 6761-6770.

(97) Buonsanti, R.; Milliron, D. J., Chemistry of Doped Colloidal Nanocrystals. *Chem. Mater.* **2013,** *25*, 1305-1317.

(98) Enright, M. J.; Sarsito, H.; Cossairt, B. M., Quantifying Cation Exchange of Cd2+ in ZnTe: A Challenge for Accessing Type II Heterostructures. *Chemistry of Materials* **2017,** *29*, 666-672.

(99) Stein, J. L.; Steimle, M. I.; Terban, M. W.; Petrone, A.; Billinge, S. J. L.; Li, X.; Cossairt, B. M., Cation Exchange Induced Transformation of InP Magic-Sized Clusters. *Chemistry of Materials* **2017,** *29*, 7984-7992.

(100) Smith, A. M.; Nie, S., Bright and Compact Alloyed Quantum Dots with Broadly Tunable Near-Infrared Absorption and Fluorescence Spectra through Mercury Cation Exchange. *J. Am. Chem. Soc.* **2011,** *133*, 24-26.

(101) Groeneveld, E.; Witteman, L.; Lefferts, M.; Ke, X.; Bals, S.; Van Tendeloo, G.; de Mello Donega, C., Tailoring ZnSe–CdSe Colloidal Quantum Dots via Cation Exchange: From Core/Shell to Alloy Nanocrystals. *ACS Nano* **2013,** *7*, 7913-7930.

(102) Chakraborty, P.; Jin, Y.; Barrows, C. J.; Dunham, S. T.; Gamelin, D. R., Kinetics of Isovalent (Cd2+) and Aliovalent (In3+) Cation Exchange in Cd1–xMnxSe Nanocrystals. *J. Am. Chem. Soc.* **2016,** *138*, 12885-12893.

(103) Barrows, C. J.; Chakraborty, P.; Kornowske, L. M.; Gamelin, D. R., Tuning Equilibrium Compositions in Colloidal Cd1–xMnxSe Nanocrystals Using Diffusion Doping and Cation Exchange. *ACS Nano* **2016,** *10*, 910-918.

(104) Pietryga, J. M.; Werder, D. J.; Williams, D. J.; Casson, J. L.; Schaller, R. D.; Klimov, V. I.; Hollingsworth, J. A., Utilizing the Lability of Lead Selenide to Produce

Heterostructured Nanocrystals with Bright, Stable Infrared Emission. *J. Am. Chem. Soc.* **2008,** *130*, 4879-4885.

(105) Zhang, J.; Chernomordik, B. D.; Crisp, R. W.; Kroupa, D. M.; Luther, J. M.; Miller, E. M.; Gao, J.; Beard, M. C., Preparation of Cd/Pb Chalcogenide Heterostructured Janus Particles via Controllable Cation Exchange. *ACS Nano* **2015,** *9*, 7151-7163.

(106) Jain, P. K.; Amirav, L.; Aloni, S.; Alivisatos, A. P., Nanoheterostructure Cation Exchange: Anionic Framework Conservation. *J. Am. Chem. Soc.* **2010,** *132*, 9997-9999.

(107) Casavola, M.; van Huis, M. A.; Bals, S.; Lambert, K.; Hens, Z.; Vanmaekelbergh, D., Anisotropic Cation Exchange in PbSe/CdSe Core/Shell Nanocrystals of Different Geometry. *Chem. Mater.* **2012,** *24*, 294-302.

(108) Bothe, C.; Kornowski, A.; Tornatzky, H.; Schmidtke, C.; Lange, H.; Maultzsch, J.; Weller, H., Solid-State Chemistry on the Nanoscale: Ion Transport through Interstitial Sites or Vacancies? *Angew. Chem. Int. Ed.* **2015,** *54*, 14183-14186.

(109) Sadtler, B.; Demchenko, D. O.; Zheng, H.; Hughes, S. M.; Merkle, M. G.; Dahmen, U.; Wang, L.-W.; Alivisatos, A. P., Selective Facet Reactivity during Cation Exchange in Cadmium Sulfide Nanorods. *J. Am. Chem. Soc.* **2009,** *131*, 5285-5293.

(110) Miszta, K.; Dorfs, D.; Genovese, A.; Kim, M. R.; Manna, L., Cation Exchange Reactions in Colloidal Branched Nanocrystals. *ACS Nano* **2011,** *5*, 7176-7183.

(111) Jr., W. R. C.; Shiozawa, L.; Augustine, F., Relationship of Copper Sulfide and Cadmium Sulfide Phases. *J. Appl. Phys.* **1970,** *41*, 3058-3063.

(112) Manna, L.; Wang; Cingolani, R.; Alivisatos, A. P., First-Principles Modeling of Unpassivated and Surfactant-Passivated Bulk Facets of Wurtzite CdSe: A Model System

for Studying the Anisotropic Growth of CdSe Nanocrystals. *J. Phys. Chem. B* **2005,** *109*, 6183-6192.

(113) Chan, E. M.; Marcus, M. A.; Fakra, S.; ElNaggar, M.; Mathies, R. A.; Alivisatos, A. P., Millisecond Kinetics of Nanocrystal Cation Exchange Using Microfluidic X-ray Absorption Spectroscopy. *J. Phys. Chem. A* **2007,** *111*, 12210-12215.

(114) White, S. L.; Banerjee, P.; Chakraborty, I.; Jain, P. K., Ion Exchange Transformation of Magic-Sized Clusters. *Chem. Mater.* **2016,** *28*, 8391-8398.

(115) Berends, A. C.; van der Stam, W.; Hofmann, J. P.; Bladt, E.; Meeldijk, J. D.; Bals, S.; de Mello Donega, C., Interplay between Surface Chemistry, Precursor Reactivity, and Temperature Determines Outcome of ZnS Shelling Reactions on CuInS2 Nanocrystals. *Chemistry of Materials* **2018,** *30*, 2400-2413.

(116) Stein, J. L.; Mader, E. A.; Cossairt, B. M., Luminescent InP Quantum Dots with Tunable Emission by Post-Synthetic Modification with Lewis Acids. *J. Phys. Chem. Lett* **2016,** *7*, 1315-1320.

(117) Grodzinska, D.; Pietra, F.; van Huis, M. A.; Vanmaekelbergh, D.; de Mello Donega, C., Thermally induced atomic reconstruction of PbSe/CdSe core/shell quantum dots into PbSe/CdSe bi-hemisphere hetero-nanocrystals. *J. Mater. Chem.* **2011,** *21*, 11556-11565.

(118) Kirsanova, M.; Nemchinov, A.; Hewa-Kasakarage, N. N.; Schmall, N.; Zamkov, M., Synthesis of ZnSe/CdS/ZnSe Nanobarbells Showing Photoinduced Charge Separation. *Chem. Mater.* **2009,** *21*, 4305-4309.

(119) Oh, N.; Shim, M., Metal Oleate Induced Etching and Growth of Semiconductor Nanocrystals, Nanorods, and Their Heterostructures. *J. Am. Chem. Soc.* **2016,** *138*, 10444-10451.

(120) Ozin, G. A.; Arsenault, A. C., *Nanochemistry: A Chemical Approach to Nanomaterials*. Cambridge, UK, 2005.

(121) Schmidt, G., *Nanoparticles: from theory to applications*. Wiley: Weinheim, Germany, 2004.

(122) Wang, X.; Zhuang, J.; Peng, Q.; Li, Y., A general strategy for nanocrystal synthesis. *Nature* **2005,** *437*, 121.

(123) Hyeon, T., Chemical synthesis of magnetic nanoparticles. *Chem. Commun.* **2003**, 927-934.

(124) Orbaek, A. W.; McHale, M. M.; Barron, A. R., Synthesis and Characterization of Silver Nanoparticles for an Undergraduate Laboratory. *J. Chem. Educ.* **2015,** *92*, 339-344.

(125) Pham, S. N.; Kuether, J. E.; Gallagher, M. J.; Hernandez, R. T.; Williams, D. N.; Zhi, B.; Mensch, A. C.; Hamers, R. J.; Rosenzweig, Z.; Fairbrother, H.; Krause, M. O. P.; Feng, Z. V.; Haynes, C. L., Carbon Dots: A Modular Activity To Teach Fluorescence and Nanotechnology at Multiple Levels. *J. Chem. Educ.* **2017,** *94*, 1143-1149.

(126) Talapin, D. V.; Nelson, J. H.; Shevchenko, E. V.; Aloni, S.; Sadtler, B.; Alivisatos, A. P., Seeded Growth of Highly Luminescent CdSe/CdS Nanoheterostructures with Rod and Tetrapod Morphologies. *Nano Letters* **2007,** *7*, 2951-2959.

(127) Peng, X.; Schlamp, M. C.; Kadavanich, A. V.; Alivisatos, A. P., Epitaxial Growth of Highly Luminescent CdSe/CdS Core/Shell Nanocrystals with Photostability and Electronic Accessibility. *Journal of the American Chemical Society* **1997,** *119*, 7019-7029.

(128) Cao, Y.; Banin, U., Growth and Properties of Semiconductor Core/Shell Nanocrystals with InAs Cores. *J. Am. Chem. Soc.* **2000,** *122*, 9692-9702.

(129) Mokari, T.; Rothenberg, E.; Popov, I.; Costi, R.; Banin, U., Selective Growth of Metal Tips onto Semiconductor Quantum Rods and Tetrapods. *Science* **2004,** *304*, 1787-1790.

(130) Kudera, S.; Carbone, L.; Casula, M. F.; Cingolani, R.; Falqui, A.; Snoeck, E.; Parak, W. J.; Manna, L., Selective Growth of PbSe on One or Both Tips of Colloidal Semiconductor Nanorods. *Nano Lett.* **2005,** *5*, 445-449.

(131) Dabbousi, B. O.; Rodriguez-Viejo, J.; Mikulec, F. V.; Heine, J. R.; Mattoussi, H.; Ober, R.; Jensen, K. F.; Bawendi, M. G., (CdSe)ZnS Core−Shell Quantum Dots: Synthesis and Characterization of a Size Series of Highly Luminescent Nanocrystallites. *The Journal of Physical Chemistry B* **1997,** *101*, 9463-9475.

(132) Carbone, L.; Nobile, C.; De Giorgi, M.; Sala, F. D.; Morello, G.; Pompa, P.; Hytch, M.; Snoeck, E.; Fiore, A.; Franchini, I. R.; Nadasan, M.; Silvestre, A. F.; Chiodo, L.; Kudera, S.; Cingolani, R.; Krahne, R.; Manna, L., Synthesis and Micrometer-Scale Assembly of Colloidal CdSe/CdS Nanorods Prepared by a Seeded Growth Approach. *Nano Lett.* **2007,** *7*, 2942-2950.

(133) Coropceanu, I.; Rossinelli, A.; Caram, J. R.; Freyria, F. S.; Bawendi, M. G., Slow-Injection Growth of Seeded CdSe/CdS Nanorods with Unity Fluorescence Quantum Yield and Complete Shell to Core Energy Transfer. *ACS Nano* **2016,** *10*, 3295-3301.

(134) Sitt, A.; Hadar, I.; Banin, U., Band-gap engineering, optoelectronic properties and applications of colloidal heterostructured semiconductor nanorods. *Nano Today* **2013,** *8*, 494-513.

(135) Biadala, L.; Siebers, B.; Gomes, R.; Hens, Z.; Yakovlev, D. R.; Bayer, M., Tuning Energy Splitting and Recombination Dynamics of Dark and Bright Excitons in CdSe/CdS Dot-in-Rod Colloidal Nanostructures. *J. Phys. Chem. C* **2014,** *118*, 22309-22316.

(136) Morello, G.; Della Sala, F.; Carbone, L.; Manna, L.; Maruccio, G.; Cingolani, R.; De Giorgi, M., Intrinsic optical nonlinearity in colloidal seeded grown CdSe/CdS nanostructures: Photoinduced screening of the internal electric field. *Phys. Rev. B* **2008,** *78*, 195313.

(137) Amirav, L.; Alivisatos, A. P., Photocatalytic Hydrogen Production with Tunable Nanorod Heterostructures. *The Journal of Physical Chemistry Letters* **2010,** *1*, 1051-1054.

(138) Talapin, D. V.; Koeppe, R.; Götzinger, S.; Kornowski, A.; Lupton, J. M.; Rogach, A. L.; Benson, O.; Feldmann, J.; Weller, H., Highly Emissive Colloidal CdSe/CdS Heterostructures of Mixed Dimensionality. *Nano Lett.* **2003,** *3*, 1677-1681.

(139) Li, J.; Wang, Shape Effects on Electronic States of Nanocrystals. *Nano Lett.* **2003,** *3*, 1357-1363.

(140) Kim, D.; Lee, Y. K.; Lee, D.; Kim, W. D.; Bae, W. K.; Lee, D. C., Colloidal Dual-Diameter and Core-Position-Controlled Core/Shell Cadmium Chalcogenide Nanorods. *ACS Nano* **2017,** *11*, 12461-12472.

(141) Bridewell, V. L.; Alam, R.; Karwacki, C. J.; Kamat, P. V., CdSe/CdS Nanorod Photocatalysts: Tuning the Interfacial Charge Transfer Process through Shell Length. *Chem. Mater.* **2015,** *27*, 5064-5071.

(142) Christodoulou, S.; Rajadell, F.; Casu, A.; Vaccaro, G.; Grim, J. Q.; Genovese, A.; Manna, L.; Climente, J. I.; Meinardi, F.; Rainò, G.; Stöferle, T.; Mahrt, R. F.; Planelles, J.; Brovelli, S.; Moreels, I., Band structure engineering via piezoelectric fields in strained anisotropic CdSe/CdS nanocrystals. *Nat. Commun.* **2015,** *6*, 7905.

(143) Oh, N.; Nam, S.; Zhai, Y.; Deshpande, K.; Trefonas, P.; Shim, M., Double-heterojunction nanorods. *Nat. Commun.* **2014,** *5*, 3642.

(144) McDaniel, H.; Zuo, J.-M.; Shim, M., Anisotropic Strain-Induced Curvature in Type-II CdSe/CdTe Nanorod Heterostructures. *J. Am. Chem. Soc.* **2010,** *132*, 3286-3288.

(145) McDaniel, H.; Oh, N.; Shim, M., CdSe-CdSexTe1-x nanorod heterostructures: tuning alloy composition and spatially indirect recombination energies. *J. Mater. Chem.* **2012,** *22*, 11621-11628.

(146) Kumar, S.; Jones, M.; Lo, S. S.; Scholes, G. D., Nanorod Heterostructures Showing Photoinduced Charge Separation. *Small* **2007,** *3*, 1633-1639.

(147) Fujishima, A.; Honda, K., Electrochemical Photolysis of Water at a Semiconductor Electrode. *Nature* **1972,** *238*, 37-38.

(148) Hoffmann, M. R.; Martin, S. T.; Choi, W.; Bahnemann, D. W., Environmental Applications of Semiconductor Photocatalysis. *Chem. Rev.* **1995,** *95*, 69-96.

(149) Zhou, H.; Qu, Y.; Zeid, T.; Duan, X., Towards highly efficient photocatalysts using semiconductor nanoarchitectures. *Energy & Environmental Science* **2012,** *5*, 6732-6743.

(150) Bard, A. J., Photoelectrochemistry. *Science* **1980,** *207*, 139-144.

(151) Hagfeldt, A.; Grätzel, M., Molecular Photovoltaics. *Acc. Chem. Res.* **2000,** *33*, 269-277.

(152) Law, M.; Greene, L. E.; Johnson, J. C.; Saykally, R.; Yang, P., Nanowire dye-sensitized solar cells. *Nat. Mater.* **2005,** *4*, 455-459.

(153) Hayden, O.; Agarwal, R.; Lieber, C. M., Nanoscale avalanche photodiodes for highly sensitive and spatially resolved photon detection. *Nat. Mater.* **2006,** *5*, 352-356.

(154) Lewis, N. S., Toward Cost-Effective Solar Energy Use. *Science* **2007,** *315*, 798-801.

(155) Gur, I.; Fromer, N. A.; Geier, M. L.; Alivisatos, A. P., Air-Stable All-Inorganic Nanocrystal Solar Cells Processed from Solution. *Science* **2005,** *310*, 462-465.

(156) Yang, C.; Barrelet, C. J.; Capasso, F.; Lieber, C. M., Single p-Type/Intrinsic/n-Type Silicon Nanowires as Nanoscale Avalanche Photodetectors. *Nano Lett.* **2006,** *6*, 2929-2934.

(157) Kelzenberg, M. D.; Turner-Evans, D. B.; Kayes, B. M.; Filler, M. A.; Putnam, M. C.; Lewis, N. S.; Atwater, H. A., Photovoltaic Measurements in Single-Nanowire Silicon Solar Cells. *Nano Lett.* **2008,** *8*, 710-714.

(158) Tian, B.; Kempa, T. J.; Lieber, C. M., Single nanowire photovoltaics. *Chem. Soc. Rev.* **2009,** *38*, 16-24.

(159) Dukovic, G.; Merkle, M. G.; Nelson, J. H.; Hughes, S. M.; Alivisatos, A. P., Photodeposition of Pt on Colloidal CdS and CdSe/CdS Semiconductor Nanostructures. *Adv. Mater.* **2008,** *20*, 4306-4311.

(160) Menagen, G.; Macdonald, J. E.; Shemesh, Y.; Popov, I.; Banin, U., Au Growth on Semiconductor Nanorods: Photoinduced versus Thermal Growth Mechanisms. *J. Am. Chem. Soc.* **2009,** *131*, 17406-17411.

(161) Schierhorn, M.; Boettcher, S. W.; Kraemer, S.; Stucky, G. D.; Moskovits, M., Photoelectrochemical Performance of CdSe Nanorod Arrays Grown on a Transparent Conducting Substrate. *Nano Lett.* **2009,** *9*, 3262-3267.

(162) Luque, A.; Martí, A.; Nozik, A. J., Solar Cells Based on Quantum Dots: Multiple Exciton Generation and Intermediate Bands. *MRS Bulletin* **2011,** *32*, 236-241.

(163) International Energy Agency (IEA), I. C. o. C. A., DECHEMA, *Technology roadmap: energy and GHG reductions in the chemical industry via catalytic processes*. IEA Publications: Paris (France), 2013.

(164) Han, Z.; Qiu, F.; Eisenberg, R.; Holland, P. L.; Krauss, T. D., Robust Photogeneration of H₂ in Water Using Semiconductor Nanocrystals and a Nickel Catalyst. *Science* **2012,** *338*, 1321-1324.

(165) Shemesh, Y.; Macdonald, J. E.; Menagen, G.; Banin, U., Synthesis and photocatalytic properties of a family of CdS-PdX hybrid nanoparticles. *Angew Chem Int Ed Engl* **2011,** *50*, 1185-9.

(166) Brown, K. A.; Dayal, S.; Ai, X.; Rumbles, G.; King, P. W., Controlled Assembly of Hydrogenase-CdTe Nanocrystal Hybrids for Solar Hydrogen Production. *J. Am. Chem. Soc.* **2010,** *132*, 9672-9680.

(167) Brown, K. A.; Wilker, M. B.; Boehm, M.; Dukovic, G.; King, P. W., Characterization of photochemical processes for H2 production by CdS nanorod-[FeFe] hydrogenase complexes. *J Am Chem Soc* **2012,** *134*, 5627-36.

(168) Wang, F.; Wang, W. G.; Wang, X. J.; Wang, H. Y.; Tung, C. H.; Wu, L. Z., A highly efficient photocatalytic system for hydrogen production by a robust hydrogenase mimic in an aqueous solution. *Angew Chem Int Ed Engl* **2011,** *50*, 3193-7.

(169) Zhu, H.; Song, N.; Lv, H.; Hill, C. L.; Lian, T., Near unity quantum yield of light-driven redox mediator reduction and efficient H2 generation using colloidal nanorod heterostructures. *J Am Chem Soc* **2012,** *134*, 11701-8.

(170) Holmes, M. A.; Townsend, T. K.; Osterloh, F. E., Quantum confinement controlled photocatalytic water splitting by suspended CdSe nanocrystals. *Chem Commun (Camb)* **2012,** *48*, 371-3.

(171) Chai, Z.; Zeng, T. T.; Li, Q.; Lu, L. Q.; Xiao, W. J.; Xu, D., Efficient Visible Light-Driven Splitting of Alcohols into Hydrogen and Corresponding Carbonyl Compounds over a Ni-Modified CdS Photocatalyst. *J Am Chem Soc* **2016,** *138*, 10128-31.

(172) Prier, C. K.; Rankic, D. A.; MacMillan, D. W. C., Visible Light Photoredox Catalysis with Transition Metal Complexes: Applications in Organic Synthesis. *Chem. Rev.* **2013,** *113*, 5322-5363.

(173) Skubi, K. L.; Blum, T. R.; Yoon, T. P., Dual Catalysis Strategies in Photochemical Synthesis. *Chem. Rev.* **2016,** *116*, 10035-10074.

(174) Romero, N. A.; Nicewicz, D. A., Organic Photoredox Catalysis. *Chem. Rev.* **2016,** *116*, 10075-10166.

(175) Kohls, P.; Jadhav, D.; Pandey, G.; Reiser, O., Visible Light Photoredox Catalysis: Generation and Addition of N-Aryltetrahydroisoquinoline-Derived α-Amino Radicals to Michael Acceptors. *Organic Letters* **2012,** *14*, 672-675.

(176) Yoon, T. P.; Ischay, M. A.; Du, J., Visible light photocatalysis as a greener approach to photochemical synthesis. *Nature Chemistry* **2010,** *2*, 527.

(177) Boerjan, W.; Ralph, J.; Baucher, M., Lignin Biosynthesis. *Annual Review of Plant Biology* **2003,** *54*, 519-546.

(178) Alonso, D. M.; Bond, J. Q.; Dumesic, J. A., Catalytic conversion of biomass to biofuels. *Green Chemistry* **2010,** *12*, 1493.

(179) Lofstedt, J.; Dahlstrand, C.; Orebom, A.; Meuzelaar, G.; Sawadjoon, S.; Galkin, M. V.; Agback, P.; Wimby, M.; Corresa, E.; Mathieu, Y.; Sauvanaud, L.; Eriksson, S.; Corma, A.; Samec, J. S., Green Diesel from Kraft Lignin in Three Steps. *ChemSusChem* **2016,** *9*, 1392-6.

(180) Ragauskas, A. J.; Williams, C. K.; Davison, B. H.; Britovsek, G.; Cairney, J.; Eckert, C. A.; Frederick, W. J.; Hallett, J. P.; Leak, D. J.; Liotta, C. L.; Mielenz, J. R.; Murphy, R.; Templer, R.; Tschaplinski, T., The Path Forward for Biofuels and Biomaterials. *Science* **2006,** *311*, 484-489.

(181) Chakar, F. S.; Ragauskas, A. J., Review of current and future softwood kraft lignin process chemistry. *Industrial Crops and Products* **2004,** *20*, 131-141.

(182) Holladay, J. E. a. W., J. F. and Bozell, J. J. and Johnson, D. *Top Value Added Chemicals from Biomass - Volume II, Results of Screening for Potential Candidates from Biorefinery Lignin*; United States, 2007.

(183) Lin, S. Y. L., I. S., *Ullmann's Encylcopedia of Industrial Chemistry*. 5th ed.; VCH: Weinheim, Germany, 1990; Vol. 15.

(184) Tuck, C. O.; Pérez, E.; Horváth, I. T.; Sheldon, R. A.; Poliakoff, M., Valorization of Biomass: Deriving More Value from Waste. *Science* **2012,** *337*, 695-699.

(185) Zakzeski, J.; Bruijnincx, P. C. A.; Jongerius, A. L.; Weckhuysen, B. M., The Catalytic Valorization of Lignin for the Production of Renewable Chemicals. *Chem. Rev.* **2010,** *110*, 3552-3599.

(186) Ralph, J.; Lundquist, K.; Brunow, G.; Lu, F.; Kim, H.; Schatz, P. F.; Marita, J. M.; Hatfield, R. D.; Ralph, S. A.; Christensen, J. H.; Boerjan, W., Lignins: Natural polymers from oxidative coupling of 4-hydroxyphenyl- propanoids. *Phytochemistry Reviews* **2004,** *3*, 29-60.

(187) Vanholme, R.; Demedts, B.; Morreel, K.; Ralph, J.; Boerjan, W., Lignin biosynthesis and structure. *Plant Physiol* **2010,** *153*, 895-905.

(188) Nguyen, J. D.; Matsuura, B. S.; Stephenson, C. R., A photochemical strategy for lignin degradation at room temperature. *J Am Chem Soc* **2014,** *136*, 1218-21.

(189) Sergeev, A. G.; Hartwig, J. F., Selective, Nickel-Catalyzed Hydrogenolysis of Aryl Ethers. *Science* **2011,** *332*, 439-443.

(190) Galkin, M. V.; Samec, J. S., Selective route to 2-propenyl aryls directly from wood by a tandem organosolv and palladium-catalysed transfer hydrogenolysis. *ChemSusChem* **2014,** *7*, 2154-8.

(191) Wang, M.; Li, L. H.; Lu, J. M.; Li, H. J.; Zhang, X. C.; Liu, H. F.; Luo, N. C.; Wang, F., Acid promoted C–C bond oxidative cleavage of β-O-4 and β-1 lignin models to esters over a copper catalyst. *Green Chemistry* **2017,** *19*, 702-706.

(192) Zhu, C.; Ding, W.; Shen, T.; Tang, C.; Sun, C.; Xu, S.; Chen, Y.; Wu, J.; Ying, H., Metallo-deuteroporphyrin as a biomimetic catalyst for the catalytic oxidation of lignin to aromatics. *ChemSusChem* **2015,** *8*, 1768-78.

(193) Sedai, B.; Díaz-Urrutia, C.; Baker, R. T.; Wu, R.; Silks, L. A. P.; Hanson, S. K., Aerobic Oxidation of β-1 Lignin Model Compounds with Copper and Oxovanadium Catalysts. *ACS Catalysis* **2013,** *3*, 3111-3122.

(194) Lancefield, C. S.; Ojo, O. S.; Tran, F.; Westwood, N. J., Isolation of functionalized phenolic monomers through selective oxidation and C-O bond cleavage of the beta-O-4 linkages in lignin. *Angew Chem Int Ed Engl* **2015,** *54*, 258-62.

(195) Galkin, M. V.; Sawadjoon, S.; Rohde, V.; Dawange, M.; Samec, J. S. M., Mild Heterogeneous Palladium-Catalyzed Cleavage of β-O-4′-Ether Linkages of Lignin Model Compounds and Native Lignin in Air. *ChemCatChem* **2014,** *6*, 179-184.

(196) Chan, J. M. W.; Bauer, S.; Sorek, H.; Sreekumar, S.; Wang, K.; Toste, F. D., Studies on the Vanadium-Catalyzed Nonoxidative Depolymerization of Miscanthus giganteus-Derived Lignin. *ACS Catalysis* **2013,** *3*, 1369-1377.

(197) Karkas, M. D.; Bosque, I.; Matsuura, B. S.; Stephenson, C. R., Photocatalytic Oxidation of Lignin Model Systems by Merging Visible-Light Photoredox and Palladium Catalysis. *Org Lett* **2016,** *18*, 5166-5169.

(198) Bosque, I.; Magallanes, G.; Rigoulet, M.; Karkas, M. D.; Stephenson, C. R. J., Redox Catalysis Facilitates Lignin Depolymerization. *ACS Cent Sci* **2017,** *3*, 621-628.

(199) Karkas, M. D.; Matsuura, B. S.; Monos, T. M.; Magallanes, G.; Stephenson, C. R., Transition-metal catalyzed valorization of lignin: the key to a sustainable carbon-neutral future. *Org Biomol Chem* **2016,** *14*, 1853-914.

(200) Rahimi, A.; Azarpira, A.; Kim, H.; Ralph, J.; Stahl, S. S., Chemoselective metal-free aerobic alcohol oxidation in lignin. *J Am Chem Soc* **2013,** *135*, 6415-8.

(201) Jasieniak, J.; Califano, M.; Watkins, S. E., Size-Dependent Valence and Conduction Band-Edge Energies of Semiconductor Nanocrystals. *ACS Nano* **2011,** *5*, 5888-5902.

(202) Wakerley, D. W.; Kuehnel, M. F.; Orchard, K. L.; Ly, K. H.; Rosser, T. E.; Reisner, E., Solar-driven reforming of lignocellulose to H2 with a CdS/CdOx photocatalyst. *Nature Energy* **2017,** *2*.

(203) Enright, M. J.; Gilbert-Bass, K.; Sarsito, H.; Cossairt, B. M., Photolytic C–O Bond Cleavage with Quantum Dots. *Chemistry of Materials* **2019,** *31*, 2677-2682.

Chapter 2. KINETICALLY CONTROLLED ASSEMBLY OF CADMIUM CHALCOGENIDE NANORODS AND NANOROD HETEROSTRUCTURES

Components of this chapter were Republished with permission of the Royal Society of Chemistry, from Kinetically controlled assembly of cadmium chalcogenide nanorods and nanorod heterostructures, Enright M. J., Sarsito, H., and Cossairt. B. M., 2, 2018; permission conveyed through Copyright Clearance Center, Inc.

The range of reaction conditions for synthesis of anisotropic nanostructures is narrow. Furthermore, most existing reports of these syntheses conclude their investigations with simply creating a mostly uniform, high aspect ratio product. However, a nanomaterial's optical and electronic properties are dictated by its size and structure. Thus, to fully realize the potential of anisotropic shape and size control, more clearly defined rules for material assembly are required to understand how to create a structure of a preconceived set of dimensions.

2.1 INTRODUCTION

Since the turn of the 19th century when the concept of interchangeability led to the dawn of modern assembly-line manufacturing, there has been great effort in developing processes that reproducibly yield products of an exact structure and composition from a set of constituent parts. A longstanding goal in the field of nanoscience has been the practical translation of this concept to the bottom-up synthesis of nanomaterials. For nanomaterial synthesis, as in nearly all other fields, it is

desirable to have the ability to control the shape and structure of a material and to tune these features to modulate the chemical and physical properties for specific applications.[1-3] Anisotropic nanostructures have unique, direction-dependent properties that enable both confinement of electrons, holes, and phonons as well as delocalization of charge carriers in specific and predictable directions.[1,2] This directional control has value in applications from energy conversion and storage devices (such as lithium ion batteries, thermoelectric devices, and solar cells)[4-11] to electronics (such as conducting platforms, transistors, and electromechanical devices).[12-15] Furthermore, anisotropic structures hold great potential for use in optical (*i.e.* lasers, photodetectors, and OLEDs)[16-18] and electrochemical devices (*i.e.* catalysis and sensors).[19-20]

Metal chalcogenide nanomaterials are a class of semiconductors that possess useful properties for photovoltaic, photodetector, and photocatalytic applications due to their ability to efficiently absorb sunlight to generate excitons.[21] Furthermore, the size and shape of metal chalcogenide nanomaterials can be inexpensively controlled using colloidal synthetic techniques.[22-24] Specifically, the ability to exploit structural differences between wurtzite and zinc blende crystal structures facilitates colloidal synthesis of nanocrystals with unique crystal facets and distinct shapes. Axial growth on wurtzite nanocrystals occurs on the (0001) axis to give high aspect ratio nanorods. Existing mechanistic studies show the importance of monomer concentration on rod growth,[25] as well as support a magic size cluster mediated pathway.[26] The impact of ligands on directional nanocrystal growth has also been examined, showing a clear impact on growth rates and specific facet coordination on asymmetric wurtzite seeds.[27]

While it is well understood that controlling anisotropic structure formation can be accomplished by establishing kinetic growth conditions, the practical extension of this knowledge to access nanorods with a specific aspect ratio has not been realized. The approach adopted in most synthetic reports is to devise a set of conditions that give nanorods. However, for nanomaterial application development, the

logic of this approach must be flipped so that the nanorod structure is considered first and then synthetic conditions are devised for obtaining the target structure. Here, existing precedents and established methods for crystal growth serve as a foundation for method development to access nanorods of specific lengths and widths. The purpose of this work is to go beyond simply creating a set of growth conditions to obtain rods, dots, rice, and tetrapods,[23] and to demonstrate how to synthesize a nanomaterial of desired aspect ratio in a premeditated fashion. Specifically, monomer addition rates are measured on seeded and unseeded CdSe nanorods. However, simply using these growth rates as monomer resupply rates during nanorod growth is insufficient to maintain kinetic, 1-D growth. Instead, it is demonstrated that maintaining high precursor concentrations is more important for extending 1-D growth and the Cd/Se to ligand ratios required for preserving a 1-D growth environment are quantified. Understanding these parameters in any system enables premeditated design of nanorods of specific aspect ratios and reduces the amount of waste from unused precursors. This work also describes how to control nanocrystal growth on a pre-existing seed, enabling greater customizability of anisotropic nanostructures. The vision for this model system is to serve as a rubric for the development of customizable anisotropic nanocrystals, and as a platform for understanding heterostructure assembly in colloidal systems.

2.2 Kinetics of Cadmium Selenide nanorod growth

Extensive work has been carried out to synthesize high aspect ratio CdSe nanorods for a variety of diverse applications.[28] Most of these procedures are based on the same recipe where a long chain cadmium alkyl phosphonate is heated to high temperature (above 300 °C) in trioctylphosphine oxide (TOPO) solvent. Then, a solution of selenium precursor, most commonly trioctylphosphine selenide (TOP=Se), is injected rapidly to facilitate nucleation of wurtzite CdSe crystals before a growth

temperature (around 250 °C) is established to grow the nanorods. For many investigations (*i.e.* functionalization with catalytically active nanoparticle tips,[29-32] exciton generation and mobility studies,[33-34] and device assembly[35-36]) simply obtaining a reasonably monodisperse sample of nanorods with a high aspect ratio is sufficient. Mechanistic studies of anisotropic assembly and shape control have illuminated the specific conditions required to enable rod growth as well as outline the general stages of rod growth construction.[26-27, 37] Despite these contributions and the apparent ease of obtaining non-isotropic cadmium chalcogenide structures, the scientific community still does not yet have sufficient synthetic control to enable the *a priori* setting of reaction conditions to obtain nanorods of a specific aspect ratio and length. In this report, a generalizable rubric is outlined for how to determine rod growth rates and use that information to design rods or heterostructures of desired dimensions.

The generally accepted mechanism for syntheses that yield nanorods proceeds through three phases.[37] First, when reagent concentrations are high, growth along the *c*-axis of a wurtzite nanocrystal is promoted and known as the 1-D growth regime. As precursors are consumed by the growing nanorod, the solubilized monomer concentration decreases, and growth is facilitated on all axes, known as the 3-D growth regime. Understanding when to expect axial growth to slow down relative to radial growth is vital for targeted structure assembly. The synthesis time it takes to reach the transition point between the two regimes is highly sensitive to each system. Evaluating precursor amounts and concentrations at these observable transition points can help accurately determine when to expect synthetic conditions to promote 1-D or 3-D nanocrystal growth. The third regime is rod-to-sphere ripening, which occurs when the concentration of precursors falls below a second threshold and no longer facilitates growth of new monomer on the nanocrystal. During this phase, monomers from the rod ends migrate to the sides of the rod to give spheres, the more thermodynamically favored product over the kinetically derived rods.

To better understand how to design nanorods of desired dimensions, a baseline evaluation of unseeded nanorod growth rate is a vital first step. As can be seen in the absorbance spectrum in Figure 1.1 and as detailed by Jiang and Kelley, the mechanism of nanorod growth proceeds *via* a magic size cluster (MSC) mediated pathway.[26] The sharp feature at 348 nm is indicative of the presence of the MSC throughout the initial 30 min of nanorod growth. Aspect ratio evaluation of the nanomaterials over this timeframe shows nanorods, once seeded, grow nearly exclusively along the wurtzite *c*-axis, for the first 16–18 min. Figure 2.1 shows that at approximately 18–20 min, the aspect ratio, as well as rate of length increase begin to slow as the growing nanorods begin to transition from the 1-D growth regime into the 3-D growth regime. Despite the tapering of length growth rate, the rate of nanocrystal volume growth remains relatively unchanged. At this transition point, there is still an abundance of precursor present to exceed the critical saturation point to make MSCs, as well as sufficient precursor present to enable nanocrystal growth at an unimpeded rate. Despite this, the available concentration of monomer has decreased enough to no longer support 1-D growth kinetics.

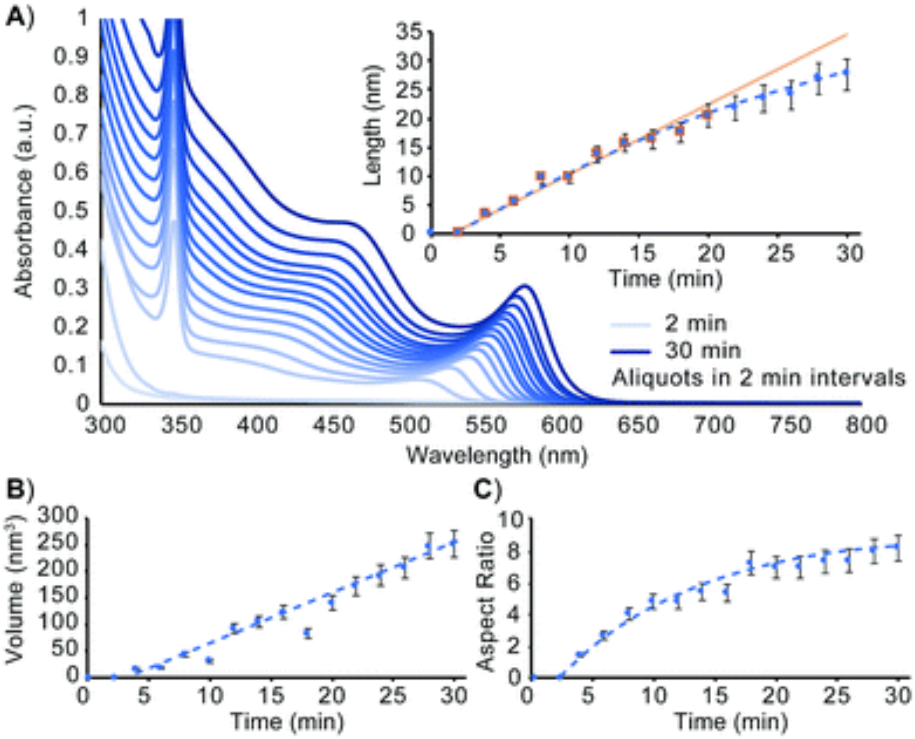

Figure 2.1. Evaluation of unseeded CdSe nanorod growth. (A) UV-Vis spectra at 2 min intervals over the first 30 min of nanorod growth. Nanorod dimensions measured using TEM analysis as a function of time are plotted for length (A, inset), volume (B), and aspect ratio (C). The equation for the line of best fit for the volume *vs.* time relationship is $y = 9.7919x - 44.591$. Associated TEM images are included in Appendix A, Figure A.1.

Nucleation of wurtzite seeds requires high temperatures (above 300 °C), which is why rod growth begins with rapid, hot-injection of the selenium precursor. Growth of elongated wurtzite rods upon a wurtzite seed (dots or rods), however, is readily facilitated at 250 °C when sufficient monomer is present. As long as there is a source of seeds and a supply of monomers, or available precursor to give monomers, rod growth can be restarted and maintained at 250 °C. Independent nucleation of new nanomaterials is not observed when the reaction is restarted from seeds below the nucleation temperature. Figure 2.2 and Figure A.2. illustrate that nanorods can be used as seeds for extended

nanorod growth in fresh precursor and that successive additions of new precursor enable continued nanorod growth to 100 nm.

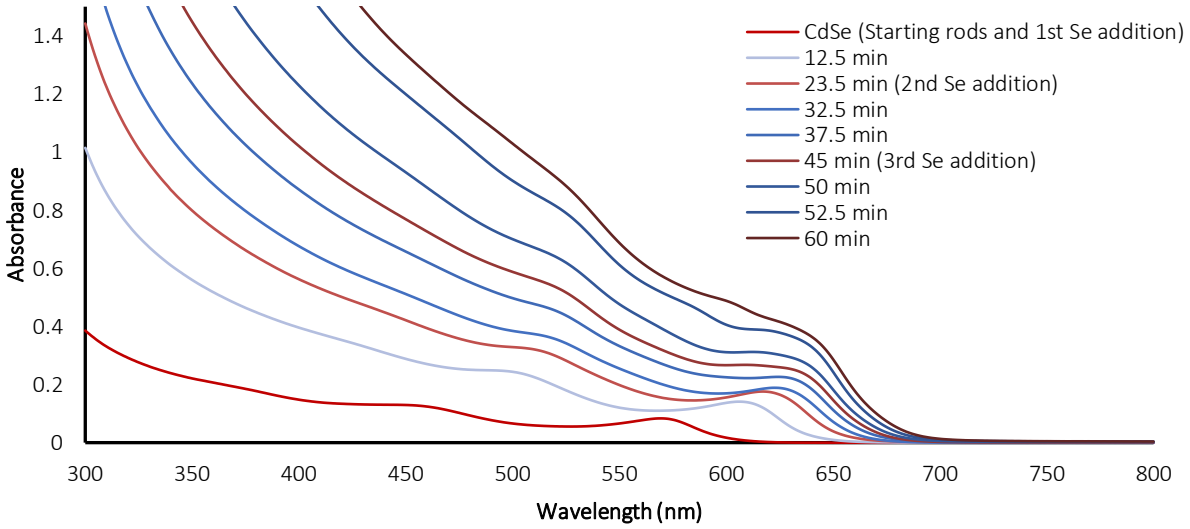

Figure 2.2. Evolving absorption spectrum over multiple selenium additions. The increasing nanorod size evolves through three subsequent additions of TOP-Se into a bath of excess cadmium tetradecylphosphonate (Cd-TDPA) precursor.

Since the 1-D growth regime only predominates over the first 20 minutes of CdSe nanorod growth, it is necessary to devise methods to prolong the duration of length growth to continue to access nanorods of increasing length. One way the duration of the 1-D growth regime is increased is to halt CdSe nanorod growth within the first 20 min and use those nanorods as seeds to restart rod growth in a fresh bath of precursor. Restarting the reaction with fresh precursor effectively reinstates the original 1-D growth regime conditions and rod growth begins again upon the nanorod seeds. The CdSe rod growth reaction can be halted and restarted by removing or providing heat to the system.

2.3 NANOROD ELONGATION BY THE GROWTH-PURIFY-RESTART METHOD

Restarting nanorod growth with a fresh supply of precursor gives longer nanorods with greater aspect ratios over the same total growth time. Figure 2.3 displays the set of nanorod seeds (column 1) used as scaffolds for continued rod growth. These rods are extracted from a solution of growing nanorods. An identical volume of each sub-sample of nanorods was extracted at each time point (10 min, 20 min, 30 min, and 60 min) and each sample of rods was purified in an identical manner to remove unreacted precursor and unbound ligand. A combination of quantification of CdSe composition using Inductively Coupled Plasma-Optical Emission Spectroscopy (ICP-OES) and TEM evaluation to determine rod volume was used to verify that the number of rod seeds to be added to fresh precursor remains the same across all growth restart procedures. Rod growth was restarted upon the purified, intermediate seeds through rapid injection of selenium precursor to a solution of seeds and cadmium tetradecylphosphonate (Cd-TDPA) at 250 °C. Figures 2.3 – 2.5 show that restarting rod growth upon nanorods originally grown for 10 min and 20 min facilitates greater rod elongation than the expectation for a growing nanorod over the same total reaction time. A nanorod that experiences 10 min of growth, purification, and an additional 10 minutes of growth in fresh precursor is both longer and exhibits a greater aspect ratio than a nanorod that grows for 20 min continuously. Every time rod growth conditions are reinitiated; width growth is curtailed, and aspect ratio increases. A comparison of nanorods that have experienced 30 min of total growth time shows that nanorods that undergo a growth–purify–restart procedure with purification at 10 min or 20 min gives higher aspect ratio nanorods than 30 min of continuous growth. Curiously, a sample that first grows for 10 min with an additional 20 min of growth has a smaller aspect ratio than its converse (20 min growth initially followed by 10 additional minutes). One explanation for this phenomenon is that there is a 4–5 min induction time between precursor injection and the start of nanocrystal growth when starting a reaction without seeds. The

restarted reactions have seeds and do not require this additional pre-growth time. Since the greatest enhancements to aspect ratio occur between 5–20 min (15 min of growth time) the 10 min + 20 min sample experiences 5 min of 1-D growth before purification but only 15 min of 1-D growth when restarted. The 20 min + 10 min sample experiences 15 min of 1-D growth pre-purification and 10 min after restart. Thus, the 10 min + 20 min sample experiences 5 fewer minutes of 1-D growth and has a smaller aspect ratio. Major caveats to rod elongation *via* the growth–purify–restart method is the increased level of waste and significant time increase with each subsequent restart.

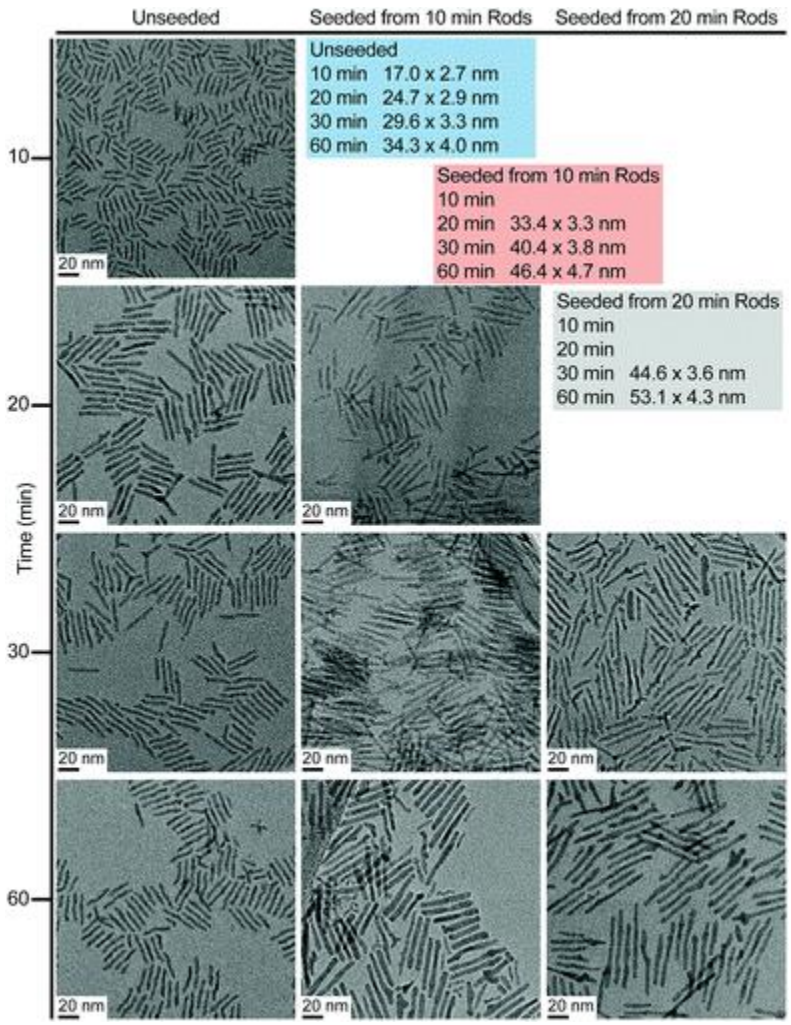

Figure 2.3. TEM images showing unseeded and seeded nanorod growth as a function of time. Nanorod dimensions (length by width) are summarized explicitly in the tables at the upper right.

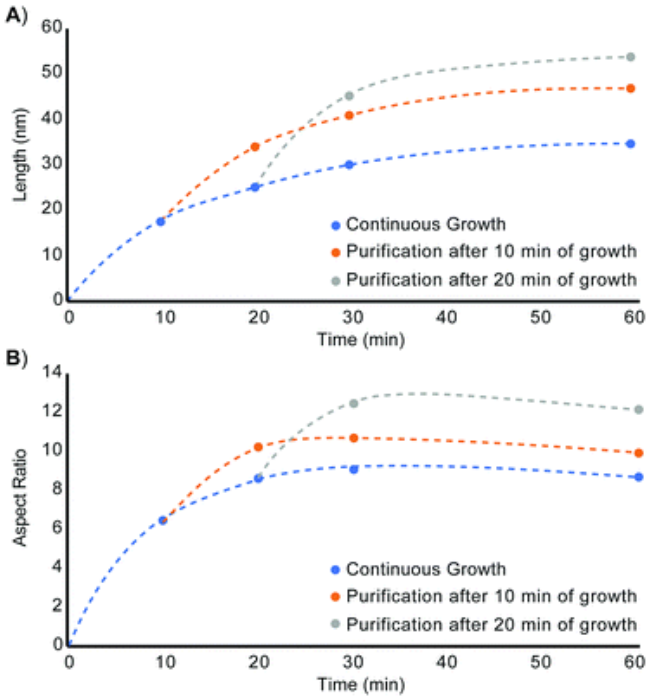

Figure 2.4. Length and aspect ratio evolution of unseeded and seeded nanorods. Length (A) and aspect ratio (B) evolution over 60 minutes of rod growth for unseeded CdSe nanorods (blue), nanorods seeded from nanorods grown for 10 minutes (orange), and nanorods seeded from nanorods grown for 20 minutes (gray).

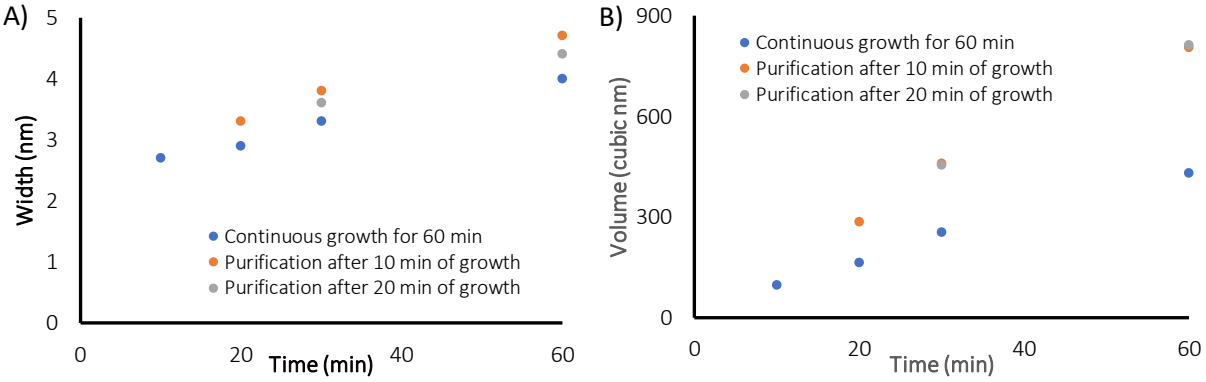

Figure 2.5. Growth-purify-restart method evaluation of width and volume. Width (A) and volume (B) vs time for the growth-purify-restart method of rod elongation corresponding to the same rod growth procedure imaged in Figure 2.3.

2.4 NANOROD ELONGATION BY RESUPPLYING PRECURSOR

In order to more readily access nanorods of prescribed dimensions without extensive intermediary purification, a more comprehensive understanding of rod growth conditions beyond knowing when a synthesis transitions between 1-D and 3-D growth regimes is needed. Revisiting the data presented in Figure 2.1, an evaluation of unseeded nanorod growth shows that nanorods increase in volume at a rate of 2.9 monomers rod^{-1} s^{-1}. This is determined by Using on the relationship between volume *vs.* time, where the slope is 9.79, and the known volume of a CdSe unit cell composed of 4 atoms (2 cadmium and 2 selenium) of 112.25 $Å^3$.

While tracking length increase and elucidating monomer addition rates can assist in understanding how to better target a specific nanostructure, it is an incomplete description of how to establish synthetic conditions for prolonging rod growth over an extended period of time. Quantifying the monomer consumption rate for a known concentration of seeds, however, is sufficient for determining the exact amount of reagent consumed by the growing nanorod ensemble. This assembly

rate can be subsequently applied to future systems in which precursor is resupplied to maintain 1-D growth regime conditions.

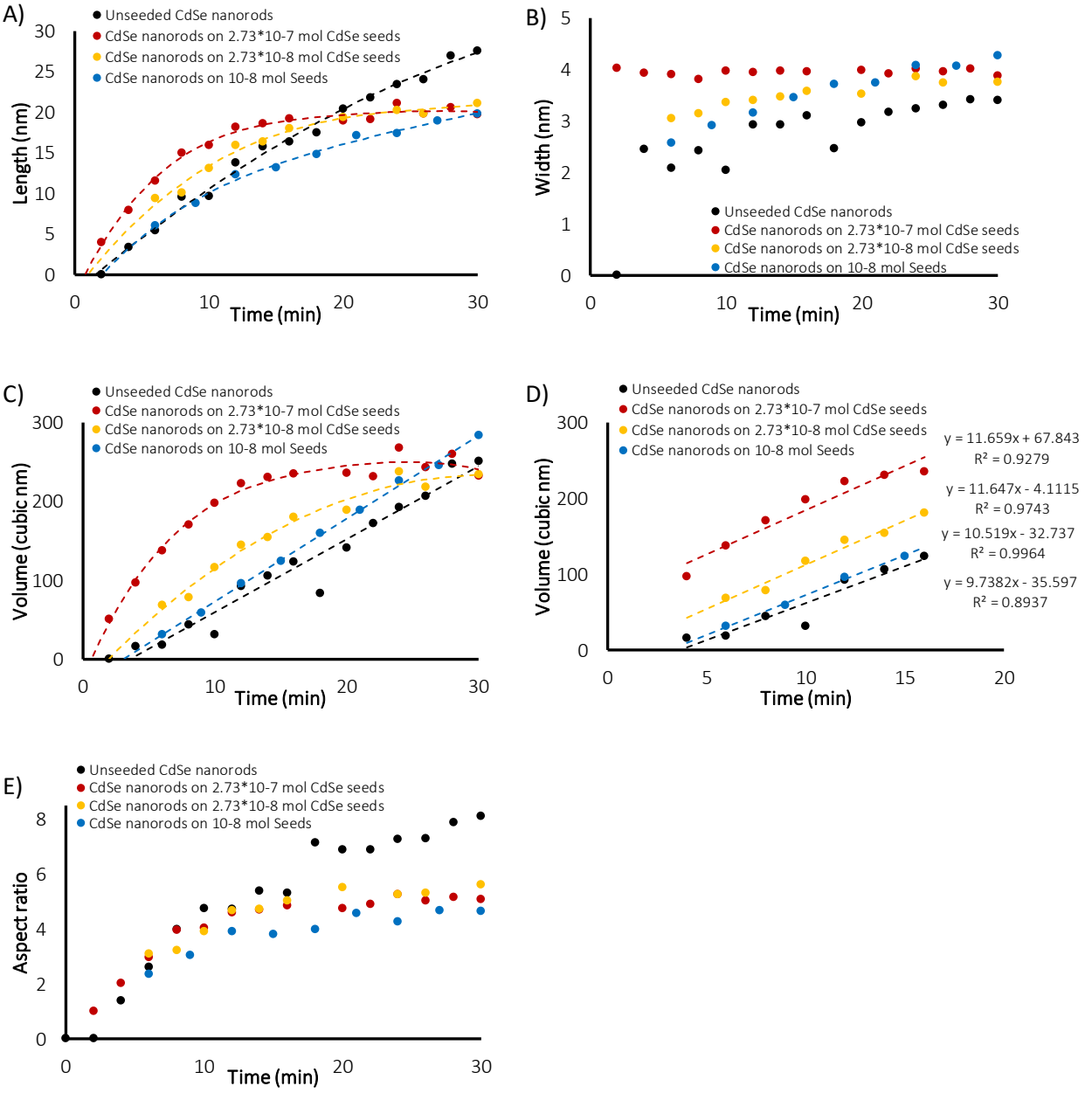

Figure 2.6. CdSe nanorod growth on CdSe seeds. Length (A), width (B), volume (C and D), and aspect ratio (E) are tracked over the duration of each reaction. (D) is a slope evaluation between 4-16 min, the period of time dominated by length growth, used to determine monomer addition rates for each seeded synthesis. Rod growth occurs at 2.9 monomers rod^{-1} s^{-1} for unseeded nanorods, 3.5 monomers rod^{-1} s^{-1} for$2.73*10^{-7}$ mol and $2.73*10^{-8}$ mol seeds.

The number of nanorods is estimated using the CdSe extinction coefficient that has been measured for CdSe quantum dots.[38] Notably, this estimation appeared consistent with nanorod quantification using a combination of ICP-OES and TEM. In an effort to best emulate the unseeded rod growth synthesis, three concentrations of wurtzite CdSe nanoparticle seeds were used as scaffolds for CdSe nanorod growth: 2.73×10^{-7} mol, 2.73×10^{-8} mol, and 1.00×10^{-8} mol seed samples. As can be seen in Figure 2.6 and TEM images presented in Appendix A, Figures A.3 – A.5, none of the three seed concentrations yielded an exact match to the growth rate of unseeded nanorods, however, the 2.73×10^{-8} mol seed synthesis tracked the closest. The 2.73×10^{-7} mol appears to have too many seeds because the length and volume of the nanocrystals appears to reach a limit of length and volume prior to 15 min of growth and this nanorod size is both shorter and has less volume than that observed for unseeded nanorods grown for 30 min. The higher seed count leads to less precursor available to grow upon each nanorod. It also gives a lower effective precursor concentration leading to a shorter period of time in the 1-D growth regime and an earlier entrance into the 3-D growth regime. While the 1.00×10^{-8} mol seed sample appears to track well to the unseeded case by volume, the rate of length growth is slower. This appears to point to a lower limit for nucleus concentration given the set of precursor conditions. The low seed concentration may lead to nucleation of new CdSe. The 2.73×10^{-8} mol seeded growth rates tracked closely to the unseeded growth rates by both length and width evaluations and is used as the starting seed concentration for precursor replenishment studies. Evaluation of the volume growth rates of all of the seeded samples over the early time points (before the rate of volume increase tapers off) shows that all three seeded samples grow at a rate of 3.5 monomers $\text{rod}^{-1}\ \text{s}^{-1}$.

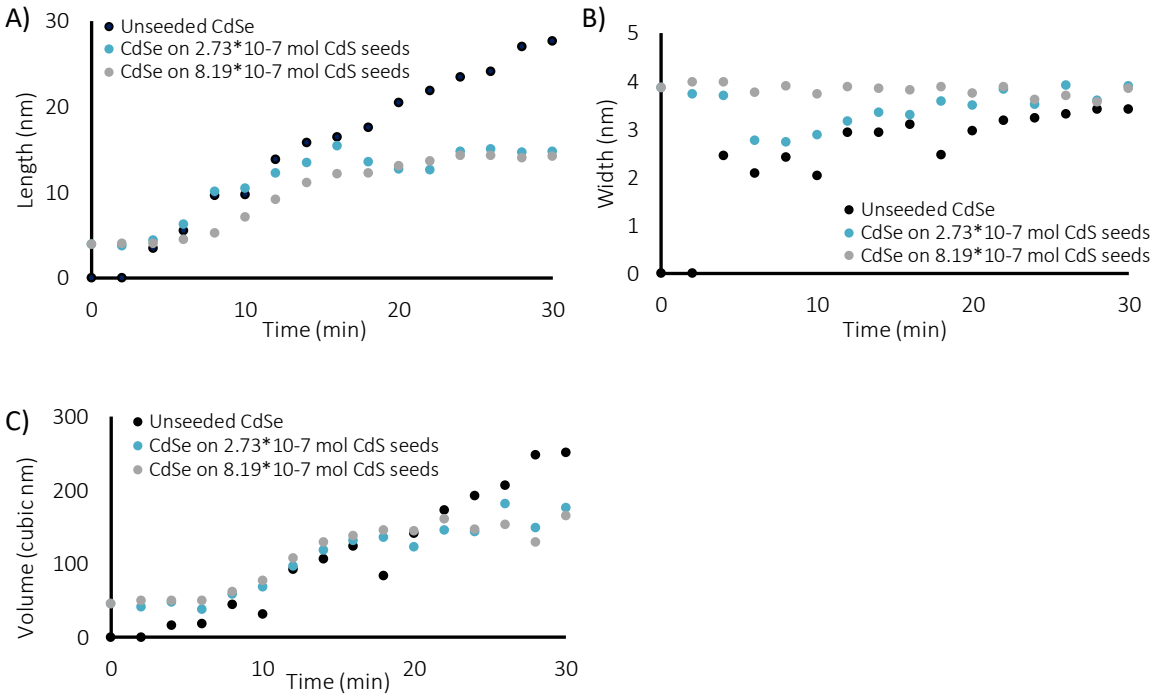

Figure 2.7. CdSe nanorod growth on CdS seeds. The length (A), width (B), and volume (C) profiles over time for CdSe nanorod growth when seeded with wurtzite CdS seeds.

Similar CdSe growth rates are observed when using wurtzite CdS seeds as a scaffold for CdSe nanorod growth. As can be seen in Figure 2.7 and TEM images presented in Appendix A, Figures A.6 – A.7, CdSe growth on two different concentrations of CdS seeds demonstrated a nearly identical volume, length, and growth rate between 5–20 min of the reaction when compared to unseeded CdSe growth. This is important for heterostructure development since changing the seed material appears to have minimal impact on the rate of the growing nanorod. It should be noted that there is an initial etching step when using CdS seeds. The width of the material when using 2.73×10^{-7} mol seeds initially decreases before retaining its original 4 nm size. When a greater concentration of seeds is provided to the system (8.19×10^{-7} mol) the etching step is less readily observable. In the high seed concentration heterostructure, the growing nanorods exit the 1-D growth regime more quickly than in any other lower

seed concentration conditions. Thus, the conditions for the high seed concentration rod growth likely enters the 3-D growth regime at an earlier time point, thereby replacing the etched surface with new monomer more quickly.

Conversely, growth rates for CdS nanorod growth on CdSe seeds can be determined using the same type of TEM evaluation. CdS nanorod growth is typically carried out at greater temperatures (340 °C) and higher chalcogenide precursor concentrations when compared to CdSe nanorod growth.[38] This is due to the decreased reactivity of TOP-S *versus* TOP-Se, which arises from the stronger binding of S to P, resulting in less available S^{2-}on a per molecule basis.[39] CdS monomers assemble on growing CdS rods at a rate of 36 monomers rod^{-1} s^{-1}. While this measured rate is about 10 times more rapid than CdSe at 250 °C, it does not serve as a direct comparison to CdSe nanorod growth due to disparate temperature and concentration conditions. Despite these differences, seeded rod growth of CdS and CdSe nanorods both exhibit an abrupt curtailment to the length extension rate of the growing material. After 15 min, 1-D growth abruptly slows, and volume increases are predominately from increases in nanorod width. Figures detailing the rates of length, width, volume, and aspect ratio of the growing nanorod sample are shown in the Figure 2.8 and TEM images in Appendix A, Figure A.8.

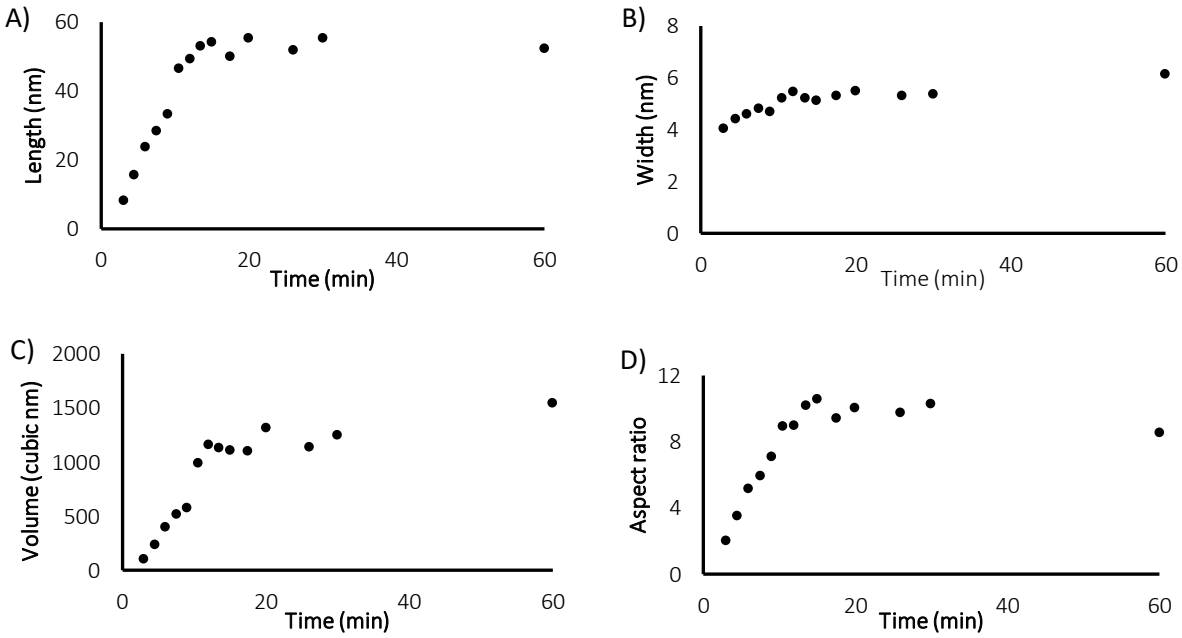

Figure 2.8. CdS growth on CdSe seeds. Length (A), width (B), volume (C), and aspect ratio (D) over time.

Knowing the exact number of seeded nanorods in the system enables accurate determination of precursor consumption and precursor to rod incorporation yields. Over the first 30 min of the reaction, the time where the highest aspect ratio nanorods are obtained, less than 10% of the precursors have been incorporated into nanorods. Evaluation of the aspect ratios for both seeded and unseeded CdSe nanorods shows that enhancements to aspect ratio decline for both seeded and unseeded rods before 20 min of reaction. At 20 min, only 6.1% and 4.3% of the available cadmium supply has been incorporated into nanorods for the seeded and unseeded cases, respectively. These low percentage yields and narrow window for reaction conditions that facilitate nanorod growth are two major challenges for anisotropic nanocrystal and heterostructure development.

Since favorable rod growth conditions only exist in a small window with abundant precursor, spiking the system with excess reagent during the reaction should replenish the reagent consumed

during the early time points of the synthesis and retain conditions for the 1-D growth regime. As can be seen in the unseeded and seeded growth cases, there is never more than a 5 min induction time to build up sufficient monomer reserves before rod growth begins. Based on these observations, replenishment at 7.5 min is late enough that it should not disrupt initial monomer formation and rod nucleation. Since rods remain in the 1-D growth regime beyond the first 15 min, there is also sufficient time to generate new monomers from the fresh precursor to promote continued length growth. As can be seen in Figure 2.9, doubling the amount of fresh precursor at 7.5 min does in fact prolong the amount of time spent in the 1-D growth regime and yields longer and thinner nanorods compared to their counterparts from non-replenishment syntheses across the same time points. Doubling the starting precursor extends the duration of 1-D growth to about 35 min, while adding 50% more precursor leads to exiting the 1-D growth regime before 25 min. The width, volume, and aspect ratio profiles over time for addition of fresh precursor at a single event are depicted in Figure 2.10 with accompanying TEM images in Appendix A, Figures A.9 – A.10, for precursor doubling and 50% more precursor respectively.

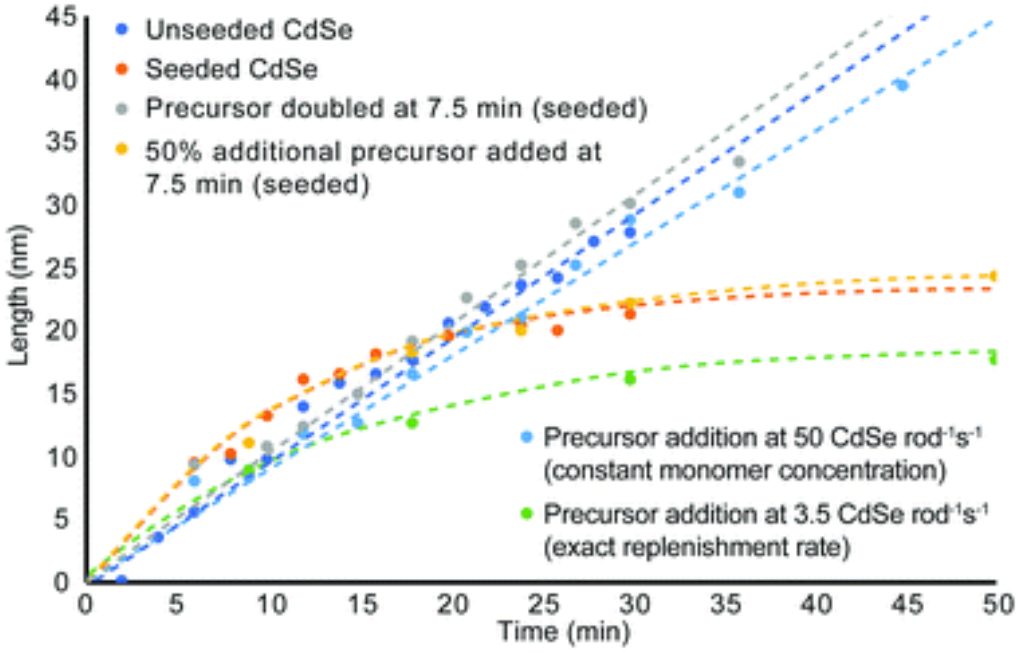

Figure 2.9. Comparison of length evolution across reaction conditions. For all precursor addition reactions, nanorod growth was seeded by wurtzite CdSe seeds and the precursor addition was initiated at 7.5 minutes.

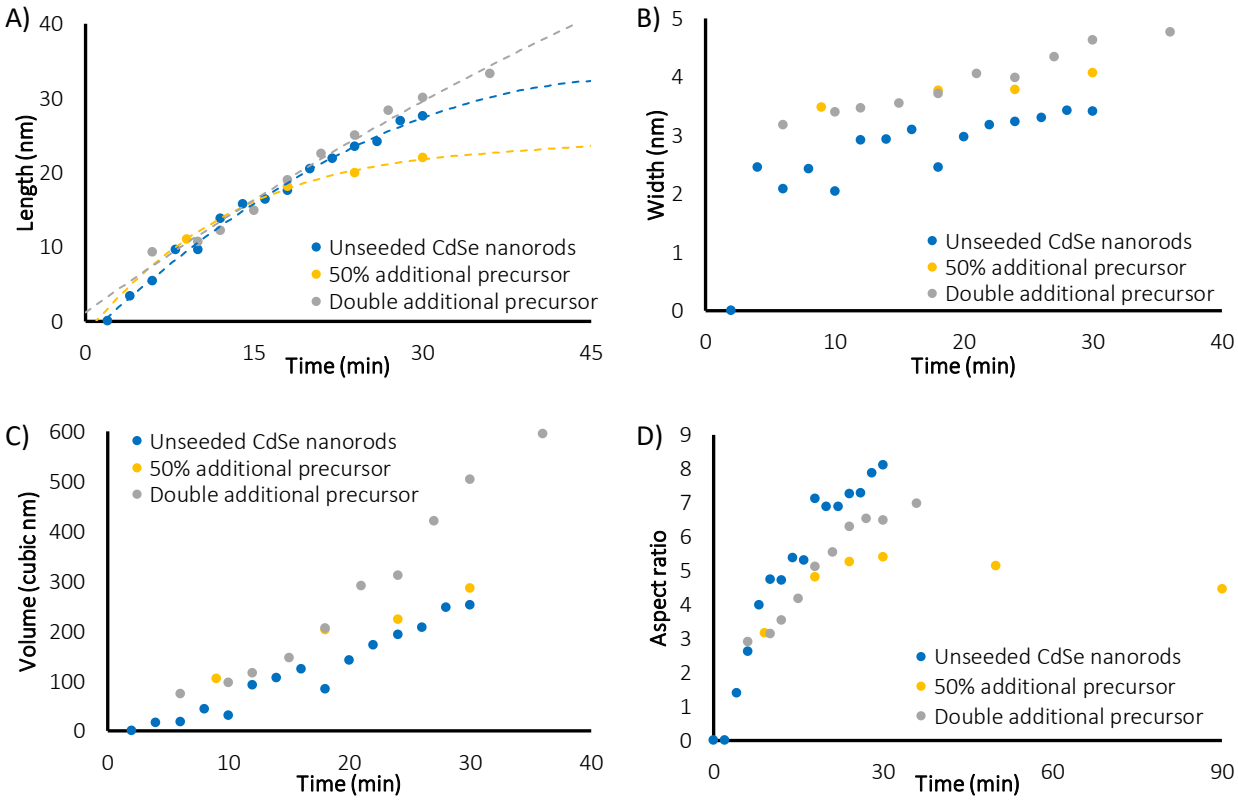

Figure 2.10. Single addition precursor replenishment. The length (A), width (B), volume (C), and aspect (D) profiles are tracked over time for CdSe nanorod growth facilitated by replenishment of additional precursor added all at once at 7 min 30 s.

2.5 EFFECTS OF LIGAND CONCENTRATION ON MONOMER FORMATION

Real-time monomer concentration is challenging to quantify directly, so instead the concentrations of cadmium and selenium to provide insights into precursor availability are projected throughout the reaction. Looking at the ratio of cadmium to its native ligand, TDPA, and selenium to trioctylphosphine, also assists in deconvoluting the availability of monomer. Figure 2.11 shows the simulated molarities of cadmium and selenium as well as the ratios of cadmium and selenium to their native ligand based on our calculated precursor consumption rates. These simulations quantify precursor

availability throughout the experiment and project what the expected precursor molarities would be assuming constant nanorod growth rate over the first 30 min of the reaction. The simulation uses the measured growth rates by volume observed over the 1-D growth regime. The constant monomer consumption measured during 1-D growth are not maintained throughout the 3-D growth regime. However, in all aforementioned unseeded, seeded, and precursor replenishment conditions, the constant growth rates by volume extend through the entire 1-D growth regime and into the early part of 3-D growth.

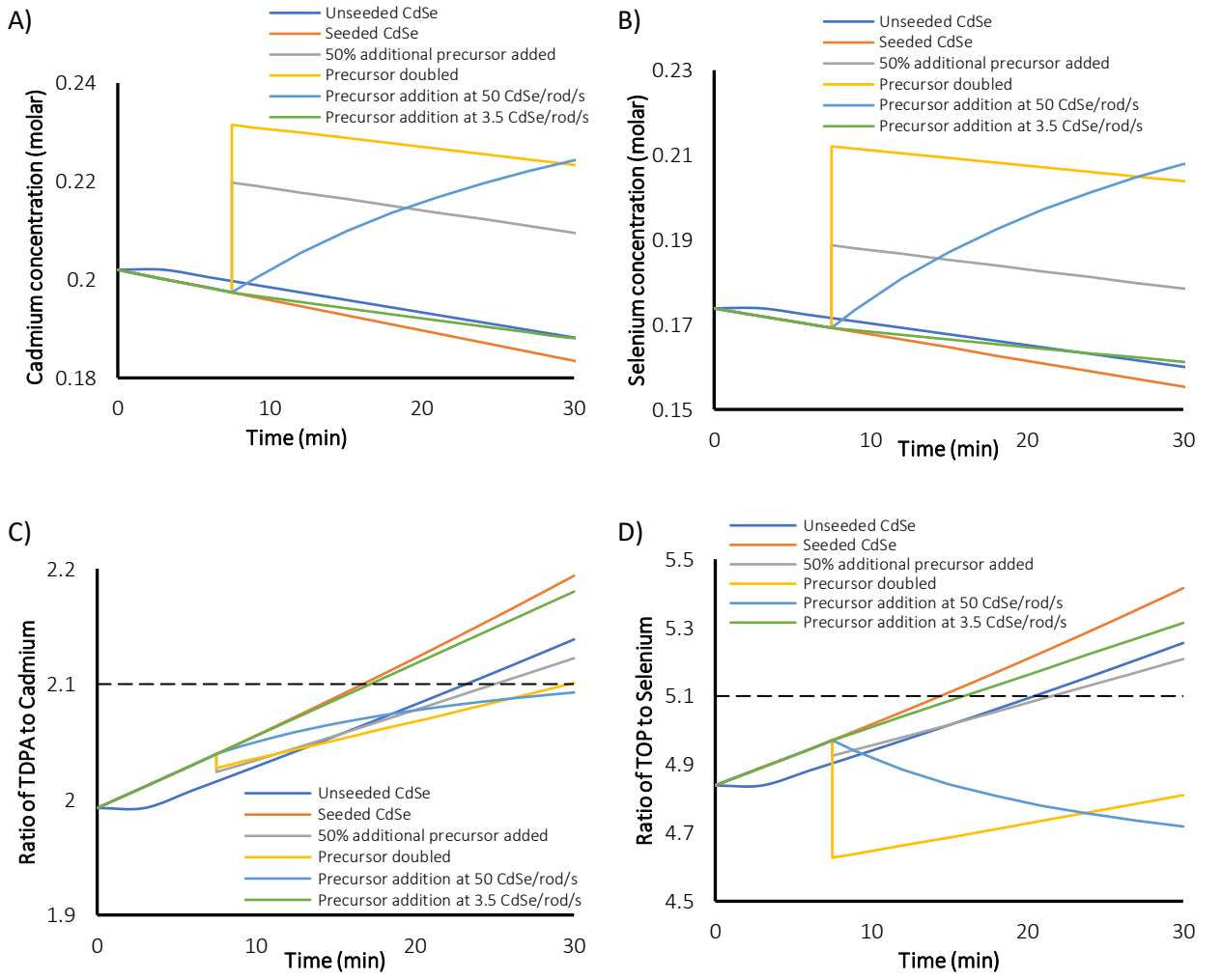

Figure 2.11. Evaluation of precursor concentrations and Cd/Se to ligand ratios to determine thresholds for extending the duration of the 1-D growth regime. Concentration of cadmium (A) and selenium (B) are shown with ligand to Cd/Se ratios for TDPA to Cadmium (C) and TOP to Selenium (D) are simulated over the first 30 min of the reaction assuming constant growth rates for the nanorods.

When the ratio of cadmium or selenium to ligand, TDPA or TOP respectively, is high, the equilibrium between bound and free precursor that can form monomers is also high. As this ratio decreases (as is the case when cadmium and selenium is consumed by the growing nanorods) the excess ligand binds available monomer precursors and reduces the relative concentration of monomer in solution available for the growing nanorods. Thus, in order to facilitate a 1-D growth environment for sustainable elongation of CdSe nanorods, a minimum ratio of cadmium to TDPA and selenium to TOP must be retained. For this system, the minimum ratio for cadmium to TDPA is approximately 0.475 (or 2.1 TDPA per cadmium) and 0.195 selenium to TOP (or 5.1 TOP per selenium). As long as these thresholds are not exceeded, conditions that support rod growth can be maintained. The known chemical equilibrium constants between trialkyl phosphine selenides lies towards the bound phosphine selenide.[39-40] As selenium is consumed by the growing nanorods, the shift in equilibrium back towards free selenide (the reactive species in monomer formation) is insufficient to resupply selenium at a rate required for nanorod growth. To maintain conditions for length elongation, the resupplied precursor must be provided at a concentration capable of shifting the equilibrium back to a concentration of available selenium high enough to continue rod growth (equation 1).

$$\text{Precursor (}\textit{i.e.}\text{ TOP-Se)} \leftrightarrows \text{monomer} + \text{free ligand} \rightarrow \text{rods} \qquad (1)$$

Cadmium and TDPA maintain a similar equilibrium relationship, however, the equilibrium between free cadmium and Cd-TDPA lies strongly towards the product. As cadmium is consumed, two TDPA ligands bind more strongly to each cadmium, thereby reducing the available cadmium that can readily form monomers and effectively reducing the concentration of monomers in the system.

From these quantitative observations, it is hypothesized that rod growth can be sustained as long as the minimum ligand to cadmium and selenium ratios are not exceeded. To test this theory, fresh precursor was resupplied at a rate sufficient to stay below the Cd/Se to ligand threshold to enable these thresholds to be un-exceeded for an extended period of time without contributing large volumes of excess waste. As can be seen in Figure 2.4, Figure 2.12, and TEM images presented in Appendix A, Figure A.11, replenishing the cadmium and selenium precursor at a rate of 0.083 mmol cadmium and selenium per min results in favorable rod growth conditions that can be maintained beyond 45 min to give longer, higher aspect ratio nanorods. While the rod growth rate proceeds at 3.5 monomers rod^{-1} s^{-1}, the necessary resupply rate for extended 1-D growth is 14.4× greater and requires precursor to be resupplied at a rate of 50 Cd or Se rod^{-1} s^{-1}.

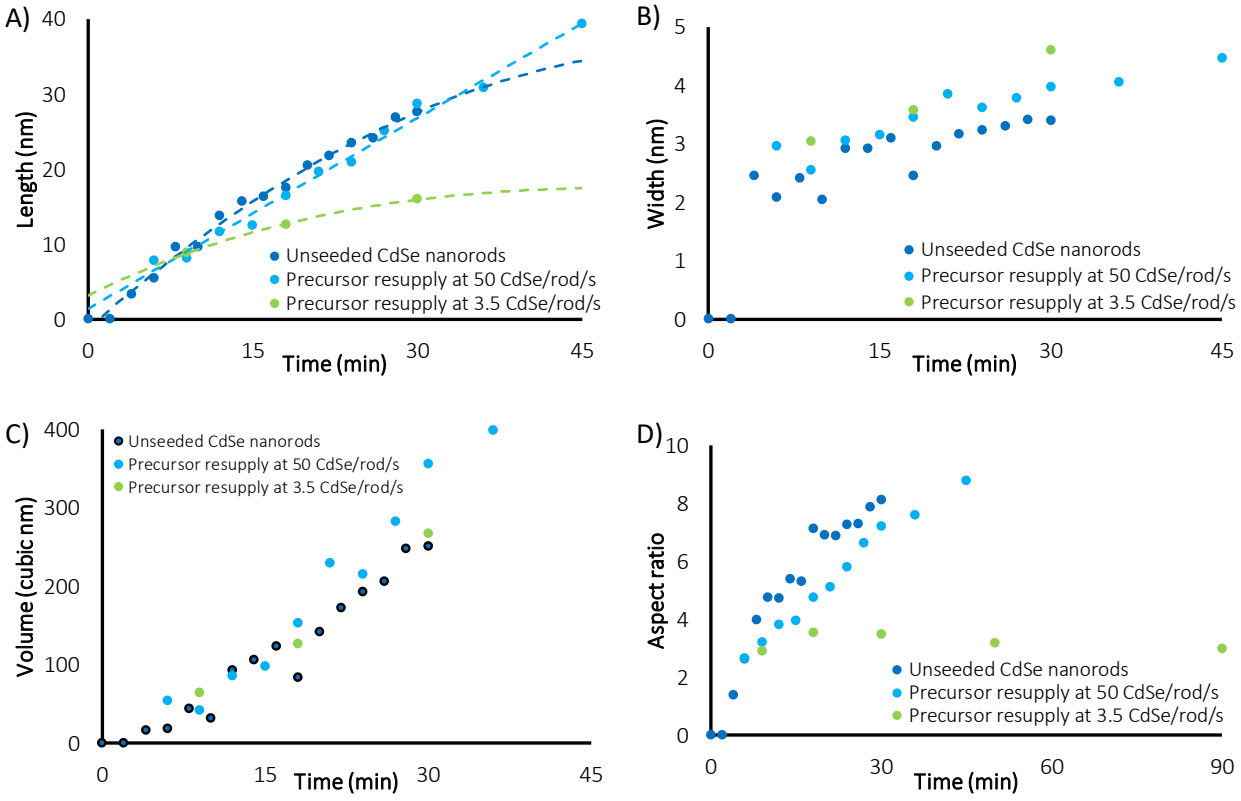

Figure 2.12. Replenishment of additional precursor by steady rate. Length (A), width (B), volume (C), and aspect (D) profiles over time when precursor is added by syringe pump.

To demonstrate that precursor replenishment is not simply a function of replacing the amount of consumed precursor, cadmium and selenium are replaced by syringe pump at the exact consumption rate. Figure 2.4, Figure 2.12, and TEM presented in Appendix A, Figure A.12, show this instead leads to exiting the 1-D growth regime prematurely and gives nanorods of reduced aspect ratio. While this is greatly inhibitory to growing longer, high aspect ratio nanorods, it is a feature that provides greater customizability to the shape of the rod. If rods with reduced aspect ratios or larger diameters than the starting seed are desired, the synthesis can be easily modified by adding additional TOP or TDPA (an amount to exceed the Cd/Se to ligand threshold) to the system. Adding TOP or TDPA led to a premature

exit from the 1-D growth regime and early aspect ratio curtailment within minutes of supplying new ligand (Figure 2.13 and TEM presented in Appendix A, Figures A.13 – A.14).

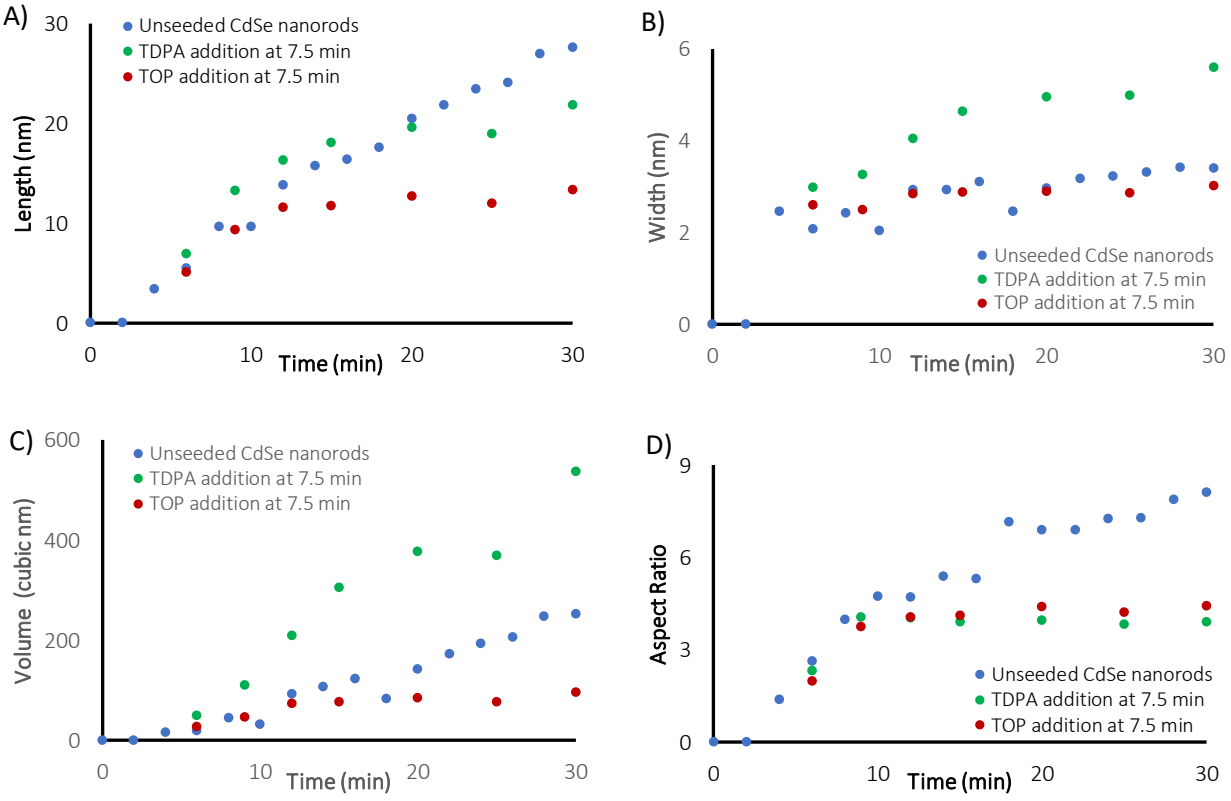

Figure 2.13. Role of ligand addition (TDPA or TOP) during CdSe nanorod growth. Additional TDPA, 0.14 g to push the TDPA:Cd ratio over 2.1:1, is added at 7.5 min to force premature exit from the 1-D growth regime. Likewise, additional TOP, 0.3 mL to push the TOP:Se ratio just over 5.1:1, is added at 7.5 min under otherwise identical growth conditions to typical CdSe nanorod growth. Length (A), width (B), volume (C), and aspect ratio (D) illustrate an early departure from the 1-D growth regime when TDPA or TOP is added to the growing nanorods.

Providing additional TOP shifts the equilibrium between bound Cd-TDPA and TOP=Se and monomer back towards the bound precursor, thereby reducing the monomer concentration. This leads to earlier 3-D growth and a slower rate of monomer addition to the nanorod, as shown in Figure 2.13. While additional TDPA also leads to an early exit from the 1-D growth regime, the extra acid facilitates an environment in which the growth rate increases but the rate of length growth is unperturbed. The addition of phosphonic acid likely leads to a systematic change in the equilibrium between ligand-bound precursor, monomer, and free ligand as well as perturbing the off-path equilibrium between monomer and magic size clusters. As shown previously, additional phosphonic acid perturbs CdSe magic size clusters and leads to more rapid nanocrystal growth, as observed by a more rapid red shift of the excitonic peak.[26, 41]

This pair of added ligand studies illustrate two distinct methods to obtain lower aspect ratio nanorods. While both TOP and TDPA addition led to a premature exit from the 1-D growth regime, additional TOP dramatically slowed nanorod growth by reducing the concentration of available monomer. TDPA addition, however, accelerated the nanorod growth rate and promoted more rapid growth about the circumference of the nanorods while axial growth continued. From a practical perspective, addition of TOP can be used for synthetic approaches where shorter and wider rods are desired. If the target rod product is wider but of a length accessible along a typical rod growth profile (Figure 2.1), addition of TOP minutes before the target length is achieved will enable length to be set while circumferential growth proceeds towards the favored structure. To access wider rods with lengths only obtainable beyond the first 15 min of rod growth, addition of TDPA will help to enhance circumferential growth without significantly inhibiting length extension.

The exact replenishment rates reported here will vary from system to system depending on the monomer to rod conversion rate and the concentrations of the starting and resupplied precursors.

However, this quantitative control over nanorod growth offers a 3-step rubric that goes beyond customizability of shape and structure of CdSe, CdS, and CdS/CdSe heterostructures. First, determine the growth rate of the nanocrystal. In these model systems CdSe nanorods assemble at a rate of 3.5 monomers rod^{-1} s^{-1} (at 250 °C) while CdS grows at 36 monomers rod^{-1} s^{-1} (at 340 °C). This growth rate is determined by evaluating changes in total volume of the growing nanorods. As can be seen throughout this set of studies, changes in rates of monomer addition to the volume of the nanorod do not directly correlate with 1-D to 3-D growth regime transitions. Some conditions, such as seeded growth with a large quantity of seeds, lead to plateauing volume growth rates after exiting the 1-D growth regime, while unseeded nanorod growth showed very little change in volume increases across this transition point. The second step is to determine the 1-D to 3-D transition time point by evaluating length growth rates or aspect ratio changes. When sufficient precursor is provided to create rod growth conditions, length growth initially proceeds at a linear rate. Departure from 1-D growth conditions are indicated by a plateau or taper away from the initial linear length growth rate. Both of these steps can be accomplished with the same sample. Unseeded growth, for example, transitions into the 3-D growth regime after 20 min. This transition is unobservable by exclusively tracking rod volume but is readily apparent from length and aspect ratio evaluations. The final step to obtain longer rods or increase aspect ratio, is to resupply precursors at high concentrations to retain high Cd/Se to ligand ratios and push the equilibrium between precursor and available monomer towards monomer formation. For radial increases and reduced aspect ratios, evaluate length growth rates to determine when rods have nearly attained the targeted length, rapidly add free ligand (*i.e.* TOP) and solvent to force premature departure from the 1-D growth regime. Note that length growth, while curtailed, does not completely stop and growth along the long axis still needs to be considered.

Using this rubric, this work demonstrates three methods of aspect ratio enhancement. The growth–purify–restart method (illustrated in Figure 2.) offers excellent control to reliably target a particular size and can be used repeatedly to give rods of significantly increased length with minimized radial growth. Abundant precursor replenishment in a single step can also prolong 1-D growth conditions by supplying concentrations of precursor that are sufficient to continue to force the equilibrium between ligand bound precursor and available monomer back towards the monomer. The third method, which arises from our improved mechanistic understanding of nanorod growth, is to directly replenish consumed monomer at the rate of its consumption. This method yields less precursor waste and offers the greatest control over the exact dimensions of the nanomaterial. For retention of length growth in this CdSe system, precursor must be provided at a rate of 50 Cd or Se rod^{-1} s^{-1}. While the physical technique for resupplying precursor is similar to dropwise addition and successive ionic layer adsorption and reaction synthetic methods, these methods are typically employed to limit the amount of precursor available in the system to prevent new, independent, nanomaterial nucleation. Quantitative resupply is more calculated and is employed to stay above a minimum threshold rather than stay below a critical concentration limit. This work provides further insights into how to construct desirable anisotropic heterostructures.[42-45]

2.6 CONCLUSIONS

In summary, this report quantifies the growth rates and establishes the conditions needed to support the anisotropic extension of CdSe, CdS, and CdS/CdSe nanorods. These measured parameters are derived from widely used synthetic methods for cadmium chalcogenide nanorods and serve as a model system for controlling the dimensions and aspect ratios of other materials and systems that follow similar assembly mechanisms. The methods used for extending 1-D growth conditions serve as a rubric

for customizability of nanorod dimensions. In particular, this work outlines the steps for customizability of anisotropic colloidal nanocrystals. Despite extensive investigations of CdS and CdSe nucleation and growth over the past 20 years, this is one of the first reports to bridge the gap between scientific knowledge and practical implementation of this knowledge to obtain nanostructures of specific dimensions. This report shows how to approach studying and subsequently modulating reaction conditions to obtain kinetic nanocrystal products.

While there exist many methods for aspect ratio enhancement, this report highlights three ways to achieve nanostructures of a set of exact dimensions: growth–purify–restart, abundant precursor replenishment, and direct replenishment/addition of precursors or additives. This report highlights the ability to grow nanorods of exact dimensions with spherical and anisotropic nanocrystals as seeds for enhanced control over the parameters of the final product. The rubric outlined here for CdS and CdSe shows that much of the information required to determine how to develop a nanostructure for any colloidal system can be learned by first quantitatively mapping the progress of the developing nanocrystals. Once this baseline has been established, a determination of the most appropriate way was (*i.e.* based on workability of precursors, cost, and available materials, *etc.*) to retain or disrupt kinetic growth conditions can be made. This rubric also extends to heterostructures and provides an outline for how to generate rod–rod heterostructures with exact control of the length of each component.

2.7 EXPERIMENTAL METHODS

2.7.1 *General methods*

All manipulations were carried out using standard Schlenk or glovebox techniques under dry nitrogen. Cadmium oxide (CdO, >99.99%), trioctylphosphine (TOP, 97%), tributylphosphine (TBP,

95%), propylphosphonic acid (95%), selenium (99.99%), and sulfur (99.5%) were all purchased from Sigma Aldrich and used as received without further purification. Tetradecylphosphonic acid (TDPA, 99%) and octadecylphosphonic acid (ODPA, 99%) were purchased from PCI Synthesis and used as received. Anhydrous methanol, toluene, and pentane were purchased from various sources. Trioctylphosphine oxide (TOPO, 90%) was purchased from Sigma Aldrich and purified by repeated recrystallization until impurities were no longer present by evaluation using ^{1}H and ^{31}P NMR spectroscopy.[46] Solutions of trioctylphosphine-selenide (TOP–Se) and trioctylphosphine-sulfide (TOP–S) were pre-prepared by dissolving metallic selenium or sulfur powder into TOP in a glovebox. Concentrations and exact solution preparation procedures are reported individually for the synthesis of each nanomaterial.

2.7.2 *Synthesis of CdSe and CdS seeds*

The syntheses of wurtzite CdSe and CdS seeds were adopted from the procedures reported by Manna, *et al.*[47] For CdSe, CdO (0.060 g, 0.47 mmol), ODPA (0.280 g, 0.837 mmol) and TOPO (3.00 g, 7.76 mmol) were loaded into a 50 mL three neck flask. This mixture was flushed with nitrogen and degassed at room temperature for 30 min before heating to 150 °C. The mixture was held under vacuum for 1 h. Then, the solution was heated to 300 °C under flowing nitrogen. Upon reaching 300 °C, TOP (1.50 g, 4.05 mmol) was injected by syringe and the temperature was increased to 370 °C. The temperature of the cadmium precursor was allowed to stabilize at 370 °C before addition of the selenium precursor. Once the cadmium precursor turned clear (this typically happens by the time the temperature stabilizes), TOP–Se was rapidly injected by syringe addition. The TOP–Se precursor was prepared by dissolving 0.058 g of selenium powder (0.74 mmol) in 0.360 g of TOP (0.971 mmol). The reaction was allowed to proceed for 10 s before the heat was removed. When the reaction mixture cooled to about

100 °C, 10 mL of toluene was added to the sample to better facilitate purification. The quantum dots were purified under a nitrogen atmosphere by repeated dissolution in toluene and centrifuge assisted precipitation with methanol. Purified CdSe seeds were suspended in anhydrous toluene or pentane and centrifuged after 8–24 h to remove excess ligand before filtration with a 0.45-micron PDFE syringe filter. The quantum dot size and concentration were quantified by UV-Vis spectroscopy.[48-49] The size of the wurtzite seed can be adjusted by adjusting the reaction time prior to quenching. Immediate removal of the heating mantle yields ~2.5 nm seeds, 10 s reaction time yields ~3.6 nm particles, and 30 s reaction time yields ~5.2 nm nanocrystals although exact reaction conditions will vary slightly across set-ups.

2.7.3 *Synthesis of CdS nanorods*

The synthesis of CdS nanorods from wurtzite CdSe seeds is based on the procedure reported by Alivisatos, *et al.*[38] In a 50 mL three-neck flask, CdO (0.230 g, 1.79 mmol), ODPA (1.08 g, 3.22 mmol), propylphosphonic acid (0.075 g, 0.604 mmol) and TOPO (3.35 g, 8.66 mmol) were loaded and degassed for 30 min at room temperature. The sample was then heated to 120 °C and held under vacuum for 1 h. After degassing, the solution was heated to 320 °C under nitrogen until the solution was clear, indicating the formation of cadmium octadecylphosphonate. After the cadmium precursor was formed, the solution was cooled to 120 °C and exposed to a vacuum for 2 h to remove water that is generated during precursor formation. After 2 h, the solution was placed back under nitrogen and heated to 340 °C and TOP (1.00 g, 2.70 mmol) was added by syringe addition. When the temperature re-stabilized at 340 °C, TOP–S was added by rapid syringe injection. The TOP–S precursor was made by dissolving sulfur (0.0518 g, 1.62 mmol) in TOP (0.598 g, 1.62 mmol) and was stirred overnight. Gentle heating (60 °C) and sonication may be necessary to fully dissolve the sulfur. 20 s after the injection of TOP–S, the

wurtzite CdSe seeds dissolved in 1.00 g TOP (2.70 mmol) were rapidly injected into the reaction mixture. Approximately 5.5×10^{-7} mol of CdSe quantum dots were added in this reaction. This reaction was quenched by removing heat after 10 min of growth to obtain nanorods with dimensions of 16.9 ± 1.0 nm by 4.5 ± 0.3 nm. Reaction times can be varied to obtain structures of desired length/width. When the CdS nanorods cooled to about 100 °C, 10 mL of toluene was added to solubilize the nanocrystals. Several repeated purification steps of suspension in toluene, precipitation with methanol, and centrifugation were carried out in a nitrogen atmosphere to remove unreacted reactants, solvent, and excess ligand. Purified nanorods were suspended in anhydrous toluene or pentane and centrifuged after 8–24 h to remove excess ligand before filtration with a 0.45-micron PDFE syringe filter.

Seed concentration, reaction time, and TOP–S volume all impact the resulting structure. Increasing seed concentration yields shorter rods (less CdS per rod) but longer reaction times yields longer rods (longer growth time). Increasing the volume of TOP–S added to the reaction also facilitates longer, thinner rods over 10 min while the rod length is dictated by absolute precursor concentration.

2.7.4 *Synthesis of CdSe nanorods*

CdSe nanorod growth experiments were modified off of procedures reported by Koo and Korgel.[50] CdO (0.241 g, 1.87 mmol), TDPA (1.04 g, 3.74 mmol), and TOPO (0.75 g, 1.94 mmol) were mixed together in a 50 mL three-neck flask and degassed under vacuum for 1 h. Then, the mixture was heated to 300 °C under nitrogen to form cadmium tetradecylphosphonate. Note: due to the small volume of TOPO, CdO will sometimes cake to the side of the flask. Ensure all of the reagents are well mixed to evolve the clear cadmium precursor. This solution was then cooled to room temperature and was aged for 24 h under nitrogen. The aging step is important for reproducible rod growth.[50] After 24 h of aging, and additional 2.325 g TOPO (6.01 mmol) was added to the flask and the mixture of white solids

was degassed at room temperature for 1 h. Next the reaction mixture was heated to 320 °C under nitrogen for rod growth. Once the temperature stabilized at 320 °C, the selenium precursor was added rapidly by syringe injection. The temperature was immediately dropped to about 250 °C for the duration of the rod growth experiment. The selenium precursor was prepared by dissolving selenium powder (0.126 g, 1.61 mmol) in TOP (3.482 mL, 7.81 mmol), TBP (0.468 mL, 1.90 mmol), and toluene (0.694 mL, 6.53 mmol) in a glovebox. After about 30 min of CdSe rod growth, increases to aspect ratio cease and the reaction can be stopped unless low aspect ratio nanorods (less than 5:1) are desired. The reaction is terminated by removal of the heat source and 10 mL of toluene is added to solubilize the reaction mixture for purification. Methanol or ethanol are used as the anti-solvent. Repeated resuspension in toluene followed by methanol addition and centrifugation purifies the nanorods. Purified nanorods are suspended in anhydrous toluene and centrifuged after 8–24 h to remove excess ligand before filtration with a 0.45-micron PDFE syringe filter.

For seeded CdSe rod growth, the desired quantity of seeds in pentane or toluene is added to the reaction flask 1 h after adding the additional 2.325 g TOPO. The solvent is evaporated at 50 °C for pentane and 100 °C for toluene. Additionally, instead of heating to 320 °C for the selenium injection, heat to the rod growth temperature of 250 °C to avoid independent nucleation of CdSe and to facilitate CdSe growth directly on the seeds.

2.7.5 *Sample characterization*

For evaluation of structures presented in this report, UV-Vis spectra were recorded using an Agilent Cary 5000 spectrophotometer. TEM images were obtained on an FEI Technai G2 F20 microscope. Analysis of TEM images was performed *via* manual counting using the ImageJ software

package. Elemental quantification was carried out using a Perkin Elmer Optima 8300 Inductively Coupled Plasma-Optical Emission Spectrophotometer.

ICP-OES was used to quantify the amount of cadmium in a sample. Calculating the rod volume by TEM approximates the per rod cadmium content. Concentrations of rods/sample can be calculated by dividing the cadmium/sample measured using ICP-OES by cadmium/rod calculated from TEM. The purification procedure used to remove excess ligand, solvent, and unreacted precursor and monomer from the nanorod sample is rigorous and leads to loss of an unquantifiable number of rods. Thus, this concentration estimation for the number of growing rods in an unseeded CdSe nanorod synthesis is likely an overestimation of the number of nanorods that seed and grow during the reaction.

2.8 REFERENCES

(1) Shi, W.; Hughes, R. W.; Denholme, S. J.; Gregory, D. H., Synthesis design strategies to anisotropic chalcogenidenanostructures. *CrystEngComm* **2010,** *12*, 641-659.

(2) Sajanlal, P. R.; Sreeprasad, T. S.; Samal, A. K.; Pradeep, T., Anisotropic nanomaterials: structure, growth, assembly, and functions. *Nano Rev* **2011,** *2*.

(3) Burda, C.; Chen, X.; Narayanan, R.; El-Sayed, M. A., Chemistry and Properties of Nanocrystals of Different Shapes. *Chemical Reviews* **2005,** *105*, 1025-1102.

(4) Aricò, A. S.; Bruce, P.; Scrosati, B.; Tarascon, J.-M.; van Schalkwijk, W., Nanostructured materials for advanced energy conversion and storage devices. *Nat. Mater.* **2005,** *4*, 366-377.

(5) Li, H.; Wang, Z.; Chen, L.; Huang, X., Research on Advanced Materials for Li-ion Batteries. *Adv. Mater.* **2009,** *21*, 4593-4607.

(6) Wang, X.; Zhi, L.; Müllen, K., Transparent, Conductive Graphene Electrodes for Dye-Sensitized Solar Cells. *Nano Lett.* **2008,** *8*, 323-327.

(7) Hochbaum, A. I.; Yang, P., Semiconductor Nanowires for Energy Conversion. *Chem. Rev.* **2010,** *110*, 527-546.

(8) Harman, T. C.; Taylor, P. J.; Walsh, M. P.; LaForge, B. E., Quantum Dot Superlattice Thermoelectric Materials and Devices. *Science* **2002,** *297*, 2229-2232.

(9) Hsu, K. F.; Loo, S.; Guo, F.; Chen, W.; Dyck, J. S.; Uher, C.; Hogan, T.; Polychroniadis, E. K.; Kanatzidis, M. G., Cubic AgPb(m)SbTe(2+m): bulk thermoelectric materials with high figure of merit. *Science* **2004,** *303*, 818-821.

(10) Venkatasubramanian, R.; Siivola, E.; Colpitts, T.; O'Quinn, B., Thin-film thermoelectric devices with high room-temperature figures of merit. *Nature* **2001,** *413*, 597-602.

(11) Wang, X.; Song, J.; Wang, Z. L., Nanowire and nanobelt arrays of zinc oxide from synthesis to properties and to novel devices. *J. Mater. Chem.* **2007,** *17*, 711-720.

(12) Zhu, J.; Shim, B. S.; Di Prima, M.; Kotov, N. A., Transparent Conductors from Carbon Nanotubes LBL-Assembled with Polymer Dopant with π−π Electron Transfer. *J. Am. Chem. Soc.* **2011,** *133*, 7450-7460.

(13) De, S.; Lyons, P. E.; Sorel, S.; Doherty, E. M.; King, P. J.; Blau, W. J.; Nirmalraj, P. N.; Boland, J. J.; Scardaci, V.; Joimel, J.; Coleman, J. N., Transparent, Flexible, and Highly Conductive Thin Films Based on Polymer−Nanotube Composites. *ACS Nano* **2009,** *3*, 714-720.

(14) Lee, J.-Y.; Connor, S. T.; Cui, Y.; Peumans, P., Solution-Processed Metal Nanowire Mesh Transparent Electrodes. *Nano Lett.* **2008,** *8*, 689-692.

(15) Azulai, D.; Belenkova, T.; Gilon, H.; Barkay, Z.; Markovich, G., Transparent Metal Nanowire Thin Films Prepared in Mesostructured Templates. *Nano Lett.* **2009,** *9*, 4246-4249.

(16) Cho, C.-H.; Aspetti, C. O.; Turk, M. E.; Kikkawa, J. M.; Nam, S.-W.; Agarwal, R., Tailoring hot-exciton emission and lifetimes in semiconducting nanowires via whispering-gallery nanocavity plasmons. *Nat. Mater.* **2011,** *10*, 669-675.

(17) Schuller, J. A.; Barnard, E. S.; Cai, W.; Jun, Y. C.; White, J. S.; Brongersma, M. L., Plasmonics for extreme light concentration and manipulation. *Nat. Mater.* **2010,** *9*, 193-204.

(18) McDonald, S. A.; Konstantatos, G.; Zhang, S.; Cyr, P. W.; Klem, E. J. D.; Levina, L.; Sargent, E. H., Solution-processed PbS quantum dot infrared photodetectors and photovoltaics. *Nat. Mater.* **2005,** *4*, 138-142.

(19) Lim, B.; Jiang, M.; Camargo, P. H. C.; Cho, E. C.; Tao, J.; Lu, X.; Zhu, Y.; Xia, Y., Pd-Pt Bimetallic Nanodendrites with High Activity for Oxygen Reduction. *Science* **2009,** *324*, 1302-1305.

(20) Kauffman, D. R.; Sorescu, D. C.; Schofield, D. P.; Allen, B. L.; Jordan, K. D.; Star, A., Understanding the Sensor Response of Metal-Decorated Carbon Nanotubes. *Nano Lett.* **2010,** *10*, 958-963.

(21) Talapin, D. V.; Lee, J.-S.; Kovalenko, M. V.; Shevchenko, E. V., Prospects of Colloidal Nanocrystals for Electronic and Optoelectronic Applications. *Chem. Rev.* **2010,** *110*, 389-458.

(22) Peng, X.; Manna, L.; Yang, W.; Wickham, J.; Scher, E.; Kadavanich, A.; Alivisatos, A. P., Shape control of CdSe nanocrystals. *Nature* **2000,** *404*, 59-61.

(23) Peng, Z. A.; Peng, X., Nearly Monodisperse and Shape-Controlled CdSe Nanocrystals via Alternative Routes: Nucleation and Growth. *Journal of the American Chemical Society* **2002,** *124*, 3343-3353.

(24) Peng, X., Mechanisms for the Shape-Control and Shape-Evolution of Colloidal Semiconductor Nanocrystals. *Advanced Materials* **2003,** *15*, 459-463.

(25) Manna, L.; Scher, E. C.; Alivisatos, A. P., Synthesis of Soluble and Processable Rod-, Arrow-, Teardrop-, and Tetrapod-Shaped CdSe Nanocrystals. *Journal of the American Chemical Society* **2000,** *122*, 12700-12706.

(26) Jiang, Z.-J.; Kelley, D. F., Role of Magic-Sized Clusters in the Synthesis of CdSe Nanorods. *ACS Nano* **2010,** *4*, 1561-1572.

(27) Kim, D.; Lee, Y. K.; Lee, D.; Kim, W. D.; Bae, W. K.; Lee, D. C., Colloidal Dual-Diameter and Core-Position-Controlled Core/Shell Cadmium Chalcogenide Nanorods. *ACS Nano* **2017,** *11*, 12461-12472.

(28) Zhao, L.; Hu, L.; Fang, X., Growth and Device Application of CdSe Nanostructures. *Adv. Funct. Mater.* **2012,** *22*, 1551-1566.

(29) Mokari, T.; Rothenberg, E.; Popov, I.; Costi, R.; Banin, U., Selective Growth of Metal Tips onto Semiconductor Quantum Rods and Tetrapods. *Science* **2004,** *304*, 1787-1790.

(30) Nakibli, Y.; Amirav, L., Selective Growth of Ni Tips on Nanorod Photocatalysts. *Chem. Mater.* **2016,** *28*, 4524-4527.

(31) Kim, S. M.; Lee, S. J.; Kim, S. H.; Kwon, S.; Yee, K. J.; Song, H.; Somorjai, G. A.; Park, J. Y., Hot Carrier-Driven Catalytic Reactions on Pt–CdSe–Pt Nanodumbbells and Pt/GaN under Light Irradiation. *Nano Lett.* **2013,** *13*, 1352-1358.

(32) Amirav, L.; Alivisatos, A. P., ACS NanoPhotocatalytic Hydrogen Production with Tunable Nanorod Heterostructures. *J. Phys. Chem. Lett.* **2010,** *1*, 1051-1054.

(33) Kunneman, L. T.; Zanella, M.; Manna, L.; Siebbeles, L. D. A.; Schins, J. M., Mobility and Spatial Distribution of Photoexcited Electrons in CdSe/CdS Nanorods. *J. Phys. Chem. C* **2013,** *117*, 3146-3151.

(34) Zhu, H.; Lian, T., Enhanced Multiple Exciton Dissociation from CdSe Quantum Rods: The Effect of Nanocrystal Shape. *J. Am. Chem. Soc.* **2012,** *134*, 11289-11297.

(35) Salant, A.; Shalom, M.; Tachan, Z.; Buhbut, S.; Zaban, A.; Banin, U., Quantum Rod-Sensitized Solar Cell: Nanocrystal Shape Effect on the Photovoltaic Properties. *Nano Lett.* **2012,** *12*, 2095-2100.

(36) Lee, S.; Flanagan, J. C.; Kang, J.; Kim, J.; Shim, M.; Park, B., Integration of CdSe/CdSexTe1−x Type-II Heterojunction Nanorods into Hierarchically Porous TiO2 Electrode for Efficient Solar Energy Conversion. *Sci. Rep.* **2015,** *5*, 17472.

(37) Peng, Z. A.; Peng, X., Mechanisms of the Shape Evolution of CdSe Nanocrystals. *J. Am. Chem. Soc.* **2001,** *123*, 1389-1395.

(38) Talapin, D. V.; Nelson, J. H.; Shevchenko, E. V.; Aloni, S.; Sadtler, B.; Alivisatos, A. P., Seeded Growth of Highly Luminescent CdSe/CdS Nanoheterostructures with Rod and Tetrapod Morphologies. *Nano Letters* **2007,** *7*, 2951-2959.

(39) García-Rodríguez, R.; Hendricks, M. P.; Cossairt, B. M.; Liu, H.; Owen, J. S., Conversion Reactions of Cadmium Chalcogenide Nanocrystal Precursors. *Chem. Mater.* **2013,** *25*, 1233-1249.

(40) Baechler, R. D.; Stack, M.; Stevenson, K.; Vanvalkenburgh, V., ATOM TRANSFER AND EXCHANGE REACTIONS INVOLVING OXYGEN, SULFUR AND SELENIUM. *Phosphorus, Sulfur Silicon Relat. Elem.* **1990,** *48*, 49-52.

(41) Liu, H.; Owen, J. S.; Alivisatos, A. P., Mechanistic Study of Precursor Evolution in Colloidal Group II−VI Semiconductor Nanocrystal Synthesis. *J. Am. Chem. Soc.* **2007,** *129*, 305-312.

(42) Shieh, F.; Saunders, A. E.; Korgel, B. A., General Shape Control of Colloidal CdS, CdSe, CdTe Quantum Rods and Quantum Rod Heterostructures. *J. Phys. Chem. B* **2005,** *109*, 8538-8542.

(43) Enright, M. J.; Sarsito, H.; Cossairt, B. M., Quantifying Cation Exchange of Cd2+ in ZnTe: A Challenge for Accessing Type II Heterostructures. *Chemistry of Materials* **2017,** *29*, 666-672.

(44) Halpert, J. E.; Porter, V. J.; Zimmer, J. P.; Bawendi, M. G., Synthesis of CdSe/CdTe Nanobarbells. *J. Am. Chem. Soc.* **2006,** *128*, 12590-12591.

(45) Kumar, S.; Jones, M.; Lo, S. S.; Scholes, G. D., Nanorod Heterostructures Showing Photoinduced Charge Separation. *Small* **2007,** *3*, 1633-1639.

(46) Wang, F.; Tang, R.; Buhro, W. E., The Trouble with TOPO; Identification of Adventitious Impurities Beneficial to the Growth of Cadmium Selenide Quantum Dots, Rods, and Wires. *Nano Lett.* **2008,** *8*, 3521-3524.

(47) Carbone, L.; Nobile, C.; De Giorgi, M.; Sala, F. D.; Morello, G.; Pompa, P.; Hytch, M.; Snoeck, E.; Fiore, A.; Franchini, I. R.; Nadasan, M.; Silvestre, A. F.; Chiodo, L.; Kudera, S.; Cingolani, R.; Krahne, R.; Manna, L., Synthesis and Micrometer-Scale Assembly of

Colloidal CdSe/CdS Nanorods Prepared by a Seeded Growth Approach. *Nano Lett.* **2007,** *7*, 2942-2950.

(48) Jasieniak, J.; Smith, L.; van Embden, J.; Mulvaney, P.; Califano, M., Re-examination of the Size-Dependent Absorption Properties of CdSe Quantum Dots. *The Journal of Physical Chemistry C* **2009,** *113*, 19468-19474.

(49) Yu, W. W.; Qu, L.; Guo, W.; Peng, X., Experimental Determination of the Extinction Coefficient of CdTe, CdSe, and CdS Nanocrystals. *Chem. Mater.* **2003,** *15*, 2854-2860.

(50) Koo, B.; Korgel, B. A., Coalescence and Interface Diffusion in Linear CdTe/CdSe/CdTe Heterojunction Nanorods. *Nano Lett.* **2008,** *8*, 2490-2496.

Chapter 3. QUANTIFYING CATION EXCHANGE OF CADMIUM IN ZINC TELLURIDE NANORODS

Development of dot-in-rod and rod-rod heterostructures of cadmium chalcogenide holds great fundamental value for understanding the basic design principles of heterostructures synthesis. However, in any CdE_1/CdE_2 heterostructure (E = S, Se, Te), there are limitations with respect to tuning the band edge and opto-electronic properties. Thus, utilization of material combinations beyond cadmium chalcogenide is valuable for tuning heterostructure properties. Thus, utilization of material combinations beyond cadmium chalcogenide is valuable for tuning heterostructure properties. The staggered conduction and valence bands of ZnTe and CdSe provide a clearly defined type II band alignment which is expected to provide improved charge separation compared to quasi type II CdE_1/CdE_2 structures. During the process of using ZnTe nanorods as a scaffold for CdSe growth in a similar manner to the seeded growth systems of Chapter 2, the competitive cation exchange process between cadmium and zinc in the telluride lattice is favored over new CdSe nanorod growth. Chapter 3 describes the mechanism and reaction rates that govern cation exchange within the tellurium lattice. This competitive cation exchange process in anisotropic lattices can be used to derive customizable alloys but also highlights the challenges with heterostructure assembly upon ZnTe nanostructures.

3.1 INTRODUCTION

The use of nanoscale semiconductors in light absorbing applications is attractive due to their size-dependent optoelectronic properties and compatibility with solution-based manufacturing methods.[1] This versatile class of nanomaterials holds great promise for applications in next generation solar energy conversion technologies.[2-3] However, one problem with nanoscale materials for this application is efficient electron-hole recombination that results from confining charge carriers physically in space. This issue can be overcome through the fabrication of advanced heterojunction nanostructures, such as core-shell quantum dots,[4] branched tetrapods,[5-7] and linear heterojunction nanorods,[8-10] which enable electron and hole accumulation and depletion in different segments of the nanostructure.[11-13]

In particular, type II heterojunction semiconductor nanomaterials have great potential in photovoltaic and photocatalytic applications since the conduction band minimum and valence band maximum are composed of orbitals physically separated in two distinct materials. This physical separation of the orbitals and the energy difference between them promotes photoinduced electron-hole pair separation across the interface of the semiconductor junction thereby increasing carrier lifetimes.[14] On the other hand, a type I structure confines both charge carriers in a single material. A quasi-type II heterostructure is a hybrid between type I and type II structures; wherein one charge carrier is localized to one side of the heterostructure interface while the other carrier is delocalized across the whole nanostructure. While quasi-type II heterostructures, such as CdTe/CdSe core-shell particles, lead to improvements in charge separation over single material structures,[15] the ability to separate charges can be further improved by increasing the energy difference between the offset bands at the heterojunction; in the normal Marcus region, the energy difference between the bands is proportional to the driving force for charge transfer.[16-18] Anisotropic type II

heterostructures, such as nanorods, are of particular interest for applications that depend on charge separation because of the ability to separate charge carriers over the length of the heterostructure.[7-10]

When considering semiconductors for the design of type II heterostructures, ZnTe emerges as a useful material to serve as the electron donor due to its bulk band gap of 2.25 eV and its high relative conduction band edge energy, which allows for efficient electron hole separation even with thin layers of an acceptor material such as CdSe.[15, 19-21] ZnTe and CdSe are also well-suited to form heterostructures because they have a lattice mismatch of only 0.8%.[20] Prior studies of ZnTe/CdSe nanostructures have so far been limited primarily to isotropic quantum dots.[15, 20-21] These studies have shown that the lifetime of excitons can be prolonged by increasing the thickness of the outer shell.[21] One challenge inherent to type II core-shell quantum dots is the inability to replenish charge carriers in the core material. In ZnTe/CdSe shelled systems, electrons must tunnel through the CdSe shell to refill holes left behind in the ZnTe core; thus, structures are limited to thin CdSe shells for photocatalytic applications. The thin shells both decrease the lifetime of the separated electron-hole pair as well as restrict the ability to tune the CdSe band edge energy and thus limit the driving force for exciton dissociation.

The utilization of a heterojunction rod structure in which CdSe rod ends are grown on either end of the ZnTe nanorod core both enables tailoring of the material size and offers an exposed ZnTe surface for rapid refilling of holes. In the pursuit of a ZnTe/CdSe heterojunction nanorod structure using conventional controlled growth techniques for heterostructure synthesis, such as SILAR and slow injection of precursors to limit new nucleation events, instead it was found these techniques facilitate cation exchange over heterostructure growth. Elemental analysis revealed a decrease in the Zn:Te ratio accompanied by incorporation of significant amounts of cadmium with

no selenium uptake. The simultaneous incorporation of cadmium with zinc loss is indicative of cation exchange and suggests cation exchange will occur preferentially to CdSe growth. Cation exchange and heterostructure growth have both been used to customize nanomaterial properties, and both procedures share similar synthetic conditions: precursor concentrations, temperatures between 150 and 250 °C, short (<1 h) synthesis time, and the use of separate anion and cation precursors. In this report, the reaction rates governing cation exchange between molecular Cd^{2+} precursors and ZnTe nanostructures is determined. The concentration, temperature, and time dependence of cation exchange have been experimentally mapped to provide an all-inclusive rubric for tuning the rate and extent of cation exchange in these nanomaterials. To date, this is the most extensive evaluation of cation exchange in a metal telluride lattice and demonstrates that cation exchange poses a significant challenge to cadmium chalcogenide heterostructure growth on ZnTe nanostructures.

3.2 CATION EXCHANGE IN ZNTE NANORODS

With the goal of developing a bottom-up synthesis of colloidal anisotropic type II heterostructure nanorods based on ZnTe as the electron donor, first, ZnTe nanorods are synthesized and characterized. As can be seen in Figure 3.1, using a synthetic procedure developed by Zhang *et al.*, nanorods with 10 ± 2.5 nm lengths and 3.1 ± 0.6 nm widths were obtained from hot injection of a polytelluride solution (the product of a 1:1 mixture of trioctylphosphine telluride and superhydride in excess oleylamine) into *in-situ* synthesized zinc oleate ($Zn(OA)_2$) at 160 °C followed by a 60 minute growth period at 190 °C.[22] Hundred-milligram scale syntheses of ZnTe nanorods consistently yielded the same size and polydispersity batch to batch; however, increasing the scale of the synthesis led to an increase in the prevalence of quantum dots, possibly due to differences in the heating profile during the reaction. Characterization of the nanorods by

inductively coupled plasma-optical emission spectroscopy (ICP-OES) indicates that the ZnTe nanorods are tellurium-rich with a tellurium to zinc ratio of 0.9:10. Synthesis of ZnTe nanorods by the same synthetic conditions have yielded nanomaterials with similar compositions.[23]

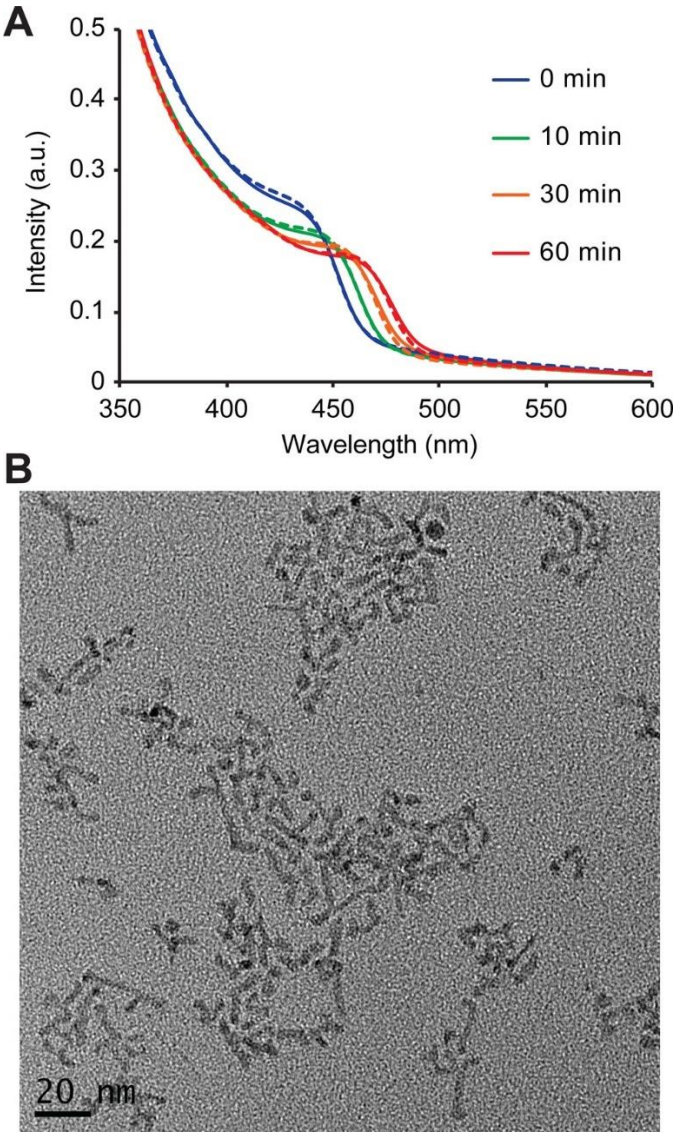

Figure 3.1. Characterization of ZnTe nanorods. UV-Vis absorbance (A) and TEM (B) data for 10 ± 2.5 nm ZnTe nanorods. UV-Vis data show rod growth over time as well as reproducibility of the data for two unique batches (solid vs. dashed lines).

ZnTe nanorods were exposed to solutions of cadmium oleate ($Cd(OA)_2$) at a variety of temperatures as an initial control experiment toward growing anisotropic type II heterostructures of ZnTe and CdSe. The products of these control experiments were extensively analyzed, supporting the transformation of the starting ZnTe rods *via* cation exchange. The spectral shifts obtained from the lowest energy electronic transition of the absorption profiles upon treatment of ZnTe with Cd^{2+} as a function of time and temperature are shown in Figure 3.2. It can be seen that the parent ZnTe nanorod sample (λ_{max} = 463 nm) is immediately modified within the first 10 s of the reaction as cadmium oleate coordinates the surface of the ZnTe nanorods. Since the starting ZnTe nanorod sample is tellurium-rich, there is an abundance of available coordination sites for cadmium to adsorb to the surface of the nanomaterial. Over time, it is hypothesized that this surface coordination is followed by cation exchange into the telluride lattice to form a (Zn,Cd)Te alloy, consistent with powder X-ray diffraction analysis of the resulting nanorods (Figure 3.2B, Figure 3.3, and Table 3.1). It is of note that the band gap of the resulting (Zn,Cd)Te nanorods can be varied over a range of 1 eV by simply controlling the solution temperature and reaction time.

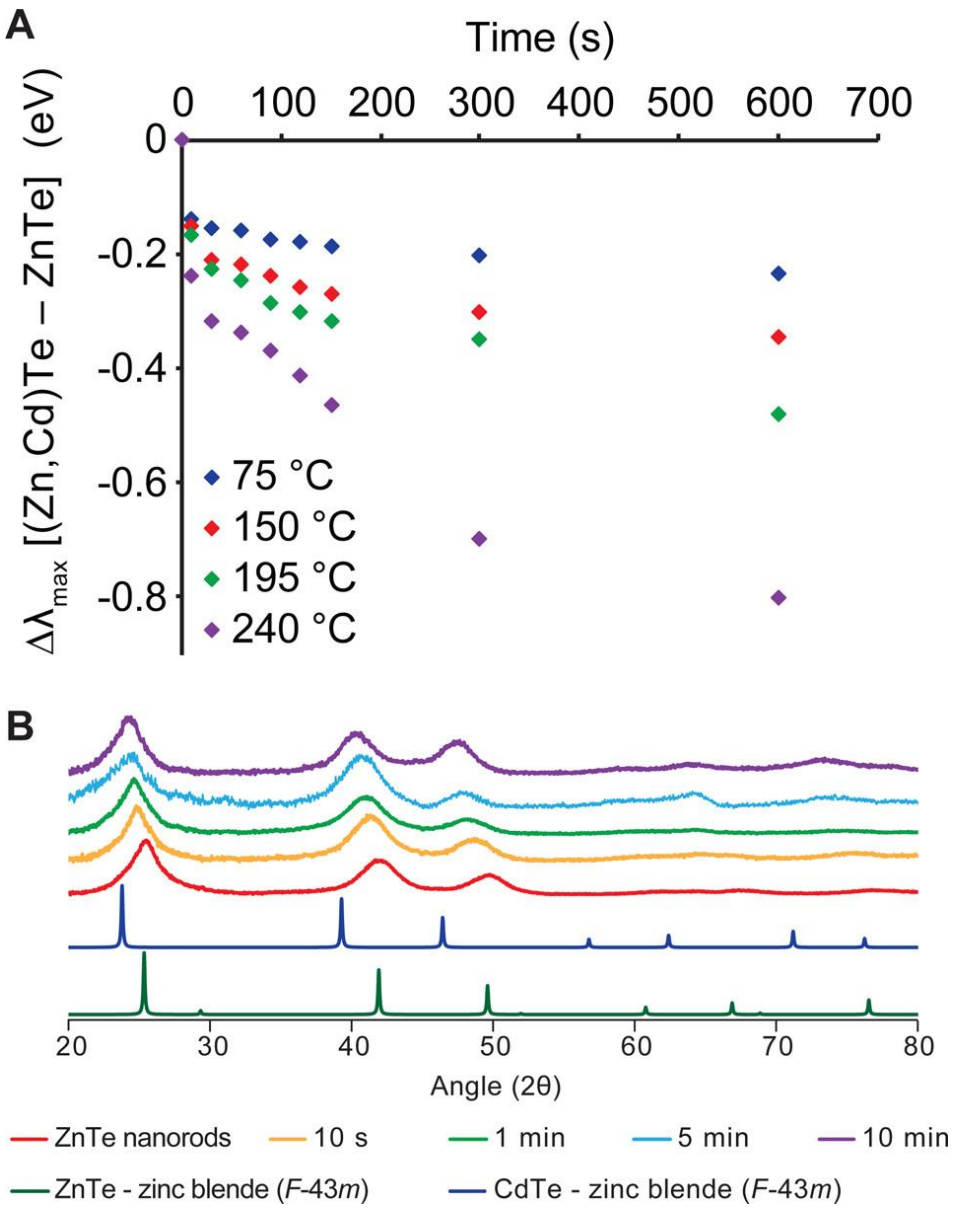

Figure 3.2. Spectral shifts of absorbance maxima and XRD pattern of cation exchange. (A) Spectral shifts of absorbance maxima relative to the starting ZnTe nanorods during cation exchange reactions, demonstrating a progressive bathochromic shift as Cd^{2+} is incorporated. $\Delta\lambda_{max}$ is the energy change of the lowest energy electronic transition from the starting ZnTe nanorods. (B) Powder X-ray diffraction data showing the structural evolution of ZnTe nanorods during cation exchange as a function of time at 195 °C. CdTe (9008840) and ZnTe (9008858) reference patterns were obtained from the Crystallography Open Database.[24]

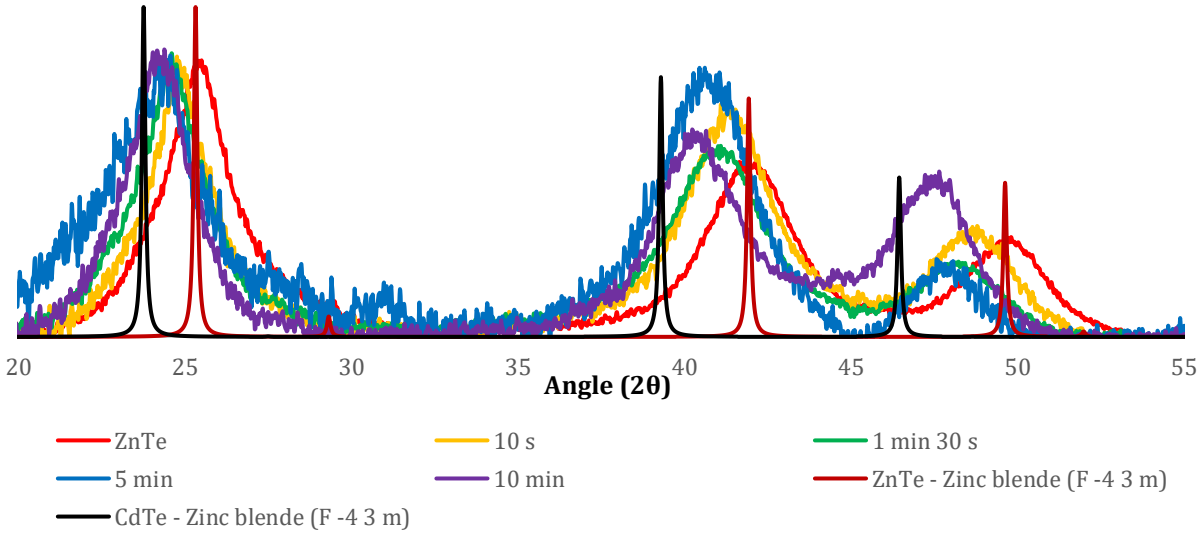

Figure 3.3. XRD evaluation of ZnTe nanorods treated with cadmium oleate at 195 ºC over time. Bulk zinc blende ZnTe and zinc blende CdTe are shown for reference. The Crystallography Open Database numbers are 9008840 for CdTe Zinc blende and 9008858 for ZnTe Zinc blende bulk spectra.[24]

Table 3.1. Compositional evaluation of (Zn,Cd)Te alloys. Vegard's Law is used to determine the composition of each alloy.

Sample	Crystal plane	Angle (2θ)	Lattice constant (nm)	% CdTe*	Average % CdTe
(Zn,Cd)Te 10 s	(1,1,1)	24.82	0.621	33.3	25.7
	(2,2,0)	41.38	0.617	21.1	
	(3,1,1)	48.80	0.619	26.3	
(Zn,Cd)Te 1 min 30 s	(1,1,1)	24.60	0.627	47.1	39.4
	(2,2,0)	41.14	0.621	30.2	
	(3,1,1)	48.20	0.626	45.1	
(Zn,Cd)Te 5 min	(1,1,1)	24.48	0.630	54.7	50.6
	(2,2,0)	40.64	0.628	49.1	
	(3,1,1)	47.96	0.629	52.7	
(Zn,Cd)Te 10 min	(1,1,1)	24.30	0.634	66.0	61.5
	(2,2,0)	40.40	0.631	58.2	
	(3,1,1)	47.58	0.634	64.6	

** The percentage of CdTe determined for the nanocrystal is based on the lattice constant 0.609 nm for ZnTe and 0.648 nm for CdTe*

Data obtained from evaluation of the elemental composition of the Cd^{2+}-exposed nanorods by ICP-OES is displayed in Figure 3.4. This figure shows that zinc composition decreases while cadmium incorporation increases over time. Furthermore, it can be seen that the rates of these processes increase with temperature. These data also show that it would be inaccurate to assign these alloys as $(Zn_{1-x}Cd_x)Te$ since the cation to anion ratio is neither constant nor 1:1 before or after the cation exchange reaction. Other systems, such as ZnSe, report an unchanging cation to anion ratio during cation exchange where all Cd^{2+} incorporation proceeds *via* exchange with cations in the original nanostructure.[25-27] In this telluride lattice, there are likely two distinct sources of cadmium: cadmium that has exchanged with zinc and excess cadmium adsorbed to the rod surface in the form of Z-type cadmium carboxylate.[28-29]

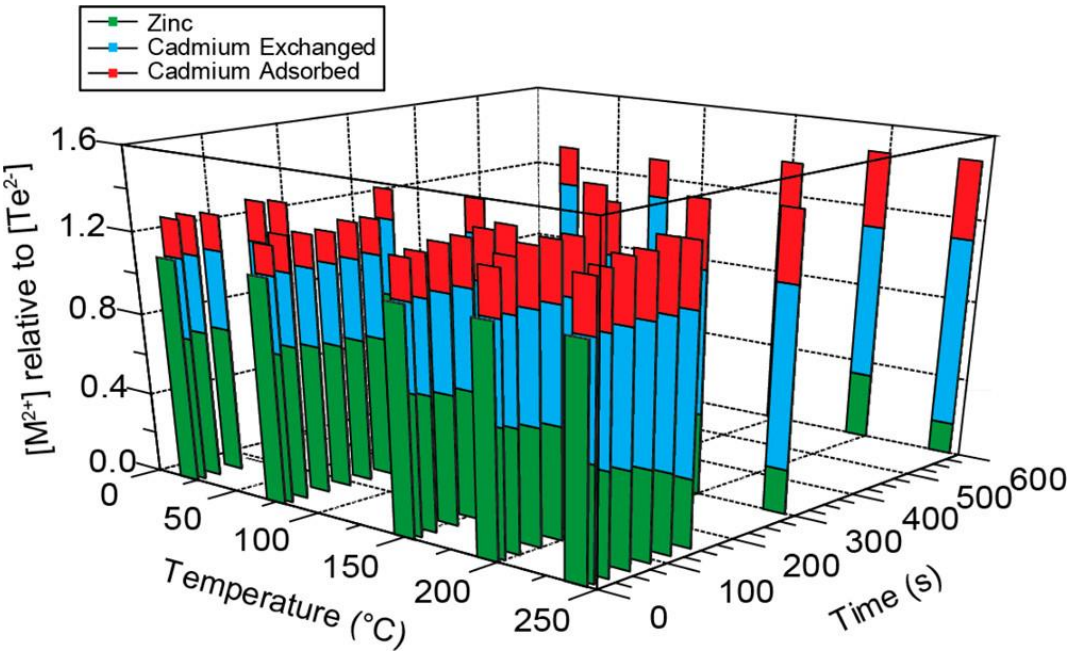

Figure 3.4. Elemental composition of Cd^{2+}-exposed ZnTe nanorods as a function of time and temperature. 2-D plots across a single temperature are shown in Figure 3.5. Elemental composition is reported as a relative amount normalized against the tellurium content in the nanorod structure. The relative $[Zn^{2+}]$ (green) decreases at an increasing rate as temperature is increased. Cadmium uptake, both through exchange with zinc (blue) and *via* surface adsorption (red), also occurs at a faster rate as temperature increases.

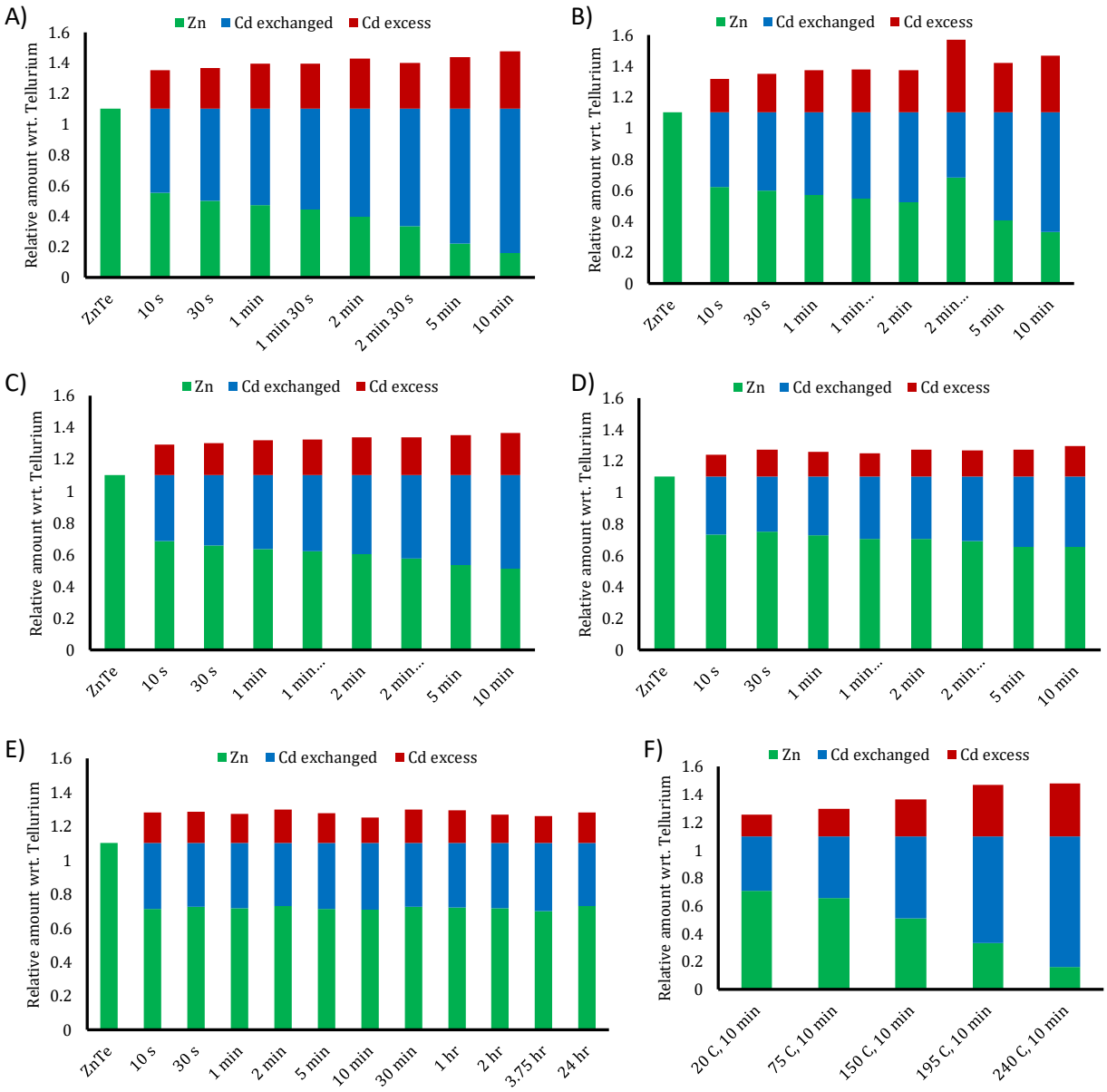

Figure 3.5. 2-D plots of elemental composition of Cd^{2+} exposed ZnTe nanorods as a function of time and temperature. 2-D plots of independent temperatures shown together in Figure 3.4. The relative specie amounts over time at 240 °C (A), 195 °C (B), 150 °C (C), 75 °C (D), and room temperature (E). The final plot (F) is a cross section of relative specie composition of the cation exchange product after 10 minutes across temperature. The relative molar specie composition is determined relative to the amount of tellurium measured in the nanomaterial.

Since accurate elemental composition measurement techniques are unable to distinguish between cadmium incorporated through the two mechanisms (adsorption vs. cation exchange), parsing out the fraction of cadmium added due to exchange with zinc is a prerequisite for evaluating the rate of cation exchange. At room temperature all cadmium uptake through both mechanisms is completed within the first 10 s as the rod composition remains constant after that time, yielding a final composition of Zn:Cd:Te = 0.71:0.57:1.0. Based on the relative change in the Zn:Te ratio in the nanorods, 40% of the measured Cd^{2+} is incorporated through exchange with Zn^{2+} ions in the rod while the other 60% is adsorbed to the nanorod surface. At higher temperatures it is believed that cation exchange is still preceded by Cd^{2+} adsorption, but the cation exchange process persists for a longer time as more cadmium is incorporated into the nanorod. This suggests that there is a measurable barrier to cation exchange at room temperature and that barrier may be a function of cation depth in the rod (*i.e.* Zn^{2+} near the rod surface are more easily exchanged than Zn^{2+} near the rod center). The cation to tellurium ratio exceeds 1:1 at temperatures above 150 °C, marking the crossover from anion to cation-rich rods as the relative cadmium concentration increases.

3.3 MECHANISM AND RATE OF CATION EXCHANGE

Scheme 3.1 illustrates the proposed mechanism by which cadmium is incorporated into the ZnTe nanorods. Step 1 is the initial fast step that occurs immediately upon mixing ZnTe nanorods and molecular Cd^{2+} precursors. Cadmium adsorption to the surface dominates this step, but a small amount of cation exchange does occur. This is the extent of exchange at low temperature. At elevated temperatures, cation exchange occurs throughout the structure and the rate limiting step (step 2) goes from a cadmium-saturated surface to cadmium exchanging in the core. It should be noted that while a sufficient number of cadmium ions have adsorbed to the surface to enable cation

exchange at an unimpeded rate, it is postulated that there are still available surface sites that become progressively passivated by additional cadmium throughout the reaction. Cation migration within the nanorod (step 3) is governed by both temperature and Cd^{2+} concentration.

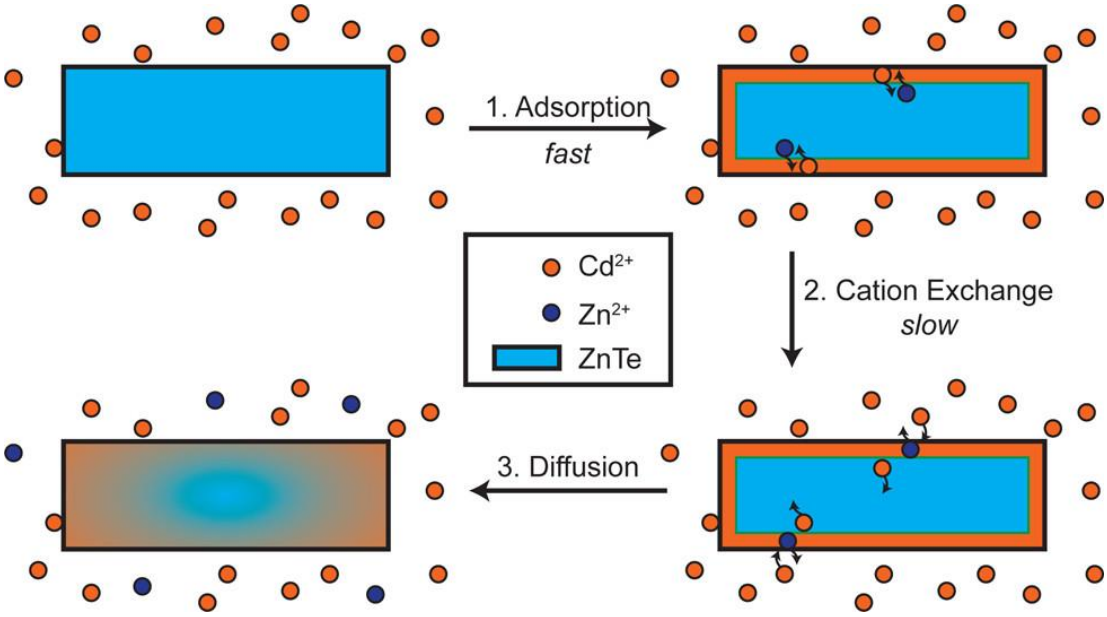

Scheme 3.1. Proposed Mechanism for Cation Exchange in ZnTe Nanorods

Molecular Cd^{2+} rapidly saturates the ZnTe exterior with modest exchange with surface zinc (step 1). Adsorption is followed by the rate determining step of incorporation of cadmium into the core of the nanorod (step 2). The extent of cadmium incorporation into the nanorod can be increased by both increasing the temperature and cadmium oleate concentration (diffusion, step 3).

Tracking the loss of zinc over time allows us to differentiate between cadmium adsorption and cation exchange since the amount of cadmium incorporated *via* exchange should correlate directly with zinc loss. The proposed mechanism suggests cadmium adsorption onto the tellurium-rich nanorod surface is fast and is followed by cation exchange into the rod interior—the rate-

determining step in the reaction. Assuming cation exchange is facilitated by rods with a cadmium-saturated surface, this process can be modeled using pseudo-first order kinetics, as shown in Figure 3.6. In this model it is assumed that the supply of Cd^{2+} at the rod surface is in large excess over the exchanging Zn^{2+}. Once a single zinc has left the nanostructure, the vacant site in the nanorod is replaced by cadmium migrating to the core. Zinc cations at the surface readily depart the surface to form zinc oleate and are replenished by excess cadmium in solution. The integrated rate law for this process is shown in eq 3.1 as:

$$(ln([A_t]) = -k't + ln([A_0]), \tag{3.1}$$

Where *A* is the concentration of the Cd^{2+} exchanging into the rod core, which is readily equated to the Zn^{2+} loss in the nanorods. From this analysis, the observed rate constant, k', varies from approximately 0.03×10^{-3} s^{-1} at 20 °C to 2.8×10^{-3} s^{-1} at 240 °C. Using the Eyring equation (eq 3.2, Figure 3.7), an approximation of the enthalpy of activation, $\Delta H^{\ddagger}$, is determined to be 15 kJ/mol (error associated with $\Delta S^{\ddagger}$ is too large to allow meaningful interpretation).

$$(ln\left(\frac{k}{T}\right) = \left(\frac{-\Delta H^{\ddagger}}{R}\right)\left(\frac{1}{T}\right) + ln\left(\frac{k_B}{h}\right) + \left(\frac{\Delta S^{\ddagger}}{R}\right) \tag{3.2}$$

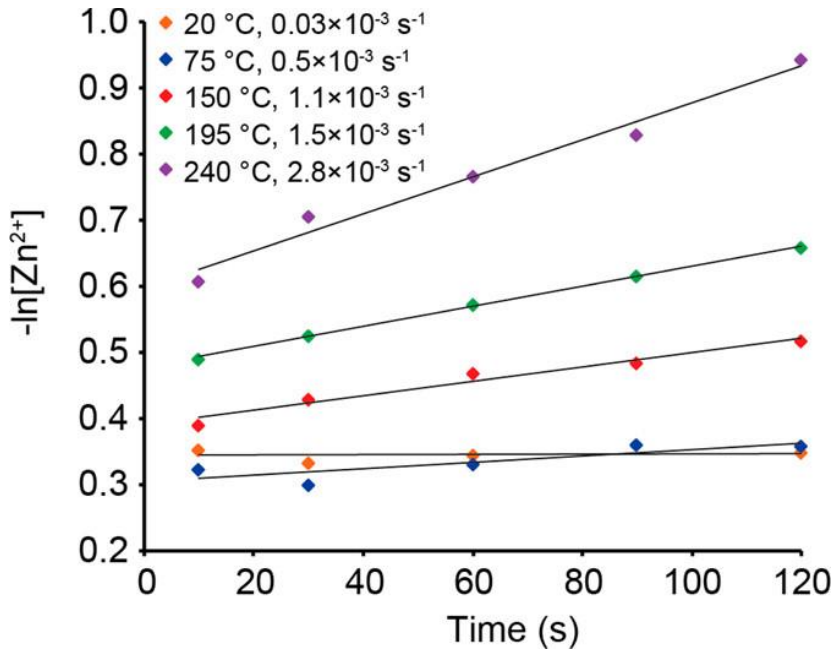

Figure 3.6. Pseudo-first order rates for the loss of Zn^{2+} from ZnTe nanorods during cation exchange as a function of temperature. The y-axis measures the loss of Zn^{2+} from the nanorods where $-\ln[Zn^{2+}] = \ln[(Zn,Cd)Te]$.

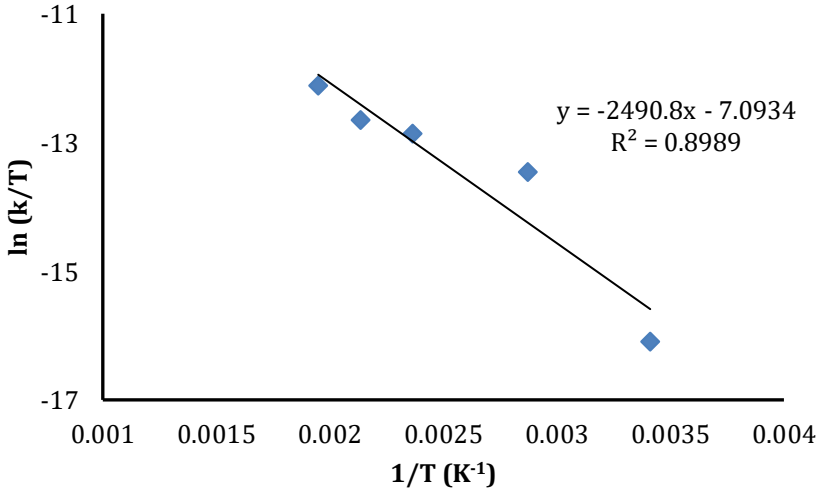

Figure 3.7. Eyring plot of cation exchange rates across temperature. From the Eyring relationship, $ln\left(\frac{k}{T}\right) = \left(\frac{-\Delta H^{\ddagger}}{R}\right)\left(\frac{1}{T}\right) + ln\left(\frac{k_B}{h}\right) + \left(\frac{\Delta S^{\ddagger}}{R}\right)$, $\Delta H^{\ddagger}$ = 14.6 kJ/mol.

An Arrhenius relationship for reactions of the first order (Equation 3, Figure 3.8) can also be used to extract an activation energy for comparison to the enthalpy of activation calculated using the Eyring Relationship (eq 3.3, Figure 3.8).

$$k = Ae^{\frac{-E_a}{RT}} \tag{3.3}$$

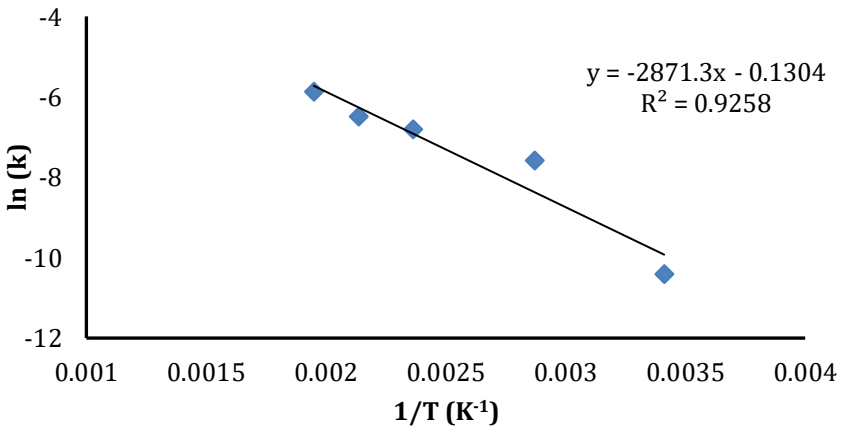

Figure 3.8. Arrhenius plot of cation exchange rates across temperature. From the Arrhenius relationship, $k = Ae^{\frac{-E_a}{RT}}$, the activation energy is 24 kJ/mol.

The activation energy for the cation exchange process is thus determined to be 24 kJ/mol. The similarity of the experimentally determined enthalpy of activation, 15 kJ/mol, and the activation energy, 24 kJ/mol, confirms that the energy barrier for cation exchange for replacement of zinc with cadmium is small, barely exceeding the strength of a strong hydrogen bond. Due to such a small energy barrier for cation exchange, it is expected that cation exchange between cadmium molecular precursors and zinc in telluride lattices is unavoidable under temperatures typically used for synthesis of crystalline nanomaterials. For comparison it should be noted that

the activation barrier determine for the telluride system is smaller than, yet of the same order of magnitude as, those in other similar systems, such as ZnSe, where the activation barrier is between 30 and 40 kJ/mol for Cd^{2+}.[26]

3.4 ROLE OF CADMIUM CONCENTRATION IN CATION EXCHANGE RATE

Over the course of the cation exchange reaction, the rate of Zn^{2+} loss from the nanorods decreases. Adjustments to cadmium concentration, however, have no influence on the initial rate of cation exchange so long as there is sufficient Cd^{2+} to completely coat the surface of the ZnTe nanorods. As can be seen in Figure 3.9, the rate of Zn^{2+} loss in the nanorods as a function of Cd^{2+} concentration ranging from 0.125:1 to 2:1 (Cd:Zn) is nearly identical over the first 120 s of exchange at 195 °C. At concentrations below 0.0625:1 (Cd:Zn), it is hypothesized that there is insufficient cadmium available to saturate the rod surface and the rate of exchange becomes concentration dependent with the rate slowing as the Cd:Zn ratio decreases. These observations are consistent with typical saturation kinetics, where the rate of exchange saturates as the reaction is depleted of substrate.

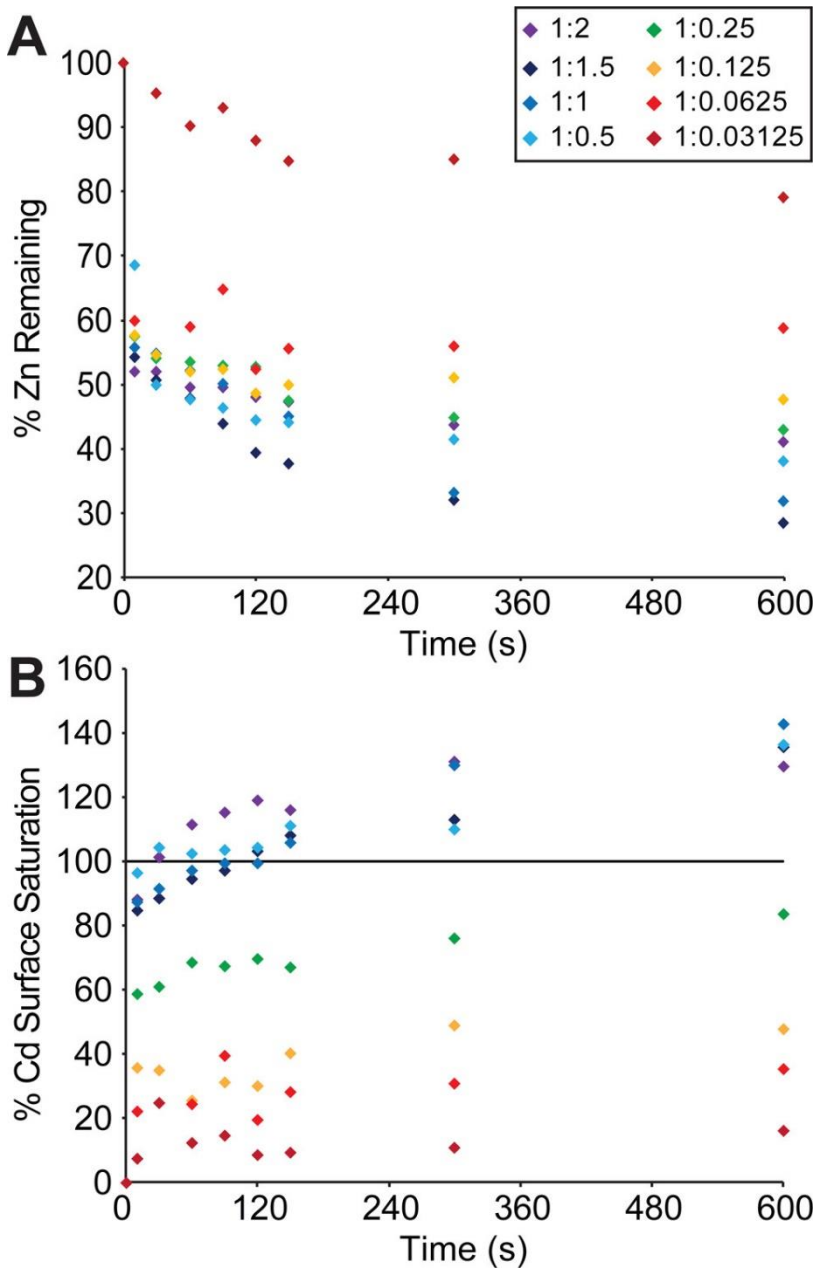

Figure 3.9. Effect of Cd^{2+} concentration on the rates of cation exchange. (A) Percentage of zinc remaining in the nanorod as a function of time and concentration. (B) Percentage of surface sites passivated by Cd^{2+} as a function of time and concentration. Percent surface saturation is based on the calculated number of available surface sites, where 0.4:1 (Cd:Zn) is set at 100%. These experiments were carried out at 195 °C.

By measuring the amount of excess cadmium in the nanorod, it can also be shown that so long as the cadmium concentration is above 0.5:1 (Cd:Zn), there is no difference in excess cadmium adsorption at the surface. Based on surface area calculations, it is estimated that the available surface sites can readily accommodate 0.4 cadmium atoms per zinc in the nanorod (Figure 3.10).

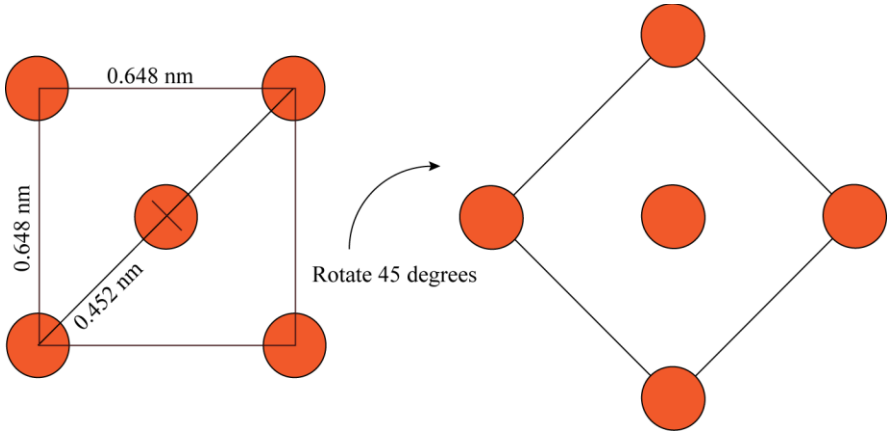

Figure 3.10. Location of cadmium atoms on a single face of a face centered cubic lattice.

The starting ZnTe nanorods are 10 nm long by 3.1 nm wide. Assuming the shape to be approximately a cylinder, the nanorod has a surface area of 112 nm^2 and a volume of 75 nm^3. To approximate the number of available sites on the surface for cadmium coordination, the distance between two nearest cadmium neighbors must first be determined. Both the surface and cation exchange product are zinc blende lattices with a face centered cubic unit cell. The lattice parameter for CdTe zinc blende is 0.648 nm.[24] Thus, the distance between two nearest cadmium atoms is half the length of the diagonal of a CdTe zinc blende unit cell. This distance between two cadmium atoms is 0.452 nm. Furthermore, this distance between cadmium atoms is also a measurement of the diameter occupied by each cadmium atom. Since nearest cadmium atoms are located at right angles to one another, each adsorbed cadmium effectively occupies a square of area on the rod's

surface. This area of occupation by each cadmium atom is 0.204 nm^2 with a length and width of 0.452 nm. With each cadmium atom occupying 0.204 nm^2 on a rod surface area of 112 nm^2, it is estimated that there are 551 cadmium atoms adsorbed to the surface of the nanorod. The density of a ZnTe nanocrystal is 5.65 g/cm^3 and the formula mass of ZnTe is 193.01 g/mol.[24] From a volume of 75 nm^3, the number of zinc atoms is estimated to be 1330 per nanorod.

The surface cadmium to zinc contentment ratio is 0.41 surface cadmium adsorption spots per zinc in the nanorod. This number is used to approximate the amount of cadmium expected to saturate the nanorod surface. This approximation is in line with prior surface atom estimations used to evaluate CdSe nanorods.[30] It is important to note that the cation exchange rate is not necessarily slowed when there is insufficient Cd^{2+} to completely saturate the surface. As shown in the 0.25:1, 0.125:1, and 0.0625:1 (Cd:Zn) cases, the surface is not fully saturated, however, there is no obvious decrease in cation exchange rate compared to the systems with higher concentrations. Hence, this system may reach its saturation limit with respect to cation exchange rate without having to fully saturate the nanorod surface. Our studies show that when the ratio of cadmium to zinc in the system is 0.03125:1, there is notable cadmium uptake with almost no zinc loss over the first 120 s, implying only surface adsorption being relevant under these conditions.

3.5 LONG-TERM RIPENING OF NANORODS

During prolonged reaction times (24 h and more, Figure 3.11), a third process of cadmium incorporation emerges. The first two regimes, described in detail through the aforementioned studies, are an initial rapid cadmium adsorption to the surface of the nanorods in the first 10 s and cadmium exchange within the core over the subsequent 30 min. The third regime is Ostwald ripening and loss of anisotropy, which continues to add more cadmium to the nanorods without loss of zinc as the nanostructures evolve toward a more isotropic shape (Figure 3.12 and 3.13).

The amount of excess cadmium triples at 240 °C and increases by a factor of 2.6 at 150 °C between 1 and 72 h due to uptake of available cation during ripening.

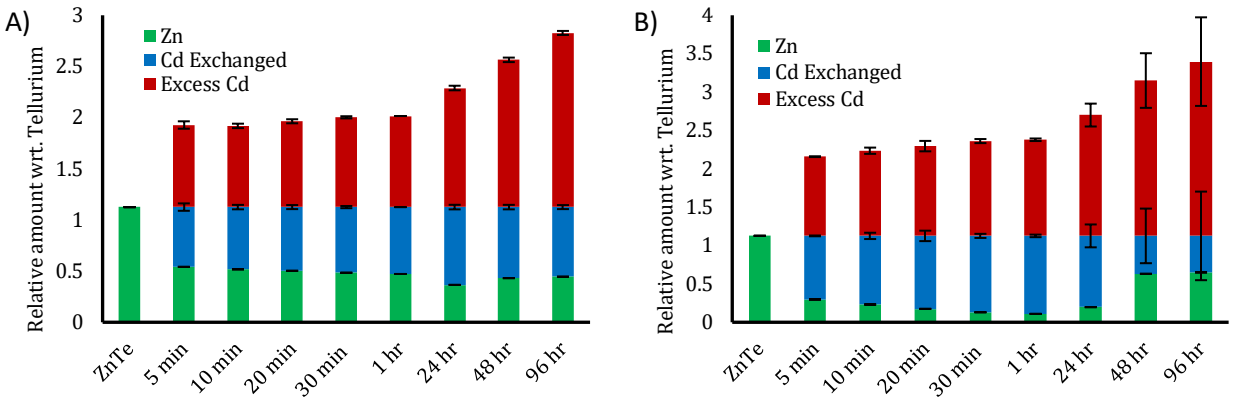

Figure 3.11. Elemental composition evaluation of relative molar specie amounts with respect to Tellurium over 3 days. Cation exchange occurs at 150 °C (a) and 240 °C (b). After 1 hour, changes of zinc content are unchanged within error, but excess cadmium amount increases due to nanorod reconfiguration.

150 °C – 10 s

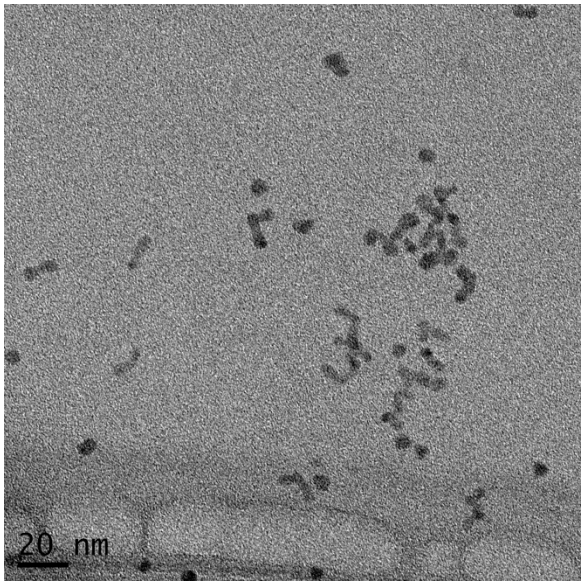

150 °C – 1 min

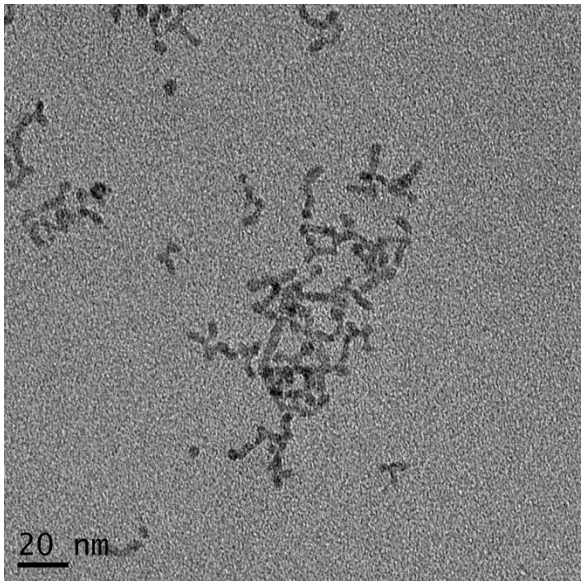

150 °C – 2 min 30 s

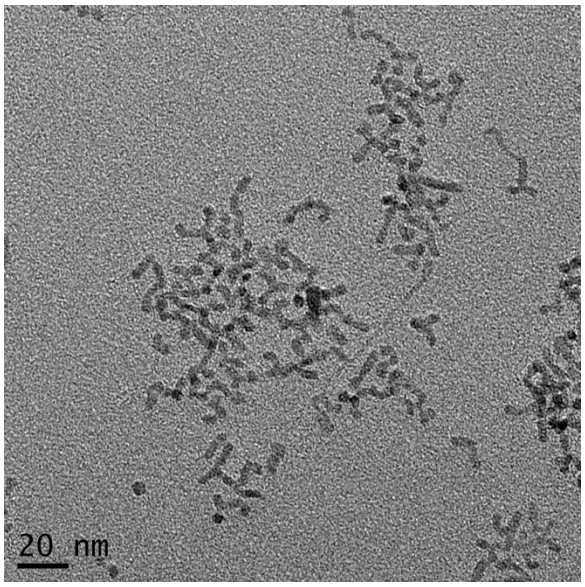

150 °C – 10 min

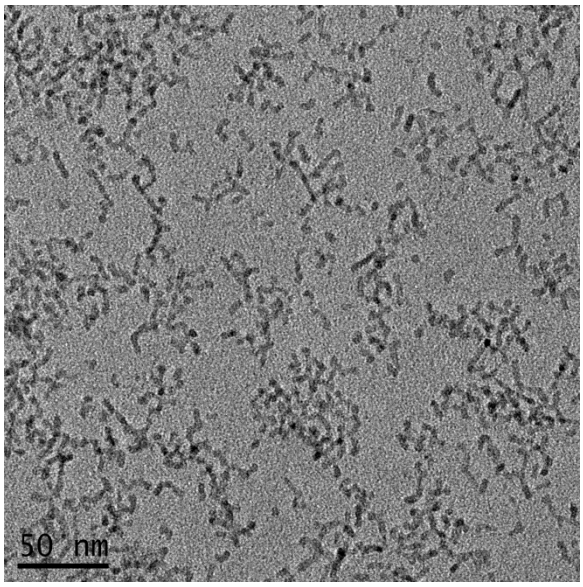

Figure 3.12. Cation exchange products over time at 150 °C.

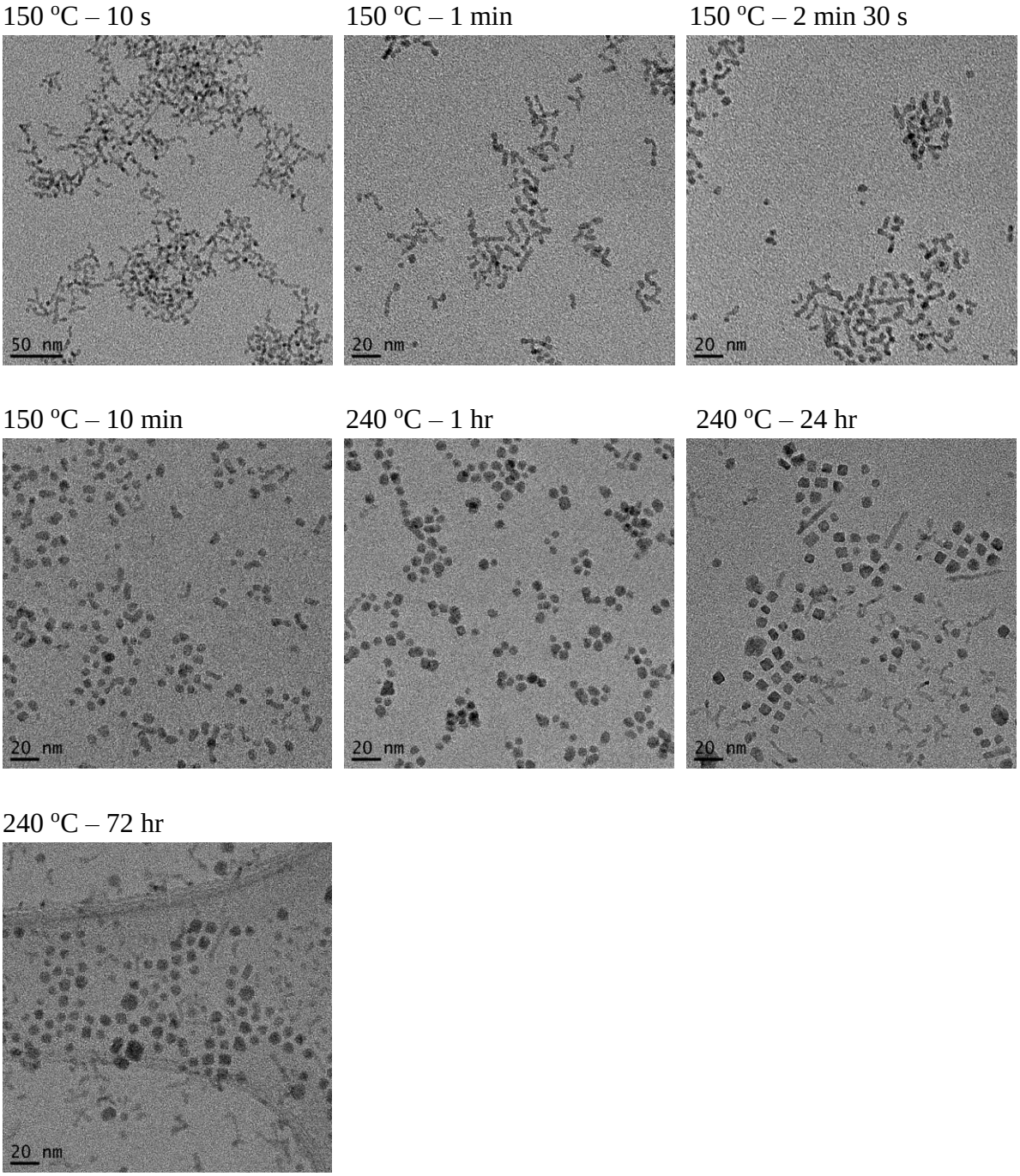

Figure 3.13. Cation exchange products over time at 240 °C.

Our data would suggest that cation exchange of Cd^{2+} into ZnTe lattices is facile even under mild conditions. Even in the presence of selenide in the form of TOP-Se, cation exchange products are exclusively observed (Figures 3.14 and 3.15). No selenium incorporation is observed across a range of temperatures and precursor addition methods.

3.6 Synthetic effects to access ZnTe/CdSe heterostructures

CdSe growth attempts were unsuccessful using successive ionic layer adsorption and reaction (SILAR) type growth procedures. For example, treating purified ZnTe nanorods with alternate injections of cadmium oleate and trioctylphosphine selenide every five minutes yielded nanorods with a Zn:Te:Cd ratio of 1.0:1.0:0.8 with no observed selenium. The molar ratios of zinc, tellurium, cadmium, and selenium were equivalent in the starting reagents. The final product has a smaller band gap than the starting ZnTe nanorods and has a length and width of 11.5 ± 2.4 nm by 3.3 ± 0.5 nm. Figure 3.13 shows one example of the UV-Vis and TEM observed after SILAR growth treatment at 170 ^{o}C. Similar results were observed when cadmium tetradecylphosphonate was used as the cadmium precursor. It was observed that greater bathochromic shifts were observed at higher temperatures between 150 °C and 240 °C.

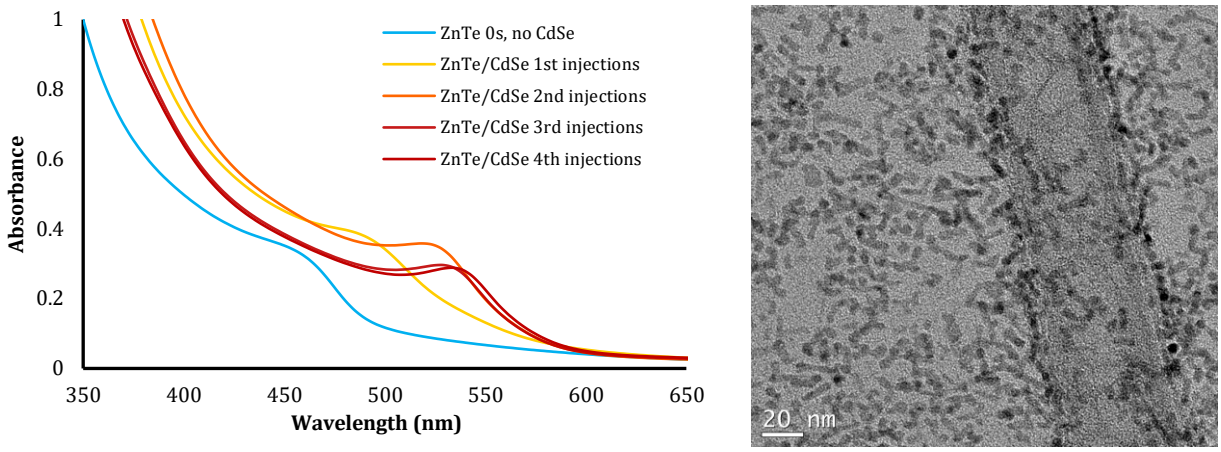

Figure 3.14. CdSe SILAR treatment of ZnTe nanorods. UV-Vis absorbance (left) and TEM (right) evaluations of 11.5 ± 2.4 nm ZnTe nanorods exposed to SILAR technique to grow CdSe rod ends. Cd^{2+} and Se^{2-} precursor injections were made every 5 minutes. The nanorods have undergone a 68 nm bathochromic shift.

In an alternative effort to target CdSe growth on ZnTe nanorods, purified ZnTe was added to a bath of preheated cadmium oleate precursor. Trioctylphosphine selenide was added by syringe pump over the course of the reaction to limit CdSe nucleation independent of growth on ZnTe. Figure 3.14 shows the UV-Vis and TEM of an example in which ZnTe nanorods were injected into a solution of cadmium oleate at 75 °C followed by immediate heating to 215 °C, at which point trioctylphosphine selenide addition began by syringe pump over 20 minutes. The resulting nanorods have a Zn:Te:Cd ratio of 1.0:1.7:1.5 with no measured selenium and have a length and width of to 15.5 ± 4.6 nm with 3.8 ± 0.6 nm. Similar results were observed when cadmium tetradecylphosphonate was used as the cadmium precursor. It was observed that greater bathochromic shifts were observed at higher temperatures between 150 °C and 240 °C.

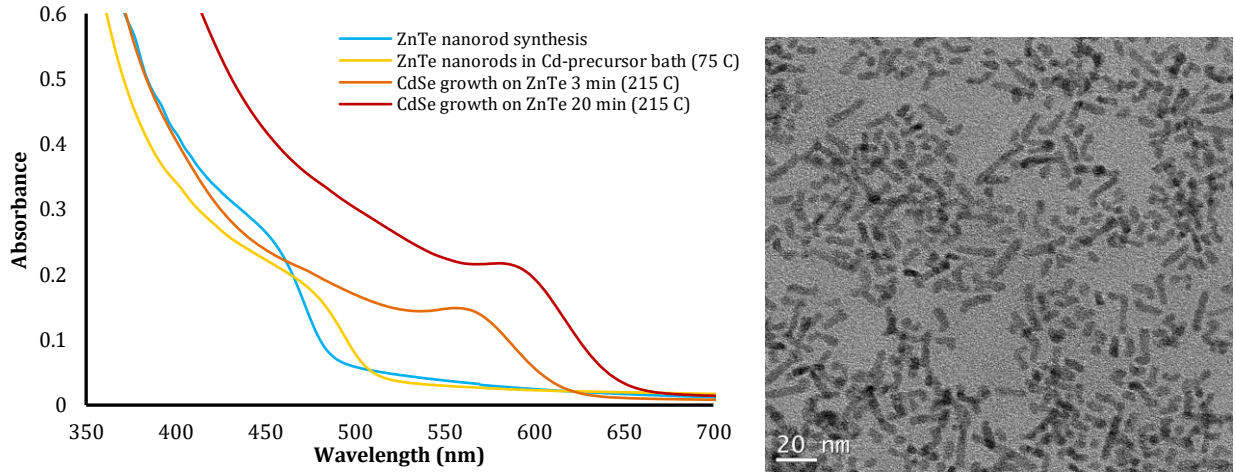

Figure 3.15. CdSe growth attempted in presence of excess cadmium tetradecylphosphonate. UV-Vis absorbance (left) and TEM (right) evaluations of 15.5 ± 4.6 nm ZnTe nanorods in a Cd-TDPA bath with drop-wise addition of TOP-Se at 215ºC for 20 min. A 126 nm bathochromic shift is observed by UV-Vis.

3.7 RECTIFICATION WITH EXISTING CLAIMS OF CORE-SHELL ZNTE/CDSE

However, there is significant literature precedent for the existence of ZnTe/CdSe core/shell quantum dots, which demonstrate altered carrier dynamics in the final heterostructures.[15, 20-21] Many of the core/shell synthetic procedures share similar reaction conditions (such as temperature and growth time) to the above-reported cation exchange experiments with ZnTe nanorods. Thus, either there is some unique characteristic of the ZnTe nanorods that more readily facilitates cation exchange compared to the spherical nanocrystals or the shelling reports have failed to address cation exchange in the resultant nanostructures. In existing ZnTe/CdSe quantum dot studies, the observation of a bathochromic shift in the UV–vis spectrum upon addition of Cd^{2+} and Se^{2-} precursors is considered indicative of CdSe shell growth.[20] Although the reports validate claims of CdSe shell growth with studies that measure increased lifetimes of separated electron–hole pairs and more rapid charge transfer rates between the core and shell, the reports do not assess the elemental composition of the final nanostructures. To evaluate previously studied core/shell structures for their elemental composition, core–shell particles were prepared using methods described in prior reports in which ZnTe quantum dots are treated with alternating injections of cadmium oleate and TOP-Se *via* a SILAR growth method. Single monolayer amounts of Cd^{2+} and Se^{2-} precursors are added and reacted with the ZnTe cores for a period of 10 min before subsequent additions are made to increase shell thickness. TEM and UV–vis analyses (Figure 3.16) suggest the synthesized quantum dots are highly similar to the quantum dots previously reported in the literature.[20]

Figure 3.16 shows the characterization of previously reported core-shell ZnTe/CdSe quantum dots.[15, 20-21] Figure 3.17 illustrates the structure hypothesized to have been observed in prior reports.

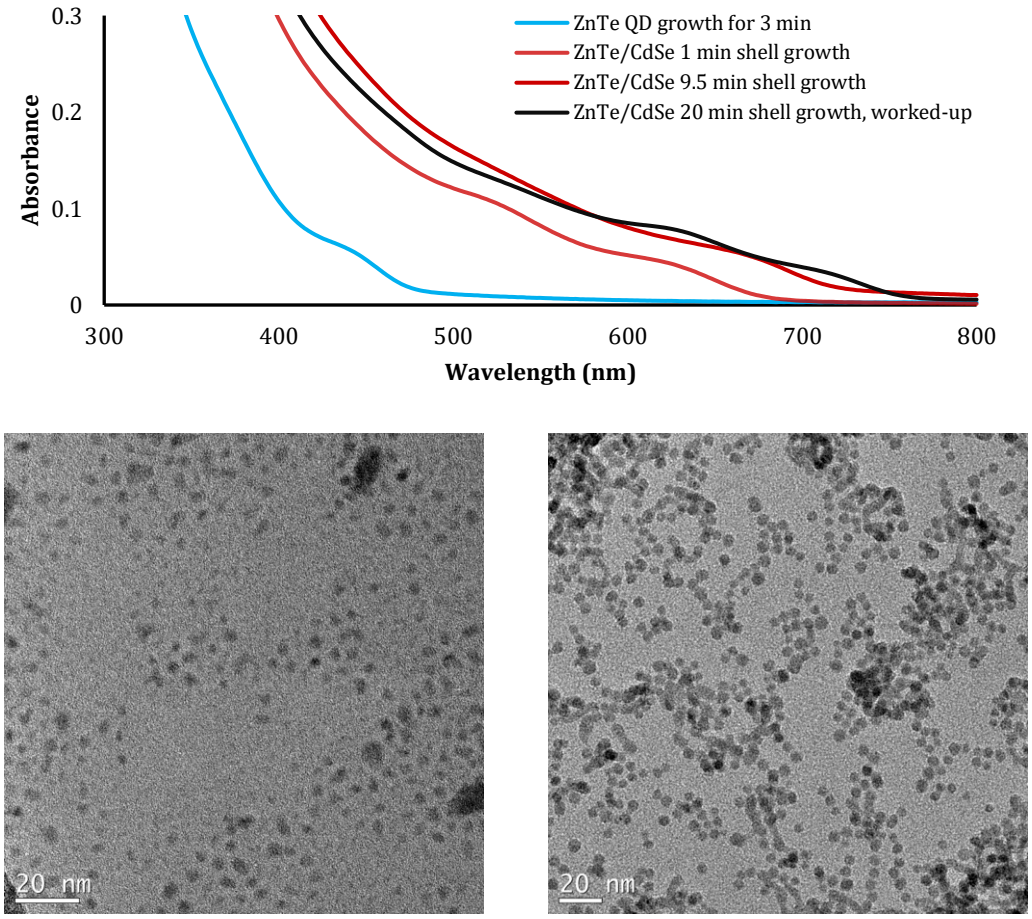

Figure 3.16. Characterization of ZnTe/CdSe core-shell quantum dots. UV-Vis absorbance (top) and TEM (bottom) evaluations of 3.9 ± 0.6 nm ZnTe quantum dots (left) and 5.3 ± 0.8 nm ZnTe/CdSe quantum dots (right) synthesized following procedures described in work by Basché *et al.*[20]

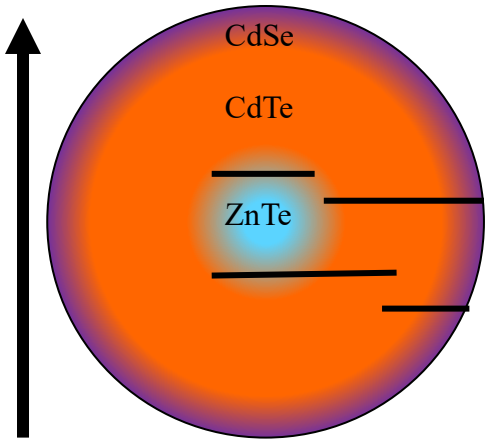

Figure 3.17. Hypothesized ZnTe/CdTe/CdSe gradient alloy observed in prior reports.

ICP-OES evaluation of the samples prepared here indicates a Zn:Cd:Te:Se ratio of 1.0:14.7:14.4:2.0 starting from a Zn:Te ratio of 1.0:0.9 in the starting quantum dot cores. This suggests that prior reports that use these conventional synthetic methods yield a ZnCdTeSe alloy instead of a core/shell quantum dot. The zinc to tellurium ratio decreases dramatically to 1.0:14.4 after exposure to the cadmium and selenium precursors. Since additional tellurium is never added after purification of the cores, the increase in the tellurium to zinc ratio must be attributed to the loss of zinc from the nanocrystal. It is worth noting that, in the core/shell particles, there is selenium present in the nanostructures. The ratio of elements present in these reported nanostructures suggests that the structure is predominately CdTe with a small amount of Zn^{2+} and Se^{2-} present in the alloy and an overall cation to anion ratio of roughly 1:1. At similar temperatures in ZnSe systems, gradient alloys were observed after Cd^{2+} cation exchange.[25] Furthermore, there is minimal evidence of anion exchange occurring between selenium and tellurium due to the small relative amount of selenium present in the quantum dot experiments. Thus, it is hypothesized that the particles synthesized by prior literature methods are actually a gradient alloy whose character would evolve from the core outward as ZnTe/CdTe/CdSe (Figure 3.16). These are not discrete

segments but rather an alloy where the material's band gap is dictated most significantly by the predominant species in the quantum dot, CdTe.

This type of gradient alloy structure offers a reasonable explanation for the previously observed increased charge separation and charge mobility characteristics.[15, 20-21] The small ZnTe core and thin CdSe shell separated by a CdTe segment would promote localization of the electron toward the outer layers of the particle while confining the holes toward the core. ZnTe/CdTe and CdTe/CdSe would be expected to demonstrate pseudo-type-II behavior due to similar energy levels of the valence and conduction bands, respectively.

These prior studies have made important contributions toward developing type II nanomaterials. While the absence of elemental quantification mistakenly suggested the nanostructures are type II heterostructures, the majority of the experimental setup, observations, and conclusions are the results of a significant effort and analysis. Moving forward, the ease of Cd^{2+} cation exchange into telluride lattices poses significant challenges for heterostructure growth using ZnTe as the electron donor. While the SILAR method may serve as a useful method for designing some heterostructures, any presence of molecular cadmium precursors with zinc telluride will readily facilitate cation exchange. Among the alternative options for obtaining ZnTe/CdSe heterostructures are starting with a CdSe nanorod scaffold and growing ZnTe nanorod ends or treating a ZnTe nanorod with a single source precursor, such as CdSe magic size clusters or molecular precursors with preformed CdSe bonds. Preliminary investigations confirm the potential viability of these approaches (Figure 3.18).

Preliminary studies with ZnTe and CdSe quantum dots demonstrate that cation exchange does not occur to a noticeable extent when CdSe bonds are preformed. Furthermore, cation exchange between cadmium and zinc only proceed through cadmium exchanging into the lattice

and pushing zinc out. The reverse exchange is not readily facilitated. As can be seen in Figure 3.18 shows that heating ZnTe and CdSe quantum dots together only leads to a change in the UV-Vis spectrum at temperatures at 270 °C or higher, at which point the ZnTe quantum dots decompose to molecular species. Also, zinc oleate and CdSe quantum dots shows no evidence of cation exchange between cadmium and zinc when the cadmium-selenide bonds are preformed.

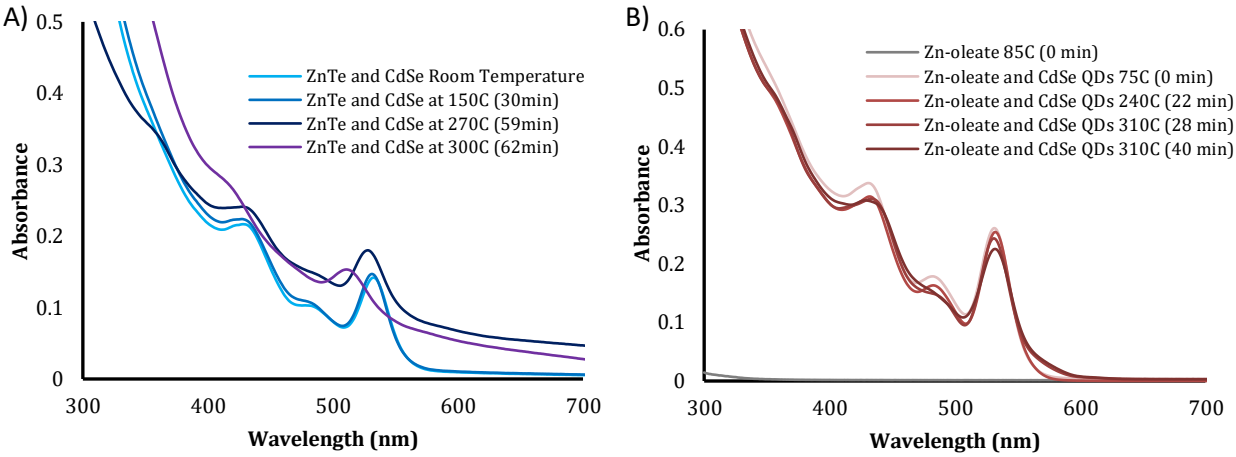

Figure 3.18. Treatment of CdSe QDs with zinc sources. Heating up CdSe quantum dots in the presence of ZnTe quantum dots (A) and zinc oleate molecular precursors (B).

3.8 CONCLUSION

This investigation provides a comprehensive evaluation of the cation exchange mechanism between Cd^{2+} and Zn^{2+} in ZnTe. An initial rapid cadmium adsorption step onto the tellurium-rich surface of ZnTe occurs immediately upon injection. This adsorption step is followed by a rate determining exchange step, with a measured activation energy of 24 kJ/mol. As long as there is sufficient cadmium to occupy the available surface sites, the solution concentration of cadmium has little influence on the rate of cation exchange, consistent with our modeling of the exchange

process using pseudo-first order kinetics. When cadmium concentrations are decreased below 0.4:1 (Cd:Zn), Cd^{2+} will not fully saturate the ZnTe nanorod surface. However, only when the cadmium concentration falls below 0.125:1 (Cd:Zn) does the rate of cation exchange into the tellurium lattice become impacted over the first few minutes of the reaction.

This study demonstrates that cation exchange in ZnTe is a controllable and tunable process in which the elemental composition of specific alloys can be obtained through controlling the temperature, time, and concentration of the reaction. While these findings demonstrate how to obtain (Zn,Cd)Te alloys of desired composition, they also reveal that cation exchange in colloidal ZnTe nanostructures imposes significant challenges for synthesizing type II heterostructures. Future investigations will explore alternative approaches in order to obtain a true, unalloyed ZnTe/CdSe type II heterostructure.

3.9 EXPERIMENTAL METHODS

3.9.1 *General Considerations*

All manipulations were carried out using standard Schlenk or glovebox techniques under dry nitrogen. Zinc acetate (99.99%), oleic acid (OA, 90%), 1-octadecene (1-ODE, 90%), metallic tellurium (Te, 99.997%), trioctylphosphine (TOP, 97%), and superhydride ($LiBH(CH_2CH_3)_3$) solution in THF (1 M) were all purchased from Sigma Aldrich and used as received without further purification. Anhydrous ethanol and pentane were purchased from various sources. Trioctylphosphine-telluride (TOP-Te, 1 M Te) solution was prepared by dissolving metallic Te into TOP in a glovebox.

Abbreviations:

Cd(OA)2 cadmium oleate

ICP-OES inductively coupled plasma–optical emission spectroscopy

TOP trioctylphosphine

TOP-Se trioctylphosphine selenide

TOP-Te trioctylphosphine telluride

Zn(OA)2 zinc oleate

3.9.2 *Synthesis of ZnTe Nanorods*

In a 50 mL three-neck flask, 0.26 g (1.4 mmol) of zinc acetate was mixed with 4 mL (12.7 mmol) of oleic acid and 20 mL of 1-ODE. The mixture was degassed under vacuum for at least 30 min before being heated to 200 °C under nitrogen. After 1 h, a clear solution was formed and the temperature was dropped to 160 °C. The tellurium precursor was prepared by adding 1.6 mL of superhydride solution (0.7 M in THF) and 2 mL of oleylamine to 1.0 mL of TOP-Te (1.0 M Te in TOP). This tellurium precursor mixture was stirred for 20 min at room temperature until the solution became homogeneous before being injected rapidly into the zinc solution at 160 °C. The reaction temperature was increased to 190 °C over the course of 5 min and was maintained at 190 °C for 60 min before quenching the reaction by removing the heating mantel to cool the reaction mixture to room temperature. Excess solvent and volatile organics were removed by vacuum distillation at 150 °C. The ZnTe nanorods were separated and purified by adding ethanol to the resulting oily residue followed by centrifugation and re-dispersion into pentane. This process was repeated a minimum of five times. Purity was checked by ^{1}H NMR spectroscopy, and the purified nanorods were used as a solution in pentane.

3.9.3 *Cation Exchange Procedure*

By UV–vis spectroscopy, the molar absorptivity of the ZnTe nanorods was determined to be 420 L mol^{-1} cm^{-1} at 375 nm with respect to the amount of zinc in the nanorod (Figure 3.19). To reliably control the amount of zinc used in each cation exchange reaction, a molar absorptivity constant was determined for the amount of zinc in ZnTe nanorods. For a 30 mL ZnTe stock solution in pentane, the amount of zinc was determined to be 0.5 mmol by ICP-OES. At 375 nm, the molar absorptivity constant was determined to be ε = 420 L/mol*cm with respect to the amount of zinc.

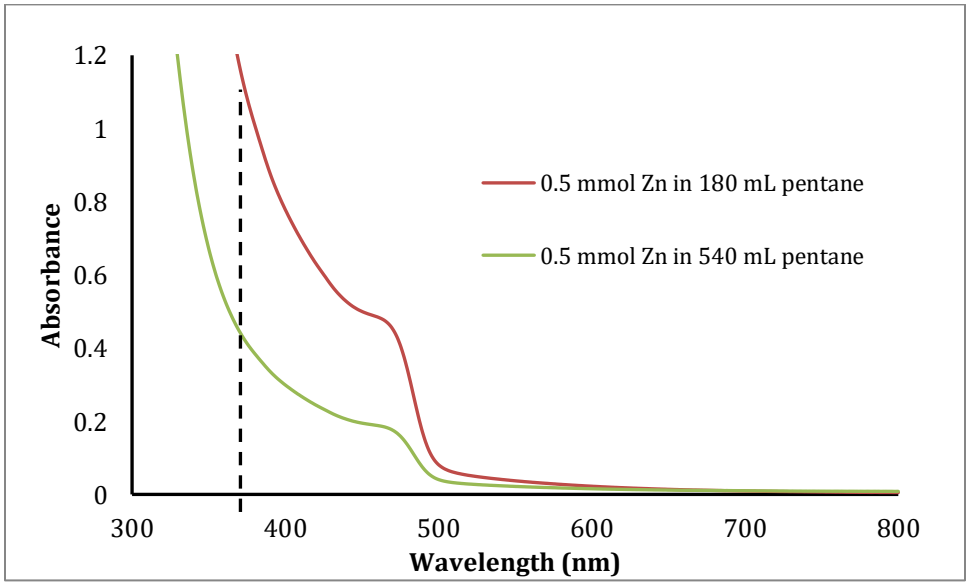

Figure 3.19. Determination of the molar absorptivity constant for the amount of zinc in ZnTe nanorod stock solution. At 375 nm, ε = 420 L/mol*cm for the amount of zinc. The dashed line highlights absorbencies at 375 nm.

In a typical cation exchange reaction, the pentane solvent was removed from a stock solution of the ZnTe nanorods containing 0.5 mmol of zinc and the nanorods were then suspended in 1.8 mL of 1-ODE. The cadmium precursor was prepared by adding cadmium oxide (0.5 mmol), oleic acid (4 mmol),

and 1-ODE (3.6 mL) in a 25 mL three-neck flask. This solution was degassed for 1 h before being heated to 240 °C for 60 min or until the solution became clear. The cadmium solution temperature was adjusted to the desired cation exchange temperature, and the ZnTe nanorods were injected rapidly at this temperature. Aliquots of 0.3 mL were taken at each time point and transferred to a vial purged with nitrogen at room temperature before purification. Each aliquot was purified by suspending the nanorods in pentane, adding ethanol as a precipitant, and centrifugation at 7830 rpm for 10 min. Five consecutive purification repetitions were carried out until all excess ligand was removed. Selected samples were evaluated by ^{1}H NMR spectroscopy on a Bruker Avance 500 MHz NMR spectrometer to verify sample purity (Figure 3.20).

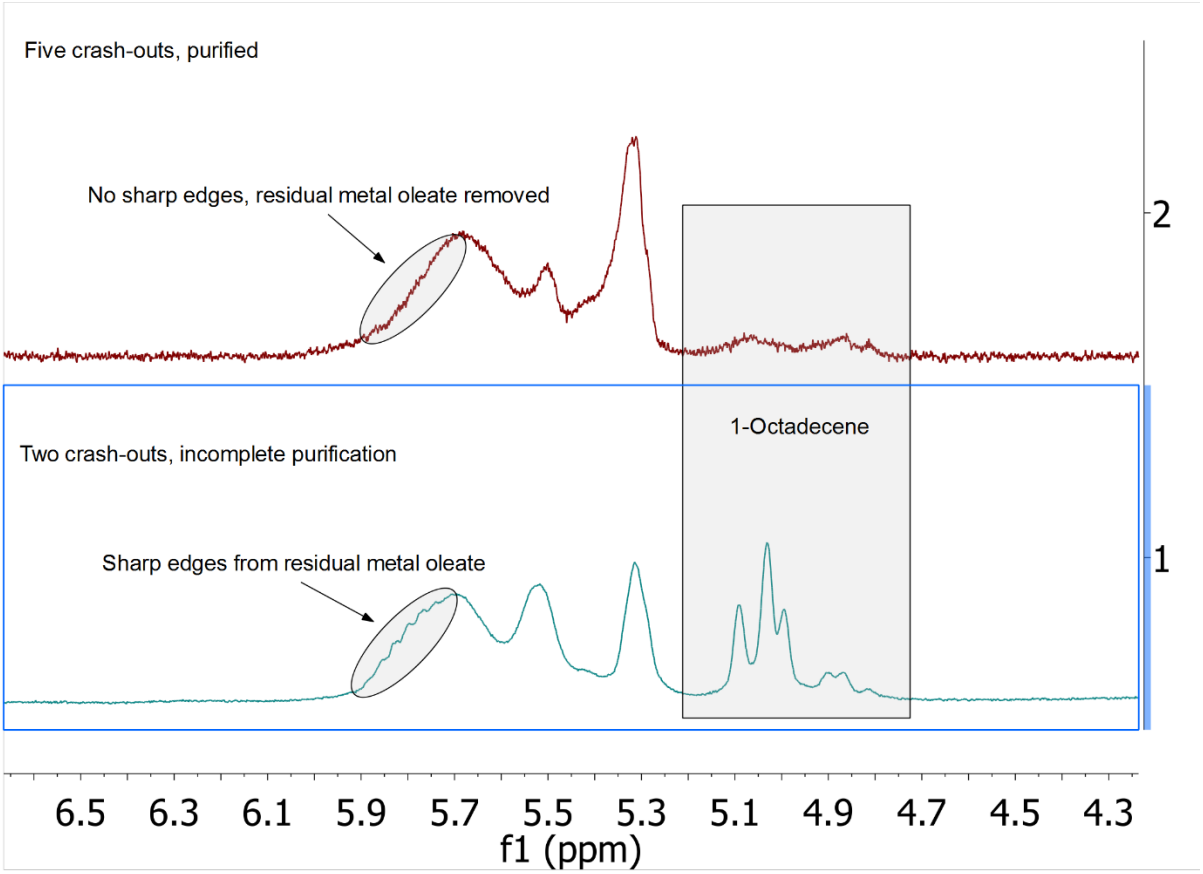

Figure 3.20. ^{1}H NMR spectra of the results of the purification process of ZnTe nanorods. A typical purification process includes five crash-outs. After two crash-outs, molecular metal oleate species remain in the sample, as can be seen by the sharp features from 5.8 – 6.0 ppm and 5.0 – 5.3 ppm. However, the residual metal oleate is removed after the fifth crash-outs. Five crash-outs were carried out on each sample before evaluation by ICP-OES.

3.9.4 *Sample Characterization*

All cation exchange samples were evaluated for zinc, tellurium, cadmium, and selenium composition using a PerkinElmer Optima 8300 inductively coupled plasma–optical emission spectrophotometer. UV–vis spectra were recorded using an Agilent Cary 5000 spectrophotometer.

TEM images were obtained on an FEI Technai G2 F20 microscope. Analysis of TEM images was performed *via* manual counting using the ImageJ software package. Powder X-ray diffraction data were recorded on a Bruker D8 Discover instrument with a GADDS 2-D XRD system.

3.10 REFERENCES

(1) Talapin, D. V.; Steckel, J., Quantum dot light-emitting devices. *MRS Bulletin* **2013,** *38*, 685-691.

(2) Lunt, R. R.; Osedach, T. P.; Brown, P. R.; Rowehl, J. A.; Bulović, V., Practical Roadmap and Limits to Nanostructured Photovoltaics. *Advanced Materials* **2011,** *23*, 5712-5727.

(3) Kramer, I. J.; Sargent, E. H., Colloidal Quantum Dot Photovoltaics: A Path Forward. *ACS Nano* **2011,** *5*, 8506-8514.

(4) Dabbousi, B. O.; Rodriguez-Viejo, J.; Mikulec, F. V.; Heine, J. R.; Mattoussi, H.; Ober, R.; Jensen, K. F.; Bawendi, M. G., (CdSe)ZnS Core−Shell Quantum Dots: Synthesis and Characterization of a Size Series of Highly Luminescent Nanocrystallites. *J. Phys. Chem. B* **1997,** *101*, 9463–9475.

(5) Mokari, T.; Rothenberg, E.; Popov, I.; Costi, R.; Banin, U., Selective growth of metal tips onto semiconductor quantum rods and tetrapods. *Science* **2004,** *304*, 1787-1790.

(6) Yong, K. T.; Sahoo, Y.; Swihart, M. T.; Prasad, P. N., Growth of CdSe Quantum Rods and Multipods Seeded by Noble-Metal Nanoparticles. *Adv. Mater.* **2006,** *18*, 1978-1982.

(7) Milliron, D. J.; Hughes, S. M.; Cui, Y.; Manna, L.; Li, J.; Wang, L.-W.; Alivisatos, a. P., Colloidal nanocrystal heterostructures with linear and branched topology. *Nature* **2004,** *430*, 190-195.

(8) Shieh, F.; Saunders, A. E.; Korgel, B. A., General shape control of colloidal CdS, CdSe, CdTe quantum rods and quantum rod heterostructures. *Journal of Physical Chemistry B* **2005,** *109*, 8538-8542.

(9) Halpert, J. E.; Porter, V. J.; Zimmer, J. P.; Bawendi, M. G., Synthesis of CdSe / CdTe Nanobarbells. *Journal of the American Chemical Society* **2006,** *128*, 12590-12591.

(10) Kumar, S.; Jones, M.; Lo, S. S.; Scholes, G. D., Nanorod heterostructures showing photoinduced charge separation. *Small* **2007,** *3*, 1633-1639.

(11) Coe, S.; Woo, W. K.; Bawendi, M.; Bulovic, V., Electroluminescence from single monolayers of nanocrystals in molecular organic devices. *Nature* **2002,** *420*, 800-803.

(12) Zhong, H.; Zhou, Y.; Yang, Y.; Yang, C.; Li, Y., Synthesis of Type II CdTe−CdSe Nanocrystal Heterostructured Multiple-Branched Rods and Their Photovoltaic Applications. *J. Phys. Chem. C.* **2007,** *111*, 6538-6543.

(13) Konstantatos, G.; Howard, I.; Fischer, A.; Hoogland, S.; Clifford, J.; Klem, E.; Levina, L.; Sargent, E. H., Ultrasensitive solution-cast quantum dot photodetectors. *Nature* **2006,** *442*, 180-183.

(14) Kim, S.; Fisher, B.; Eisler, H. J.; Bawendi, M., Type-II quantum dots: CdTe/CdSe(core/shell) and CdSe/ZnTe(core/shell) heterostructures. *Journal of the American Chemical Society* **2003,** *125*, 11466-11467.

(15) Jin, S.; Zhang, J.; Schaller, R. D.; Rajh, T.; Wiederrecht, G. P., Ultrafast Charge Separation from Highly Reductive ZnTe / CdSe Type II Quantum Dots. *J. Phys. Chem. Lett* **2012,** *3*, 2052-2058.

(16) Tvrdy, K.; Frantsuzov, P. A.; Kamat, P. V., Photoinduced electron transfer from semiconductor quantum dots to metal oxide nanoparticles. *Proceedings of the National Academy of Sciences* **2011,** *108*, 29-34.

(17) Huang, J.; Stockwell, D.; Huang, Z.; Mohler, D. L.; Lian, T., Photoinduced Ultrafast Electron Transfer from CdSe Quantum Dots to Re-bipyridyl Complexes. *Journal of the American Chemical Society* **2008,** *130*, 5632-5633.

(18) Robel, I.; Kuno, M.; Kamat, P. V., Size-Dependent Electron Injection from Excited CdSe Quantum Dots into TiO2 Nanoparticles. *Journal of the American Chemical Society* **2007,** *129*, 4136-4137.

(19) Lo, S. S.; Mirkovic, T.; Chuang, C. H.; Burda, C.; Scholes, G. D., Emergent properties resulting from type-II band alignment in semiconductor nanoheterostructures. *Advanced Materials* **2011,** *23*, 180-197.

(20) Xie, R.; Zhong, X.; Basché, T., Synthesis, characterization, and spectroscopy of type-II core/shell semiconductor nanocrystals with ZnTe cores. *Advanced Materials* **2005,** *17*, 2741-2745.

(21) Jiang, Z. J.; Kelley, D. F., Effects of inhomogeneous shell thickness in the charge transfer dynamics of ZnTe/CdSe nanocrystals. *Journal of Physical Chemistry C* **2012,** *116*, 12958-12968.

(22) Zhang, J.; Jin, S.; Fry, H. C.; Peng, S.; Shevchenko, E.; Wiederrecht, G. P.; Rajh, T., Synthesis and characterization of wurtzite ZnTe nanorods with controllable aspect ratios. *Journal of the American Chemical Society* **2011,** *133*, 15324-15327.

(23) Groeneveld, E.; van Berkum, S.; van Schooneveld, M. M.; Gloter, A.; Meeldijk, J. D.; van den Heuvel, D. J.; Gerritsen, H. C.; de Mello Donega, C., Highly Luminescent

(Zn,Cd)Te/CdSe Colloidal Heteronanowires with Tunable Electron–Hole Overlap. *Nano Letters* **2012,** *12*, 749-757.

(24) Wyckoff, R. W. G., *Crystal Structures*. Wiley: 1971; Vol. 1.

(25) Groeneveld, E.; Witteman, L.; Lefferts, M.; Ke, X.; Bals, S.; Tendeloo, G. V.; de Mello Donega, C., Tailoring ZnSe - CdSe Colloidal Quantum Dots via Cation Exchange : From Core / Shell to Alloy Nanocrystals. *ACS Nano* **2013**, 7913-7930.

(26) Mews, A.; Eychmueller, A.; Giersig, M.; Schooss, D.; Weller, H., Preparation, characterization, and photophysics of the quantum dot quantum well system cadmium sulfide/mercury sulfide/cadmium sulfide. *J. Phys. Chem.* **1994,** *98*, 934–941.

(27) Justo, Y.; Sagar, L. K.; Flamee, S.; Zhao, Q.; Vantomme, A.; Hens, Z., Less Is More. Cation Exchange and the Chemistry of the Nanocrystal Surface. *ACS Nano* **2014,** *8*, 7948-7957.

(28) Anderson, N. C.; Hendricks, M. P.; Choi, J. J.; Owen, J. S., Ligand Exchange and the Stoichiometry of Metal Chalcogenide Nanocrystals: Spectroscopic Observation of Facile Metal-Carboxylate Displacement and Binding. *Journal of the American Chemical Society* **2013,** *135*, 18536-18548.

(29) Cottrell, T., *THE STRENGTHS OF CHEMICAL BONDS*. LONDON, BUTTERWORTHS: 1954.

(30) Peng, Z. A.; Peng, X., Nearly Monodisperse and Shape-Controlled CdSe Nanocrystals via Alternative Routes: Nucleation and Growth. *Journal of the American Chemical Society* **2002,** *124*, 3343-3353.

Chapter 4. GENERALIZED SYNTHESIS OF TETRAPOD HETEROSTRUCTURES

The range of anisotropic heterostructures extends beyond linear architectures. However, anisotropic structures are typically found in the hexagonal crystal phase, with the structures of Chapter 3 standing out as an exception to this general rule. Furthermore, many of the most well studied hexagonal nanostructures in combination give type-I heterostructures while many desirable material combinations or are prone to cation exchange, thus posing a challenge to obtaining a true type-II structure. Using a seeded growth approach, tetrapod heterostructures can be obtained via anisotropic tetrapod assembly upon a cubic phase core. The profusion of cubic structures makes the more symmetrical seeds a more versatile core and starting point for heterostructure development.

4.1 INTRODUCTION

The synthesis of nanomaterials of various shapes and sizes is well established.[1-14] However, methodologies for assembling multicomponent heterostructures with independently tunable constituents are less ubiquitous. Despite it being well known that heterostructure formation is an ideal strategy to tune charge localization and enhance the function of semiconductor nanomaterials, synthetic techniques to access a broad spectrum of material combinations with independently customizable dimensions are currently underdeveloped.[15-16]

The simplest and most well-studied heterostructure is the core-shell motif.[17-21] Typically, core-shell heterostructures are composed of a spherical, quantum-confined semiconductor nanocrystal core encompassed by a second semiconductor material, evenly coating each face of

the core. This outer shell can serve as a protective layer capable of passivating surface traps and defects to enhance luminescence, or it can serve to promote charge separation by creating a thermodynamic gradient for electrons and holes.[22-29] Core-shell structures have become important luminescent materials across a spectrum of advanced technologies due to their demonstrated performance in displays, high color purity, stability, high emission efficiency, solution processability, and broad excitation range.[8, 21, 30-31] Unfortunately, the customizability of each component is limited since the core size and shell thickness are the only tunable parameters.[21, 31-33] Furthermore, while the core-shell motif is a leading architecture for enhancing light emission,[31, 34-35] this structure is a poor choice for other applications such as photocatalysis, since as the shell thickness increases, the ability to replenish charge carriers from chemical or electrochemical sources is reduced.[36-38]

Dot-in-rod heterostructures begin to address some of these challenges.[39-40] In these heterostructures, both the seed and rod components have an exposed or only thinly shelled face that is both kinetically and thermodynamically accessible. This enables more efficient quenching of charge carriers within the heterostructure after charge separation. This motif also enables tuning of the rod length as well as the location of the dot within the rod.[14, 41-42] The width of the rod, however, is set by the width of the seed with a limited number of exceptions.[41] Furthermore, the seed requires a wurtzite crystal structure to serve as a scaffold for rod elongation and many nanomaterials do not have easily accessible wurtzite crystal phases.[43-47]

Tetrapod assemblies represent a potentially versatile and tunable heterostructure configuration. One advantage of the tetrapod configuration is the customizability of the cubic-phase seed. A wide variety of nanomaterials can be synthesized in the zinc blende phase with tunable sizes to serve as cores.[48-50] In addition to controlling the size of the core, both the arm

length and width can also be modified, even independently of the core size.[16, 51-52] Furthermore, the exposed or nominally shelled core should readily enable replenishment of charge carriers. In type-II heterostructure assemblies, the arm component may also be readily accessed.

This work demonstrates a generalized synthesis of tunable tetrapod heterostructures starting from a broad range of cubic and tetragonal semiconductor core materials that serve as scaffolds for wurtzite-phase CdS arm growth. Figure 4.1 highlights the idealized band edge energies of materials used within this investigation relative to the CdS arms. Both the core size and CdS arm width and length can be tuned in this system to access a range of colloidal tetrapod heterostructures that were previously unknown.

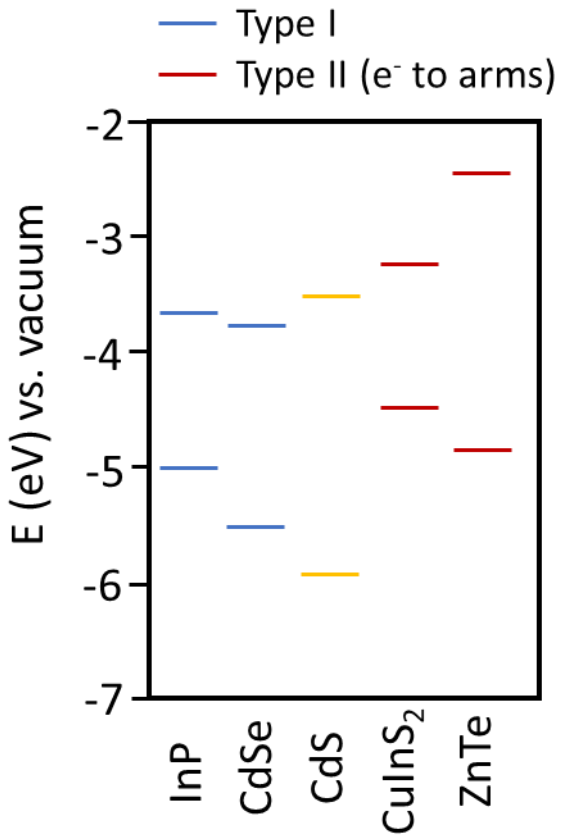

Figure 4.1. The bulk semiconductor band edge energies for each core material relative to vacuum are displayed relative to cadmium sulfide. Data for this figure was compiled from multiple sources.[53-55]

4.2 SYNTHESIS OF CADMIUM SELENIDE/CADMIUM SULFIDE

Starting with the most well studied and straightforward tetrapod heterostructure, CdSe cores with CdS arms, tetrapod heterostructures with long, highly anisotropic arms and short, relatively isotropic arms were synthesized to establish a tunable arm-growth procedure. These CdSe/CdS tetrapods were synthesized by injecting 4.0 nm zinc blende CdSe nanocrystals and trioctylphosphine sulfide (TOP-S) into a reaction mixture containing the cadmium precursor and trioctylphosphine oxide, similar to prior syntheses.[16, 56] The cadmium precursor used for CdS arm

growth is an *in situ* mixture of cadmium octadecylphosphonate and cadmium oleate. The aspect ratio of the arms is tuned by adjusting the ratio of octydecylphosphonic acid (ODPA) and oleic acid (OA) used to form the cadmium precursor – higher amounts of ODPA give thinner arms. Prior work has shown that CdS arm growth occurs along the wurtzite arm (0001) axis and growth in this direction is seeded at four of the CdSe core (111) faces. As can be seen in Figure 4.2, there is no band-edge emission from the CdS arms, and the CdSe cores seem to dominate the heterostructure's emissive properties, consistent with the assignment as a type-I heterostructure. A slight blue shift of the emission maximum is observed in the case of the long arms where more phosphonic acid is used, which may be indicative of minor etching of the CdSe seed. Conversely, a slight red shift is observed in the case of the short arms consistent with minor shelling of the CdSe seed. Figure 4.2 also highlights TEM images of the tetrapods with both long and short arms.

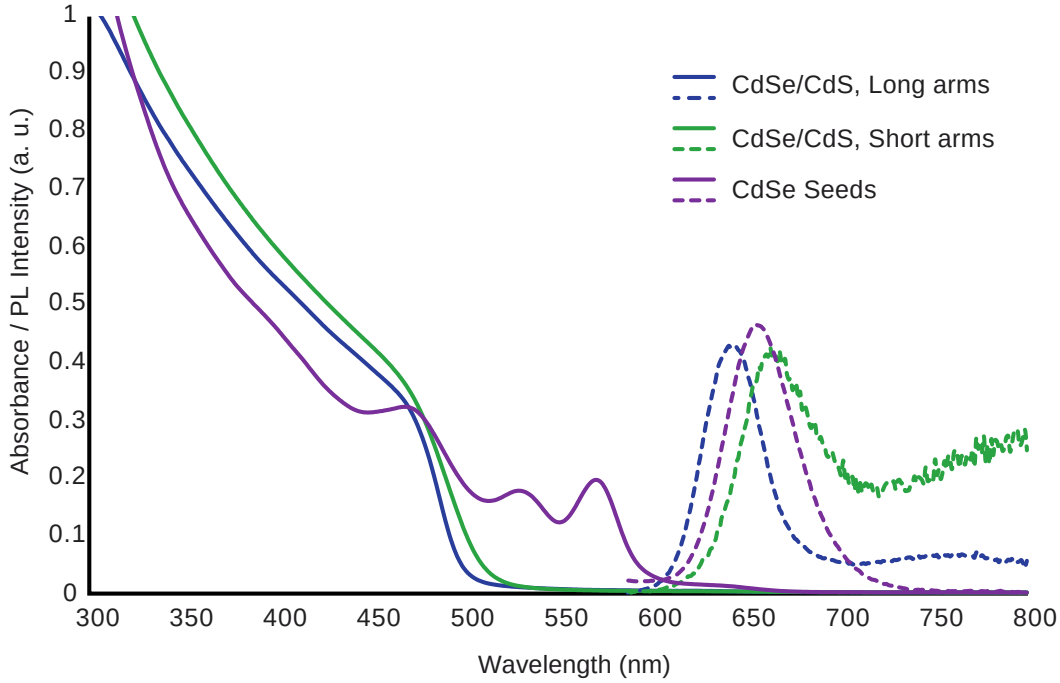

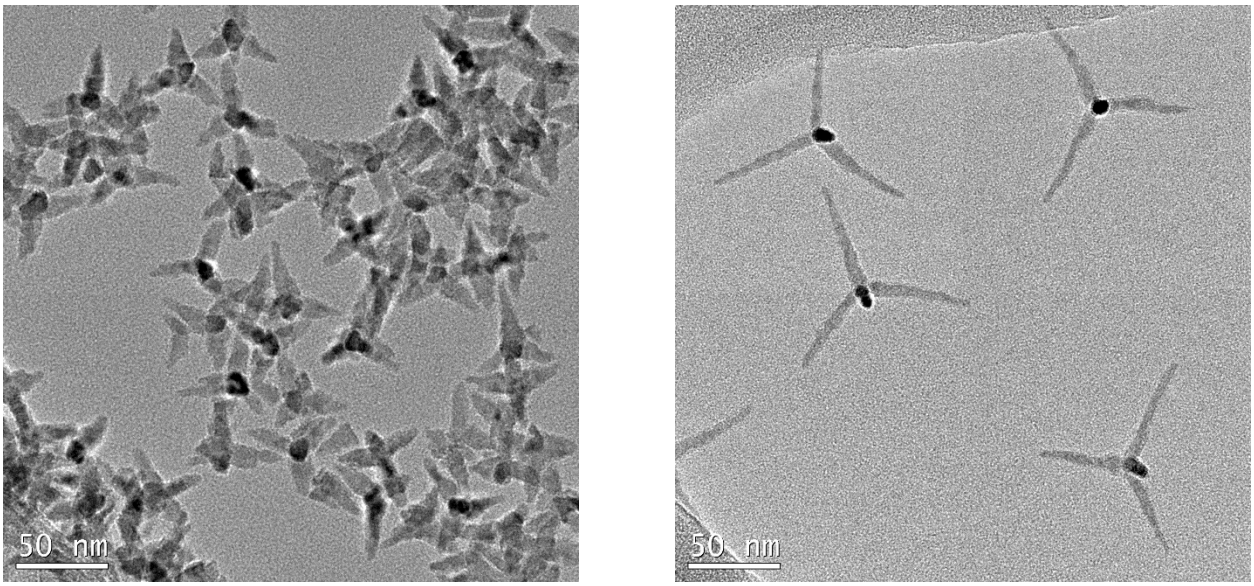

Figure 4.2. Characterization of CdSe/CdS. Absorbance and emission for CdSe/CdS (top) along with TEM of CdSe/CdS in the fat arm (left) and thin arm (right) motifs.

The starting CdSe cores are cadmium rich (~1.3:1, Cd:Se) and the resultant tetrapods, as expected, retain this cation rich property. Selenium accounts for only 0.1% of the heterostructure and due to the minority presence of the CdSe cores compared to CdS in the heterostructure, the signal from CdSe in the heterostructure is too small to be observed by XRD. Evaluation by EDS upon a single tetrapod indicates the presence of increased Se at the core, consistent with the CdSe cores serving as scaffolds for tetrapod growth.

4.3 SEEDLESS SYNTHESIS OF CADMIUM SULFIDE ARMS

Cadmium sulfide is known to exhibit wurtzite-zinc blende polytypism.[52] Given this, it was essential to evaluate tetrapod growth in the absence of seeds to confirm that the tetrapod growth is the result of the postulated seeded growth mechanism, rather than *via* independent nucleation of CdS seeds. The conditions for arm growth give CdS nanostructures that highly resemble their respective arm motifs, but the number of CdS tetrapods formed is minimal, <1% of the structures observed in the ensemble by TEM analysis. By elemental analysis using ICP-OES, the CdS nanostructures are roughly 2:1 Cd:S for both the long and fat materials respectively. As observed in Figure 4.3, the majority of the steady-state luminescence arises from trap emission with a small component from the CdS band edge.

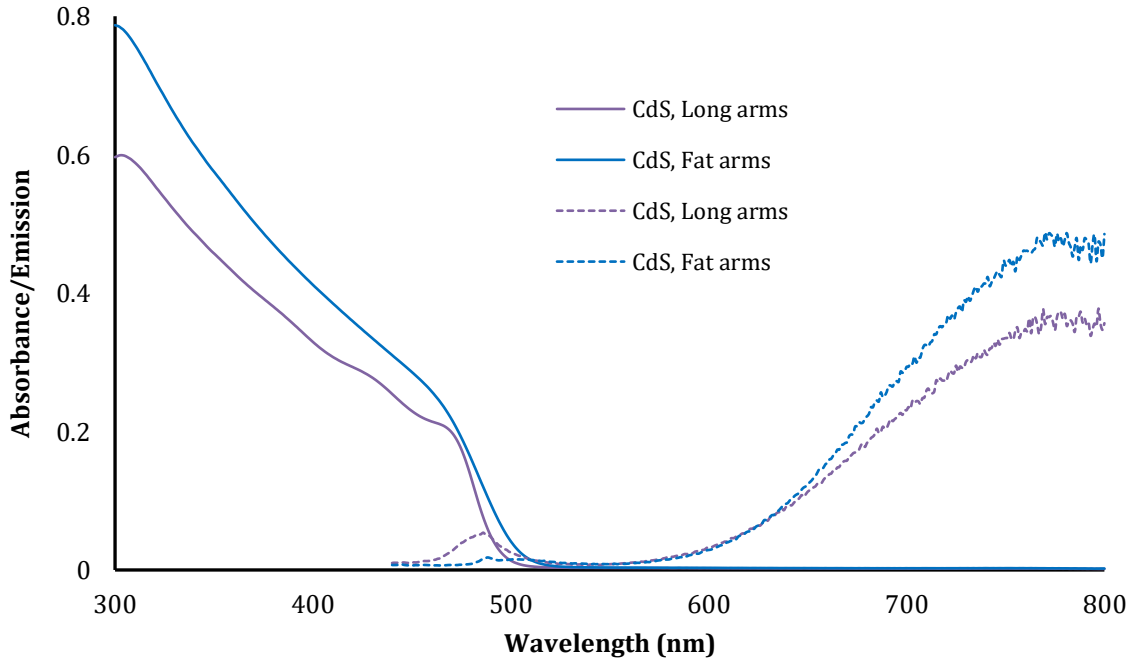

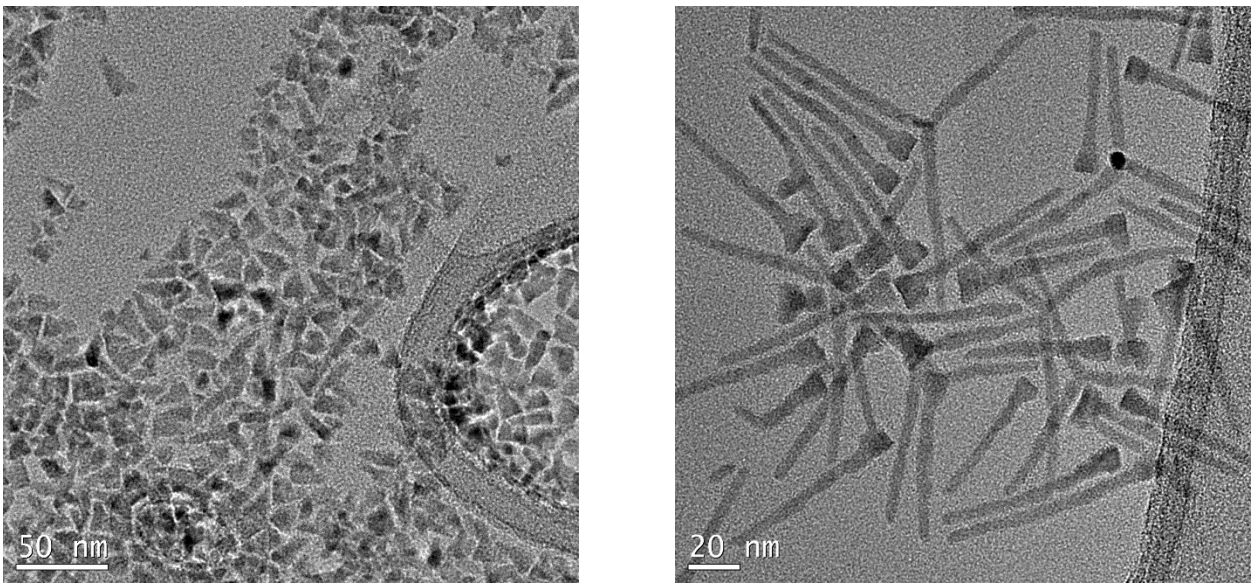

Figure 4.3. Characterization of CdS arm growth without seeds. Absorbance and emission for spectra (top) along with TEM of CdS in the fat arm (left) and thin arm (right) motifs.

4.4 Synthesis of Indium Phosphide/cadmium sulfide

Indium phosphide has been promoted as a lower-toxicity alternative to CdSe due to its similar optical properties. However, anisotropic InP has been challenging to obtain. Reports of incorporating InP into heterostructures is also uncommon due to its strong thermodynamic preference for the zinc blende crystal phase, with the hexagonal phase being only metastable.[43] This ends up being advantageous for our purposes and InP/CdS tetrapods are synthesized with moderate success (Figure 4.4). However, the small size of the 3.0 nm zinc blende cores likely provides less clearly defined and more strained planes at the surface to serve as a platform for CdS growth compared to the larger, 4.0 nm CdSe cores. Starting from 2:1, In:P cores, the final tetrapod heterostructures show a majority of cadmium and sulfur compared to only a small percentage of phosphorous (~3%) in the final tetrapod structure. Cadmium octadecylphosphonate is used as the precursor for CdS arm growth. The phosphorous content measured by ICP in other tetrapod heterostructures without phosphorous in the core and seedless CdS arms all have detectable phosphorous amounts (between 1-3%). Thus, it is challenging to distinguish between phosphorous in the core and on the arm. Indium was not observed in an elemental analysis by ICP, which may point to cation exchange whereby indium is removed and replaced by cadmium as seen previously.[57] Single particle EDS evaluation of tetrapods shows a broadened signal in the spectral region associated with cadmium and indium, especially at the core. This, coupled with a relatively stronger signal from phosphorus, suggests that there may be some remaining indium phosphide character in the core component of the heterostructure. The signal from the CdS arms by XRD overwhelms any signal from indium phosphide or cadmium phosphide, so the exact structure of the core is yet to be definitively determined. The absorption and luminescence are similar to CdS in character, as shown in Figure 4.4.

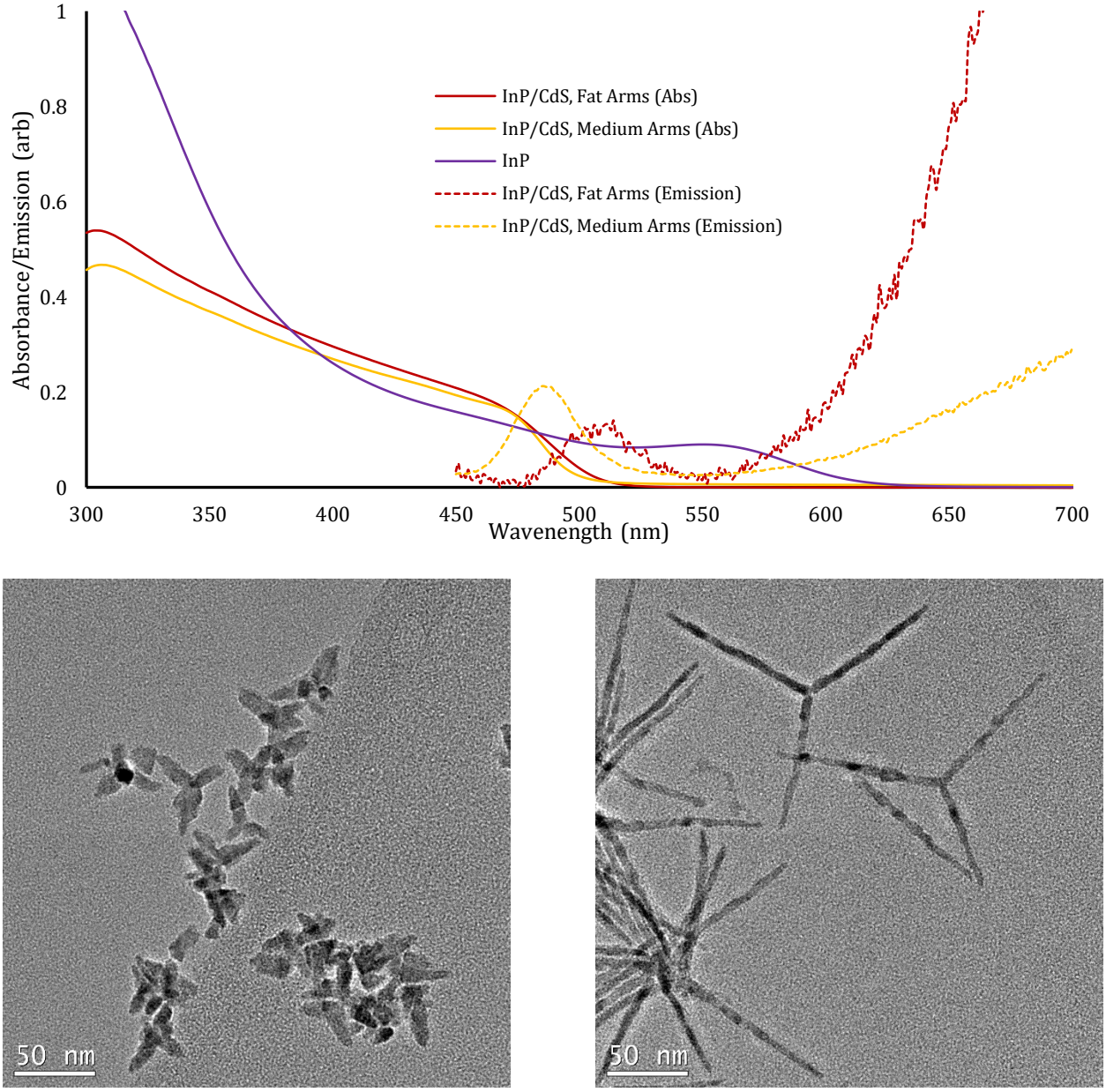

Figure 4.4. Characterization of InP/CdS. Absorbance and emission for InP/CdS (top) along with TEM of InP/CdS in the fat arm (left) and thin arm (right) motifs.

4.5 SYNTHESIS OF ZINC TELLURIDE/CADMIUM SULFIDE

We postulate that a tetrapod heterostructure may offer advantages for applications that benefit from the separation of charge carriers, such as photocatalysis, when a type-II electronic structure is achieved. Zinc telluride and copper indium sulfide (CIS) are two seed candidates with an offset band edge alignment relative to CdS. While it is known that cation exchange readily occurs in telluride lattices with a low activation energy barrier (24 kJ/mol), we hypothesized that the short arm growth duration may enable tetrapod assembly without full conversion of the ZnTe core to CdTe.[58] Indeed we observe that large ZnTe quantum dots serve as excellent scaffolds for tetrapod assembly, as can be seen Figure 4.5. The ZnTe cores are elongated dots with aspect ratios of 2 and 8 nm in length. By ICP, we can observe partial cation exchange in the final tetrapod products. Starting from 1.1:1 Zn:Te cores, this ratio of Zn:Te diminishes to 1:5 and 1:3 in the fat and long arm motifs, respectively, in the final cation-rich tetrapods. Overall, the tetrapods display a cation-rich composition with a 2:1 cation to anion ratio. Thus, over only 10 min of heterostructure growth, complete cation exchange is not observed, likely giving core/shell/arm structures of ZnTe/CdTe/CdS or more alloyed core $Zn_{1-x}Cd_xTe$/CdS heterostructures. However, no new absorbance or emission features emerge after tetrapod assembly (Figure 4.5). By EDX on a single tetrapod, weak signals from tellurium are observed as well as a small signal from zinc at the core suggesting that some ZnTe character is retained in the core of the tetrapod.

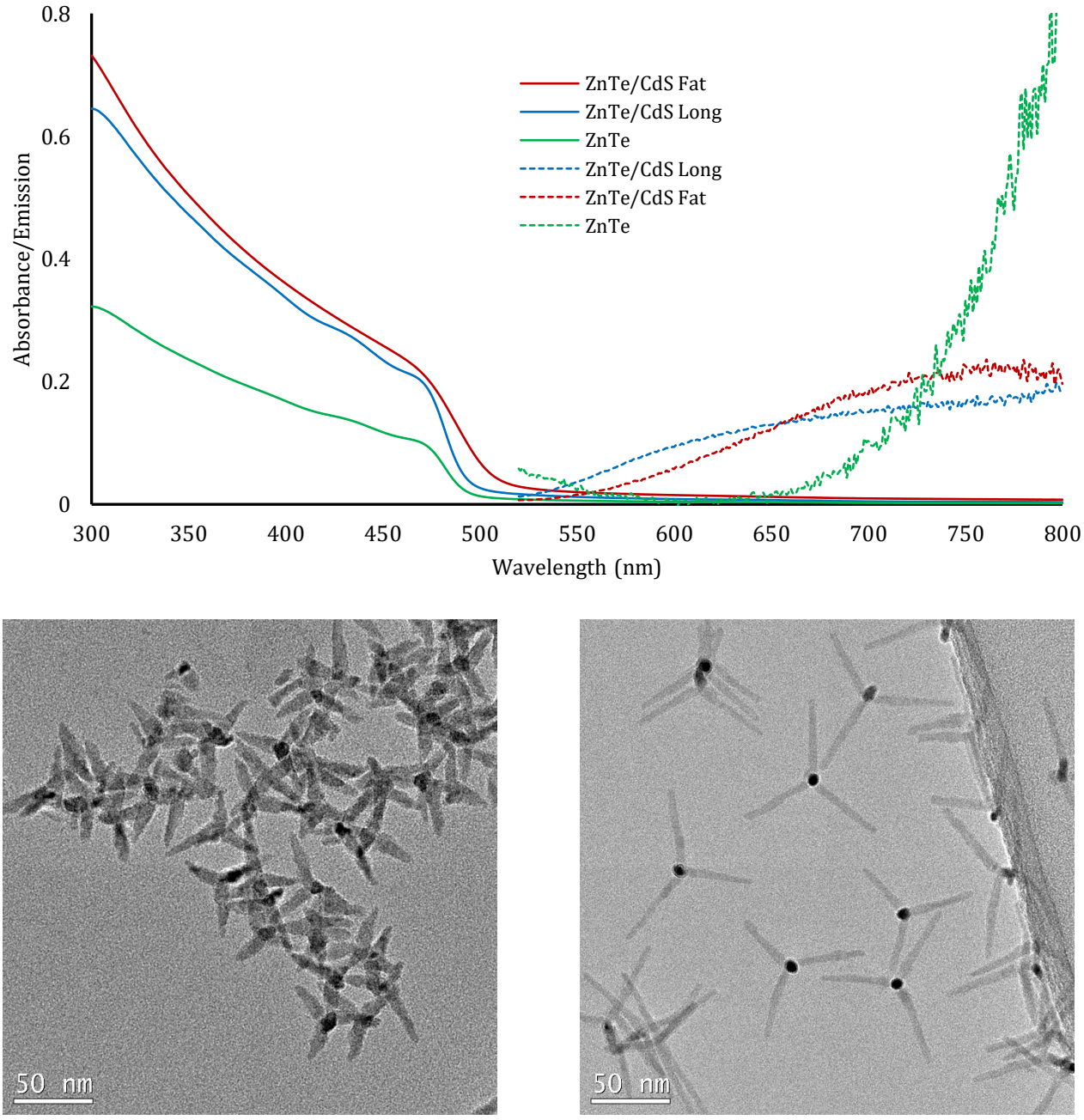

Figure 4.5. Characterization of ZnTe/CdS. Absorbance and emission for ZnTe/CdS (top) along with TEM of ZnTe/CdS in the fat arm (left) and thin arm (right) motifs.

4.6 SYNTHESIS OF COPPER INDIUM SULFIDE/CADMIUM SULFIDE

Copper indium sulfide nanoparticles have emerged as an alternative to cadmium and lead based materials due to their tunable photoluminescence across the visible and near-infrared spectrum, low toxicity, and large absorption cross section.[59-65] These attractive properties have led to the development of size tunable CIS nanocrystals. Despite sharing similar optical properties to CdSe and InP, the conduction and valence band edges of CIS are higher in energy with respect to vacuum. Thus, CIS/CdS tetrapod heterostructures exhibit a type II band configuration but unlike ZnTe, they are not known to undergo cation exchange in traditional core-shell motifs. Furthermore, CIS has a tetragonal crystal structure, not a cubic, zinc blende lattice as was possessed by the previously examined seeds. This elongated lattice enables testing the versatility of CdS arm growth by providing a distorted (111) plane as the surface for seeding wurtzite CdS arm growth. CIS/CdS tetrapod heterostructures are readily obtained when using 3 nm and 6 nm CIS cores.

The larger 6 nm cores result in more uniform and greater yields of CIS/CdS tetrapods prior to size selective precipitation. This is likely due to more well defined and less strained (111) planes in the larger CIS nanocrystal seeds. However, despite a lack of literature precedent for cation exchange in CIS, the CIS/CdS tetrapods show no presence of indium by elemental analysis with ICP. The copper content in both the long, anisotropic and shorter, more isotropic arm motifs assembled from both 3 nm and 6 nm CIS is 0.1% in a system that is 2:1 Cd:S. The starting 3 nm and 6 nm CIS cores are both slightly copper and cation rich with compositional ratios of 1.2:1.0:1.7 for Cu:In:S, similar to prior reports.[66-67] EDX of a single tetrapod shows weak signal from copper and no indium starting from the 6 nm CIS cores. Absorbance, photoluminescence, and TEM characterization of CIS cores and heterostructures with CdS arms are shown in Figures 4.6 and 4.7. The photoluminescence spectra show emission from the tetrapods is dominated by trap emission, but complete suppression of any

CdS band edge emission is also notable. This may suggest that the broadened, highly red-shifted emission may be copper rather than CdS based.[68-72]

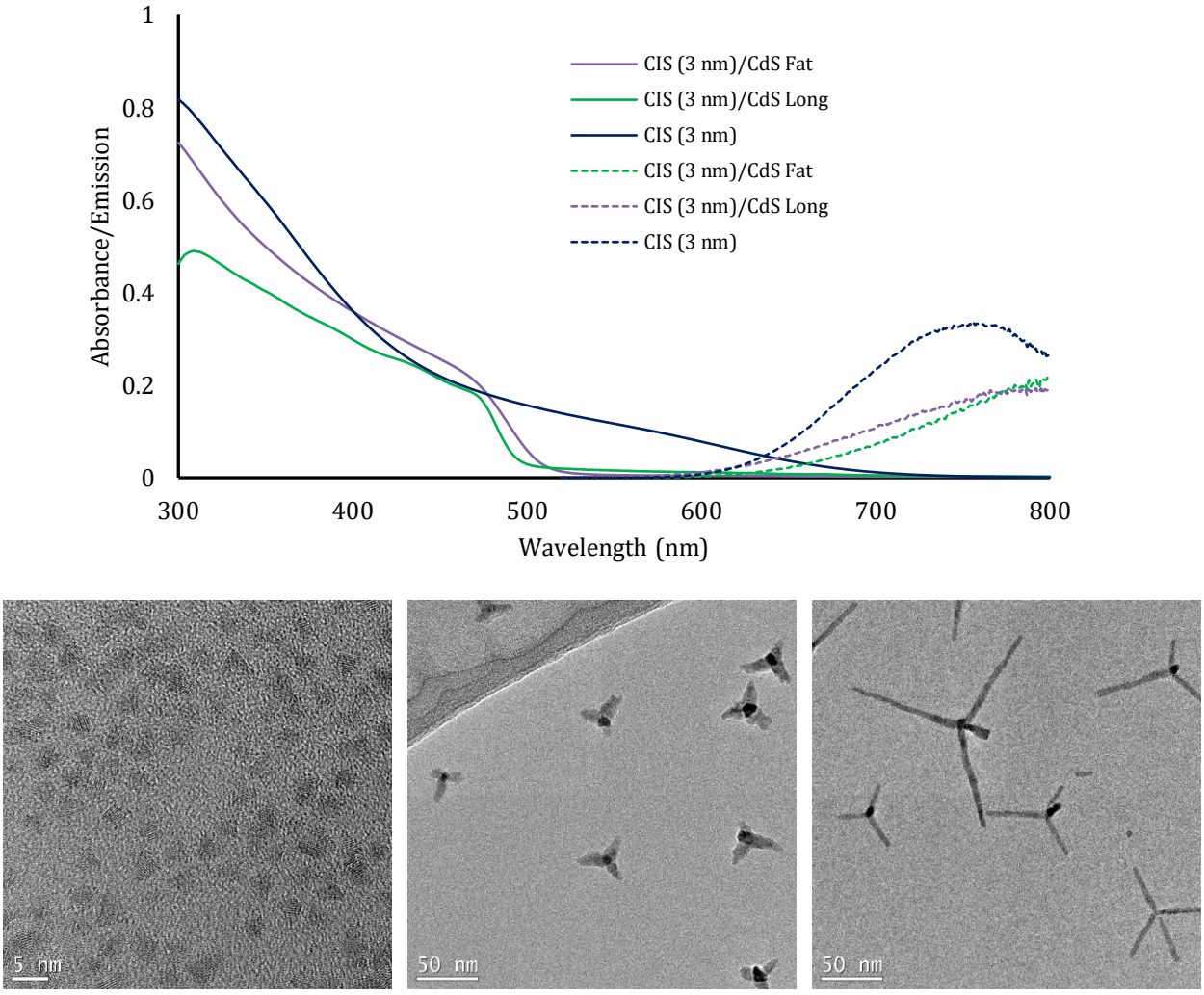

Figure 4.6. CIS (3 nm)/CdS characterization. The absorbance and fluorescence spectra (top), with TEM images of 3 nm CIS cores (left), fat CIS/CdS arm (middle), and long CIS/CdS (right) arm motifs.

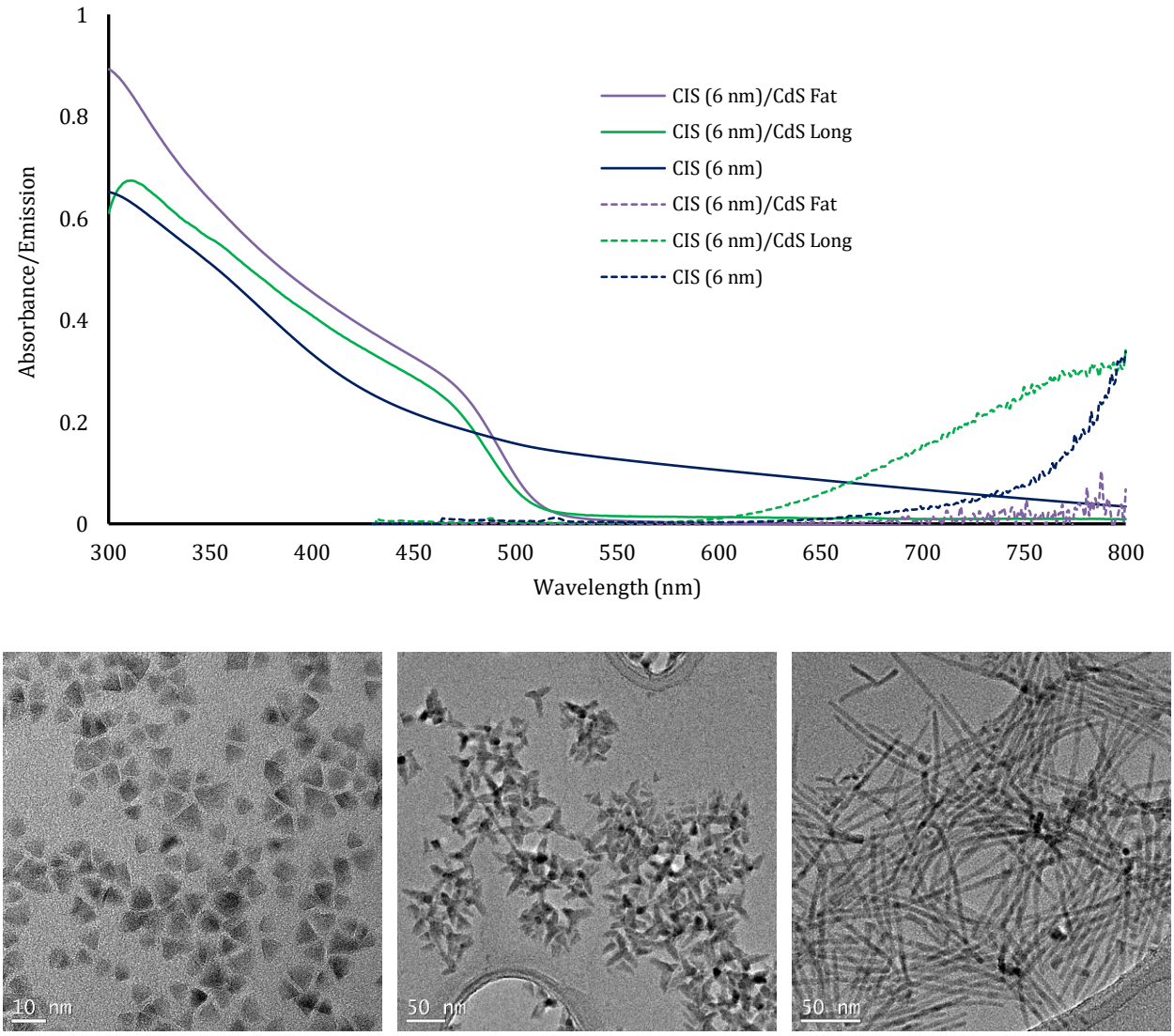

Figure 4.7. CIS (6 nm)/CdS characterization. The absorbance and fluorescence spectra (top), with TEM images of 6 nm CIS cores (left), fat CIS/CdS arm (middle), and long CIS/CdS (right) arm motifs.

4.7 CONCLUSIONS

The summation of this work demonstrates that tetrapod heterostructures with CdS arms can be assembled from a wide spectrum of shapes and sizes of zinc blende and tetragonal cores. Furthermore, both long-thin and short-fat arm motifs can be obtained in all cases. While there is substantial evidence of cation exchange at the core, the cation exchange process did not impede the growth of CdS arms to give tetrapod heterostructures. Unfortunately, definitive characterization of the exact nature and composition of the core in samples that are now likely the products of cation exchange remains a challenge. Developing strategies to impede cation exchange during arm growth will be a focus of the Cossairt lab moving forward, since this objective is central to achieving true type-II tetrapod heterostructures.

4.8 EXPERIMENTAL METHODS

4.8.1 *General Considerations*

All manipulations were carried out using standard Schlenk or glovebox techniques under dry nitrogen. Zinc acetate (99.99%), cadmium oxide (99.9%), indium acetate (99.99%), copper iodide (≥99.5%), oleic acid (OA, 90%), myristic acid (≥99%), dodecane thiol (98%), 1-octadecene (1-ODE, 90%), metallic tellurium (Te, 99.997%), selenium (99.999%), sulfur (99.5%), trioctylphosphine (TOP, 97%), and superhydride ($LiBH(CH_2CH_3)_3$) solution in THF (1 M) were all purchased from Sigma-Aldrich and used as received without further purification. Octadecylphosphonic acid (ODPA, 99%) was purchased from PCI Synthesis and used as received. Anhydrous ethanol and pentane were purchased from various sources. Trioctylphosphine oxide (TOPO, 90%) was purchased from Sigma-Aldrich and twice recrystallized from acetonitrile until

no impurities remain in ^{31}PNMR and ^{1}HNMR. Trioctylphosphine-chalcogenide solutions were prepared by dissolving sulfur, selenium, or tellurium into TOP in a glovebox.

4.8.2 *Synthesis of CdSe quantum dots*

This synthesis uses a previously reported method.[73] The selenium precursor, trioctylphosphine selenide, was prepared by dissolving 0.060 g of 100 mesh Se powder (99.999%) in 0.84 g of TOP (1.01 mL) and 4.16 mL of ODE until the solution turned completely clear. Next, the cadmium precursor was prepared by loading 0.134 g of CdO, 1.20 mL of OA, and 8.00 mL of ODE into a 50 mL three-neck flask. The flask was degassed for 30 min at room temperature before heating to 240 °C under nitrogen. After a short time, between 5-10 min, the cadmium precursor turned clear, indicating formation of cadmium oleate. Once the cadmium solution was completely clear, 5 mL of selenium precursor was added rapidly. The reaction was monitored by UV–Vis and photoluminescence spectroscopy as the solution color advances from yellow to orange to red.[74] The size of the particles was controlled by quenching the reaction (by removing the heating mantle) when the target size of the nanoparticles was achieved. Particles with a diameter of 4.0 nm were obtained after ~5 min. The nanocrystals were purified by repeat dissolution/precipitation using toluene as the solvent and precipitation with methanol. The first two precipitation steps required ethyl acetate as a cosolvent to remove ODE.

4.8.3 *Synthesis of ZnTe quantum dots*

This synthesis is modified from prior reports.[58] In a 50 mL three-neck flask, 0.26 g (1.4 mmol) of zinc acetate was mixed with 4 mL (12.7 mmol) of oleic acid and 20 mL of 1-ODE. The mixture was degassed under vacuum for at least 30 min before being heated to 200 °C under nitrogen. After 1 h, a clear solution was formed and the temperature was dropped to 160 °C. The

tellurium precursor was prepared by adding 1.6 mL of superhydride solution (0.7 M in THF) and 2 mL of oleylamine to 1.0 mL of TOP-Te (1.0 M Te in TOP). This tellurium precursor mixture was stirred for 1 h at room temperature until the solution became homogeneous before being injected rapidly into the zinc solution at 160 °C. The reaction temperature was increased to 190 °C over the course of 5 min and was maintained at 190 °C for 60 min before quenching the reaction by removing the heating mantel to cool the reaction mixture to room temperature. Excess solvent and volatile organics were removed by vacuum distillation at 180 °C. The ZnTe nanorods were separated and purified by adding ethanol to the resulting oily residue followed by centrifugation and re-dispersion into pentane. This process was repeated a minimum of five times. The resulting ZnTe oblong quantum dots have an aspect ratio of 2. Note of comparison to other procedures: other similar procedures have been used to give ZnTe nanorods with aspect ratios of 3 and higher. The present synthesis stirred the tellurium precursor for longer (at least 1 h as opposed to 20 min) and vacuum distillation was carried out at a higher temperature (180 °C as opposed to previously used 150 °C). These two procedural modifications lead to the formation of a more isotropic product.

4.8.4 *Synthesis of InP quantum dots*

Indium phosphide quantum dots were synthesized via a two-step synthetic procedure reported previously.[75] Briefly, 0.93 g (3.20 mmol) of indium acetate and 2.65 g (11.6 mmol) of myristic acid were heated under vacuum at 100 °C in a 100 mL three-neck flask for 12 h to generate indium myristate. After indium myristate was formed under vacuum, the apparatus was placed under nitrogen and 20 mL of toluene was added. This solution is was heated to 110 °C and a mixture of 465 μL of tris(trimethylsilyl)phosphine and 10 mL of toluene was quickly injected to

form indium phosphide magic size clusters (MSCs). InP MSC formation was monitored by UV-Vis until no changes were observed between extractions obtained every 10 minutes. Purification of MSCs was achieved by repeated precipitation with acetonitrile and resuspension in toluene. For storage, solvent was removed and MSCs were stored dry in an oxygen and water-free environment.

To obtain 3.0 nm InP quantum dots, 200 mg of MSCs were dissolved in 2 mL of octadecene and injected into a nitrogen purged 100 mL 3-neck round bottom flask with 38 mL of additional octadecene at 270 °C. The growth of quantum dots was tracked by UV-Vis and growth for 20 min yielded 3.0 nm InP nanoparticles. Excess octadecene was removed by vacuum distillation at 150 °C and quantum dots were purified by multiple resuspension in toluene and precipitation with ethanol.

4.8.5 *Synthesis of Copper Indium Sulfide nanoparticles*

CIS-QDs were synthesized based on recently reported methods.[67] First, 73 mg (0.25 mmol) of indium acetate, 47.5 mg (0.25 mmol) of copper iodide, and 4 mL DDT were added to a three-necked round-bottom flask fitted with a condenser column. The flask was purged with argon for 30 min and subsequently heated while stirring to 120 °C over 20 min. The solution was heated at 120 °C for an additional 10 min, until a clear yellow solution was formed. The solution was then heated to 230 °C and the solution gradually changed color from yellow to dark red. After refluxing for a set time (1-30 min), the reaction was quenched by removing the flask from heat.

4.8.6 *Synthesis of tetrapods with CdS arms*

Core/CdS tetrapod heterostructures were synthesized with modification upon prior seeded growth approaches.[16, 56] Briefly, 2.65 g of TOPO (99%), 0.05175 g of CdO, 0.5 mL oleic acid, and either 0.135 mg of ODPA (for long-thin arms) or 0.54 mg of ODPA (for short-fat arms) was degassed at 150 °C for 1.5 h

in a 50 mL three-neck round-bottom flask. The reaction mixture was heated to 350 °C under nitrogen, and the reddish-brown solution turned colorless. Separately, a stock solution of trioctylphosphine sulfide (TOP-S) was made from 70 mg of sulfur with 6 mL of TOP. 0.6 mL of TOP-S was mixed with 25 μL of the quantum dot stock solution (2.5×10^{-9} mol of dots) as determined by the optical absorbance of the quantum dot solution. Size and concentration quantification of quantum dot cores has been reported previously for CdSe,[74] ZnTe,[58] InP,[76] and CIS.[67] Upon reaching the desired injection temperature of 350 °C, 1.8 mL of TOP was added, and the temperature was allowed to recover to 350 °C before the mixture of TOP-S and quantum dots were swiftly injected. The temperature was again allowed to recover to 350 °C and the anisotropic CdS arm was grown at this temperature for 10 min. The heating mantle was removed, and the solution was cooled to room temperature. The core/CdS tetrapods were purified by repeated precipitation in ethanol and redispersion in toluene.

4.9 REFERENCES

(1) Shi, W.; Hughes, R. W.; Denholme, S. J.; Gregory, D. H., Synthesis design strategies to anisotropic chalcogenide nanostructures. *CrystEngComm* **2010,** *12*, 641-659.

(2) Burda, C.; Chen, X.; Narayanan, R.; El-Sayed, M. A., Chemistry and Properties of Nanocrystals of Different Shapes. *Chemical Reviews* **2005,** *105*, 1025-1102.

(3) Sajanlal, P. R.; Sreeprasad, T. S.; Samal, A. K.; Pradeep, T., Anisotropic nanomaterials: structure, growth, assembly, and functions. *Nano Reviews* **2011,** *2*, 5883.

(4) Peng, X.; Manna, L.; Yang, W.; Wickham, J.; Scher, E.; Kadavanich, A.; Alivisatos, A. P., Shape control of CdSe nanocrystals. *Nature* **2000,** *404*, 59-61.

(5) Peng, Z. A.; Peng, X., Nearly Monodisperse and Shape-Controlled CdSe Nanocrystals via Alternative Routes: Nucleation and Growth. *Journal of the American Chemical Society* **2002,** *124*, 3343-3353.

(6) Enright, M. J.; Cossairt, B. M., Synthesis of tailor-made colloidal semiconductor heterostructures. *Chemical Communications* **2018,** *54*, 7109-7122.

(7) Peng, X., Mechanisms for the Shape-Control and Shape-Evolution of Colloidal Semiconductor Nanocrystals. *Advanced Materials* **2003,** *15*, 459-463.

(8) Talapin, D. V.; Rogach, A. L.; Kornowski, A.; Haase, M.; Weller, H., Highly Luminescent Monodisperse CdSe and CdSe/ZnS Nanocrystals Synthesized in a Hexadecylamine−Trioctylphosphine Oxide−Trioctylphospine Mixture. *Nano Letters* **2001,** *1*, 207-211.

(9) Murray, C. B.; Norris, D. J.; Bawendi, M. G., Synthesis and characterization of nearly monodisperse CdE (E = sulfur, selenium, tellurium) semiconductor nanocrystallites. *Journal of the American Chemical Society* **1993,** *115*, 8706-8715.

(10) Peng, X.; Wickham, J.; Alivisatos, A. P., Kinetics of II-VI and III-V Colloidal Semiconductor Nanocrystal Growth: "Focusing" of Size Distributions. *Journal of the American Chemical Society* **1998,** *120*, 5343-5344.

(11) Hu, J.; Li, L.-s.; Yang, W.; Manna, L.; Wang, L.-w.; Alivisatos, A. P., Linearly Polarized Emission from Colloidal Semiconductor Quantum Rods. *Science* **2001,** *292*, 2060-2063.

(12) Tsivion, D.; Schvartzman, M.; Popovitz-Biro, R.; von Huth, P.; Joselevich, E., Guided Growth of Millimeter-Long Horizontal Nanowires with Controlled Orientations. *Science* **2011,** *333*, 1003-1007.

(13) Manna, L.; Scher, E. C.; Alivisatos, A. P., Synthesis of Soluble and Processable Rod-, Arrow-, Teardrop-, and Tetrapod-Shaped CdSe Nanocrystals. *Journal of the American Chemical Society* **2000,** *122*, 12700-12706.

(14) Enright, M. J.; Sarsito, H.; Cossairt, B. M., Kinetically controlled assembly of cadmium chalcogenide nanorods and nanorod heterostructures. *Materials Chemistry Frontiers* **2018,** *2*, 1296-1305.

(15) Talapin, D. V.; Nelson, J. H.; Shevchenko, E. V.; Aloni, S.; Sadtler, B.; Alivisatos, A. P., Seeded Growth of Highly Luminescent CdSe/CdS Nanoheterostructures with Rod and Tetrapod Morphologies. *Nano Letters* **2007,** *7*, 2951-2959.

(16) Mishra, N.; Wu, W.-Y.; Srinivasan, B. M.; Hariharaputran, R.; Zhang, Y.-W.; Chan, Y., Continuous Shape Tuning of Nanotetrapods: Toward Shape-Mediated Self-Assembly. *Chemistry of Materials* **2016,** *28*, 1187-1195.

(17) Ghosh Chaudhuri, R.; Paria, S., Core/Shell Nanoparticles: Classes, Properties, Synthesis Mechanisms, Characterization, and Applications. *Chemical Reviews* **2012,** *112*, 2373-2433.

(18) Gawande, M. B.; Goswami, A.; Asefa, T.; Guo, H.; Biradar, A. V.; Peng, D.-L.; Zboril, R.; Varma, R. S., Core–shell nanoparticles: synthesis and applications in catalysis and electrocatalysis. *Chemical Society Reviews* **2015,** *44*, 7540-7590.

(19) Kortan, A. R.; Hull, R.; Opila, R. L.; Bawendi, M. G.; Steigerwald, M. L.; Carroll, P. J.; Brus, L. E., Nucleation and Growth of CdSe on ZnS Quantum Crystallite Seeds, and Vice Versa, in Inverse Micelle Media. *Journal of the American Chemical Society* **1990,** *112*, 1327-1332.

(20) Hines, M. A.; Guyot-Sionnest, P., Synthesis and Characterization of Strongly Luminescing ZnS-Capped CdSe Nanocrystals. *The Journal of Physical Chemistry* **1996,** *100*, 468-471.

(21) Dabbousi, B. O.; Rodriguez-Viejo, J.; Mikulec, F. V.; Heine, J. R.; Mattoussi, H.; Ober, R.; Jensen, K. F.; Bawendi, M. G., (CdSe)ZnS Core−Shell Quantum Dots: Synthesis and

Characterization of a Size Series of Highly Luminescent Nanocrystallites. *The Journal of Physical Chemistry B* **1997,** *101*, 9463-9475.

(22) Nandan, Y.; Mehata, M. S., Wavefunction Engineering of Type-I/Type-II Excitons of CdSe/CdS Core-Shell Quantum Dots. *Scientific Reports* **2019,** *9*, 2.

(23) Jiao, S.; Shen, Q.; Mora-Seró, I.; Wang, J.; Pan, Z.; Zhao, K.; Kuga, Y.; Zhong, X.; Bisquert, J., Band Engineering in Core/Shell ZnTe/CdSe for Photovoltage and Efficiency Enhancement in Exciplex Quantum Dot Sensitized Solar Cells. *ACS Nano* **2015,** *9*, 908-915.

(24) Wang, J.; Mora-Seró, I.; Pan, Z.; Zhao, K.; Zhang, H.; Feng, Y.; Yang, G.; Zhong, X.; Bisquert, J., Core/Shell Colloidal Quantum Dot Exciplex States for the Development of Highly Efficient Quantum-Dot-Sensitized Solar Cells. *Journal of the American Chemical Society* **2013,** *135*, 15913-15922.

(25) Kim, S.; Fisher, B.; Eisler, H.-J.; Bawendi, M., Type-II Quantum Dots: CdTe/CdSe(Core/Shell) and CdSe/ZnTe(Core/Shell) Heterostructures. *Journal of the American Chemical Society* **2003,** *125*, 11466-11467.

(26) Zhong, H.; Zhou, Y.; Yang, Y.; Yang, C.; Li, Y., Synthesis of Type II CdTe−CdSe Nanocrystal Heterostructured Multiple-Branched Rods and Their Photovoltaic Applications. *The Journal of Physical Chemistry C* **2007,** *111*, 6538-6543.

(27) Scholes, G. D.; Jones, M.; Kumar, S., Energetics of Photoinduced Electron-Transfer Reactions Decided by Quantum Confinement. *The Journal of Physical Chemistry C* **2007,** *111*, 13777-13785.

(28) Zhu, H.; Song, N.; Lian, T., Wave Function Engineering for Ultrafast Charge Separation and Slow Charge Recombination in Type II Core/Shell Quantum Dots. *Journal of the American Chemical Society* **2011,** *133*, 8762-8771.

(29) Lo, S. S.; Mirkovic, T.; Chuang, C.-H.; Burda, C.; Scholes, G. D., Emergent Properties Resulting from Type-II Band Alignment in Semiconductor Nanoheterostructures. *Advanced Materials* **2011,** *23*, 180-197.

(30) Mekis, I.; Talapin, D. V.; Kornowski, A.; Haase, M.; Weller, H., One-Pot Synthesis of Highly Luminescent CdSe/CdS Core−Shell Nanocrystals via Organometallic and "Greener" Chemical Approaches. *The Journal of Physical Chemistry B* **2003,** *107*, 7454-7462.

(31) Peng, X.; Schlamp, M. C.; Kadavanich, A. V.; Alivisatos, A. P., Epitaxial Growth of Highly Luminescent CdSe/CdS Core/Shell Nanocrystals with Photostability and Electronic Accessibility. *Journal of the American Chemical Society* **1997,** *119*, 7019-7029.

(32) Chen, Y.; Vela, J.; Htoon, H.; Casson, J. L.; Werder, D. J.; Bussian, D. A.; Klimov, V. I.; Hollingsworth, J. A., "Giant" Multishell CdSe Nanocrystal Quantum Dots with Suppressed Blinking. *Journal of the American Chemical Society* **2008,** *130*, 5026-5027.

(33) Pal, B. N.; Ghosh, Y.; Brovelli, S.; Laocharoensuk, R.; Klimov, V. I.; Hollingsworth, J. A.; Htoon, H., 'Giant' CdSe/CdS Core/Shell Nanocrystal Quantum Dots As Efficient Electroluminescent Materials: Strong Influence of Shell Thickness on Light-Emitting Diode Performance. *Nano Letters* **2012,** *12*, 331-336.

(34) Cragg, G. E.; Efros, A. L., Suppression of Auger Processes in Confined Structures. *Nano Letters* **2010,** *10*, 313-317.

(35) Saha, A.; Chellappan, K. V.; Narayan, K. S.; Ghatak, J.; Datta, R.; Viswanatha, R., Near-Unity Quantum Yield in Semiconducting Nanostructures: Structural Understanding

Leading to Energy Efficient Applications. *The Journal of Physical Chemistry Letters* **2013,** *4*, 3544-3549.

(36) Purcell-Milton, F.; Visheratina, A. K.; Kuznetsova, V. A.; Ryan, A.; Orlova, A. O.; Gun'ko, Y. K., Impact of Shell Thickness on Photoluminescence and Optical Activity in Chiral CdSe/CdS Core/Shell Quantum Dots. *ACS Nano* **2017,** *11*, 9207-9214.

(37) Jiang, Z.-J.; Kelley, D. F., Effects of Inhomogeneous Shell Thickness in the Charge Transfer Dynamics of ZnTe/CdSe Nanocrystals. *The Journal of Physical Chemistry C* **2012,** *116*, 12958-12968.

(38) Kong, D.; Jia, Y.; Ren, Y.; Xie, Z.; Wu, K.; Lian, T., Shell-Thickness-Dependent Biexciton Lifetime in Type I and Quasi-Type II CdSe@CdS Core/Shell Quantum Dots. *The Journal of Physical Chemistry C* **2018,** *122*, 14091-14098.

(39) Zhu, H.; Song, N.; Lv, H.; Hill, C. L.; Lian, T., Near Unity Quantum Yield of Light-Driven Redox Mediator Reduction and Efficient H2 Generation Using Colloidal Nanorod Heterostructures. *Journal of the American Chemical Society* **2012,** *134*, 11701-11708.

(40) Amirav, L.; Alivisatos, A. P., Photocatalytic Hydrogen Production with Tunable Nanorod Heterostructures. *The Journal of Physical Chemistry Letters* **2010,** *1*, 1051-1054.

(41) Kim, D.; Lee, Y. K.; Lee, D.; Kim, W. D.; Bae, W. K.; Lee, D. C., Colloidal Dual-Diameter and Core-Position-Controlled Core/Shell Cadmium Chalcogenide Nanorods. *ACS Nano* **2017,** *11*, 12461-12472.

(42) Wu, K.; Hill, L. J.; Chen, J.; McBride, J. R.; Pavlopolous, N. G.; Richey, N. E.; Pyun, J.; Lian, T., Universal Length Dependence of Rod-to-Seed Exciton Localization Efficiency in Type I and Quasi-Type II CdSe@CdS Nanorods. *ACS Nano* **2015,** *9*, 4591-4599.

(43) De Trizio, L.; Gaspari, R.; Bertoni, G.; Kriegel, I.; Moretti, L.; Scotognella, F.; Maserati, L.; Zhang, Y.; Messina, G. C.; Prato, M.; Marras, S.; Cavalli, A.; Manna, L., Cu3-xP Nanocrystals as a Material Platform for Near-Infrared Plasmonics and Cation Exchange Reactions. *Chemistry of Materials* **2015,** *27*, 1120-1128.

(44) De Luca, M.; Zilli, A.; Fonseka, H. A.; Mokkapati, S.; Miriametro, A.; Tan, H. H.; Smith, L. M.; Jagadish, C.; Capizzi, M.; Polimeni, A., Polarized Light Absorption in Wurtzite InP Nanowire Ensembles. *Nano Letters* **2015,** *15*, 998-1005.

(45) De, A.; Pryor, C. E., Predicted band structures of III-V semiconductors in the wurtzite phase. *Physical Review B* **2010,** *81*, 155210.

(46) Dacal, L. C. O.; Cantarero, A., Ab initio electronic band structure calculation of InP in the wurtzite phase. *Solid State Communications* **2011,** *151*, 781-784.

(47) Murayama, M.; Nakayama, T., Chemical trend of band offsets at wurtzite/zinc-blende heterocrystalline semiconductor interfaces. *Physical Review B* **1994,** *49*, 4710-4724.

(48) Mohamed, M. B.; Tonti, D.; Al-Salman, A.; Chemseddine, A.; Chergui, M., Synthesis of High Quality Zinc Blende CdSe Nanocrystals. *The Journal of Physical Chemistry B* **2005,** *109*, 10533-10537.

(49) Lincheneau, C.; Amelia, M.; Oszajca, M.; Boccia, A.; D'Orazi, F.; Madrigale, M.; Zanoni, R.; Mazzaro, R.; Ortolani, L.; Morandi, V.; Silvi, S.; Szaciłowski, K.; Credi, A., Synthesis and properties of ZnTe and ZnTe/ZnS core/shell semiconductor nanocrystals. *Journal of Materials Chemistry C* **2014,** *2*, 2877-2886.

(50) Micic, O. I.; Curtis, C. J.; Jones, K. M.; Sprague, J. R.; Nozik, A. J., Synthesis and Characterization of InP Quantum Dots. *The Journal of Physical Chemistry* **1994,** *98*, 4966-4969.

(51) Li, L.-s.; Hu, J.; Yang, W.; Alivisatos, A. P., Band Gap Variation of Size- and Shape-Controlled Colloidal CdSe Quantum Rods. *Nano Letters* **2001,** *1*, 349-351.

(52) Manna, L.; Milliron, D. J.; Meisel, A.; Scher, E. C.; Alivisatos, A. P., Controlled growth of tetrapod-branched inorganic nanocrystals. *Nature Materials* **2003,** *2*, 382-385.

(53) Tran, P. D.; Wong, L. H.; Barber, J.; Loo, J. S. C., Recent advances in hybrid photocatalysts for solar fuel production. *Energy & Environmental Science* **2012,** *5*, 5902-5918.

(54) Reiss, P.; Protière, M.; Li, L., Core/Shell Semiconductor Nanocrystals. *Small* **2009,** *5*, 154-168.

(55) Kroupa, D. M.; Vörös, M.; Brawand, N. P.; McNichols, B. W.; Miller, E. M.; Gu, J.; Nozik, A. J.; Sellinger, A.; Galli, G.; Beard, M. C., Tuning colloidal quantum dot band edge positions through solution-phase surface chemistry modification. *Nature Communications* **2017,** *8*, 15257.

(56) Mishra, N.; Lian, J.; Chakrabortty, S.; Lin, M.; Chan, Y., Unusual Selectivity of Metal Deposition on Tapered Semiconductor Nanostructures. *Chemistry of Materials* **2012,** *24*, 2040-2046.

(57) Stein, J. L.; Steimle, M. I.; Terban, M. W.; Petrone, A.; Billinge, S. J. L.; Li, X.; Cossairt, B. M., Cation Exchange Induced Transformation of InP Magic-Sized Clusters. *Chemistry of Materials* **2017,** *29*, 7984-7992.

(58) Enright, M. J.; Sarsito, H.; Cossairt, B. M., Quantifying Cation Exchange of Cd2+ in ZnTe: A Challenge for Accessing Type II Heterostructures. *Chemistry of Materials* **2017,** *29*, 666-672.

(59) Berends, A. C.; van der Stam, W.; Hofmann, J. P.; Bladt, E.; Meeldijk, J. D.; Bals, S.; de Mello Donega, C., Interplay between Surface Chemistry, Precursor Reactivity, and

Temperature Determines Outcome of ZnS Shelling Reactions on CuInS2 Nanocrystals. *Chemistry of Materials* **2018,** *30*, 2400-2413.

(60) van der Stam, W.; Berends, A. C.; de Mello Donega, C., Prospects of Colloidal Copper Chalcogenide Nanocrystals. *ChemPhysChem* **2016,** *17*, 559-581.

(61) Xia, C.; Meeldijk, J. D.; Gerritsen, H. C.; de Mello Donega, C., Highly Luminescent Water-Dispersible NIR-Emitting Wurtzite CuInS2/ZnS Core/Shell Colloidal Quantum Dots. *Chemistry of Materials* **2017,** *29*, 4940-4951.

(62) Kolny-Olesiak, J.; Weller, H., Synthesis and Application of Colloidal CuInS2 Semiconductor Nanocrystals. *ACS Applied Materials & Interfaces* **2013,** *5*, 12221-12237.

(63) Sandroni, M.; Wegner, K. D.; Aldakov, D.; Reiss, P., Prospects of Chalcopyrite-Type Nanocrystals for Energy Applications. *ACS Energy Letters* **2017,** *2*, 1076-1088.

(64) Leach, A. D. P.; Macdonald, J. E., Optoelectronic Properties of CuInS2 Nanocrystals and Their Origin. *The Journal of Physical Chemistry Letters* **2016,** *7*, 572-583.

(65) Deng, D.; Chen, Y.; Cao, J.; Tian, J.; Qian, Z.; Achilefu, S.; Gu, Y., High-Quality CuInS2/ZnS Quantum Dots for In vitro and In vivo Bioimaging. *Chemistry of Materials* **2012,** *24*, 3029-3037.

(66) Zhong, H.; Zhou, Y.; Ye, M.; He, Y.; Ye, J.; He, C.; Yang, C.; Li, Y., Controlled Synthesis and Optical Properties of Colloidal Ternary Chalcogenide CuInS2 Nanocrystals. *Chemistry of Materials* **2008,** *20*, 6434-6443.

(67) Booth, M.; Brown, A. P.; Evans, S. D.; Critchley, K., Determining the Concentration of CuInS2 Quantum Dots from the Size-Dependent Molar Extinction Coefficient. *Chemistry of Materials* **2012,** *24*, 2064-2070.

(68) Whitham, P. J.; Knowles, K. E.; Reid, P. J.; Gamelin, D. R., Photoluminescence Blinking and Reversible Electron Trapping in Copper-Doped CdSe Nanocrystals. *Nano Letters* **2015,** *15*, 4045-4051.

(69) Nelson, H. D.; Li, X.; Gamelin, D. R., Computational Studies of the Electronic Structures of Copper-Doped CdSe Nanocrystals: Oxidation States, Jahn–Teller Distortions, Vibronic Bandshapes, and Singlet–Triplet Splittings. *The Journal of Physical Chemistry C* **2016,** *120*, 5714-5723.

(70) Knowles, K. E.; Hartstein, K. H.; Kilburn, T. B.; Marchioro, A.; Nelson, H. D.; Whitham, P. J.; Gamelin, D. R., Luminescent Colloidal Semiconductor Nanocrystals Containing Copper: Synthesis, Photophysics, and Applications. *Chemical Reviews* **2016,** *116*, 10820-10851.

(71) Knowles, K. E.; Nelson, H. D.; Kilburn, T. B.; Gamelin, D. R., Singlet–Triplet Splittings in the Luminescent Excited States of Colloidal Cu+:CdSe, Cu+:InP, and CuInS2 Nanocrystals: Charge-Transfer Configurations and Self-Trapped Excitons. *Journal of the American Chemical Society* **2015,** *137*, 13138-13147.

(72) Marchioro, A.; Whitham, P. J.; Knowles, K. E.; Kilburn, T. B.; Reid, P. J.; Gamelin, D. R., Tunneling in the Delayed Luminescence of Colloidal CdSe, Cu+-Doped CdSe, and CuInS2 Semiconductor Nanocrystals and Relationship to Blinking. *The Journal of Physical Chemistry C* **2016,** *120*, 27040-27049.

(73) Enright, M. J.; Gilbert-Bass, K.; Sarsito, H.; Cossairt, B. M., Photolytic C–O Bond Cleavage with Quantum Dots. *Chemistry of Materials* **2019,** *31*, 2677-2682.

(74) Jasieniak, J.; Smith, L.; van Embden, J.; Mulvaney, P.; Califano, M., Re-examination of the Size-Dependent Absorption Properties of CdSe Quantum Dots. *The Journal of Physical Chemistry C* **2009,** *113*, 19468-19474.

(75) Gary, D. C.; Terban, M. W.; Billinge, S. J. L.; Cossairt, B. M., Two-Step Nucleation and Growth of InP Quantum Dots via Magic-Sized Cluster Intermediates. *Chemistry of Materials* **2015,** *27*, 1432-1441.

(76) Xie, L.; Shen, Y.; Franke, D.; Sebastián, V.; Bawendi, M. G.; Jensen, K. F., Characterization of Indium Phosphide Quantum Dot Growth Intermediates Using MALDI-TOF Mass Spectrometry. *Journal of the American Chemical Society* **2016,** *138*, 13469-13472.

Chapter 5. PHOTOCATALYTIC C-O BOND CLEAVAGE

The majority of recent nanomaterial driven photocatalysis work has focused on the hydrogen and oxygen evolution reactions with hydrogen generation as an inexpensive method of generating a clean, renewable, and energy dense fuel serving as a primary goal for the scientific community. However, nanomaterials are capable of much more than hydrogen evolution. While hydrogen evolution is a valuable process for replacing non-renewable fuel sources, there remain a wealth of untapped photocatalytic reactions that can benefit from using nanomaterials as catalysis. Utilization of biomass as an inexpensive, renewable, and abundant chemical feedstock holds the potential to replace other chemical processes that require petroleum-based precursors. In Chapter 5, quantum dots are used for the first time to catalyze carbon-oxygen bond cleavage in substrates that resemble components of lignin in biomass to simulate selective breaking of C-O linkers that occur regularly within the greater biopolymer framework. Aromatic chemical feedstocks are often obtained from crude oil but the success of quantum dots mediated C-O bond cleavage in lignin model substrates opens the door to harvesting these high value aromatic species directly from biomass.

5.1 INTRODUCTION

Photocatalysis has re-emerged at the forefront of synthetic methodology development as a powerful means of activating a wide range of bond-making and bond-breaking transformations in

organic chemistry. In particular, photoredox catalysis has experienced a recent expansion beyond the traditional area of solar fuels into the realm of organic synthesis.[1] Although metal polypyridyl complexes and organic dyes have dominated photoredox platform development, quantum dots have recently emerged as excellent candidates for coupling light and organic synthesis.[1-5] Quantum dots are excellent candidate photocatalysts because of their high photostability, large extinction coefficients (10^5–10^6 L/mol·cm), tunable optoelectrical properties, and customizable surface chemistry. For these reasons, quantum dots have been used extensively as photocatalysts in hydrogen evolution and related solar fuel applications.[6-14] However, they remain relatively limited with respect to exploration across the vast landscape of light-catalyzed reactions.[4, 15-19]

One such untapped application is biomass conversion. Biomass is a globally abundant, renewable carbon source and is widely considered the most sustainable carbon alternative to petroleum.[20-21] A primary component of dry plant matter (lignocellulosic biomass) is lignin, an amorphous polymer that lends structural integrity to plants. Lignin accounts for 15–35% of the mass of plant matter but 40% of the energy content. Furthermore, lignin accounts for 30% of non-fossil organic carbon and is the only major biopolymer heavily composed of aromatic groups that could serve as an ideal renewable source of high-value aromatic commodity chemicals (such as coumaryl, coniferyl, and sinapyl alcohols) if these high-value units could be apportioned from the parent structure.[22-23]

A variety of approaches have been explored to isolate these high-value components by targeting cleavage of the abundant β-O-4 linkages, which account for 45–60% of all linkages in the complex lignin polymer backbone.[24-25] Cleavage of C_α–O bonds has been successfully accomplished via reductive, oxidative, and redox-neutral pathways for both model substrates and in larger lignin bioframeworks.[26-35] However, these processes often require an over pressure of

hydrogen, temperatures of 80 °C, or expensive transition-metal catalysts. One series of studies of notable interest uses a visible light absorbing iridium catalyst, $[Ir(ppy)_2(dtbbpy)]PF_6$, to selectively drive the C–O bond cleavage at ambient temperature and pressure.[26, 35-37] It is important to note that the β-O-4 linkages are composed of benzylic alcohols in native lignin, as can be seen in Figure 5.1. Lignin depolymerization often first requires oxidation of benzylic alcohols prior to photochemical reduction, thereby requiring a multistep route to depolymerization products that involves purification, filtration, and solvent transfer between each step.[26, 38-39]

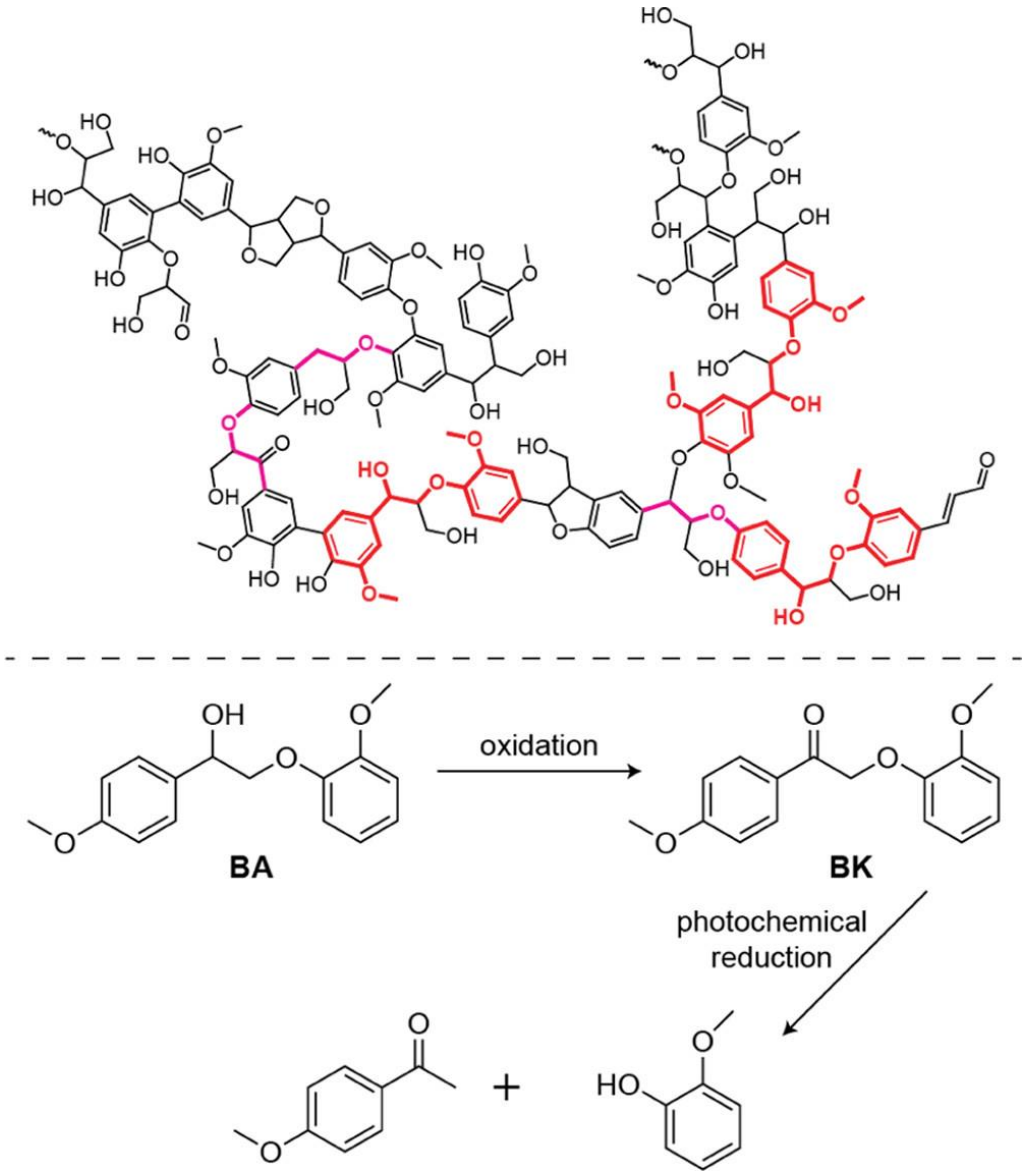

Figure 5.1. Lignin molecular structure and general scheme for β-O-4 bond cleavage. (Top) Molecular structure of lignin from a spruce tree[40] with highlighted examples of model benzylic alcohol substrates explored in this study (red) embedded in the biopolymer backbone and other β-O-4 linkages (pink) indicated. Soft woods, such as spruce, typically have a lower content of β-O-4 linkages than other plant matter. (Bottom) General scheme of oxidation and photochemical reduction of a lignin model substrate from benzylic alcohol (**BA**) to guaiacol and 4′-methoxyacetophenone via a benzylic ketone (**BK**) intermediate.

As reaction conditions are developed for improved biomass degradation, it is important to consider quantum dots as viable photoredox catalysts for these processes. In comparison to molecular light harvesters and traditional transition-metal-based photocatalysts, quantum dots have demonstrated longer-lived excited states, greater photostability, increased photon absorbance per molecule, and broader absorption spectra.[41-42] Furthermore, both the electronic properties and redox potentials of quantum dots can be finely tuned by modifying the size and surface chemistry of the nanocrystal.[43] Moreover, the increased surface area of a quantum dot when compared to a molecular catalyst would translate to an increased probability of catalyst–substrate encounters, thereby enhancing charge transfer and turnover rate. Quantum dots have been used previously in combination with lignocellulose, which served as an electron reservoir for hydrogen evolution in acidic media.[44]

In this work, the versatility of quantum dots as photocatalysts in C_α–O bond cleavage using lignin model substrates is demonstrated. Compared to the best transition-metal-based molecular catalysts for these applications, quantum dots demonstrated improved turnover frequency with lower catalyst loading across several common organic solvents. Furthermore, when using quantum dots as photocatalysts, lignin model substrates, such as 2-(2-methoxyphenoxy)-1-(4-methoxyphenyl)ethanol (**BA**), could be taken from benzylic alcohols to cleavage products, 4′-methoxyacetophenone and guaiacol, in a single vessel without any purification, isolation, filtration, or solvent exchange required. This improved performance is observed for both cadmium selenide quantum dots (CdSe QDs) with native, long-chain oleate or phosphonate ligands in dichloromethane (DCM), or following ligand exchange in acetonitrile.

5.2 PHOTOLYTIC C-O BOND CLEAVAGE WITH QUANTUM DOTS

Stephenson and co-workers report an iridium catalyst capable of C_{α}–O bond cleavage across a set of lignin model substrates at room temperature within a single day.[26] Most notably, they report nearly 90% conversion of 2-(2-methoxyphenoxy)-1-(4-methoxyphenyl)ethenone (**BK**), to 4′-methoxyacetophenone and guaiacol within 12 h with 1 mol % catalyst using formic acid as a proton donor and diisopropylethylamine as a hole quencher. This catalytic process was successfully reproduced and then exceeded using quantum dot photocatalysts after system optimization (Table 5.1 and Figures 5.2-5.4).

Table 5.2. Relevant conditions used to optimize photoredox mediated C-O bond cleavage

Comparison	Catalyst	Cat. loading (mol %)	Proton source	Solvent	Time (hr)	Yield (%)	Notes
Acetonitrile	Ir	1.00	Formic Acid	MeCN	16 hr	100	Original Stephenson
	CdSe	0.03	Formic Acid	MeCN	16 hr	0	Not suspended
	Ir	1.00	TEAH BPh4	MeCN	16 hr	100	
	CdSe	0.03	TEAH BPh4	MeCN	16 hr	100	Ligand exchange
	CdSe	0.003	TEAH BPh4	MeCN	16 hr	89	98% yield by 24 hr
	Ir	1.00	Ascorbic Acid	MeCN	16 hr	54	
Solvent	Ir	1.00	Formic Acid	10:1 THF:MeCN	16 hr	0	Not suspended
	CdSe	0.003	Formic Acid	THF	16 hr	0	
	Ir	1.00	Formic Acid	DCM	16 hr	100	
	Ir	1.00	Formic Acid	DMF	16 hr	100	
	Ir	1.00	Formic Acid	DMSO	16 hr	---	No CH2 or CH3 peaks
Proton Source	CdSe	0.003	Formic Acid	DCM	16 hr	0	Not suspended
	CdSe	0.003	Ascorbic Acid	DCM	16 hr	0	Briefly suspended
	CdSe	0.003	TEAH PF6	DCM	16 hr	60	1x
Concentration	CdSe	0.03	TEAH PF6	DCM	16 hr	65	10x more QD Conc.
	CdSe	0.003	TEAH PF6	DCM	16 hr	60	1x QD Concentration
	CdSe	0.0003	TEAH PF6	DCM	16 hr	12	1/10x less QD Conc.
	CdSe	0.00003	TEAH PF6	DCM	16 hr	2	1/100x less QD Conc.
Control Rxns	CdSe	0.003	TEAH PF6	DCM	24 hr	63	1x QD Conc.
	CdSe	0.003	TEAH PF6	DCM	24 hr	0	No amine
	CdSe	0.003	--	DCM	24 hr	0	No TEAH PF6
	--	--	TEAH PF6	DCM	24 hr	10^	No QDs
	CdSe	0.003	TEAH PF6	DCM	24 hr	0	No light
Ir Cat. Concentration	Ir	1.00	Formic Acid	MeCN	16 hr	100	Original Stephenson
	Ir	1.00	TEAH BPh4	MeCN	16 hr	100	
	Ir	1.00	TEAH PF6	DCM	16 hr	100	
	Ir	0.003	Formic Acid	MeCN	16 hr	12*	
	Ir	0.003	TEAH BPh4	MeCN	16 hr	17*	
	Ir	0.003	TEAH PF6	DCM	16 hr	28*	

*Estimated values based on a linear trend between measured percentage yields at 12 and 18 hrs.

^There is an uncatalyzed background reaction that occurs in DCM with light, TEAH PF_6, and *N*,*N*-diisopropylamine. The exact uncatalyzed percentage yield was challenging to reproduce across trials. However, never more than 1% C-O cleavage was obsrved after 5 hrs and no more than 5% after 7 hrs in DCM. After about 24 hrs, upwards of 10% percent yield could be observed and up to 23% after 100 hrs, though 23% yield after 100 hrs was only achieved once. Comparitively, up to 5% C-O cleavage was observed with light, TEAH PF_6, and *N*,*N*-diisopropylamine in acetonitrile without a catalyst.

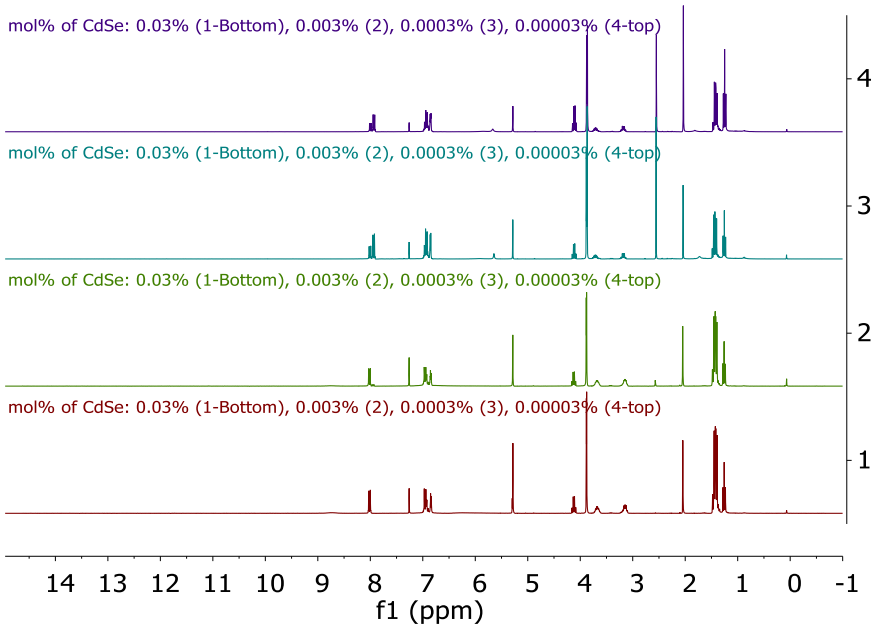

Figure 5.2. Evaluation of mole percentage of quantum dots on conversion of **BK** to products after 16 hrs. Mole percentages of CdSe: 0.03% (1-Bottom), 0.003% (2), 0.0003% (3), 0.00003% (4-top)

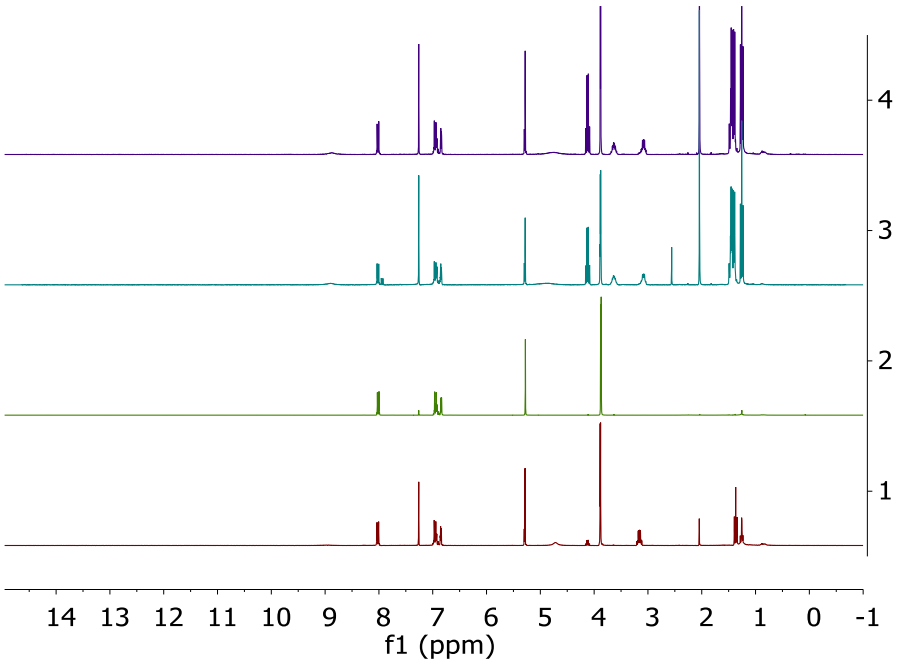

Figure 5.3. Control reactions after 16 hrs. From bottom to top: No amine (bottom, 1), No $TEAH^{+}PF6^{-}$ (2), No QDs (3), No light (top, 4).

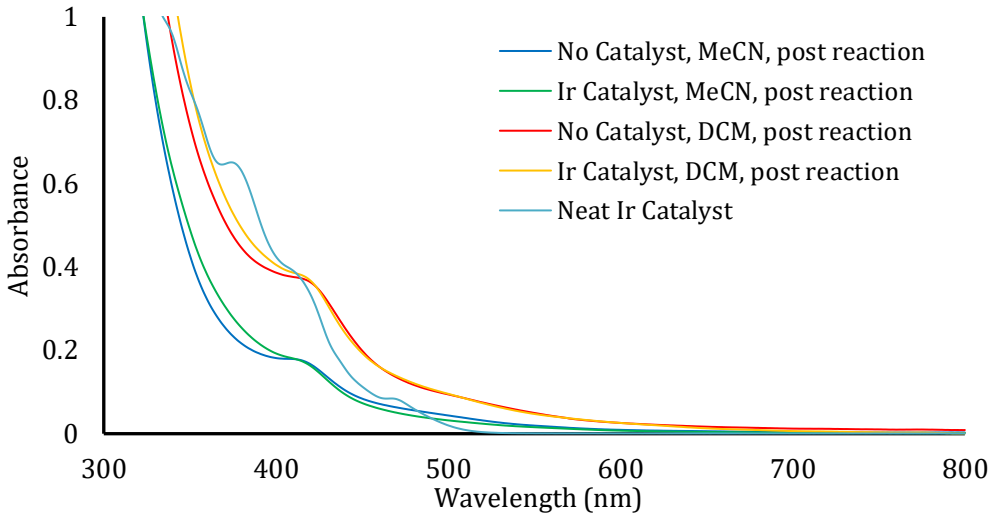

Figure 5.4. Absorption spectra of the iridium catalyst and post-reaction solutions. Absorption spectra of iridium catalyst and no catalyst control reactions after photoreduction. Comparison to the neat iridium catalyst in acetonitrile.

It is hypothesized the background reaction is due to the formation of a red species whose formation is dependent on the presence of amine. This red species could not be isolated by phase separation, dissapearsin the presence of H_2O and EtOAc, and was unobservable by GC-MS.Similar species have been observed as intermediates in other photoredox reactions and this potentially colored intermediate could serve to absorb light and facilitate some photoredox catalysis.[45-46] It is likely that in our case that this red species is a polymerized/oligomerized aromatic compound like polyguaicol,[47] which has been previously identified as an organic soluble red precipitate.

It is not expected that simply replacing quantum dots in a system designed for an iridium photocatalyst would lead to the optimal catalytic conversion. It is a prerequisite to ensure compatibility between all components (i.e., catalyst, proton source, hole quencher, and solvent) in the photodriven reaction system for C_α–O bond cleavage. Although formic acid and ascorbic acid

are common proton donors in many photocatalytic systems, stability challenges are often encountered in many solvents because of the strong coordination of the conjugate bases of these acids to the surface of the quantum dots. For example, rapid precipitation of CdSe quantum dots capped with carboxylate and phosphonate ligands was observed upon addition of formic acid. It was found that triethylammonium salts ($TEAH^+$) conveniently serve as proton sources with no detectable perturbation of quantum dot stability across a wide range of organic solvents. Suitable $TEAH^+$ salts are easily prepared, purified, and isolated in high yields from mixing triethylammonium chloride with the sodium salt of a desired counteranion. For example, [TEAH][BPh_4] is highly soluble in acetonitrile while [TEAH][PF_6] is readily solubilized by DCM. The hole quencher, diisopropylethylamine, was found to work without need for modification, likely because of the large steric bulk around the Lewis basic nitrogen, which prevents strong interactions with the quantum dot surface.

A control experiment evaluating the use of triethylammonium as a proton source shows that iridium-catalyzed reactions have improved turnover rates when compared to the previously reported formic acid system. In acetonitrile, direct replacement of formic acid for [TEAH][BPh_4] led to a 2.2× increase in turnover frequency, while a 4.7× increase in turnover frequency was observed with [TEAH][PF_6] in DCM. It should be noted that DCM had not been previously reported as a solvent in the iridium system.

In addition to substitution of the proton source, the iridium catalyst was replaced by CdSe quantum dots to facilitate conversion of the lignin model substrate (**BK**) to products. CdSe quantum dots were readily suspended in acetonitrile following ligand exchange with*trans*-4-cyanocinnamic acid.[48] Conversion of **BK** to 4′-methoxyacetophenone and guaiacol is achieved over the same 16 h time frame as the iridium catalysts. In fact, the quantum dots required

significantly less catalyst to obtain the same product conversion rates. Only 0.003 mol % (333 times less) quantum dot catalyst was required to observe near-complete C_{α}–O bond cleavage, as shown in Table 5.1. However, when 0.003 mol % of iridium catalyst was used, no more than 30% conversion was ever observed regardless of proton source over the course of 16 h. After the first 6 h, the rate of catalysis with 0.003 mol % CdSe slows but the reaction still progresses. Figure 5.5 shows the rates of catalysis over the initial 9 h for the iridium catalyst and CdSe quantum dots at the same loading. This observed slowdown after 6 h is primarily attributed to the consumption of substrate and not to catalyst degradation (*vide infra*). The *trans*-4-cyanocinamate-functionalized CdSe quantum dots demonstrate a 15-fold increase in conversion rate over the first 9 h of the reaction when compared to the optimized conditions for iridium. Despite the improvements to turnover frequency in the iridium-catalyzed system with triethylammonium as the proton source, the quantum dots still outperform the iridium catalyst by nearly a factor of 7. Figure 5.6 displays the performance of each catalyst over 50 h. It can be seen that the reaction is not yet complete after the initial 9 h but continues at a slower rate than the initial rate over the first 5 h. Characterization associated with the reaction progress is included in Figures 5.7-5.12.

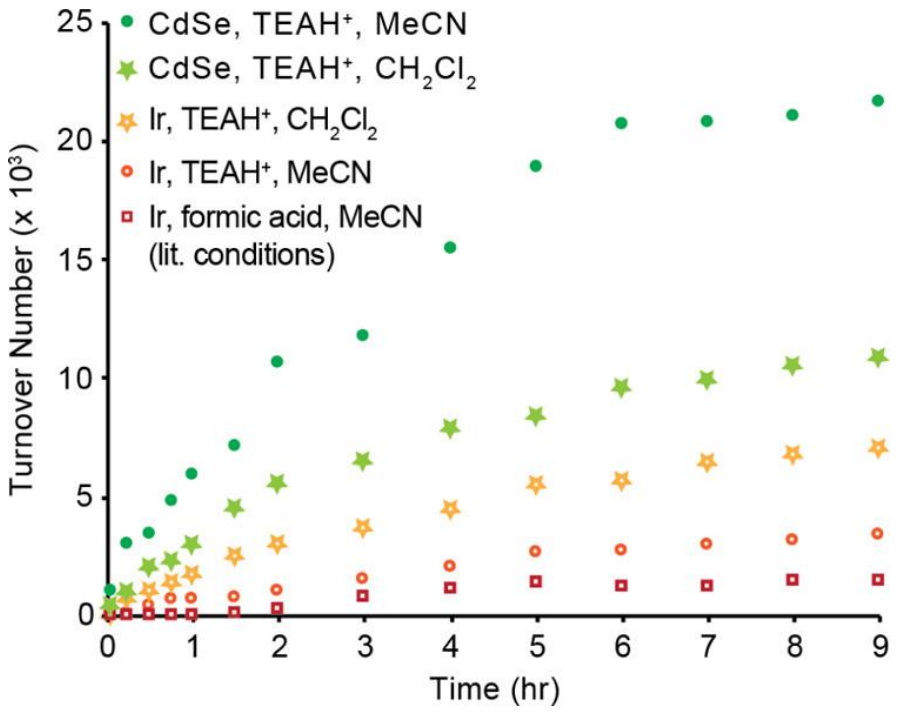

Figure 5.5. Comparison of turnover rate over the first 9 h of the reaction. The quantum dots markedly outperform their iridium catalyst counterparts at 0.003 mol % catalyst loading.[26]

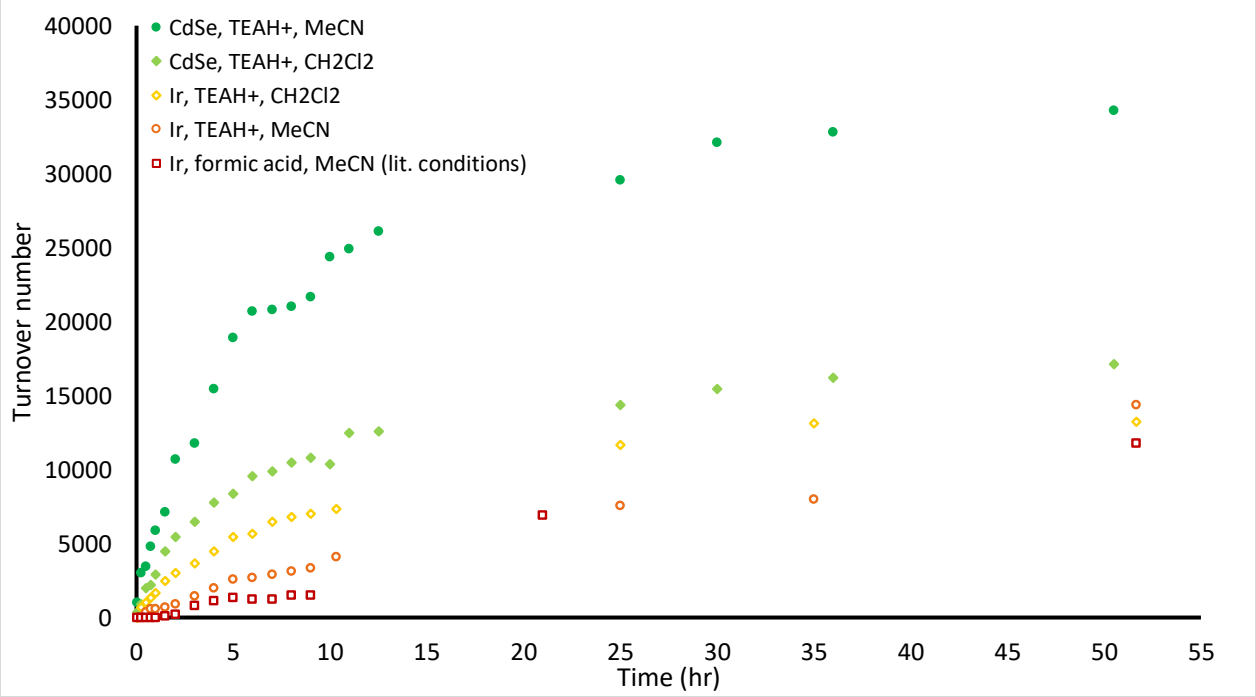

Figure 5.6. Comparison of turnover rate over 55 h of the reaction.

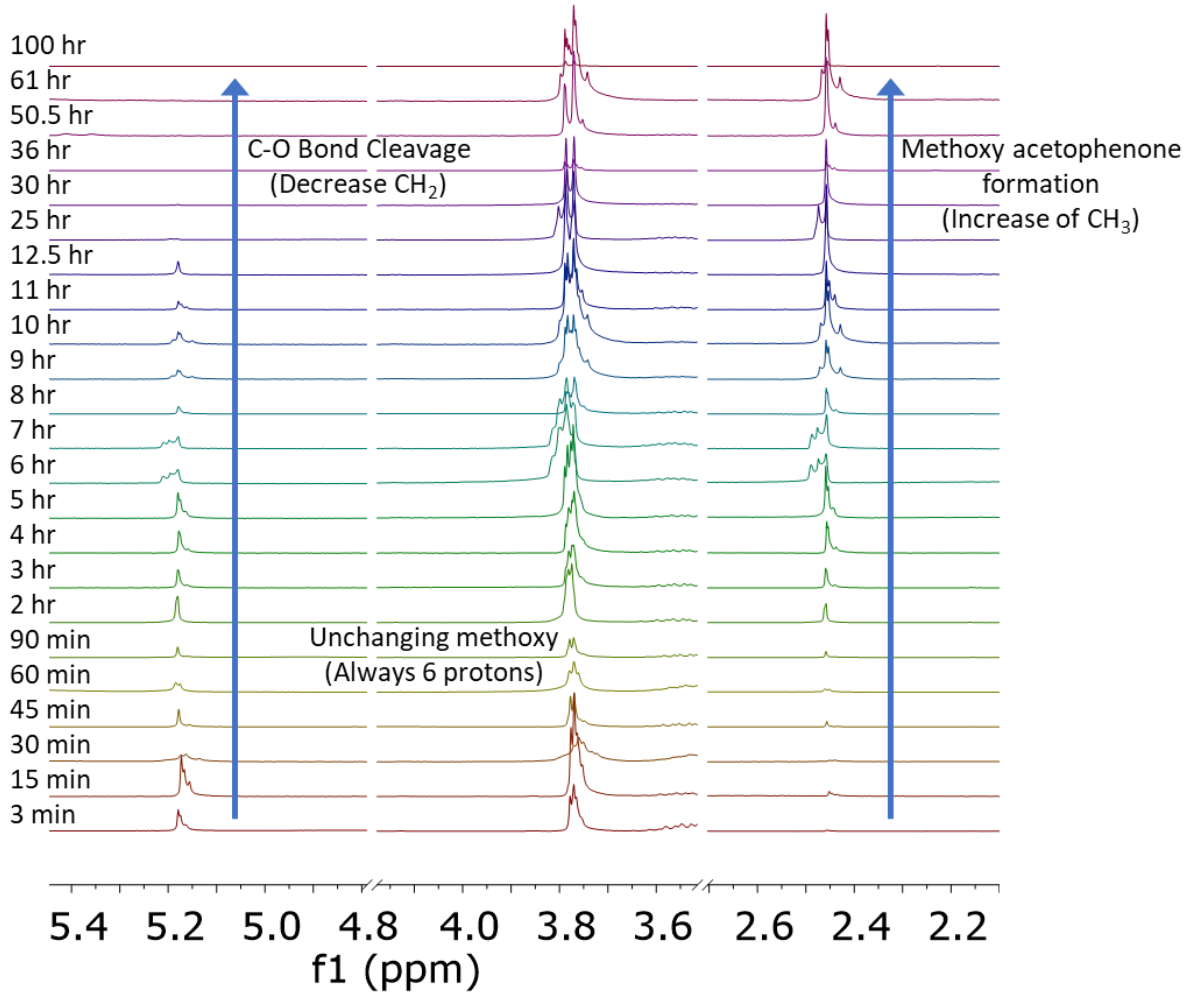

Figure 5.7. ^{1}H NMR evaluation of CdSe mediated reductive C-O bond cleavage of **BK** to guaiacol and 4'-methoxyacetophenone in acetonitrile. NMR obtained in chloroform-d at room temperature.

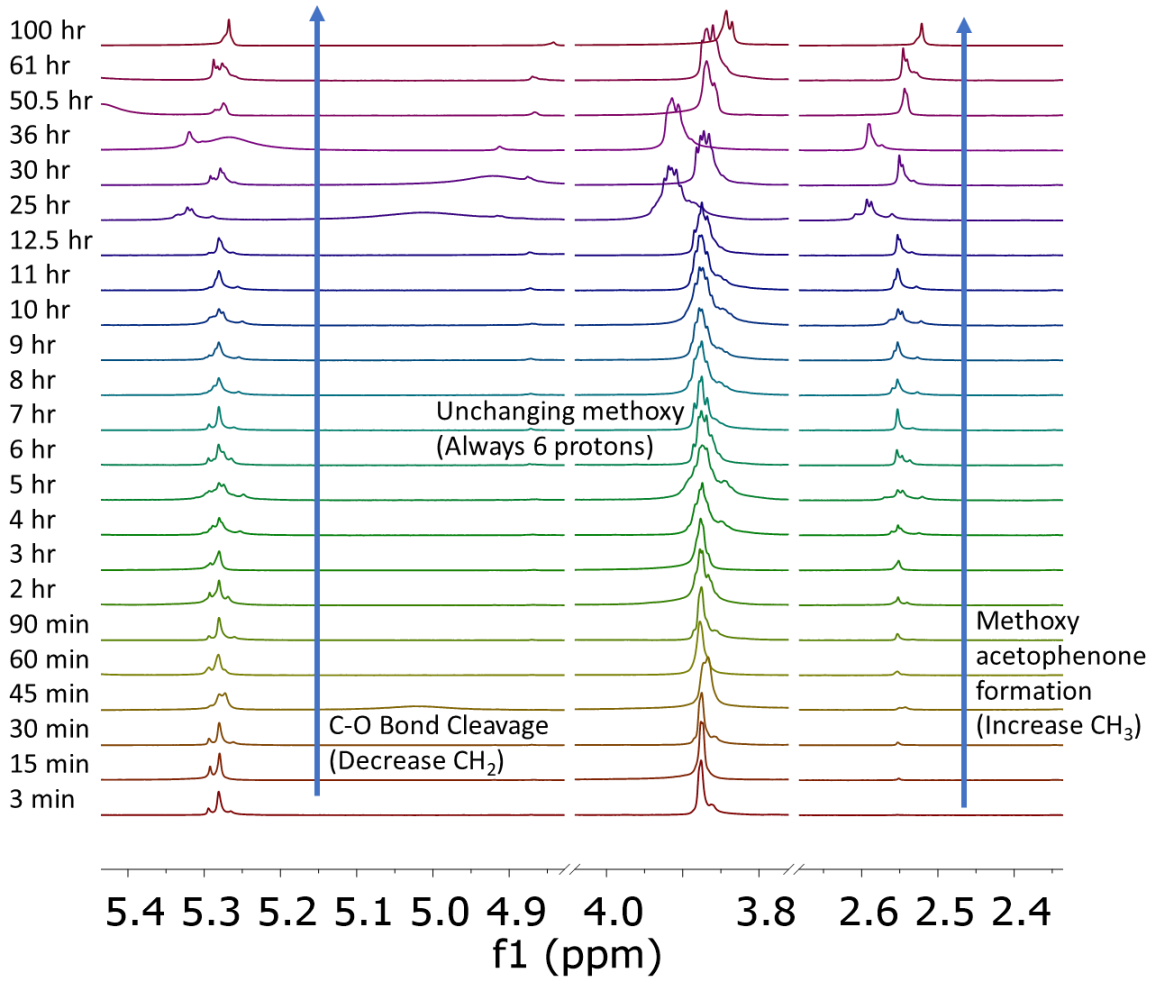

Figure 5.8. ^{1}H NMR evaluation of CdSe mediated reductive C-O bond cleavage of **BK** to guaiacol and 4'-methoxyacetophenone in dichloromethane. NMR obtained in chloroform-d at room temperature.

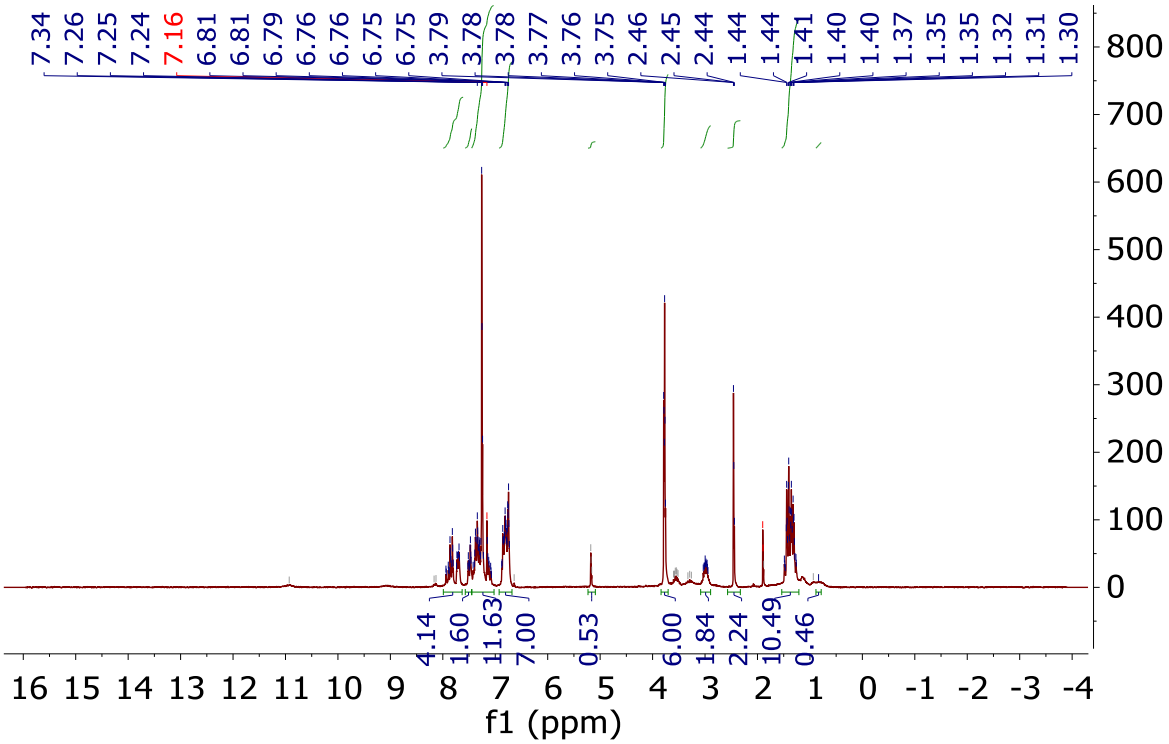

Figure 5.9. Example full ^{1}H NMR spectrum of CdSe mediated reductive C-O bond cleavage of **BK** to guaiacol and 4'-methoxyacetophenone in acetonitrile after 11 hrs. NMR obtained in chloroform-d at room temperature.

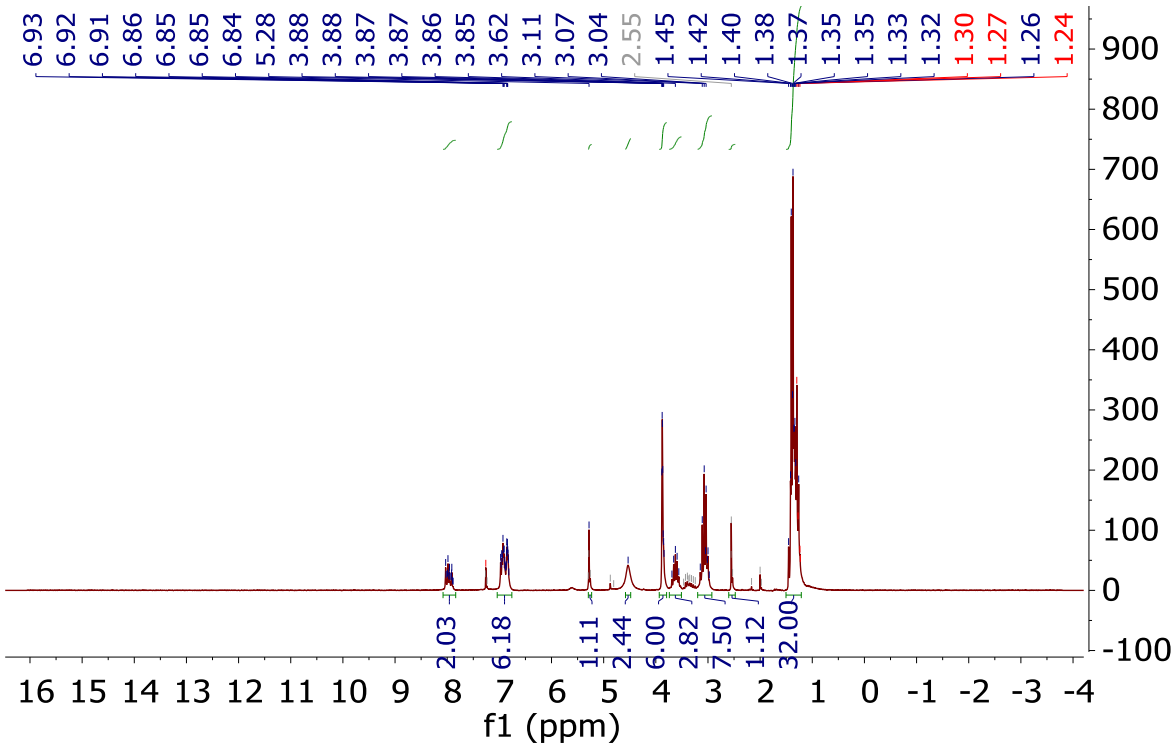

Figure 5.10. Example full ^{1}H NMR spectrum of CdSe mediated reductive C-O bond cleavage of **BK** to guaiacol and 4'-methoxyacetophenone in dichloromethane after 11 hrs. NMR obtained in chloroform-d at room temperature.

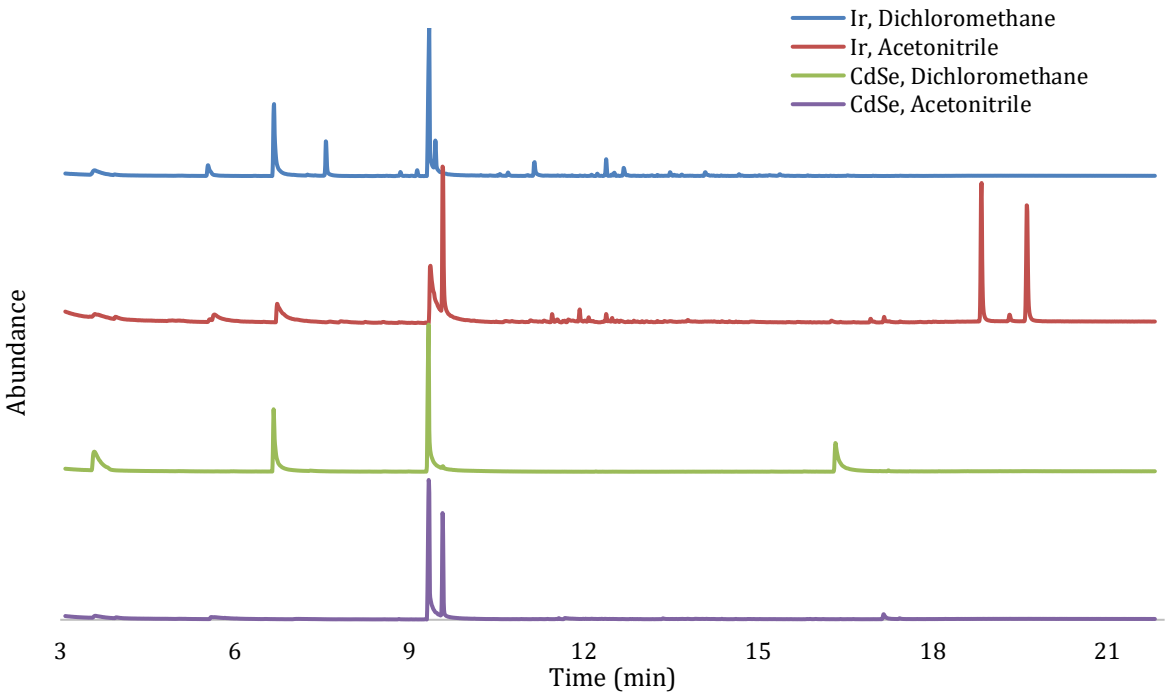

Figure 5.11. Gas chromatograms of photocatalysis reactions after 24 hrs of photocatalysis.

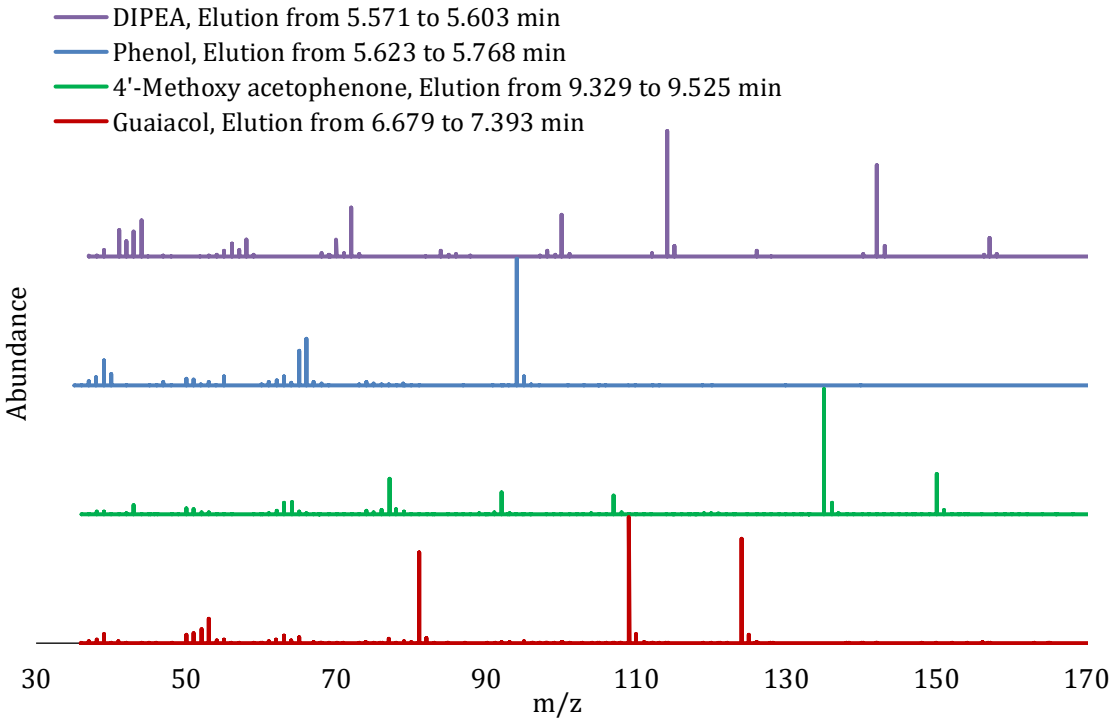

Figure 5.12. Evaluation by GC-MS highlighting the MS spectrum of each eluted species. Phenol is identified as a by-product in these reactions.

The improved performance of the quantum dots over the iridium molecular catalyst is attributed to a combination of the greater molar extinction coefficient, increased surface area, and higher energy LUMO of the QDs. The molar extinction coefficient of the 3.3 nm CdSe quantum dots is 1.96×10^6 L/mol·cm at 554 nm and increases toward the blue.[48] The absorption onset of $[Ir(ppy)_2(dtbbpy)]PF_6$ is higher energy when compared with CdSe, with molar extinction coefficients ranging from 10^3 to 10^4 L/mol·cm between 466 and 377 nm. The excited state redox potential of the 3.3 nm QDs is −1.53 V versus SCE,[1] roughly 20 meV higher than the reduction potential for the reduced Ir^{2+} catalyst with a reported Ir(III)/Ir(II) couple at −1.51 V versus SCE.[49] Furthermore, the quantum dots show robust catalysis after more than 200 h of continuous irradiance, boasting turnover numbers as high as 128,000, as shown in Figure 5.13.

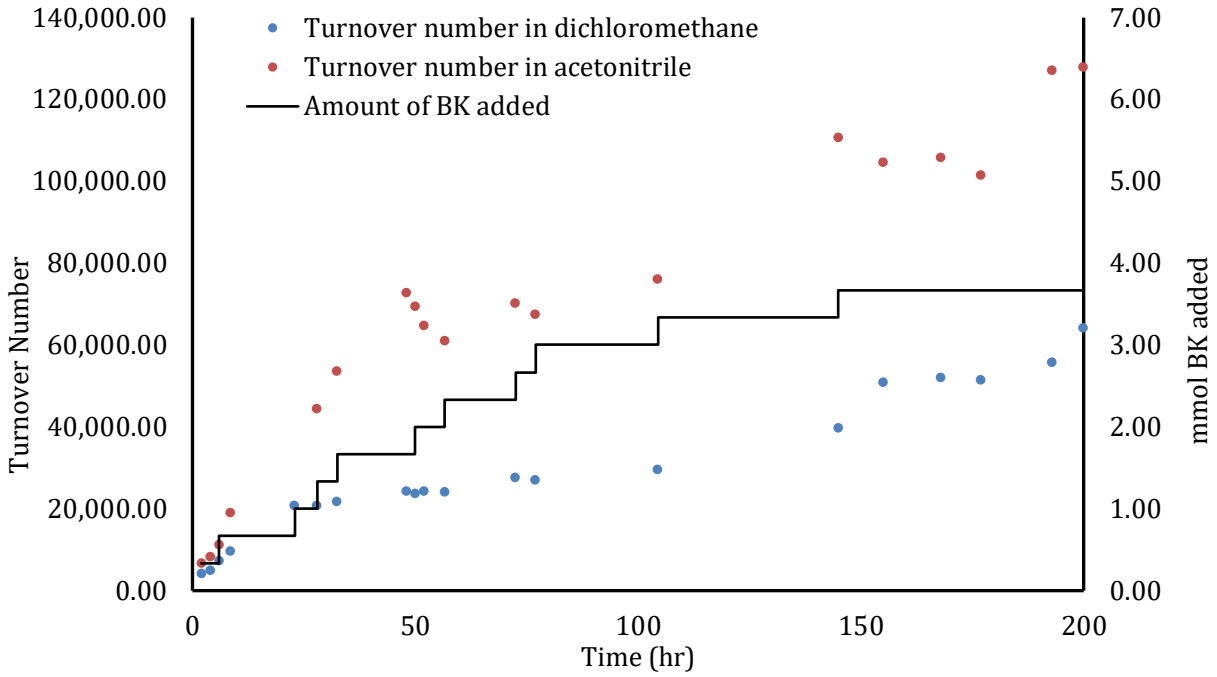

Figure 5.13. Evaluation of total turnover number. Total turnover evaluation of 0.003 mol% CdSe in acetonitrile and dichloromethane as more **BK** is added to the reaction vessel. The QD photocatalysts remain suspended after 200 hrs. Nearly 1 gram of **BK** was added over the initial 150 hrs of the reaction. Additional solvent (up to 3 mL) was added to retain a homogeneous reaction medium.

5.3 SINGLE VESSEL C-O BOND CLEAVAGE FROM REDUCED MODEL SUBSTRATE

An added advantage of using quantum dots over traditional molecular photocatalysts is the versatility to change the surface ligands for examination across a wide range of solvents. Iridium molecular catalysts are nearly exclusively used in acetonitrile in prior investigations.[26, 35-37, 46] CdSe QDs are typically synthesized in nonpolar organic solvents with long-chain aliphatic ligands. CdSe QDs with their native, oleate ligand set are readily solubilized by DCM, as is the proton source [TEAH][PF_6]. A comparison of oleate-capped CdSe and iridium catalyst in DCM with

[TEAH][PF_6] showed the quantum dots outperform their molecular counterparts by a factor of nearly 2×, ultimately leading to 63% conversion using quantum dots versus only 28% conversion with the iridium catalyst after 24 h. The previous observation of higher turnover frequency by the iridium catalyst in DCM versus acetonitrile is reversed for the quantum dot system. This is attributed to the increased conversion rate of the *trans*-4-cyanocinamate-capped quantum dots over the same-sized nanocrystals bearing oleate ligands to the shorter, more rigid, and conjugated ligands. It has been reported previously that reducing ligand chain length improves catalysis by facilitating substrate-quantum dot encounters.[50-51]

Both native lignin and processed lignin are usually found in their reduced form. Thus, oxidation of benzylic alcohol groups is often required prior to breaking the C_α–O bonds. Reports by Stahl and Stephenson have demonstrated catalytic aerobic benzylic alcohol oxidation of lignin model systems using 4-AcNH-TEMPO and its derivatives.[26, 38] Prior reports have used [4-AcNH-TEMPO][BF_4] in DCM as the first of two steps along the lignin model substrate degradation pathway. After oxidation, C_α–O bond cleavage can be executed with molecular catalysts, but only after filtration, purification, evaporation, and transfer to a new solvent (acetonitrile).[26] The solvent versatility and robustness of the quantum dot platform enables a one-pot conversion of **BA** directly to 4′-methoxyacetophenone and guaiacol in DCM by an initial oxidation of the benzylic alcohol with [4-AcNH-TEMPO][BF_4]. After oxidation, photocatalytic C_α–O cleavage is conducted by addition of CdSe, $TEAH^+$, and diisopropylethylamine directly into the same vessel and proceeds via the same reduction pathway observed previously for **BK** to products, despite the presence of silica and residual [4-AcNH-TEMPO][BF_4]. This method obviates the need for purification or even filtration before addition of the quantum dots. Using the iridium catalyst under the same

experimental conditions yielded no conversion of **BK** to products, presumably because of incompatibility between the iridium catalyst and [4-AcNH-TEMPO][BF_4].[26]

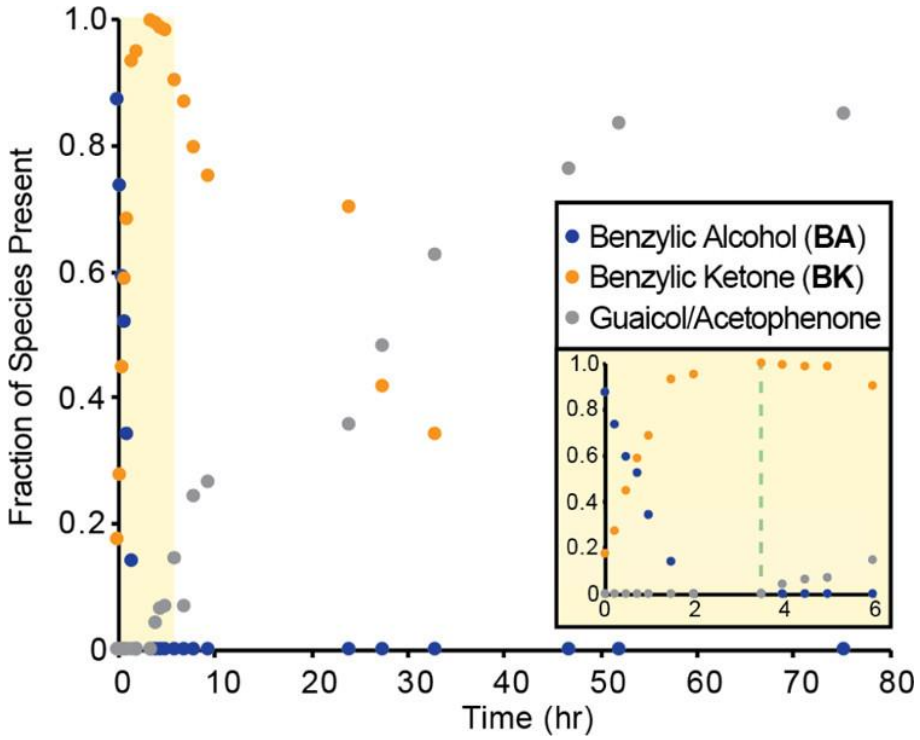

Figure 5.14. Single vessel oxidation followed by photoreduction. Complete oxidation of **BA** in the presence of Bobbitt's salt and silica in DCM occurs over 3.5 h. 85% conversion of **BK** to guaiacol and 4′-methoxyacetophenone occurs over the subsequent 40 h following addition of quantum dots, [TEAH][PF_6], and amine. The inset focuses on the initial 6 h of conversion.

As can be seen in Figure 5.14, only **BA** is present initially. After 3.5 h of oxidation by [4-AcNH-TEMPO][BF_4] in the presence of silica gel, the benzylic alcohol is completely oxidized to **BK** as determined by proton NMR spectroscopy. At this point, CdSe quantum dots, [TEAH][PF_6], and amine are added to facilitate conversion to guaiacol and 4′-methoxyacetophenone. Near-complete conversion (85%) of benzylic alcohol to guaiacol and 4′-methoxyacetophenone occurs after 40 h. This conversion is similar to the yields obtained when starting directly with **BK**. However, the rate of reductive bond cleavage is slower when starting from the benzylic alcohol. This is attributed to the presence of silica in the reaction system, which increases light scattering and likely some interaction between [4-AcNH-TEMPO][BF_4] and the quantum dots. Scheme 5.1 outlines the reaction conditions for each step in this single-vessel conversion of **BA** through **BK** to products and Scheme 5.2 depicts a proposed mechanism for C_α–O bond cleavage of **BK** to 4′-methoxyacetophenone and guaiacol.

Scheme 5.1. Overview of oxidation of **BA** to **BK** followed by QD catalyzed photoreductive C-O bond cleavage of **BK** to products.

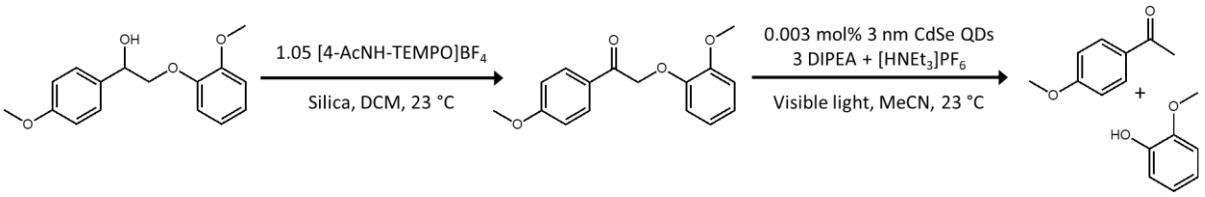

Scheme 5.2. Proposed mechanism of photoreduction using a quantum dot for C-O bond cleavage of **BK** to products.

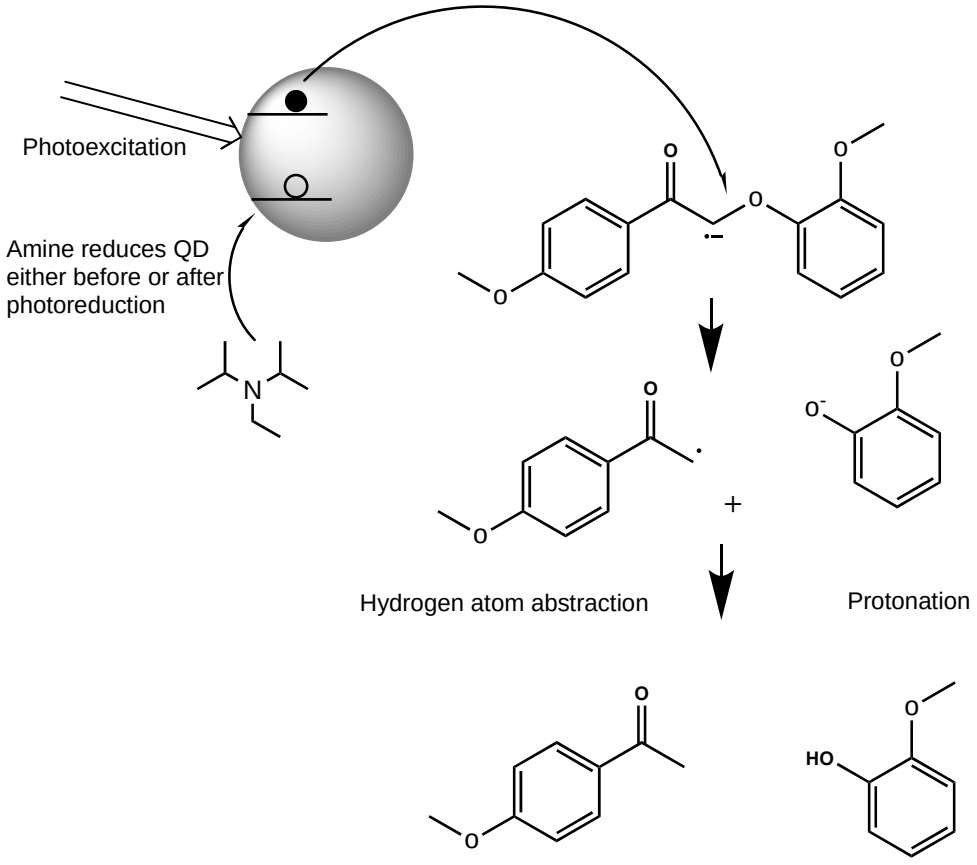

5.4 CONCLUSIONS

In conclusion, we have demonstrated the versatility of CdSe quantum dots in C–O bond cleavage using a lignin model substrate to emulate biomass depolymerization. Quantum dots outperform state-of-the-art molecular iridium catalysts with up to a factor of 15 times greater turnover frequency at equivalent catalyst loading. Additionally, the CdSe quantum dot system required 333 times less catalyst to achieve the same extent of product conversion previously reported for the optimized iridium-catalyzed systems over the same time period. The solvent versatility for the

quantum dot system permits single-vessel oxidation of the benzylic alcohol groups in lignin model substrates, followed directly by C_α–O reductive bond cleavage without any purification, filtration, or solvent changes. The robust nature of the CdSe quantum dots promotes high turnover numbers up to 128,000. This work has expanded the scope of reactions facilitated by quantum dots while also progressing the field of biomass depolymerization.

5.5 EXPERIMENTAL METHODS

5.5.1 *General Considerations*

All quantum dots were synthesized using a standard Schlenk technique, and ligand exchange was carried out in a glovebox under dry nitrogen. Cadmium oxide (CdO, >99.99%), selenium (99.99%), 1-octadecene (ODE, 90%), oleic acid (OA, 90%), trioctylphosphine (TOP, 97%), 2-bromo-1-(4-methoxyphenyl)ethanone, potassium carbonate (>99%), guaiacol (>99%), sodium borohydride (98%), [Ir(2-phenylpyridine)$_2$(4,4′-ditertbutylbipyridine)]PF6 ([Ir(ppy)$_2$(dtbbpy)]PF_6), N,N-diisopropylethylamine (99.5%), [4-AcNH-TEMPO]BF_4 (Bobbitt's salt, 97%), sodium hexafluorophosphate ($NaPF_6$, 98%), sodium tetraphenylborate ($NaPF_6$, >99.5%), and triethylammonium chloride were purchased from Sigma-Aldrich and used as received without further purification. Acetone, diethyl ether, tetrahydrofuran (THF), deionized water, DCM, and acetonitrile were purchased from various sources.

5.5.2 *Synthesis of Benzylic Ketone Model Lignin Substrate*

The synthesis of 2-(2-methoxyphenoxy)-1-(4-methoxyphenyl)ethanone (**BK**) was accomplished similarly to prior reports.[26, 52] A 500 mL round-bottom flask equipped with a large reflux condenser with flowing water was charged with 2-bromo-1-(4-methoxyphenyl)ethanone (13.7 g, 60

mmol), potassium carbonate (12.3 g, 89 mmol), guaiacol (8.2 mL, 74 mmol), and acetone (250 mL). The resulting suspension was stirred and heated to reflux (73 °C) for 3 h in an oil bath. The solution evolves from faint yellow to orange. Then, it was filtered through Celite and concentrated using the rotary evaporator in a bath of room-temperature water. The crude product is a yellow/white solid. Prior results have isolated **BK** by chromatography on SiO_2 (70:30, hexanes/EtOAc). Purified **BK** was isolated by suspending the crude product in 70:30, hexanes/EtOAc, vigorous stirring, and centrifugation to separate purified product from the colored supernatant with yields of up to 85%. **BK** could also be recrystallized in hexanes or 70:30 hexane/EtOAc. Characterization by ^{1}HNMR of reagents and **BK** is shown in Figure 5.15.

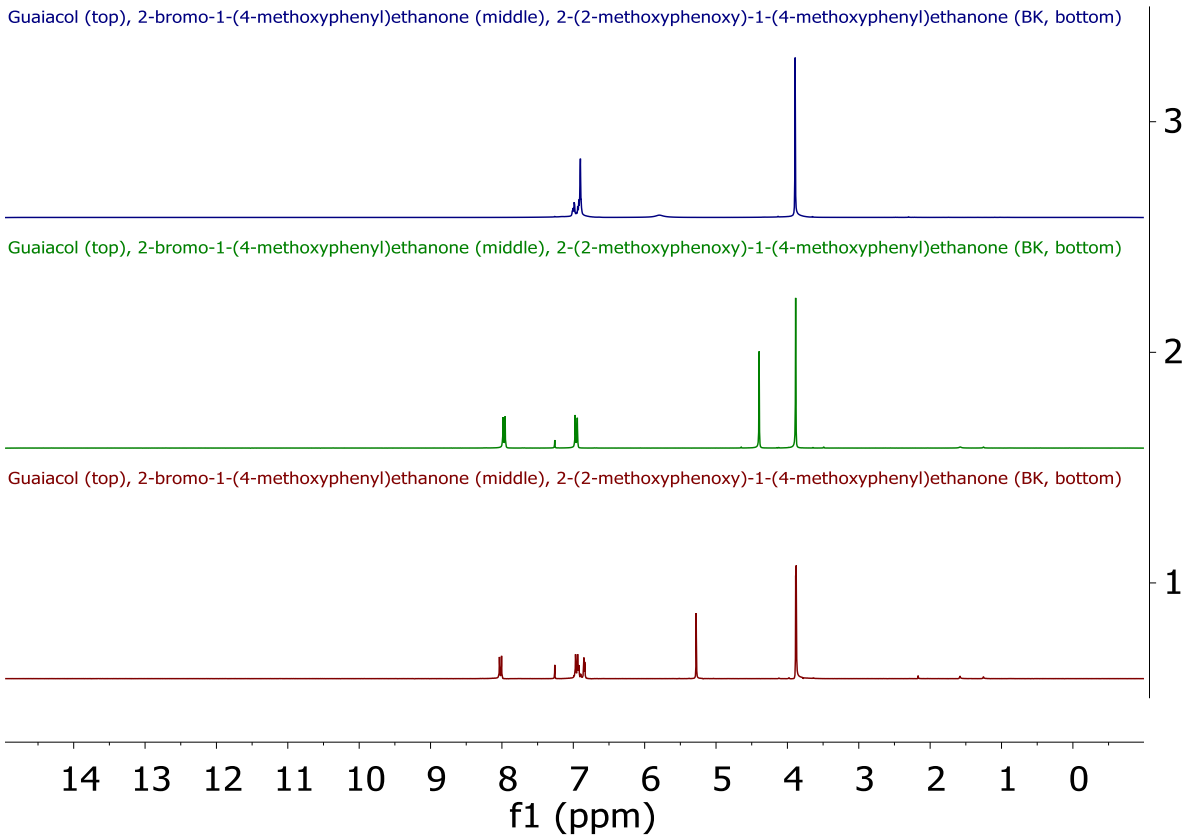

Figure 5.15. ^{1}H NMR characterization of starting materials. Commercial standards of guaiacol (top) and 2-bromo-1-(4-methoxyphenyl)ethanone (middle). Also included is synthesized **BK**, 2-(2-methoxyphenoxy)-1-(4-methoxyphenyl)ethanone (bottom).

5.5.3 *Synthesis of Benzylic Alcohol Model Lignin Substrate*

The synthesis of 2-(2-methoxyphenoxy)-1-(4-methoxyphenyl)ethanol (**BA**) was accomplished similarly to prior reports.[26, 52] A 100 mL round-bottom flask was charged with **BK** (1.7 g, 6.2 mmol), THF (28 mL), and water (7 mL). Sodium borohydride (0.47 g, 12.4 mmol) was slowly added portion wise over 3–5 min to maintain a gentle evolution of gas in the reaction vessel. After bubbling is ceased, the reaction mixture was stirred for 3 h at room temperature. The reaction was ultimately quenched with

saturated aqueous NH_4Cl solution (50 mL) before dilution into water. The aqueous portion was subsequently extracted with Et_2O (3 × 50 mL). All of the combined organic extracts were washed twice with brine, dried over $MgSO_4$, filtered, concentrated in vacuo, and purified by chromatography on SiO_2 (75:25, hexanes/EtOAc). Purified **BA** was also obtained via recrystallization in a minimum amount of 75:25, hexanes/EtOAc in yields of up to 90%.

5.5.4 *Reductive C–O Bond Cleavage of BK*

This procedure was modified to suit quantum dots as the photoredox catalysts from prior reports.[26, 36] A 1-dram vial with a small magnetic stir bar was loaded with 2-(2-methoxyphenoxy)-1-(4-methoxyphenyl)ethanone (**BK**) (0.33 mmol, 1.00 equiv), solvent (DCM or MeCN, 1.67 mL), N,N-diisopropylethylamine (1.0 mmol, 3.0 equiv), proton source (triethylammonium salt or formic acid, 1.0 mmol, 3.0 equiv), and catalyst (CdSe QDs or $[Ir(ppy)_2(dtbbpy)]PF_6$). The vial was capped, and the reaction mixture was stirred under illumination with white light-emitting diodes (LEDs) to give a constant flux of 200 mW/cm2 across the entire face of the reaction vessel. Extractions between 50 and 100 μL were made over the course of the reaction to track the reaction rate. The solvent was removed under vacuum and suspended in CDCl3 for evaluation by NMR spectroscopy. See Table 5.2 for more information.

Table 5.3. Typical reaction conditions used for reductive C-O bond cleavage reactions of **BK**.

Chemical species	Amount		MW (g/mol)	mmol	Molar Equivalents
2-(2-methoxyphenoxy)-1-(4-methoxyphenyl)ethanone (**BK**)	0.0908	g	272.3	0.33	1.00
N,N-Diisopropylethylamine	0.1733	mL	129.24	1.00	3.00
Proton Sources					
Formic acid	0.0377	mL	46.03	1.00	3.00
Triethylammonium BF_4	0.421	g	421.427	1.00	3.00
Triethylammonium PF_6	0.247	g	247.16	1.00	3.00
Solvents					
Acetonitrile (MeCN)	1.67	mL	41.05	31.98	95.89
Dichloromethane (DCM)	1.67	mL	84.93	26.15	78.43
Catalysts*					
[Ir(ppy)2(dtbbpy)]PF6	0.0033	g	913.95	$3.61*10^{-3}$	0.01
CdSe QDs				$1.00*10^{-5}$	$3.00*10^{-5}$

* Amount of catalyst described in this table represents the amount of iridium catalyst used to replicate prior reports[26, 36] while the CdSe QD amount is representative of the amount of catalyst used to track reaction rates described throughout the paper. For comaprison studies, the iridium catalyst amount was reduced to 1.00×10^{-5} mmol (3.00×10^{-3} molar equivilants).

5.5.5 *Single-Vessel C–O Bond Cleavage from BA*

(Oxidation of **BA** to **BK**) A 1-dram vial with a magnetic stir bar was charged with 2-(2-methoxyphenoxy)-1-(4-methoxy-phenyl)ethanol (**BA**) (0.20 mmol, 1.00 equiv), DCM (2.0 mL), silica gel (100 wt % of benzylic alcohol), and [4-AcNH-TEMPO]BF4 (Bobbitt's salt, 1.05 mmol, 1.05 equiv). The vial was capped and the heterogeneous mixture was stirred at room temperature under white LED illumination until all **BA** had been converted into **BK** (~ 3.5 h). Light is not necessary to facilitate this reaction, but illumination was maintained for consistency of the reaction setup. (Reduction of **BK**) After 3.5 h, N,N-diisopropylethylamine (0.6 mmol, 3.0 equiv), triethylammonium PF6 (0.6 mmol, 3.0 equiv), and CdSe QDs (6.00 × 10–6 mmol, 3.00×10^{-5} equiv) dissolved in a minimum amount of DCM (0.1

mL) were quickly added to the reaction vessel and the reaction continued under white LED illumination. No filtration or purification steps were made between oxidation and reduction steps. See Table 5.3 for more information.

Table 5.4. Typical reaction conditions used for single vessel C-O bond cleavage reactions from **BA**.

Chemical species	Amount		MW (g/mol)	mmol	Molar Equivalent
2-(2-methoxyphenoxy)-1-(4-methoxy-phenyl)ethanol (**BA**)	0.055	g	274.216	0.20	1.00
Dichloromethane (DCM)	2.0	mL	84.93	31.32	156.2
Silica gel	0.055	g	60.08	0.92	4.56
[4-AcNH-TEMPO]BF_4, Bobbitt's salt	0.063	g	300.1	0.21	1.05
Triethylammonium PF_6	0.148	g	247.16	0.60	3.00
N,N-Diisopropylethylamine	0.104	mL	129.24	0.60	3.00
CdSe QDs				$6.00*10^{-6}$	$3.00*10^{-5}$

5.5.6 *Synthesis of Triethylammonium Precursors*

(TEAH PF6) Sodium PF6 and triethylammonium chloride were each dissolved in water in their own beakers at approximately 5 mL per 5 g of solid. The two solutions were combined, stirred thoroughly, and crystalized in a refrigerator. The resulting white crystals were collected in a Buchner funnel and redissolved in a minimum amount of water. TEAH PF_6 was recrystallized once again in a refrigerator and collected again with a Buchner funnel. TEAH PF_6 was placed in a round-bottom flask, heated to 75 °C, and dried under vacuum for several hours to remove residual water. It should be noted that TEAH PF_6 melts around 100 °C under vacuum. (TEAH BPh_4) The BPh_4 analogue of the triethylammonium salt was prepared in a similar manner using $NaBPh_4$.

5.5.7 *Synthesis of CdSe QDs*

The selenium precursor, trioctylphosphine selenide, was prepared by dissolving 0.060 g of 100 mesh Se powder (99.999%) in 0.84 g of TOP (1.01 mL) and 4.16 mL of ODE until the solution turned completely clear. Next, the cadmium precursor was prepared by loading 0.134 g of CdO, 1.20 mL of OA, and 8.00 mL of ODE into a 50 mL three-neck flask. The flask was degassed for 30 min at room temperature before heating to 240 °C under nitrogen. The cadmium precursor turned clear, indicating formation of cadmium oleate. Once the cadmium solution was completely clear, 5 mL of selenium precursor was added rapidly. The reaction was monitored by UV–vis and photoluminescence spectroscopy as the solution color advances from yellow to orange to red.[53] The size of the particles was controlled by quenching the reaction (by removing the heating mantle) when the target size of the nanoparticles was achieved. Particles with a diameter of 3.3 nm were obtained after 4 min. The nanocrystals were purified by repeat dissolution/precipitation using toluene as the solvent and precipitation with methanol. The first two precipitation steps required ethyl acetate as a cosolvent to remove ODE. See Table 5.4 for more information.

Table 5.5. Reagents used to synthesize CdSe QDs with oleate ligands

Chemical species	**Amount**		**MW (g/mol)**	**mmol**
Cadmium oxide	0.134	g	128.41	1.04
Oleic Acid (OA)	1.20	mL	282.47	3.80
1-Octadecene	8.00	mL	252.49	25.0
Selenium (powder)	0.060	g	78.09	0.768
Trioctylphosphine (TOP)	0.84	g	370.635498	2.27
1-Octadecene	4.16	mL	252.49	13.0

5.5.8 *Ligand Exchange to Trans-4-cyanocinnamate-Capped CdSe*

This ligand exchange procedure was adopted from Kroupa et al.[48] A solution of oleate-capped CdSe QDs was prepared in DCM in a nitrogen-filled glovebox and its concentration was determined using absorbance spectroscopy.[53] The conjugate acid equivalent amount of trans-4-cyanocinnamate ligand necessary to completely exchange the standardized QD solution (900 ligands per QD) was suspend in 5:1 acetonitrile/isopropyl alcohol with gentle sonication. The ligand solution was added dropwise to the QD solution with vigorous stirring, and the exchange was allowed to proceed for 15 min. Ultimately, the QD solution volume to ligand solution volume was 10:1. Acetonitrile was added upon visual precipitation of the particles to ensure the particles remained suspended in the solvent mixture. The exchanged QDs were isolated from byproduct OA and excess trans-4-cyanocinnamic acid by first removing solvent in vacuo followed by multiple precipitation, centrifugation, and redissolution cycles using acetonitrile as the solvent and hexanes as the antisolvent. Figure 5.16 shows the absorbance and fluorescence spectra of CdSe compared to the iridium catalyst in acetonitrile and dichloromethane.

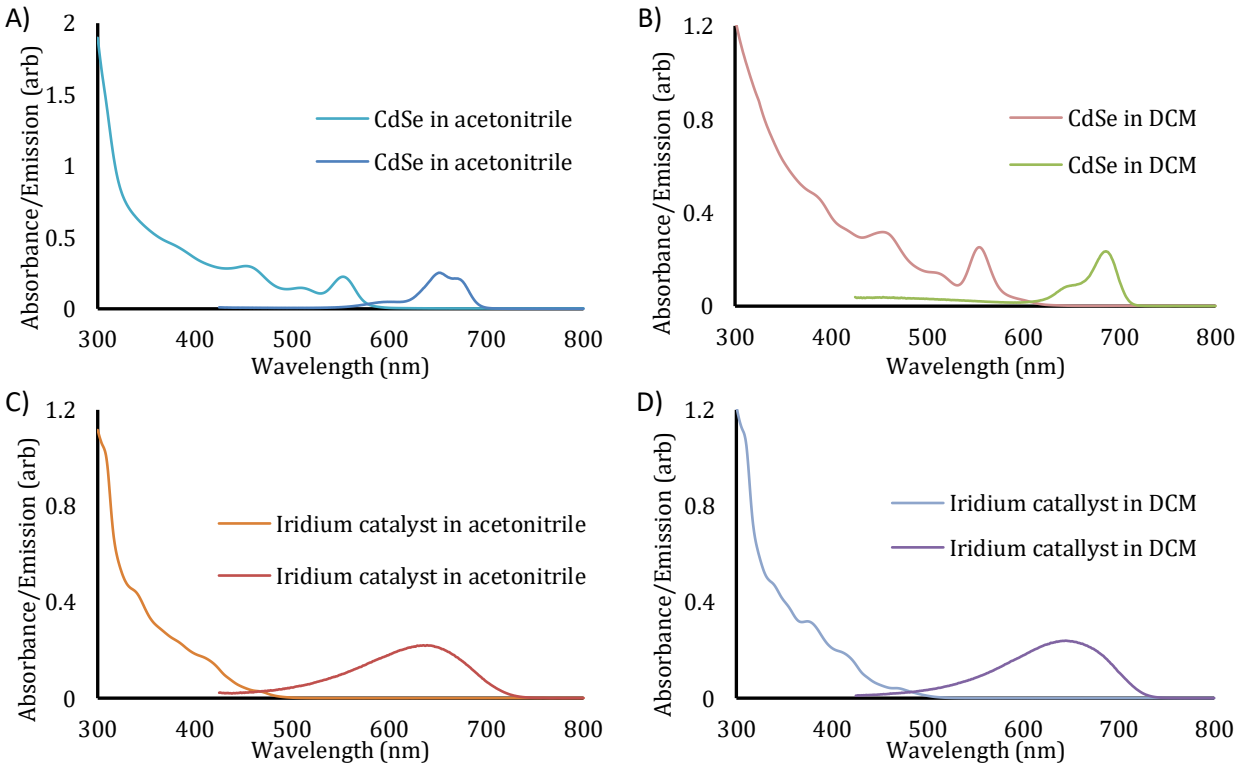

Figure 5.16. Absorbance and fluorescence characterization of catalysts in acetonitrile and dichloromethane. CdSe in acetonitrile, B) CdSe in dichloromethane, C) iridium catalyst in acetonitrile, D) iridium catalyst in dichloromethane. The quantum dots absorb at 554 nm. Using this absorption energy, the particles are 3.3 nm in diameter with a molar extinction coefficient of 196,000 L/mol·cm.[53]

5.5.9 *Additional Apparatus Details*

All photocatalytic reactions were carried out in 1-dram vials and stirred at 1500 rpm. Two illuminated white light LEDs (Hyperikon MR16 GU10, LED 6.5 W (50 W equiv), 500 Lumen, 4000 k (Daylight Glow), CRI 84+, 120 V, 40° Beam Angle), were focused on each side of the vial at a distance

of 3 cm apart with the 1-dram vial positioned. This illumination provided a measured energy flux of 200 mW/cm2 across the visible spectrum between 400 and 600 nm.

5.5.10 *Sample Characterization*

UV–visible absorption spectra were obtained with an Agilent Cary 5000 spectrophotometer, and fluorescence spectra were recorded using a Horiba Jobin Yvon FluoroMax-4 fluorescence spectrophotometer. Characterization by NMR spectroscopy and gas chromatography–mass spectrometry was carried out using a 300 MHz Bruker AVANCE spectrometer and Agilent 5973 gas chromatograph–mass spectrometer, respectively.

5.6 REFERENCES

(1) Caputo, J. A.; Frenette, L. C.; Zhao, N.; Sowers, K. L.; Krauss, T. D.; Weix, D. J., General and Efficient C-C Bond Forming Photoredox Catalysis with Semiconductor Quantum Dots. *J Am Chem Soc* **2017,** *139*, 4250-4253.

(2) Shaw, M. H.; Twilton, J.; MacMillan, D. W., Photoredox Catalysis in Organic Chemistry. *J Org Chem* **2016,** *81*, 6898-926.

(3) Weiss, E. A., Designing the Surfaces of Semiconductor Quantum Dots for Colloidal Photocatalysis. *ACS Energy Letters* **2017,** *2*, 1005-1013.

(4) Jensen, S. C.; Homan, S. B.; Weiss, E. A., Photocatalytic Conversion of Nitrobenzene to Aniline through Sequential Proton-Coupled One-Electron Transfers from a Cadmium Sulfide Quantum Dot. *J Am Chem Soc* **2016,** *138*, 1591-600.

(5) Zhang, Z.; Edme, K.; Lian, S.; Weiss, E. A., Enhancing the Rate of Quantum-Dot-Photocatalyzed Carbon-Carbon Coupling by Tuning the Composition of the Dot's Ligand Shell. *J Am Chem Soc* **2017,** *139*, 4246-4249.

(6) Han, Z.; Qiu, F.; Eisenberg, R.; Holland, P. L.; Krauss, T. D., Robust Photogeneration of H₂ in Water Using Semiconductor Nanocrystals and a Nickel Catalyst. *Science* **2012,** *338*, 1321-1324.

(7) Shemesh, Y.; Macdonald, J. E.; Menagen, G.; Banin, U., Synthesis and photocatalytic properties of a family of CdS-PdX hybrid nanoparticles. *Angew Chem Int Ed Engl* **2011,** *50*, 1185-9.

(8) Brown, K. A.; Dayal, S.; Ai, X.; Rumbles, G.; King, P. W., Controlled Assembly of Hydrogenase-CdTe Nanocrystal Hybrids for Solar Hydrogen Production. *J. Am. Chem. Soc.* **2010,** *132*, 9672-9680.

(9) Amirav, L.; Alivisatos, A. P., Photocatalytic Hydrogen Production with Tunable Nanorod Heterostructures. *The Journal of Physical Chemistry Letters* **2010,** *1*, 1051-1054.

(10) Brown, K. A.; Wilker, M. B.; Boehm, M.; Dukovic, G.; King, P. W., Characterization of photochemical processes for H2 production by CdS nanorod-[FeFe] hydrogenase complexes. *J Am Chem Soc* **2012,** *134*, 5627-36.

(11) Wang, F.; Wang, W. G.; Wang, X. J.; Wang, H. Y.; Tung, C. H.; Wu, L. Z., A highly efficient photocatalytic system for hydrogen production by a robust hydrogenase mimic in an aqueous solution. *Angew Chem Int Ed Engl* **2011,** *50*, 3193-7.

(12) Zhu, H.; Song, N.; Lv, H.; Hill, C. L.; Lian, T., Near unity quantum yield of light-driven redox mediator reduction and efficient H2 generation using colloidal nanorod heterostructures. *J Am Chem Soc* **2012,** *134*, 11701-8.

(13) Holmes, M. A.; Townsend, T. K.; Osterloh, F. E., Quantum confinement controlled photocatalytic water splitting by suspended CdSe nanocrystals. *Chem Commun (Camb)* **2012,** *48*, 371-3.

(14) Chai, Z.; Zeng, T. T.; Li, Q.; Lu, L. Q.; Xiao, W. J.; Xu, D., Efficient Visible Light-Driven Splitting of Alcohols into Hydrogen and Corresponding Carbonyl Compounds over a Ni-Modified CdS Photocatalyst. *J Am Chem Soc* **2016,** *138*, 10128-31.

(15) Li, X. B.; Li, Z. J.; Gao, Y. J.; Meng, Q. Y.; Yu, S.; Weiss, R. G.; Tung, C. H.; Wu, L. Z., Mechanistic insights into the interface-directed transformation of thiols into disulfides and molecular hydrogen by visible-light irradiation of quantum dots. *Angew Chem Int Ed Engl* **2014,** *53*, 2085-9.

(16) Ipe, B. I.; Niemeyer, C. M., Nanohybrids composed of quantum dots and cytochrome P450 as photocatalysts. *Angew Chem Int Ed Engl* **2006,** *45*, 504-7.

(17) Bernt, C. M.; Burks, P. T.; DeMartino, A. W.; Pierri, A. E.; Levy, E. S.; Zigler, D. F.; Ford, P. C., Photocatalytic carbon disulfide production via charge transfer quenching of quantum dots. *J Am Chem Soc* **2014,** *136*, 2192-5.

(18) Warrier, M.; Lo, M. K. F.; Monbouquette, H.; Garcia-Garibay, M. A., Photocatalytic reduction of aromatic azides to amines using CdS and CdSe nanoparticles. *Photochemical & Photobiological Sciences* **2004,** *3*, 859-863.

(19) Chauviré, T.; Mouesca, J.-M.; Gasparutto, D.; Ravanat, J.-L.; Lebrun, C.; Gromova, M.; Jouneau, P.-H.; Chauvin, J.; Gambarelli, S.; Maurel, V., Redox Photocatalysis with Water-Soluble Core–Shell CdSe-ZnS Quantum Dots. *J. Phys. Chem. C* **2015,** *119*, 17857-17866.

(20) Alonso, D. M.; Bond, J. Q.; Dumesic, J. A., Catalytic conversion of biomass to biofuels. *Green Chemistry* **2010,** *12*, 1493.

(21) Lofstedt, J.; Dahlstrand, C.; Orebom, A.; Meuzelaar, G.; Sawadjoon, S.; Galkin, M. V.; Agback, P.; Wimby, M.; Corresa, E.; Mathieu, Y.; Sauvanaud, L.; Eriksson, S.; Corma, A.; Samec, J. S., Green Diesel from Kraft Lignin in Three Steps. *ChemSusChem* **2016,** *9*, 1392-6.

(22) Boerjan, W.; Ralph, J.; Baucher, M., Lignin biosynthesis. *Annu Rev Plant Biol* **2003,** *54*, 519-46.

(23) Chakar, F. S.; Ragauskas, A. J., Review of current and future softwood kraft lignin process chemistry. *Industrial Crops and Products* **2004,** *20*, 131-141.

(24) Ralph, J.; Lundquist, K.; Brunow, G.; Lu, F.; Kim, H.; Schatz, P. F.; Marita, J. M.; Hatfield, R. D.; Ralph, S. A.; Christensen, J. H.; Boerjan, W., Lignins: Natural polymers from oxidative coupling of 4-hydroxyphenyl- propanoids. *Phytochemistry Reviews* **2004,** *3*, 29-60.

(25) Vanholme, R.; Demedts, B.; Morreel, K.; Ralph, J.; Boerjan, W., Lignin biosynthesis and structure. *Plant Physiol* **2010,** *153*, 895-905.

(26) Nguyen, J. D.; Matsuura, B. S.; Stephenson, C. R., A photochemical strategy for lignin degradation at room temperature. *J Am Chem Soc* **2014,** *136*, 1218-21.

(27) Sergeev, A. G.; Hartwig, J. F., Selective, Nickel-Catalyzed Hydrogenolysis of Aryl Ethers. *Science* **2011,** *332*, 439-443.

(28) Galkin, M. V.; Samec, J. S., Selective route to 2-propenyl aryls directly from wood by a tandem organosolv and palladium-catalysed transfer hydrogenolysis. *ChemSusChem* **2014,** *7*, 2154-8.

(29) Wang, M.; Li, L. H.; Lu, J. M.; Li, H. J.; Zhang, X. C.; Liu, H. F.; Luo, N. C.; Wang, F., Acid promoted C–C bond oxidative cleavage of β-O-4 and β-1 lignin models to esters over a copper catalyst. *Green Chemistry* **2017,** *19*, 702-706.

(30) Zhu, C.; Ding, W.; Shen, T.; Tang, C.; Sun, C.; Xu, S.; Chen, Y.; Wu, J.; Ying, H., Metallo-deuteroporphyrin as a biomimetic catalyst for the catalytic oxidation of lignin to aromatics. *ChemSusChem* **2015,** *8*, 1768-78.

(31) Sedai, B.; Díaz-Urrutia, C.; Baker, R. T.; Wu, R.; Silks, L. A. P.; Hanson, S. K., Aerobic Oxidation of β-1 Lignin Model Compounds with Copper and Oxovanadium Catalysts. *ACS Catalysis* **2013,** *3*, 3111-3122.

(32) Lancefield, C. S.; Ojo, O. S.; Tran, F.; Westwood, N. J., Isolation of functionalized phenolic monomers through selective oxidation and C-O bond cleavage of the beta-O-4 linkages in lignin. *Angew Chem Int Ed Engl* **2015,** *54*, 258-62.

(33) Galkin, M. V.; Sawadjoon, S.; Rohde, V.; Dawange, M.; Samec, J. S. M., Mild Heterogeneous Palladium-Catalyzed Cleavage of β-O-4′-Ether Linkages of Lignin Model Compounds and Native Lignin in Air. *ChemCatChem* **2014,** *6*, 179-184.

(34) Chan, J. M. W.; Bauer, S.; Sorek, H.; Sreekumar, S.; Wang, K.; Toste, F. D., Studies on the Vanadium-Catalyzed Nonoxidative Depolymerization of Miscanthus giganteus-Derived Lignin. *ACS Catalysis* **2013,** *3*, 1369-1377.

(35) Karkas, M. D.; Bosque, I.; Matsuura, B. S.; Stephenson, C. R., Photocatalytic Oxidation of Lignin Model Systems by Merging Visible-Light Photoredox and Palladium Catalysis. *Org Lett* **2016,** *18*, 5166-5169.

(36) Bosque, I.; Magallanes, G.; Rigoulet, M.; Karkas, M. D.; Stephenson, C. R. J., Redox Catalysis Facilitates Lignin Depolymerization. *ACS Cent Sci* **2017,** *3*, 621-628.

(37) Karkas, M. D.; Matsuura, B. S.; Monos, T. M.; Magallanes, G.; Stephenson, C. R., Transition-metal catalyzed valorization of lignin: the key to a sustainable carbon-neutral future. *Org Biomol Chem* **2016,** *14*, 1853-914.

(38) Rahimi, A.; Azarpira, A.; Kim, H.; Ralph, J.; Stahl, S. S., Chemoselective metal-free aerobic alcohol oxidation in lignin. *J Am Chem Soc* **2013,** *135*, 6415-8.

(39) Zakzeski, J.; Bruijnincx, P. C. A.; Jongerius, A. L.; Weckhuysen, B. M., The Catalytic Valorization of Lignin for the Production of Renewable Chemicals. *Chem. Rev.* **2010,** *110*, 3552-3599.

(40) Adler, E., Lignin chemistry—past, present and future. *Wood Science and Technology* **1977,** *11*, 169-218.

(41) Bruchez, M.; Moronne, M.; Gin, P.; Weiss, S.; Alivisatos, A. P., Semiconductor Nanocrystals as Fluorescent Biological Labels. *Science* **1998,** *281*, 2013-2016.

(42) Chan, W. C. W.; Nie, S., Quantum Dot Bioconjugates for Ultrasensitive Nonisotopic Detection. *Science* **1998,** *281*, 2016-2018.

(43) Jasieniak, J.; Califano, M.; Watkins, S. E., Size-Dependent Valence and Conduction Band-Edge Energies of Semiconductor Nanocrystals. *ACS Nano* **2011,** *5*, 5888-5902.

(44) Wakerley, D. W.; Kuehnel, M. F.; Orchard, K. L.; Ly, K. H.; Rosser, T. E.; Reisner, E., Solar-driven reforming of lignocellulose to H2 with a CdS/CdOx photocatalyst. *Nature Energy* **2017,** *2*.

(45) Narayanam, J. M. R.; Tucker, J. W.; Stephenson, C. R. J., Electron-Transfer Photoredox Catalysis: Development of a Tin-Free Reductive Dehalogenation Reaction. *J. Am. Chem. Soc.* **2009,** *131*, 8756-8757.

(46) Nguyen, J. D.; D'Amato, E. M.; Narayanam, J. M.; Stephenson, C. R., Engaging unactivated alkyl, alkenyl and aryl iodides in visible-light-mediated free radical reactions. *Nat Chem* **2012,** *4*, 854-9.

(47) Crawford, R. L.; Robinson, L. E.; Foster, R. D., Polyguaiacol: a Useful Model Polymer for Lignin Biodegradation Research. *Applied and Environmental Microbiology* **1981,** *41*, 1112-1116.

(48) Kroupa, D. M.; Voros, M.; Brawand, N. P.; McNichols, B. W.; Miller, E. M.; Gu, J.; Nozik, A. J.; Sellinger, A.; Galli, G.; Beard, M. C., Tuning colloidal quantum dot band edge positions through solution-phase surface chemistry modification. *Nat Commun* **2017,** *8*, 15257.

(49) Condie, A. G.; González-Gómez, J. C.; Stephenson, C. R. J., Visible-Light Photoredox Catalysis: Aza-Henry Reactions via C−H Functionalization. *J. Am. Chem. Soc.* **2010,** *132*, 1464-1465.

(50) Yun, H. J.; Paik, T.; Edley, M. E.; Baxter, J. B.; Murray, C. B., Enhanced charge transfer kinetics of CdSe quantum dot-sensitized solar cell by inorganic ligand exchange treatments. *ACS Appl Mater Interfaces* **2014,** *6*, 3721-8.

(51) Wilker, M. B.; Utterback, J. K.; Greene, S.; Brown, K. A.; Mulder, D. W.; King, P. W.; Dukovic, G., Role of Surface-Capping Ligands in Photoexcited Electron Transfer between CdS Nanorods and [FeFe] Hydrogenase and the Subsequent H2 Generation. *J. Phys. Chem. C* **2017,** *122*, 741-750.

(52) Nichols, J. M.; Bishop, L. M.; Bergman, R. G.; Ellman, J. A., Catalytic C−O Bond Cleavage of 2-Aryloxy-1-arylethanols and Its Application to the Depolymerization of Lignin-Related Polymers. *J. Am. Chem. Soc.* **2010,** *132*, 16725-16725.

(53) Jasieniak, J.; Smith, L.; van Embden, J.; Mulvaney, P.; Califano, M., Re-examination of the Size-Dependent Absorption Properties of CdSe Quantum Dots. *The Journal of Physical Chemistry C* **2009,** *113*, 19468-19474.

APPENDIX A

Collection of TEM images from Chapter 2: Kinetically controlled assembly of cadmium chalcogenide nanorods and nanorod heterostructures

6 min

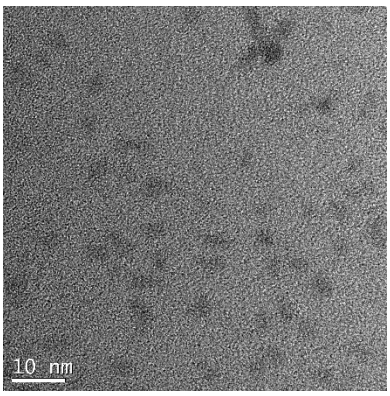

14 min

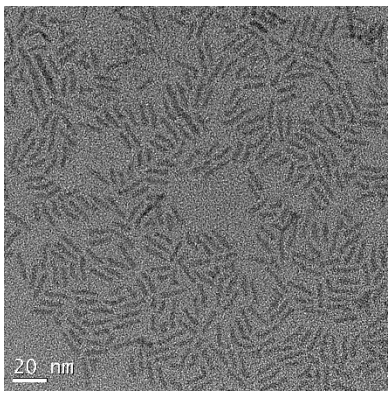

20 min

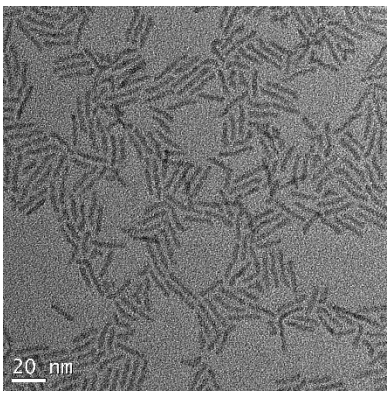

10 min

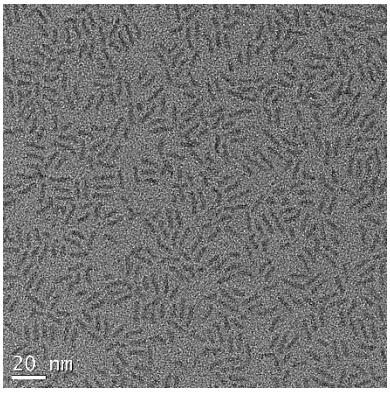

16 min

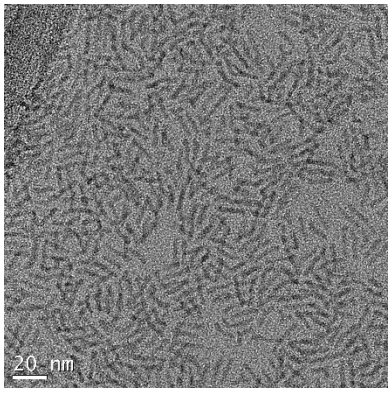

22 min

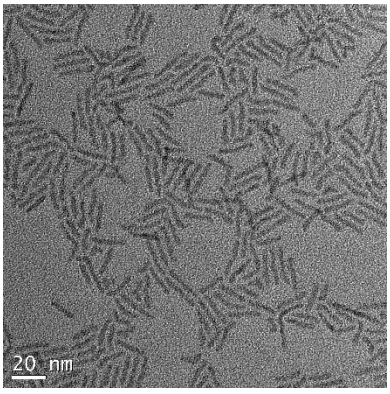

12 min

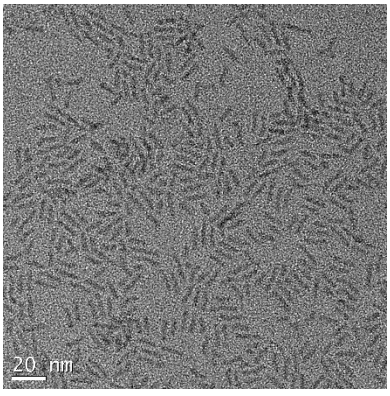

18 min

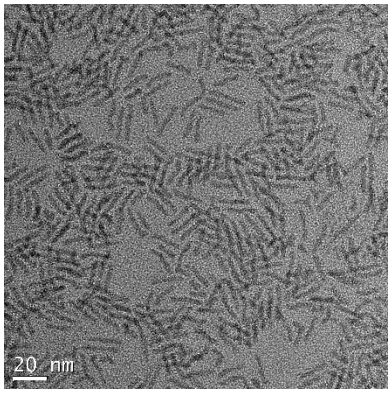

24 min

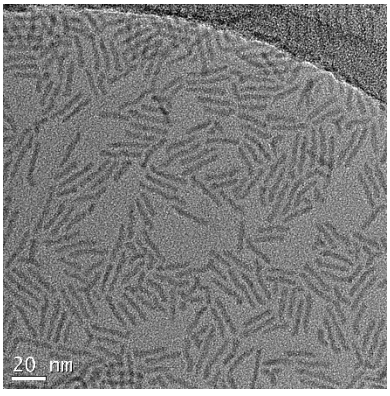

(Continues on next page)

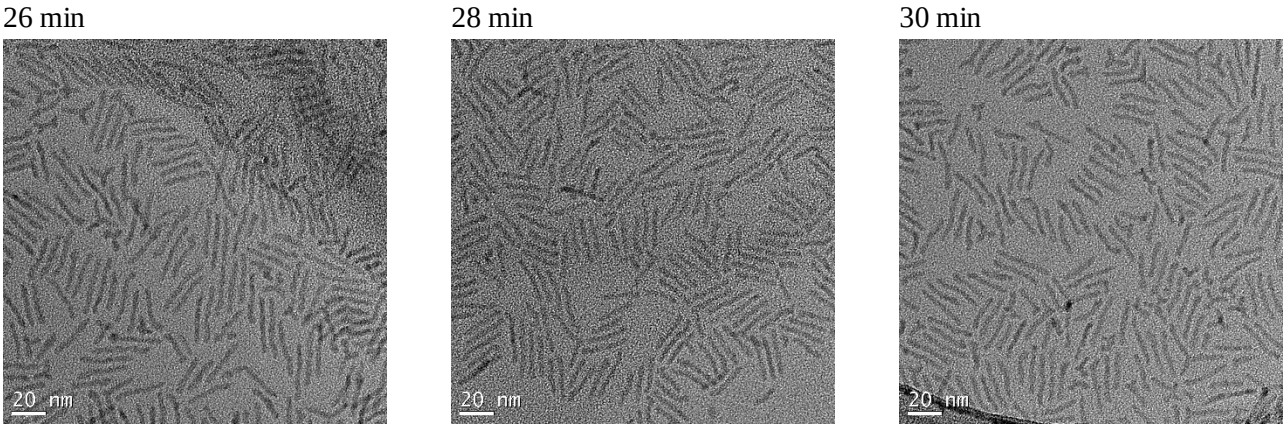

Figure A.17. TEM images of unseeded CdSe nanorod growth. These images correspond to data reported in Figure 2.1 of the main text.

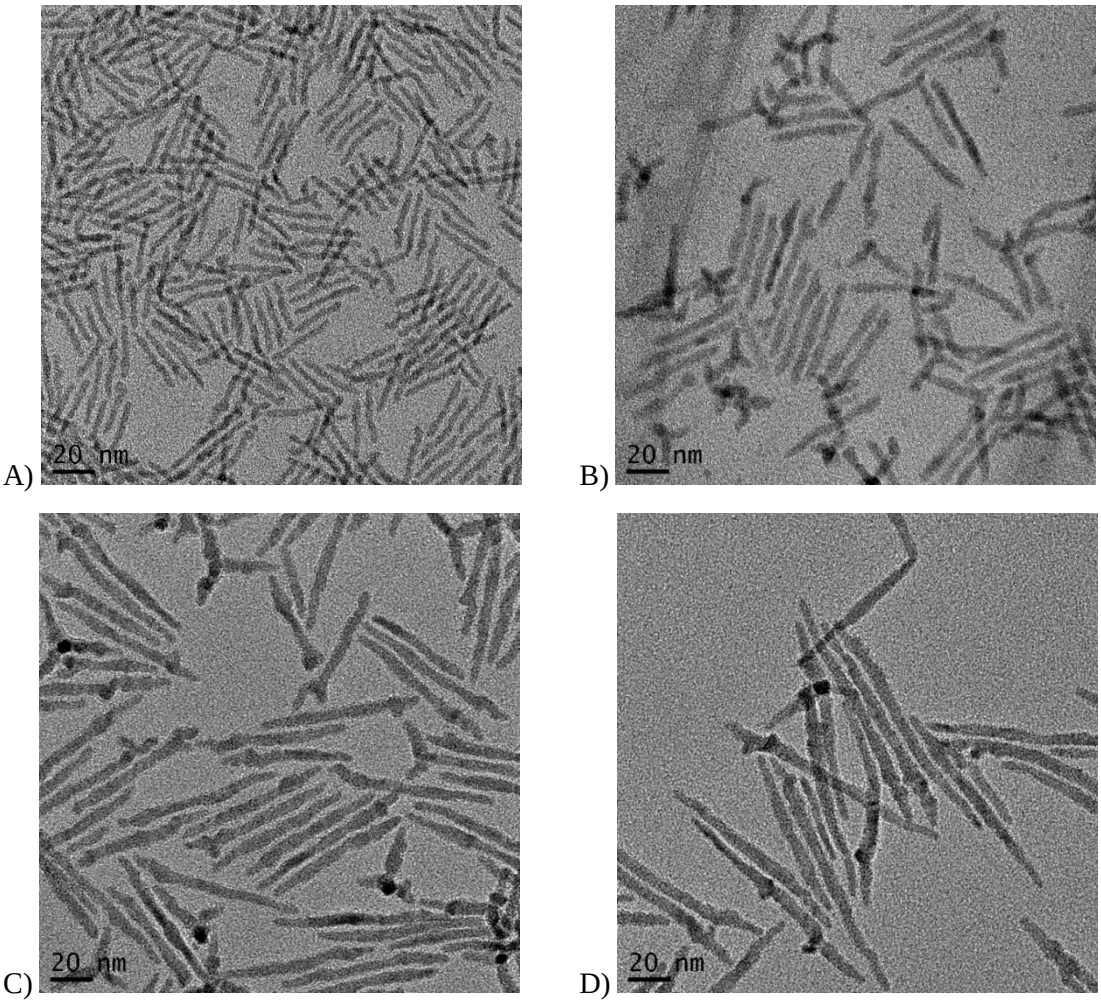

Figure A.18. Progressive elongation of CdSe starting from CdSe nanorods. The starting 27.6 ± 2.9 nm by 2.9 ± 0.4 nm nanorods (A). The increased dimensions are 44.4 ± 6.5 nm by 4.4 ± 0.6 nm after 30 min (B), 69.8 ± 9.1 nm by 5.2 ± 0.8 nm after 30 min (C), and 99.3 ± 15.1 nm 5.9 ± 1.0 nm after 65 min (D).

2 min (CdSe seeds)

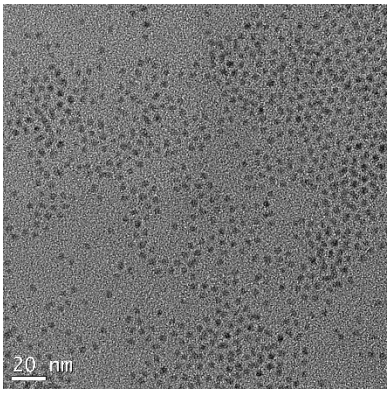

10 min

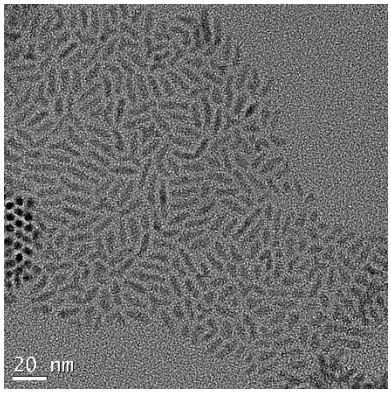

18 min

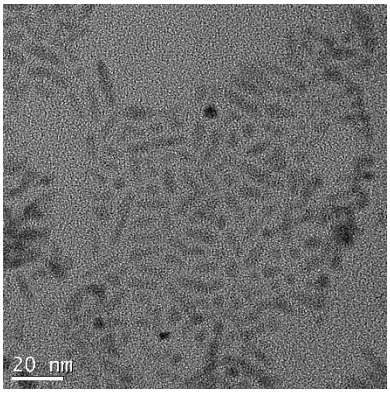

4 min

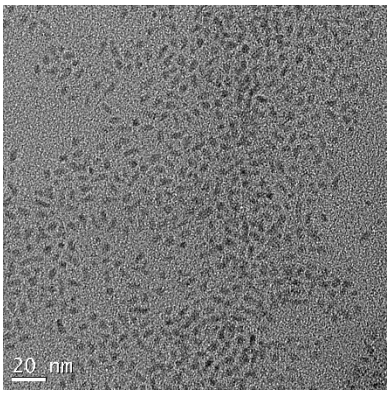

12 min

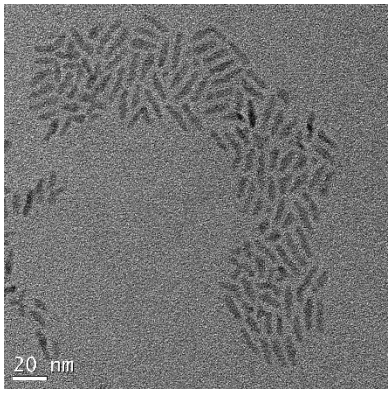

20 min

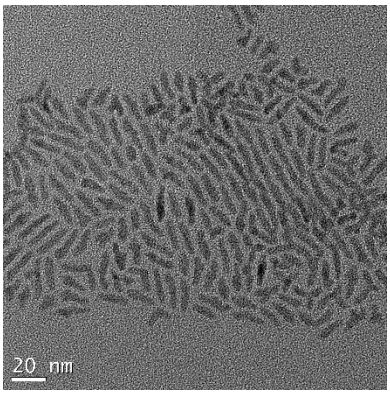

6 min

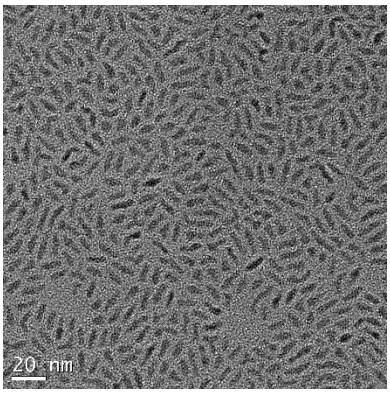

14 min

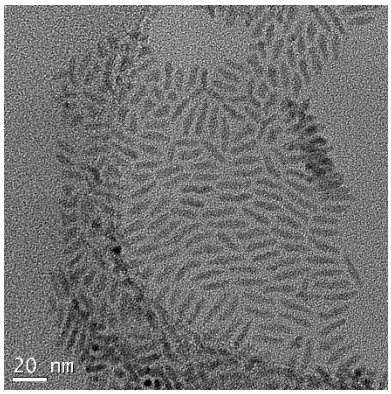

22 min

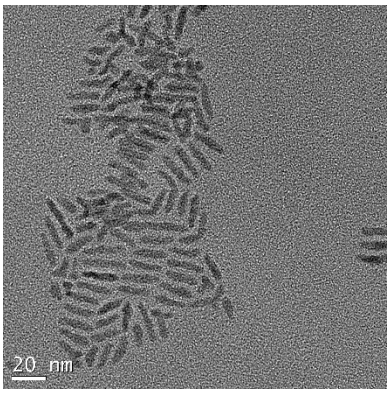

8 min

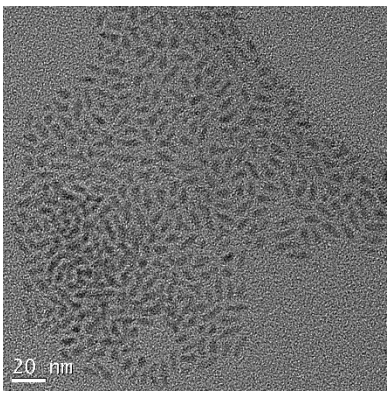

16 min

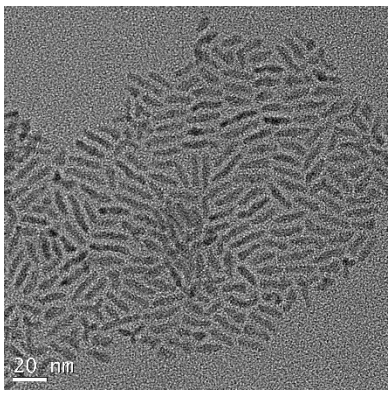

24 min

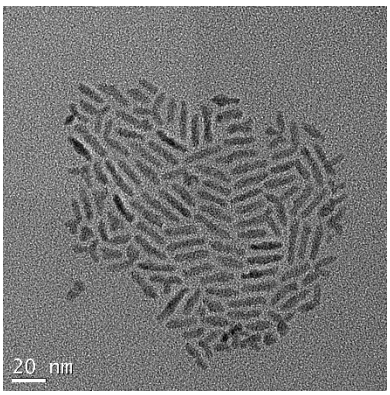

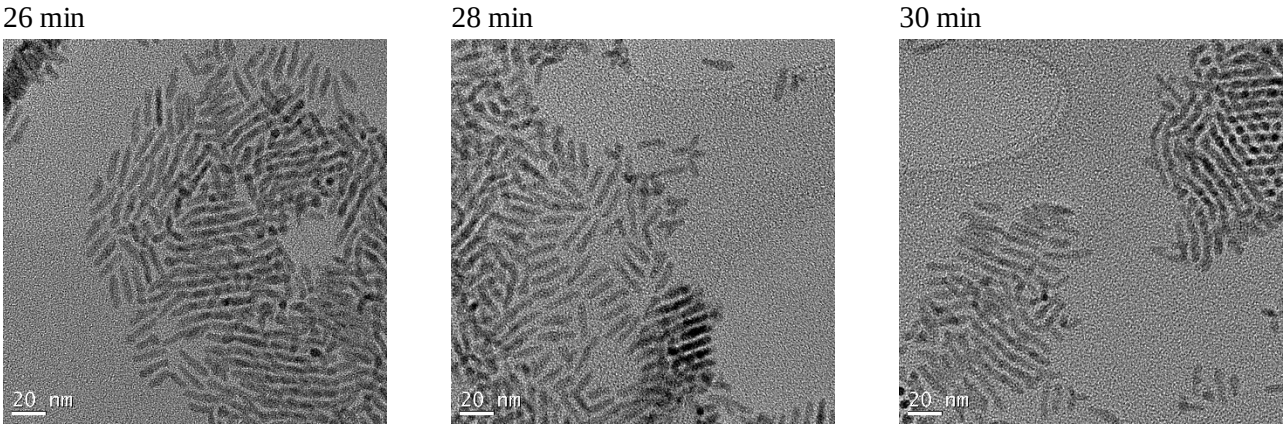

Figure A.19. TEM images of growing CdSe nanorods upon $2.73*10^{-7}$ mol seeds.

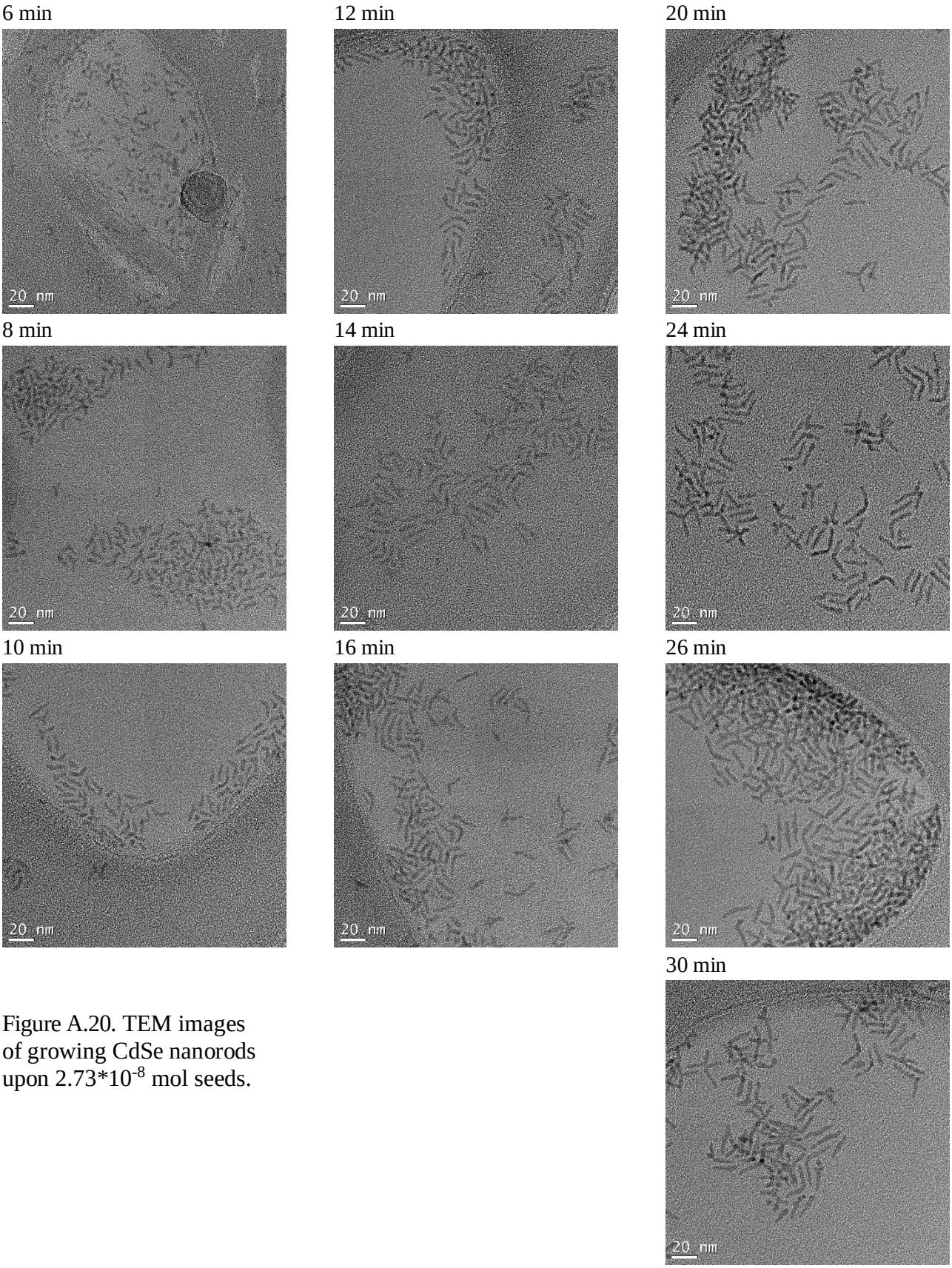

Figure A.20. TEM images of growing CdSe nanorods upon $2.73*10^{-8}$ mol seeds.

6 min

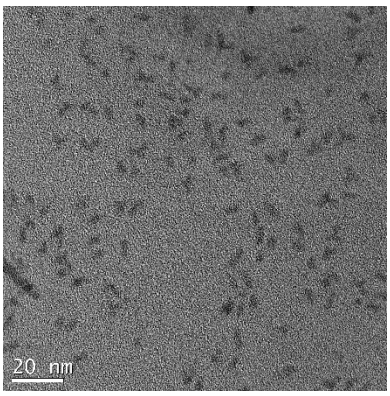

15 min

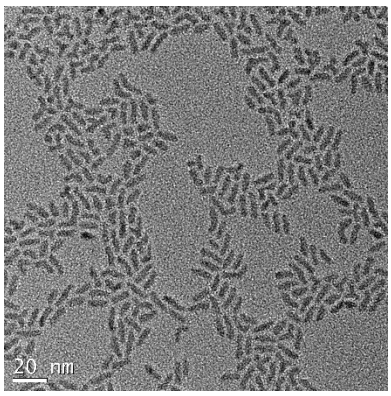

24 min

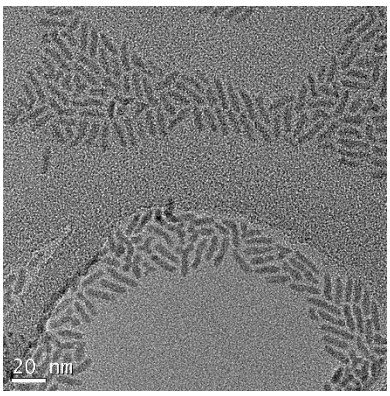

9 min

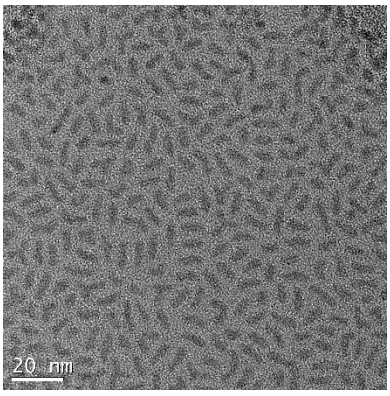

18 min

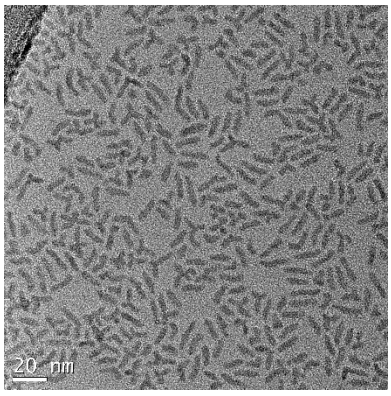

27 min

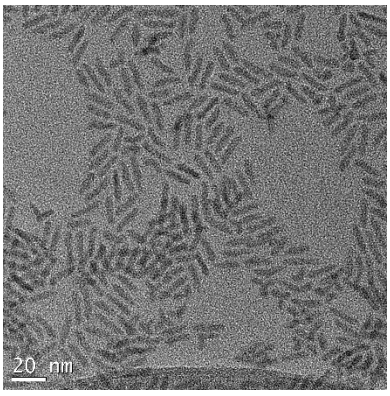

12 min

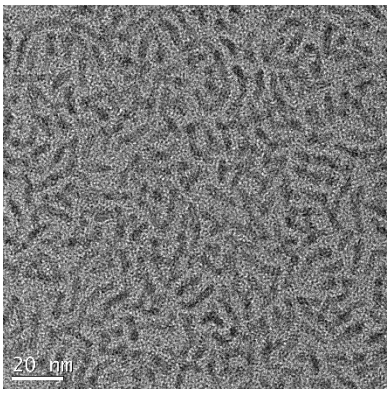

21 min

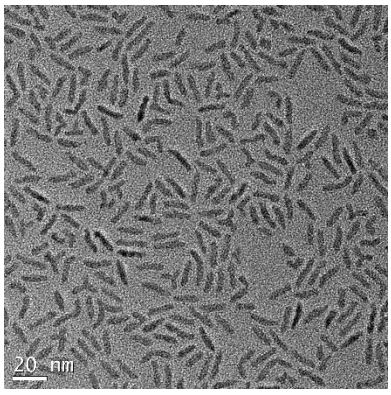

30 min

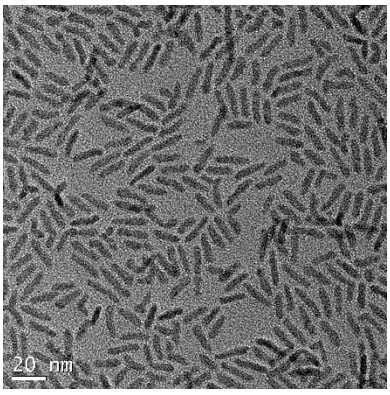

(Continues on next page)

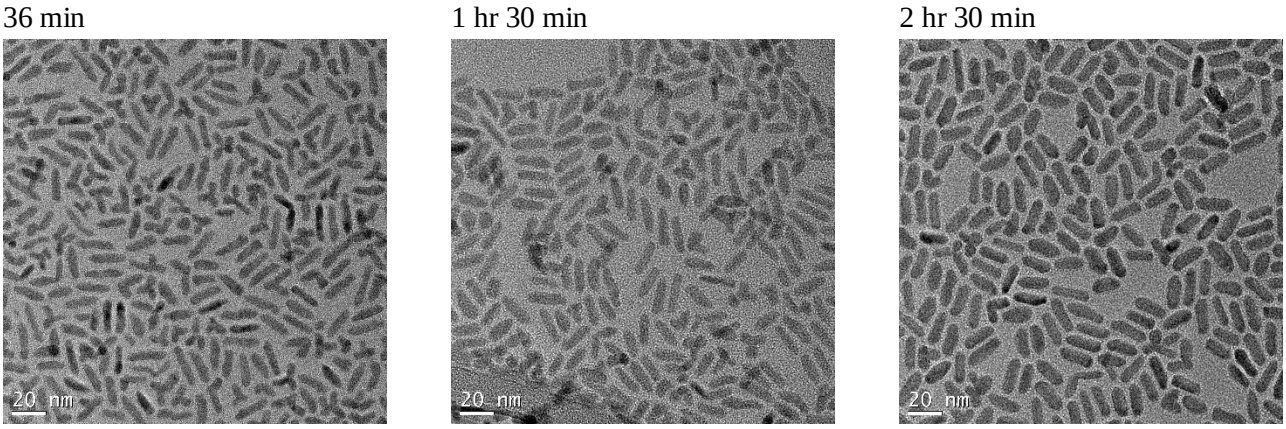

Figure A.21. TEM images of growing CdSe nanorods upon $1.0*10^{-8}$ mol seeds.

.

2 min (CdS seeds)

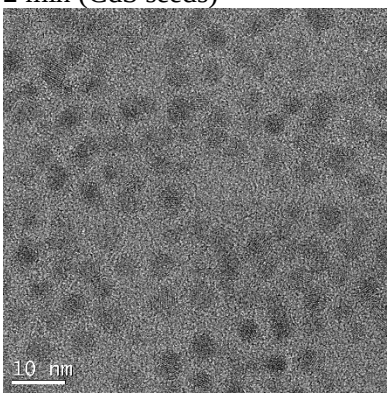

10 min

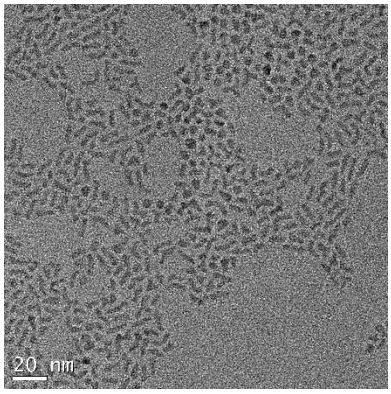

18 min

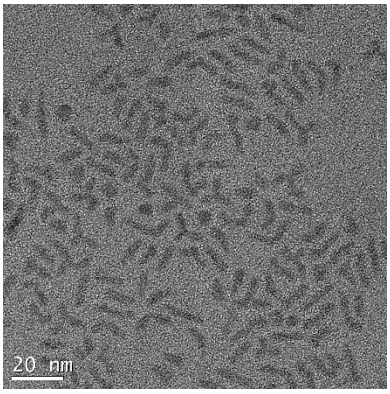

4 min

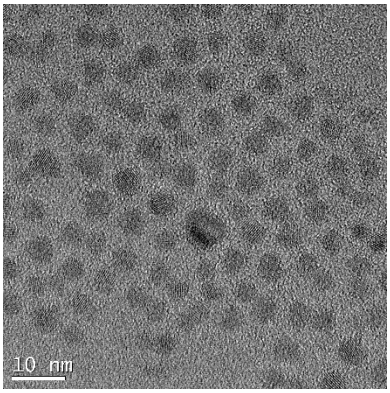

12 min

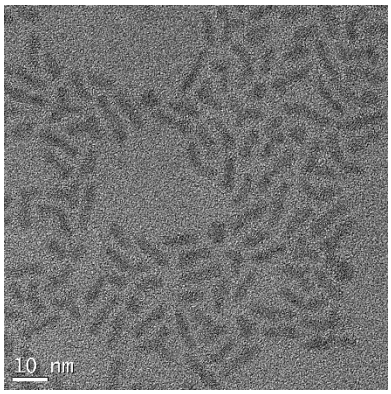

20 min

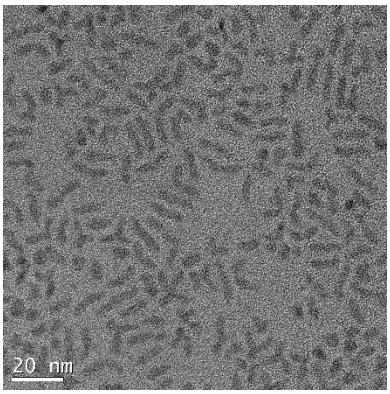

6 min

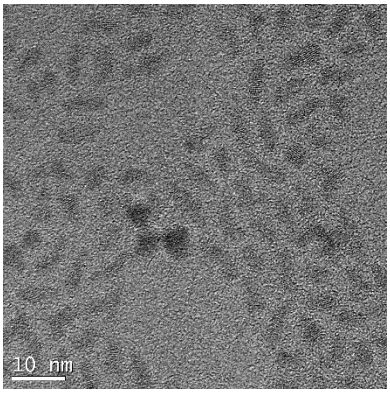

14 min

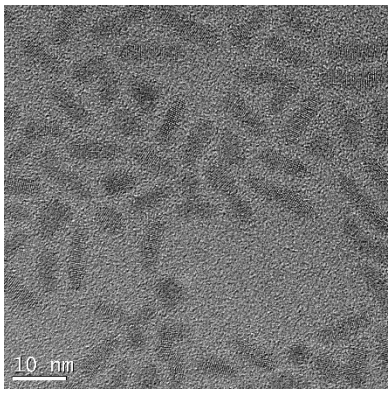

24 min

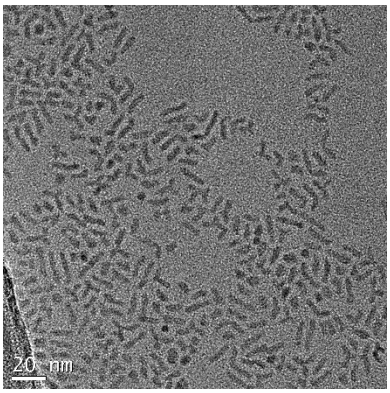

8 min

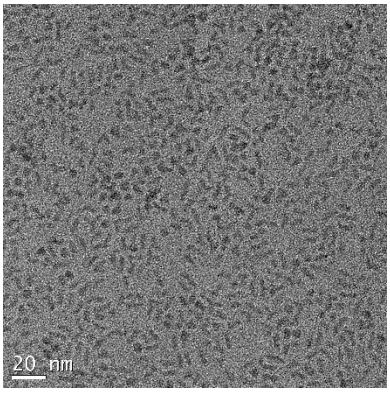

16 min

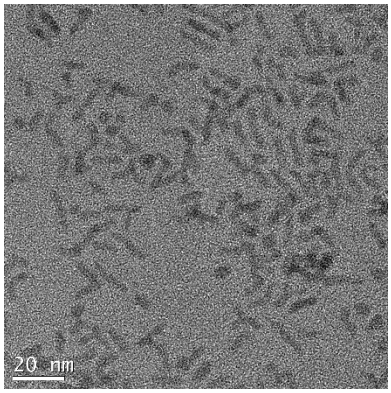

26 min

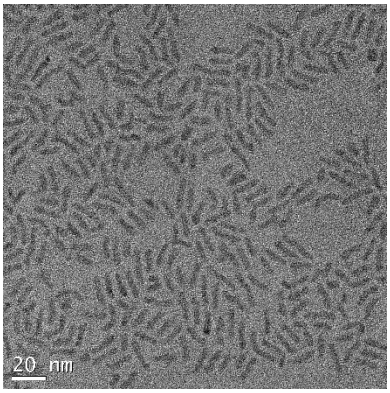

28 min

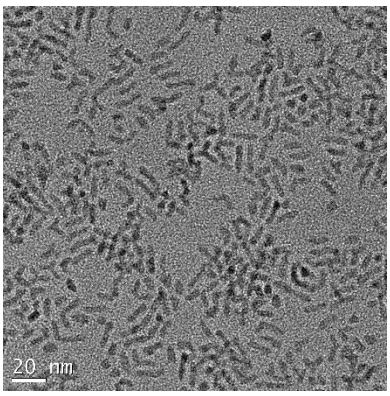

30 min

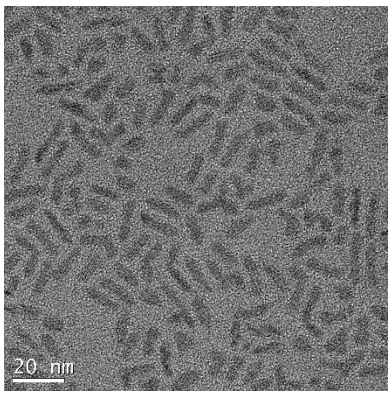

Figure A.22. TEM images of CdSe nanorod growth on $2.73*10^{-7}$ mol CdS seeds.

2 min

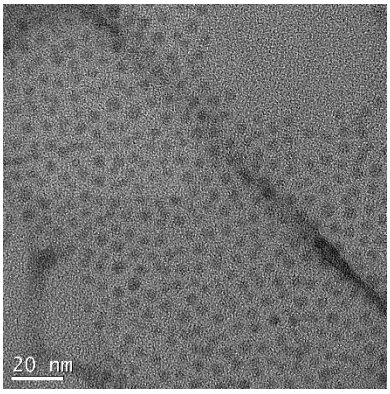

10 min

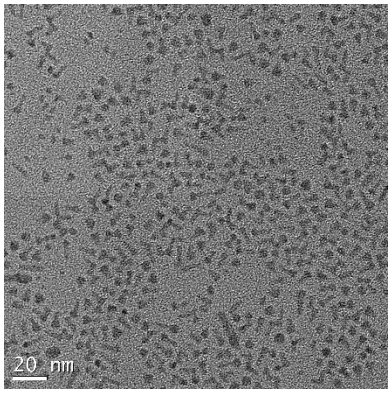

18 min

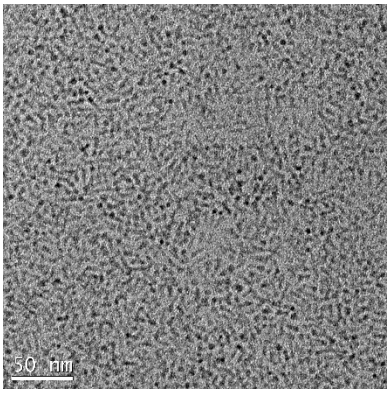

4 min

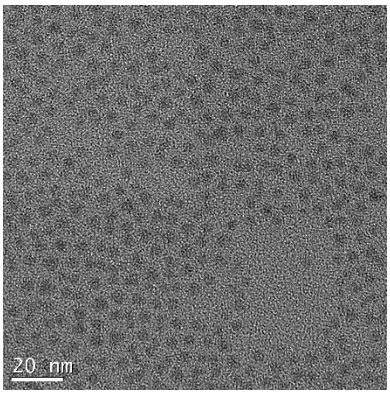

12 min

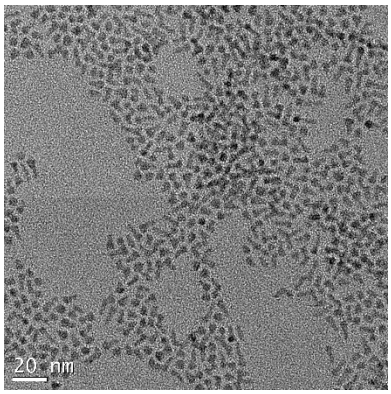

20 min

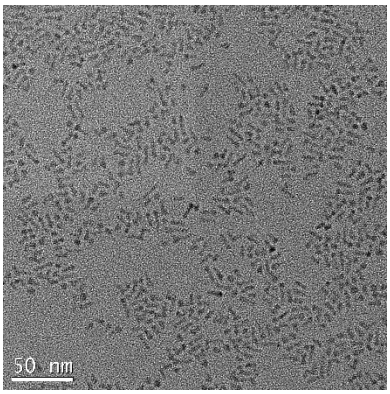

6 min

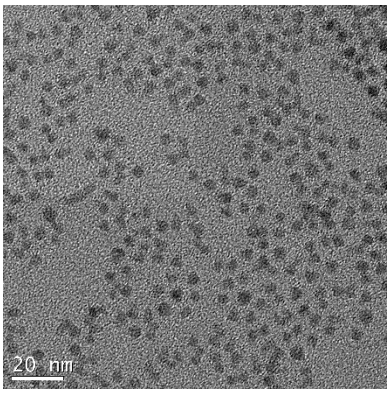

14 min

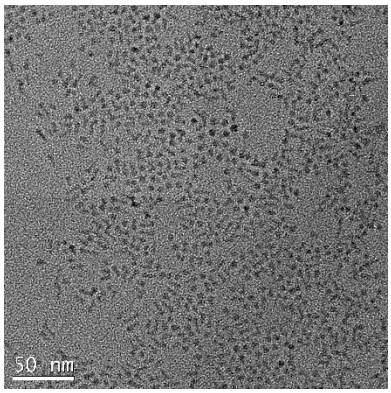

22 min

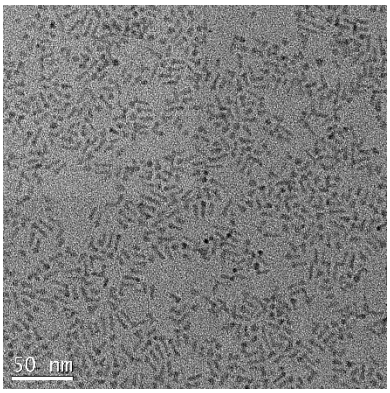

8 min

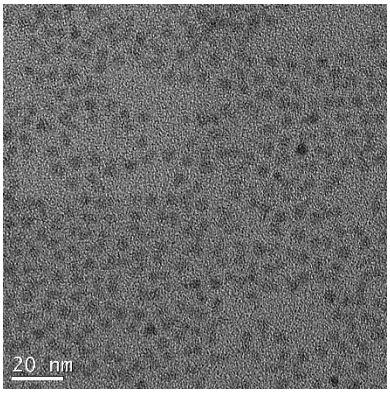

16 min

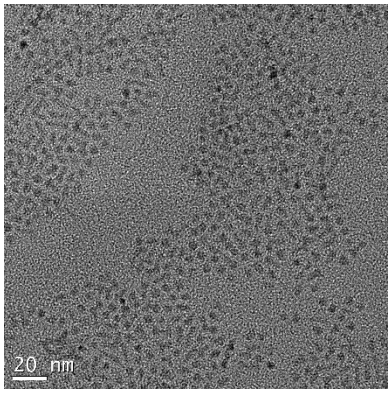

24 min

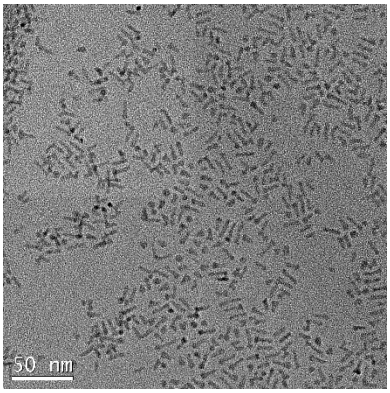

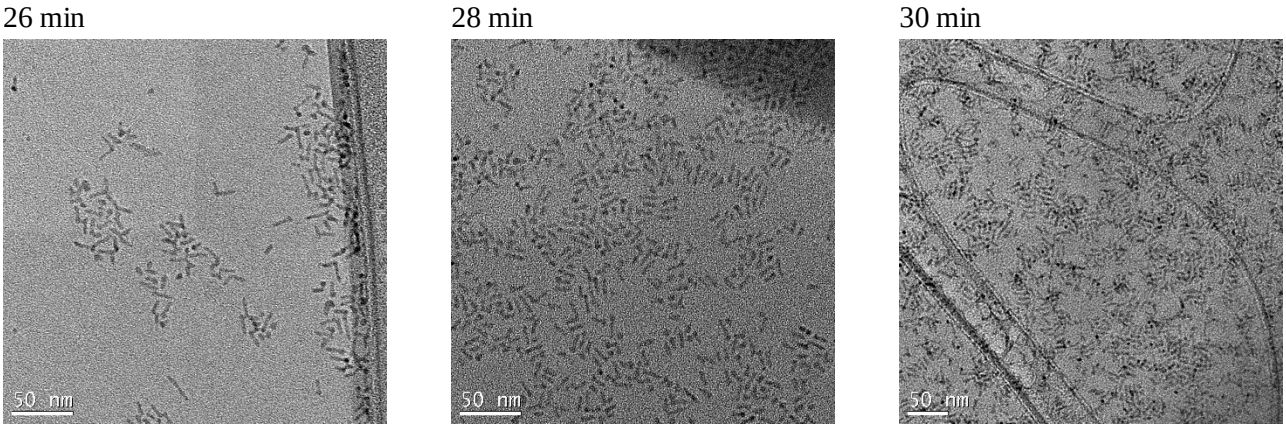

Figure A.23. TEM images of CdSe nanorod growth on $8.19*10^{-7}$ mol CdS seeds.

3 min

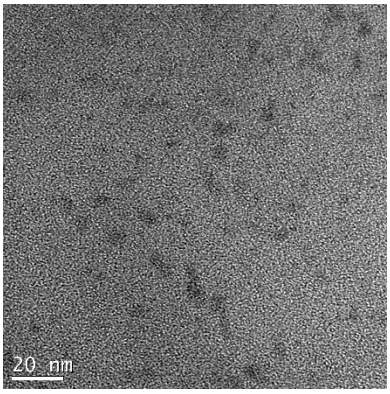

9 min

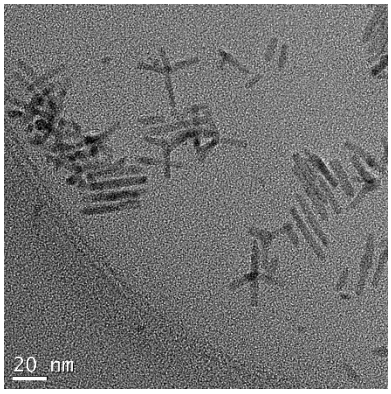

15 min

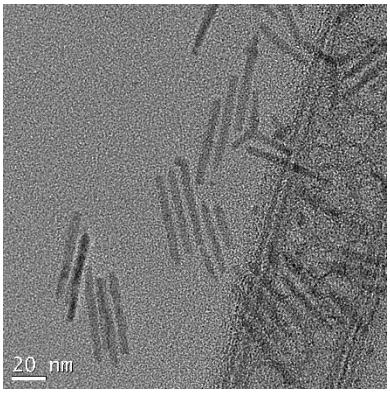

4.5 min

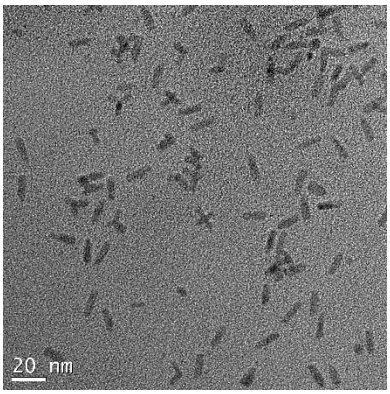

10.5 min

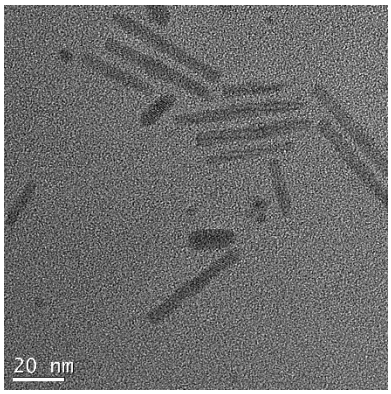

17.5 min

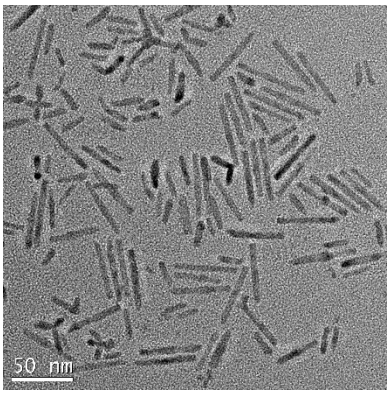

6 min

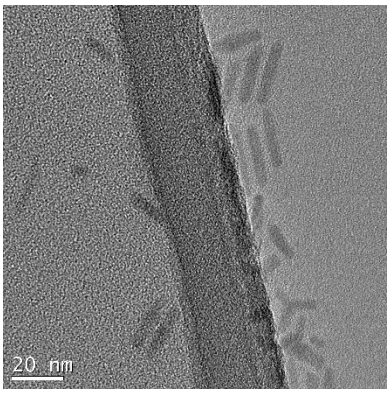

12 min

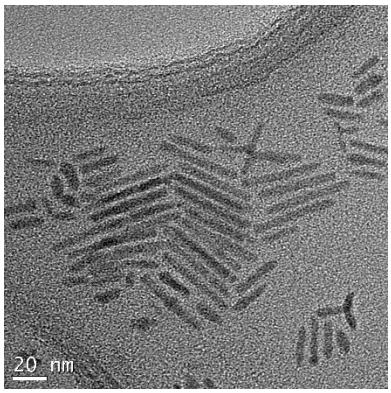

20 min

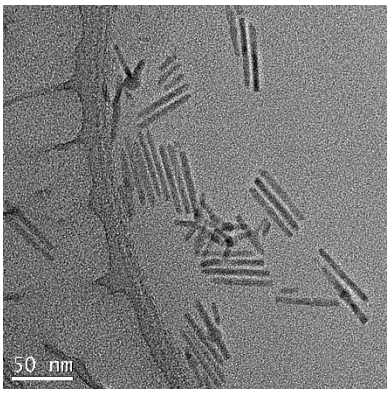

7.5 min

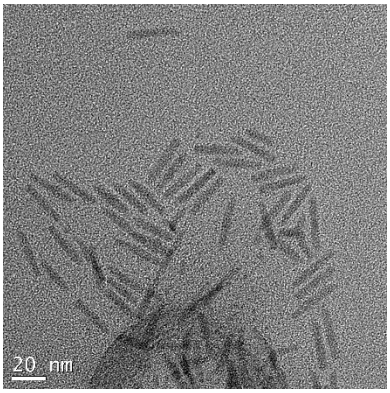

13.5 min

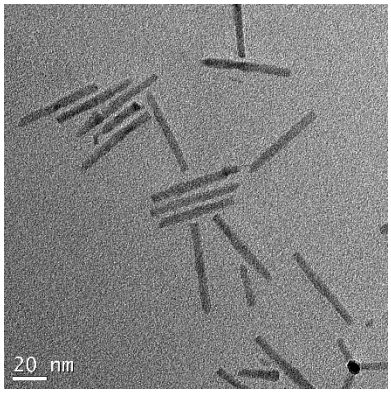

26 min

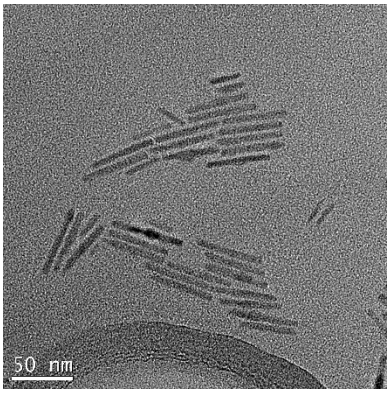

30 min

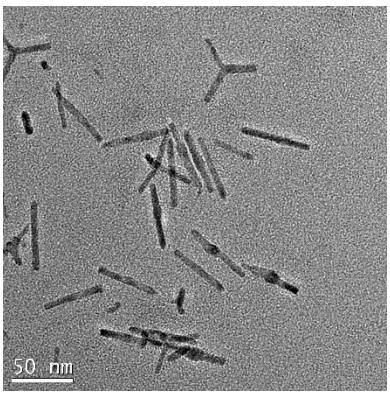

60 min

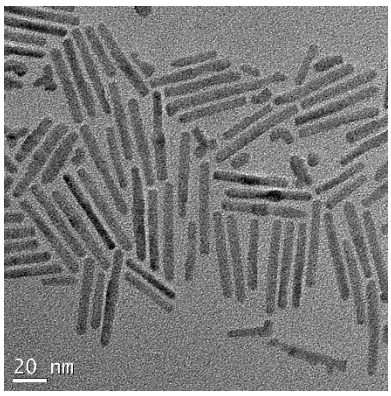

Figure A.24. TEM images of the growing CdS nanorods on CdSe seeds.

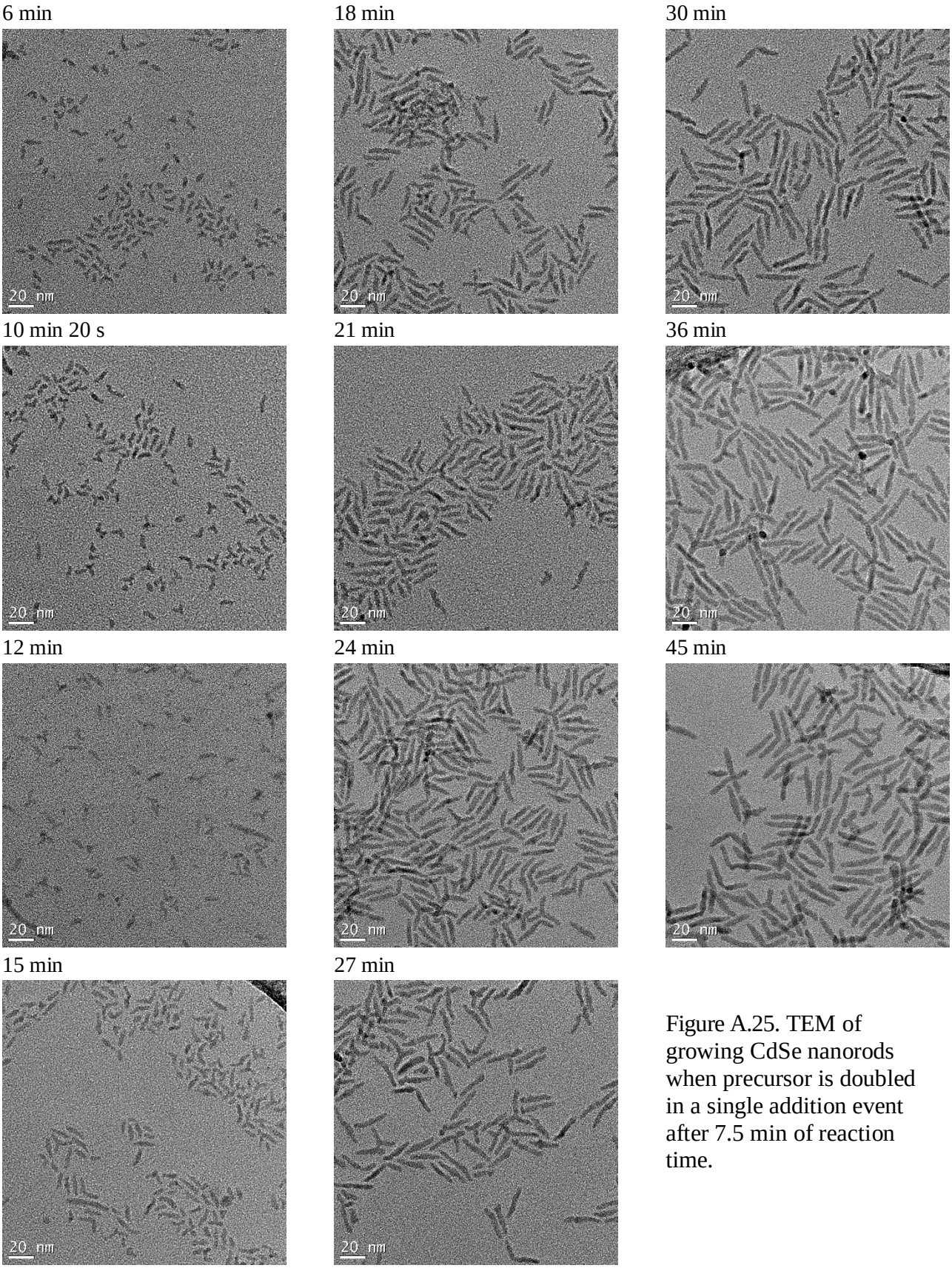

Figure A.25. TEM of growing CdSe nanorods when precursor is doubled in a single addition event after 7.5 min of reaction time.

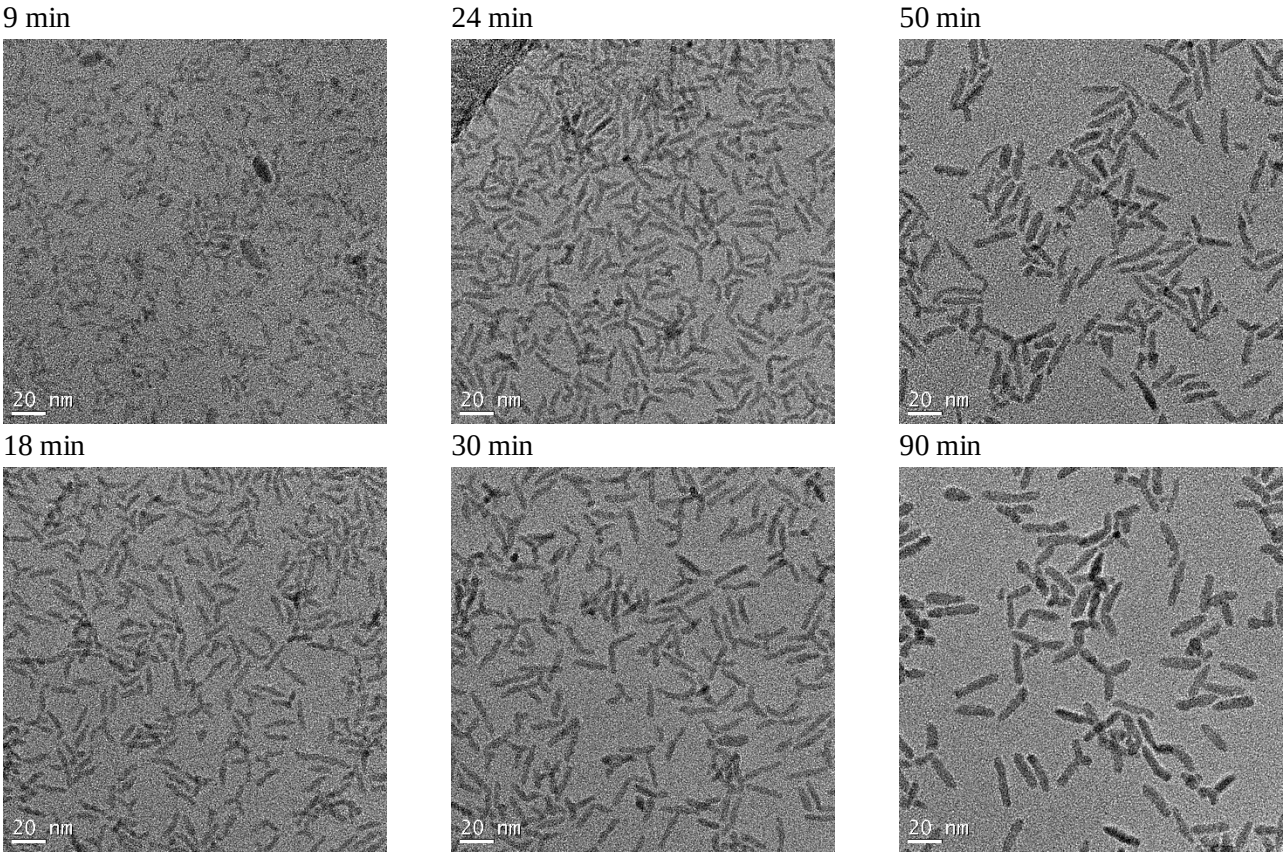

Figure A.26. TEM of growing CdSe nanorods when 50% more precursor is added in a single event after 7.5 min of reaction time.

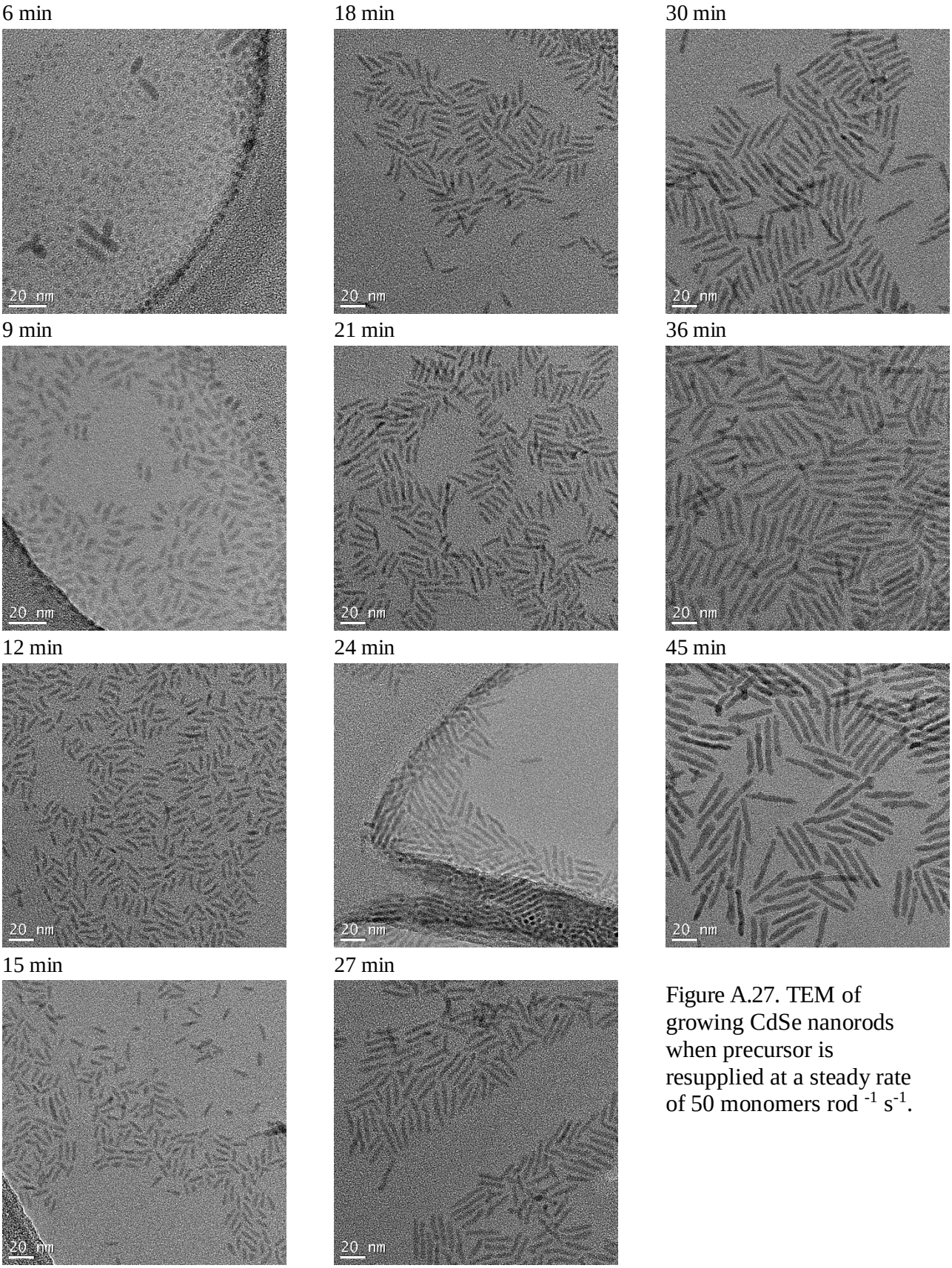

Figure A.27. TEM of growing CdSe nanorods when precursor is resupplied at a steady rate of 50 monomers rod $^{-1}$ s^{-1}.

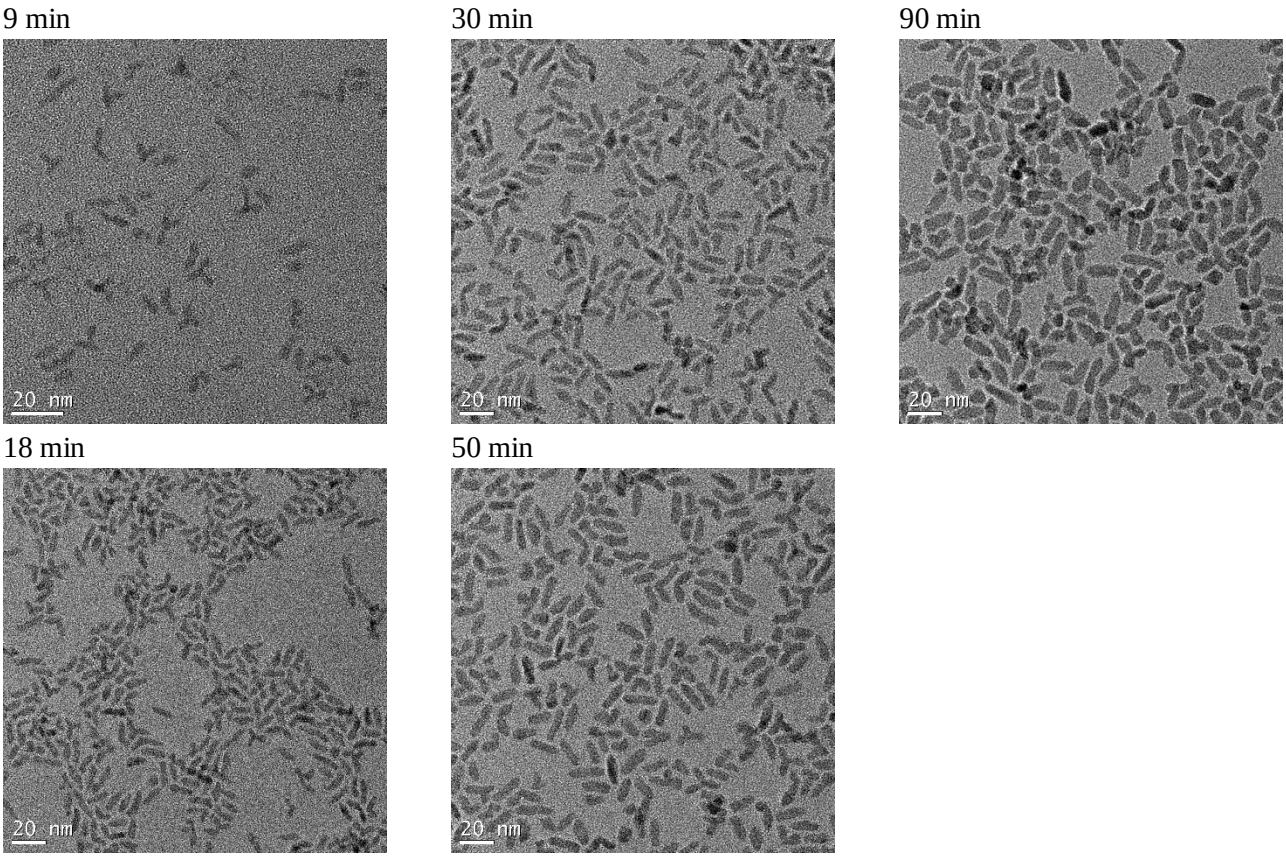

Figure A.28. TEM of growing CdSe nanorods when precursor is resupplied at a steady rate of 3.5 monomers rod $^{-1}$ s^{-1}.

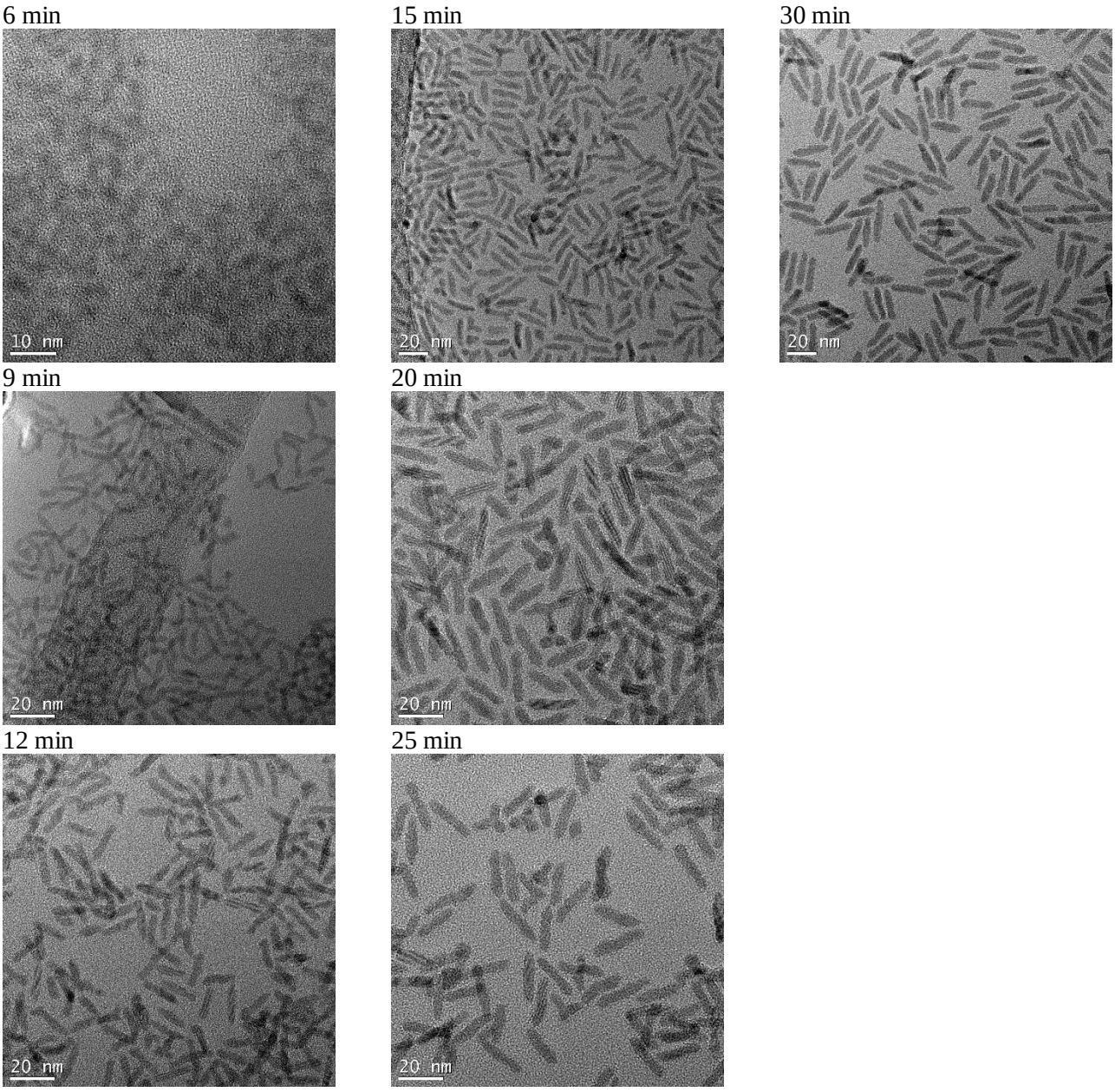

Figure A.29. TEM of growing CdSe nanorods when extra TDPA is added at 7.5 min.

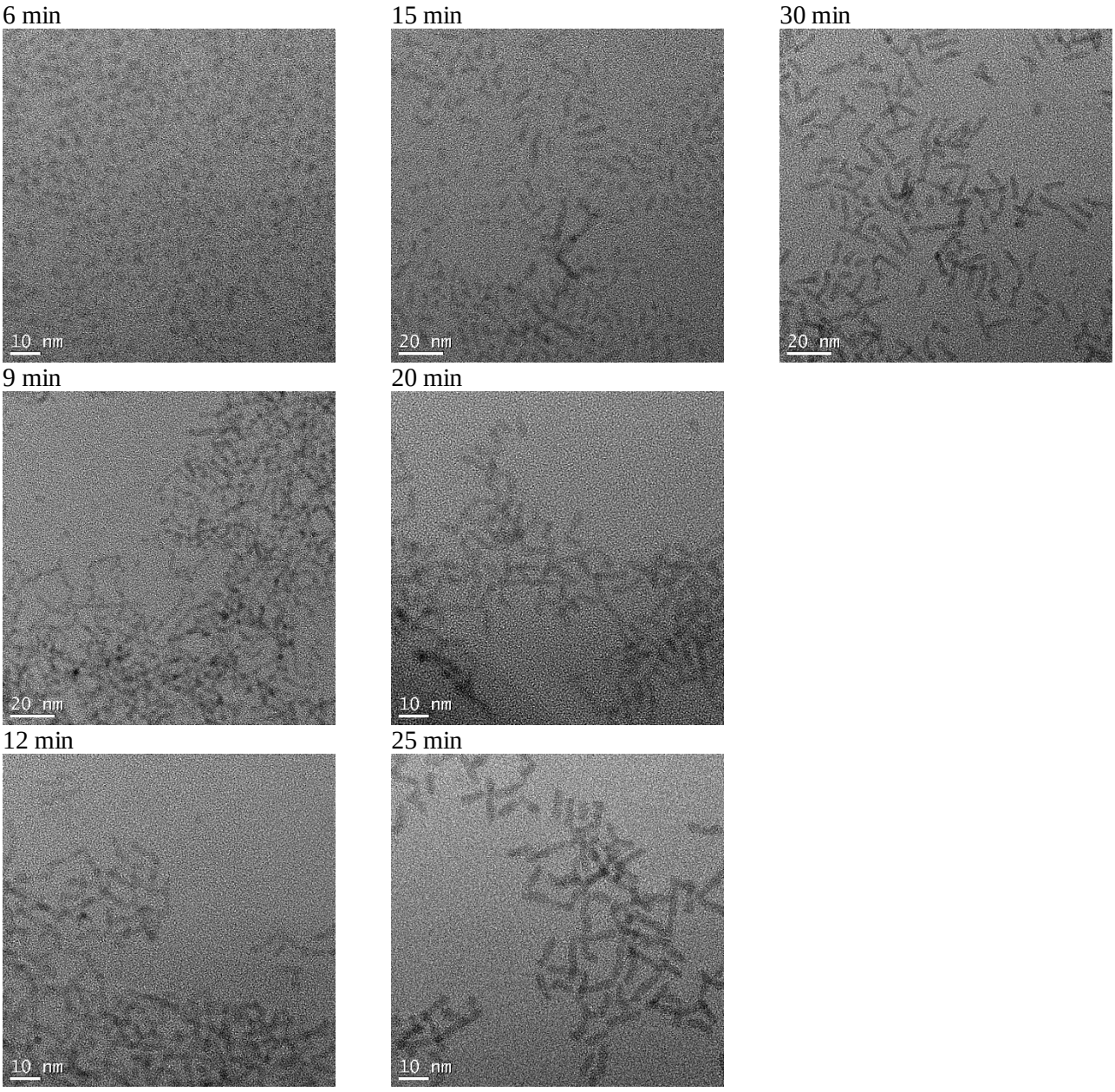

Figure A.30. TEM of growing CdSe nanorods when extra TOP is added at 7.5 min.

VITA

Michael Job Enright was born in 1991 to parents Bob and Joan Enright and grew up in Stevens Point, WI. Three years later he was joined by his brother Robert. Michael graduated from Stevens Point Area Senior High School in 2010 and went on to Ripon College to study Chemistry as the Knop Scholar. At Ripon, Michael researched silver catalyzed carbon-nitrogen bond formation computationally under the guidance of Professor Joseph Scanlon. As an undergraduate, Michael participated in two summer internships. In the summer of 2012, he traveled to the University of Massachusetts Amherst to research ligand-core interactions and ligand stability on gold nanoparticles under the direction of Professor Richard Vachet and his research mentor Bo Yan. In the fall of 2012, Michael became an EPA GRO-U fellow and conducted research over the summer of 2013 at the EPA's Western Ecological Division in Corvallis, OR, where he explored the environmental impact of human engineered nanomaterials with Dr. Mark Johnson, Dr. Chris Andersen, and Dr. Paul Rygiewicz. Michael graduated from Ripon College in 2014 with an A.B. in Chemistry and a minor in Spanish.

In the summer of 2014, Michael began his graduate research at the University of Washington with Professor Brandi Cossairt and his research is documented within this composition. As a graduate student at the University of Washington, Michael became a Clean Energy Institute (CEI) fellow and was involved in the development of the CEI's Research Training Testbeds (RTT) and the globally unique Energy, Materials, Devices, and Systems laboratory based course taught in the RTT instrument facility. Michael also taught a quarter of General Chemistry Lab II at Seattle University in the Winter of 2019 before graduating from the University of Washington with his Doctor of Philosophy in Chemistry in the Spring of 2019. Michael plans to

continue research as a postdoctoral scholar in the Summer of 2019 at the University of Illinois at Urbana-Champaign with Professor Ralph Nuzzo investigating luminescent solar concentrators.